School of Electrical Engineering Computing and Mathematical Sciences

Investigation of Metal Carbonates for Cost-Competitive Thermal Batteries

KYRAN WILLIAMSON

This thesis is presented for the degree of

Doctor of Philosophy at

Curtin University

August 2023

Declaration

To the best of my knowledge and belief, this thesis contains no material previously published by anyone except where due acknowledgement has been made.

This thesis contains no material which has been accepted for the award of any other degree or diploma in any university.

Kyran Williamson

Signature:.....

Date:..07/12/2023……

Acknowledgement of country

We acknowledge that Curtin University works across hundreds of traditional lands and custodial groups in Australia, and with First Nations people around the globe. We wish to pay our deepest respects to their ancestors and members of their communities, past, present, and to their emerging leaders. Our passion and commitment to work with all Australians and peoples from across the world, including our First Nations peoples are at the core of the work we do, reflective of our institutions' values and commitment to our role as leaders in the Reconciliation space in Australia.

Acknowledgements

I would like to acknowledge all those who helped me complete my PhD journey. First of all, I would like to express my sincerest gratitude towards my principal supervisor Associate Professor Mark Paskevicius for guiding me supporting me and always having my back in difficult times. For believing in me despite multiple personal and professional setbacks along the way. For almost always having an answer for every technical and scientific hurdle along the way.

I would like to thank Professor Craig Buckley for his guidance and support in driving the project, as well as pulling in the funding to keep the project going. Dr Terry Humphries help was invaluable for his keen editor's eye as well as excellent support with all the equipment. Special thanks for Dr Kasper Møller for plunging me straight into the lab and getting the whole PhD started. Additional thanks to my AINSE co-supervisor Dr Anita D' Angelo for inviting me to learn about the amazing technical wonder which is the Australian Synchrotron. Also, gratitude to Dr Adriana Pires Viera and Dr Yurong Liu for working together with me on the two major Strontium papers. Also Ray Stokes was a massive help for his experimental work performed during his third year project.

I would like to thank the technical support of the Physics department Mark Winstanley, Kate Putman, Ming, Ketesse Hansen, for all there help with equipment. For funding my research, I would like to thank the Australian government for a research training program scholarship (RTP) and the Australian institute of nuclear science and technology institute (AINSE) for the AINSE postgraduate research award. Also, thanks to the John De Laeter research centre and Elaine Miller for the use of equipment, assistance and training especially Veronica Avery and Mathew Rowles.

Of course, a special thanks is reserved for all my fellow PhD students, Lucas Poupin for pushing me to fix that scooter to prove I could do a PhD! Sruthy Balakrishna, your guidance and wisdom were a huge help, and building the Pink Panther with you was awesome.

Amanda Berger and Diego De Souza, your hard work and determination were so inspiring. Ainnee, Aneeka, and Lucie, thanks for the laughs and the mental support in the office. Tom, you've been there every step of the way, and I couldn't have done it without you.

Last but not least, my family, Jorge Duran, you kept me sane, and winning the Mustang Bar pool competition was epic. To my kids, Amelia and Liam, you understood what I was doing, gave me colour choice advice, and celebrated with me – you're the best. To my amazing wife, Miriam, your sacrifices and support got me through all the tough times and helped me finish this PhD journey. I couldn’t have done it without you.

Statement of Contributions

CHAPTER 1: Presents the literature review and an introduction to the thesis, this was originally written by myself and includes contributions and corrections from Assoc Prof Mark Paskevicius, Dr Terry Humphries and Prof Craig Buckley.

CHAPTER 2: Presents the experimental section of the project, it includes the synthesis techniques and characterisation of materials. It was written by myself and includes contributions and corrections by Assoc Prof Mark Paskevicius, Dr Terry Humphries and Prof Craig Buckley.

CHAPTER 3: Presents the published work "Thermochemical Energy Storage in Barium Carbonate Enhanced by Iron(III) Oxide", this work was written by myself with revisions by all co-authors. It has been published in the journal Physical Chemistry Chemical Physics (https://doi.org/10.1039/D2CP05745J). An additional statement that details the co-authors' contributions can be found at the end of this thesis (Appendix E).

CHAPTER 4: Presents the under-review work titled "Barium carbonate and barium titanate for ultra-high temperature thermochemical energy storage ". It is currently submitted for publication and undergoing the review process. It was originally written by myself and includes contributions and revisions by all other co-authors. An additional statement that details the co-authors' contributions can be found at the end of this thesis (Appendix E).

CHAPTER 5: Presents the under-review work titled Thermochemical energy storage in $SrCO_3$ composites with $SrTiO_3$ or $SrZrO_3$. It is currently submitted for publication and undergoing the review process. It was originally written by myself and Dr Yurong Liu and includes contributions and revisions by all other co-authors. An additional statement that details the co-authors' contributions can be found at the end of this thesis (Appendix E).

CHAPTER 6: Presents the conclusions of this Ph.D. thesis and includes suggestions for future research directions, it was originally written by myself with suggestions and corrections made by Assoc Prof Mark Paskevicius, Dr Terry Humphries and Prof Craig Buckley.

Appendix A: Presents the published work "Thermochemical energy storage of a barium based reactive carbonate composite" It was originally written by Dr Kasper Møller with contributions and correction by myself and all other co-authors. It is published in the Journal of Materials Chemistry A (https://doi.org/10.1039/D0TA03671D). An additional statement that details the co-authors' contributions can be found at the end of this thesis (Appendix E).

Appendix B: Presents the published work "A New Strontium Based Reactive Carbonate Composite for Thermochemical Energy Storage" with contributions and correction by myself and all other co-authors. It is published in the Journal of Materials Chemistry A (https://doi.org/10.1039/D1TA04363C). An additional statement that details the co-authors' contributions can be found at the end of this thesis (Appendix E).

Kyran Williamson	Mark Paskevicius
(Ph.D. Candidate's Signature)	(Supervisor's Signature)

Abstract

Energy storage is emerging as a technological necessity in the global drive towards decarbonisation. Fossil fuels are losing their grip as the dominant energy source due to compounding economic, political, and environmental issues. The intermittent nature of wind and solar energy necessitates storage to stabilise the electrical grid and balance out supply and demand. To address this variable demand a synergistic combination of storage technologies will be required, one of the most cost-effective on a large scale is thermal energy storage (TES).

The most energy dense form of TES is thermochemical energy storage (TCES), which stores energy via a reversible chemical reaction. Metal carbonates such as strontium and barium carbonate have high gravimetric energy density for their calcination reactions (242 and 273 $kJ \cdot mol^{-1}$ of CO_2, respectively) and are low cost, however they suffer from high operating temperatures and poor CO_2 cycling capacities. In this research, metal carbonate systems involving barium or strontium carbonate, with additives, have been investigated as high temperature TCES materials. A deep dive into the state-of-the-art literature on TCES materials, specifically metal carbonates, is explored in Chapter 1. The experimental techniques used over the course of this PhD are outlined in Chapter 2.

The core research objective of this thesis is to explore TCES additives to $BaCO_3$ and $SrCO_3$ that improve the reaction kinetics and cyclic capacity retention and/or lower the operating temperature. Chapter 3 introduces a novel reactive carbonate composite consisting of $BaCO_3$ destabilised via the addition of Fe_2O_3. This additive changed the reaction pathway and lowered the operating temperature of the calcination reaction from 1400 to 850 °C. On heating to 850 °C in a CO_2 atmosphere the composite forms $BaFe_{12}O_{19}$ and high temperature polymorphs β-$BaCO_3$ and γ-$BaCO_3$. Synchrotron radiation was used to observe the calcination *in-situ* and a two-step reaction was revealed. First β-$BaCO_3$, then γ-$BaCO_3$, reacts with $BaFe_{12}O_{19}$ to reversibly form β-$BaFe_2O_4$. The thermodynamics of

this reaction were measured using a Sieverts type apparatus and found to be ΔH_{des} = 199 ± 6 kJ·mol^{-1} of CO_2, ΔS_{des} = 180 ± 6 J·K^{-1}·mol^{-1} of CO_2 and ΔH_{des} = 212 ± 6 kJ·mol^{-1} of CO_2, ΔS_{des} =185 ± 7 J·K^{-1}·mol^{-1} of CO_2, respectively, for the two steps.

Higher temperature thermal energy storage (> 1000 °C) is required for several industrial processes. To address this, a higher temperature TCES composite was explored in Chapter 4. A mixture of $BaCO_3$ and TiO_2 (2:1 molar ratio) formed $BaCO_3$ and $BaTiO_3$ on heating to 1100°C under a CO_2 atmosphere. Subsequent removal of CO_2 leads to the reversible formation of Ba_2TiO_4 in an endothermic reaction with an enthalpy of ΔH_{des} = 295 ± 9 kJ·mol^{-1} of CO_2 and ΔS_{des} = 214 ± 7 J·K^{-1}·mol^{-1} of CO_2. Initially, the energy storage capacity declined from 65 % to 52 % of the theoretical maximum over 25 cycles, and this was identified to be due to sintering. The addition of nickel as a sintering inhibitor improved its capacity to a stable 60 % capacity retention over 70 cycles.

In Chapter 5 the potential of two different additives ($SrTiO_3$ and $SrZrO_3$) to improve the cyclic capacity of $SrCO_3$ were compared. $SrTiO_3$ reacts with $SrCO_3$ to form Sr_2TiO_4 whilst $SrZrO_3$ acts as an inert stabiliser. TGA studies showed a high potential for both materials to reversibly absorb and desorb CO_2 retaining ~ 80 % of the theoretical maximum capacity (over 15 cycles). Whereas Sieverts apparatus cycling comparisons revealed remarkably different results as the $SrZrO_3$ additive lost capacity rapidly to less than 12 % of its theoretical maximum (after 53 cycles). However, $SrTiO_3$ retained 80 % capacity retention over 55 cycles due to the formation of an intermediate phase.

The various additives used in each of these chapters have been compared on a cost basis and potential applications have been outlined. The thesis concludes with some final thoughts and future directions for research in Chapter 6.

PhD Achievements

Publications

Williamson, K.; Møller, K. T.; D'Angelo, A. M.; Humphries, T. D.; Paskevicius, M.; Buckley, C. E. Thermochemical Energy Storage in Barium Carbonate Enhanced by Iron(III) Oxide. *Phys. Chem. Chem. Phys.* **2023**, *25* (10), 7268–7277. https://doi.org/10.1039/D2CP05745J.

Møller, K. T.; Williamson, K.; Buckley, C. E.; Paskevicius, M. Thermochemical Energy Storage Properties of a Barium Based Reactive Carbonate Composite. *J. Mater. Chem. A* **2020**, *8* (21), 10935–10942. https://doi.org/10.1039/D0TA03671D.

Vieira, A. P.; Williamson, K.; Humphries, T. D.; Paskevicius, M.; Buckley, C. E. A New Strontium Based Reactive Carbonate Composite for Thermochemical Energy Storage. *J. Mater. Chem. A* **2021**, *9* (36), 20585–20594. https://doi.org/10.1039/D1TA04363C.

Submitted for publication

Williamson, K.; D'Angelo, A. M.; Humphries, T. D.; Paskevicius, M.; Buckley, C. E., *Barium carbonate and barium titanate for ultra-high temperature thermochemical energy storage*. [submitted for publication]

Williamson, K.; Liu Y; D'Angelo, A. M.; Humphries, T. D.; Paskevicius, M.; Buckley, C. E., , Thermochemical energy storage in $SrCO_3$ composites with $SrTiO_3$ or $SrZrO_3$ [submitted for publication]

Conferences

K. Williamson, A. D. D'Angelo, K.T. Møller, T.D. Humphries, C.E. Buckley, M. Paskevicius, *Energy Storage Rocks: Metal Carbonates as Thermochemical Energy Storage Materials*, Australian Institute of physics (**November 2022**). Perth – Australia

K. Williamson, M. Paskevicius, A. D. D'Angelo, K.T. Møller, T.D. Humphries, C.E. Buckley, *Metal Carbonates vs Metal Hydrides: Thermochemical Energy Storage Materials*, Metal Hydrides Conference (**July 2022**). Perth - Australia

K. Williamson, A. D. D'Angelo, K.T. Møller, M. Paskevicius, T.D. Humphries, C.E. Buckley, *Energy Storage Rocks: Metal Carbonates as Thermochemical Energy Storage*, European Materials Research Society Fall Meeting (**September 2022**). Warsaw - Poland

K. Williamson, K.T. Møller, T.D. Humphries, M. Paskevicius, C.E. Buckley, *Thermochemical Energy Storage Utilising Abundant Metal Carbonates*, European Materials Research Society Fall Meeting (**September 2021**). Warsaw- Poland

K. Williamson, M. Paskevicius, A. D. D'Angelo, K.T. Møller, C.E. Buckley, *Energy Storage Rocks: Metal Carbonates as a Thermochemical Battery,* ANSTO User Meeting (Jul 2021). (**November 2021**), Sydney- Australia

K. Williamson, A. D. D'Angelo, K.T. Møller, C.E. Buckley, M. Paskevicius, *Energy Storage Rocks: Metal Carbonates as Thermochemical Energy Storage Materials*, Australian Institute of physics (**November 2021**). Perth – Australia

K. Williamson, A. P. Viera, K.T. Møller, C.E. Buckley, M. Paskevicius, *Thermochemical Energy Storage Utilising Metal Carbonates*, Australian Institute of physics (**November 2020**). Perth – Australia

K. Williamson, K.T. Møller, T.D. Humphries, C.E. Buckley, M. Paskevicius, *Energy Storage Rocks: Metal carbonates as Thermochemical Energy Storage Materials*, Australian X-Ray Analytical Association WA Student Seminars (**November 2019**). Perth – Australia

K. Williamson, K.T. Møller, T.D. Humphries, C.E. Buckley, M. Paskevicius, *Thermochemical Energy Storage Utilising Metal Carbonates*, Australian Institute of physics (**November 2019**). Perth – Australia

Professional membership and academic experience

- Vice Chair - Australian institute of Physics, Western Australia, 2022-2023
- Lab Demonstrator - Department of Physics Curtin University, 2019 – 2023
- Member - Hydrogen society of Australia 2022-2023

Media

- Research video presentation "Storing solar in thermal batteries" https://youtu.be/qmBmcZBm1Ug?si=pCKiys-U4-e6kVPf

Awards

- Research Training Program - Australian Government, 2019-2023
- AINSE PGRA (Australian Institute of Nuclear Science Post Graduate Research Award) - AINSE, Melbourne, 2019-2023
- 2 x Beamtime award - Australian Synchrotron, Melbourne, 2021, 2022
- Runner up best small talk - AXXA (Australian X-Ray Analytical Association), Perth 2019
- Summer school scholarship - IRN-FACEs (International Research Network French-Australian research network on Conversion and Energy Storage for stand-alone & maritime applications), Bordeaux, 2021
- Student scholarship – Student-Industry Workshop, Minerals Research Institute of Western Australia, Perth, 2022
- Student Scholarship - Energy in WA Conference, Perth, 2023

Table of Contents

List of Figures

List of tables

Chapter 1

Introduction

"Heat may be generated and destroyed by certain processes, and this shows that heat is not a substance."

-James Clerk Maxwell

1.1 Demand for energy storage

The world's reliance on fossil fuels has been the cause of numerous economic, political, and environmental problems.[1] As of now an “energy crisis” caused by the Russia-Ukraine conflict shakes the world as fossil fuel prices surge.[1] The worldwide response to the crisis is a curtailing of demand for fossil fuels and a rapid transition and uptake of renewable energy sources such as hydro, geothermal, wind and solar, which currently account for over 5% of world energy supply.[2] The IEA's 2022 report anticipates a 2400 GW rise in global renewables in the next five years, an 85% acceleration compared to the prior period,(Figure 1-1) but this growth remains insufficient to meet climate goals. At COP 28, a bold plan emerged: tripling renewable energy capacity to 11,000 GW by 2030. [3] This transition would reduce the share of fossil fuels from 80% to 73%, aligning us with the goal of restraining global warming to 1.5°C.[3]

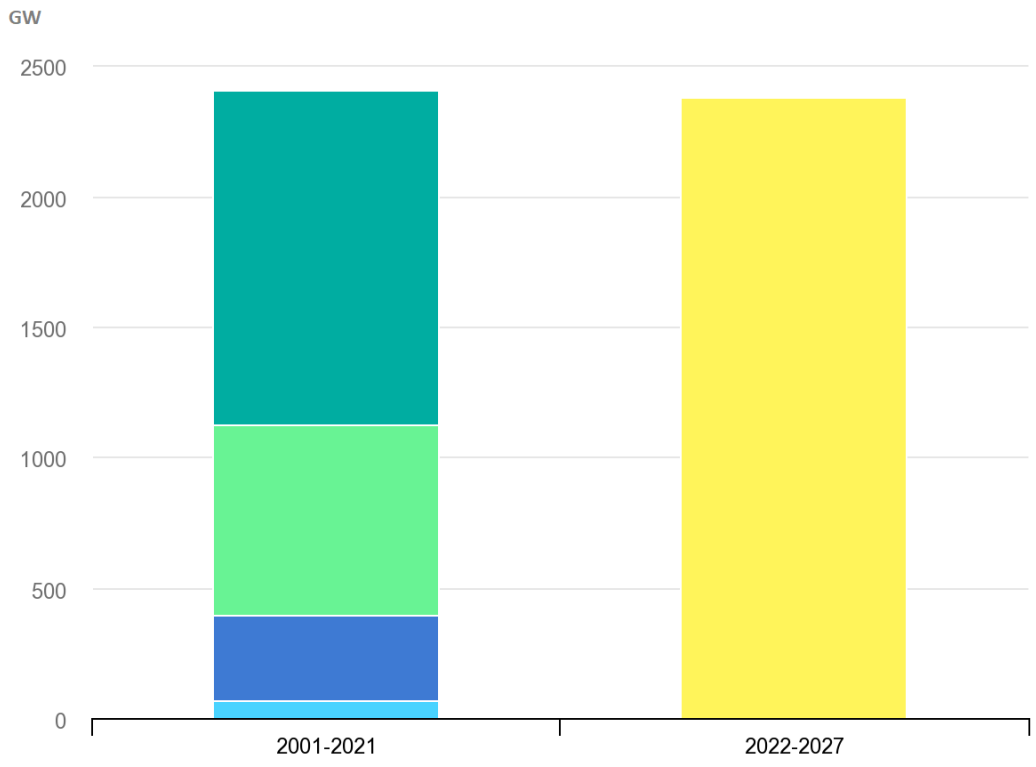

Figure 1-1: Total renewable capacity additions in Giga Watts 2001-2003 (light blue) 2004-2009 (dark blue) 2010-2015 (light green) 2016-2021 (dark green) 2022-2027 (yellow) predicted renewable capacity additions international energy agency 2022.[5]

Renewable energy sources such as wind and solar are intermittent, which can cause challenges in maintaining a stable power grid.[4] The key to balancing the supply and demand of energy is through energy storage systems, which will increase resilience and autonomy of the energy supply network. In the event of natural or man-made disasters, energy storage systems can provide a reliable and independent source of energy.[4,6,7] This independence is crucial for critical facilities such as hospitals, emergency services, and communication networks during such events. In addition, energy storage systems can be used in developing countries and remote areas where grid connections are challenging or expensive, and therefore provide a reliable and independent source of power.[8–10] Presently, fossil fuels are utilised to meet peak power demand, but this is unsustainable in the path towards net zero emissions.[11] Dispatchable energy storage can not only be used to meet peak demand in an environmentally sustainable manner but also enhances energy security.[11–13]

An additional force that is driving demand for energy storage is the growth in electric vehicles (EVs), with sales doubling to 6.6 million in 2021, which accounts for 10 % of new car sales worldwide and 15 % in Europe and China (Figure 1-2).[14] Although, with the correct policies EVs could act as additional storage capacity, they put strain on the power grid as most electric vehicles are charged overnight when solar energy is unavailable.[15–17]

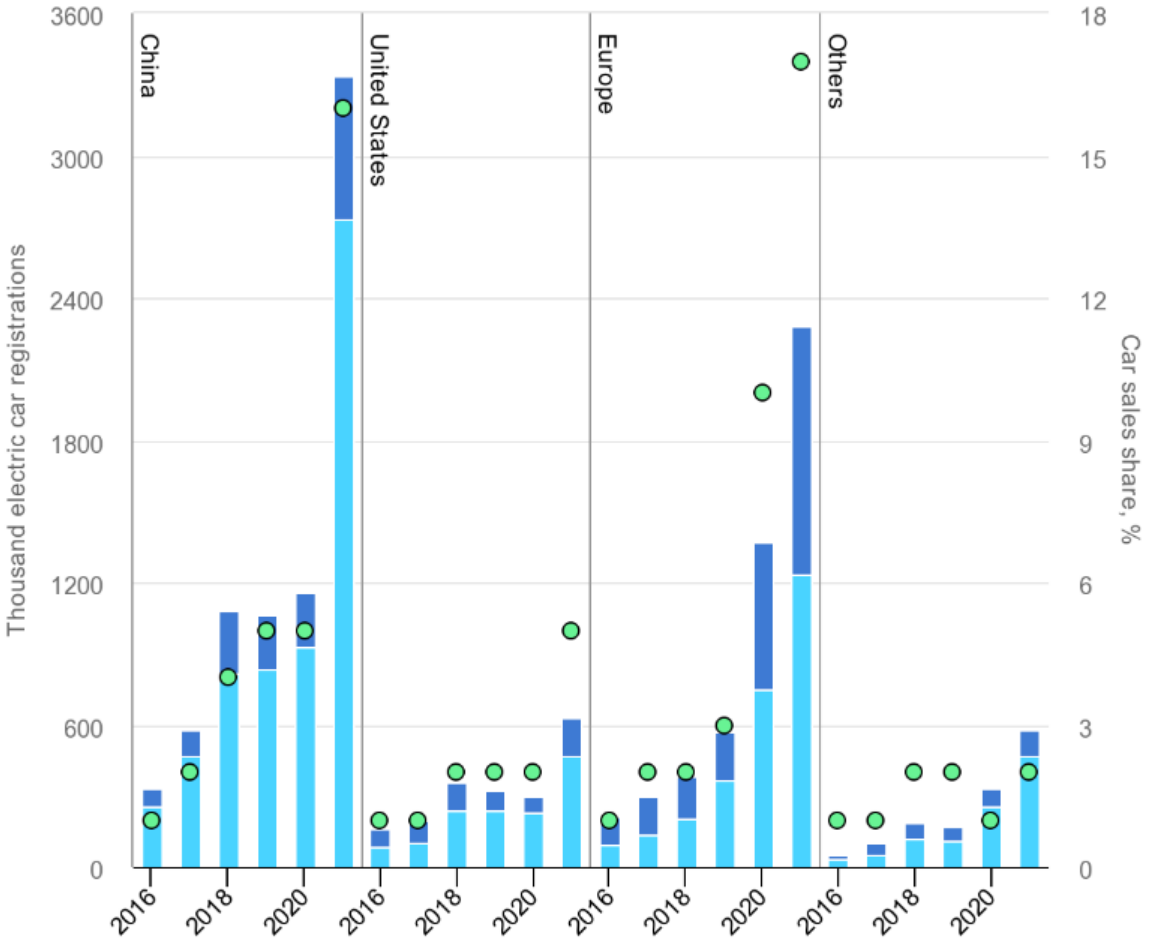

Figure 1-2: Battery Electric Vehicles (light blue), Plug in hybrid electric vehicles (dark blue), Electric car sales percentage share (green circle), International energy agency 2022.[18]

Energy storage is crucial in supporting the transition to renewable energy sources and ensuring a reliable and stable power grid. It can reduce the reliance on fossil fuels, manage the demand for electricity from electric vehicles, provide reliable and affordable energy to developing countries and remote areas. This introductory thesis chapter sets the stage for further research and exploration of energy storage as a key enabler of a sustainable and reliable energy future.

1.2 Types of energy storage

1.2.1 Electrochemical

Electrochemical energy storage is a process that converts electrical energy into chemical energy and stores it for later use in devices such as batteries, fuel cells, and supercapacitors. Installed battery storage was reported by the IEA to be over 27 GW (utility scale + behind the meter) at the end of 2021.[19]

The dominant type of electrochemical battery is lithium-ion (LIBs), which store energy via the reversible reduction of lithium ions. LIBs have a high gravimetric energy density of approximately 100 - 300 $Wh \cdot kg^{-1}$ (depending on the application) and have a moderate material cost of 150 - 500 USD $kW \cdot h^{-1}$.[20–22] They have a high energy efficiency (more than 95 %) and excellent cyclic capacity over more than 3000 cycles at 80 % discharge.[23]

The production of LIBs require scarce critical minerals such as lithium, nickel, graphite and cobalt which could increase costs in the future.[24,25] Additionally, lithium batteries can be prone to explosions or fires leading to significant product recalls. These safety concerns are triggered by an electrochemical system instability, which can result in heat and gas production, a rupture of the casing and ignition of the combustible materials.[26–28]

1.2.2 Mechanical

Mechanical energy storage utilises kinetic or gravitational potential energy. Pumped hydro storage is widely used and currently accounts for 95 % of the world's current energy storage capacity, due to its cyclic stability and long life, however it requires a large amount of land and requires specific topology.[29] The round-trip efficiency of pumped hydro is approximately 70 - 85%, which makes it a competitive technology.[30]

Flywheels operate by accelerating a rotor to very high speeds (up to 20,000 - 50,000 rpm) and exhibit very high energy densities of 360 - 500 kJ/kg. However, they are not efficient for long-term storage and are better suited for applications such as frequency and voltage regulation.[31,32]

1.2.3 Thermal energy storage

TES is a vital component of modern energy systems, which can enable efficient utilisation of renewable and non-renewable energy sources. Currently there is a global presence of 234 GWh of installed capacity that is expected to grow to 800 GWh of installed capacity by the end of 2030.[33] TES is not a new concept, and has been employed in various applications such as solar hot water heating, district heating and industrial processes. Rising interest in renewable energy and sustainable systems has sparked interest in the field resulting in over 27,000 papers on thermal energy storage available today.[34]

1.2.4 Types of thermal energy storage – sensible, latent thermochemical

Sensible heat storage: Stores energy by modifying the temperature of a material with high heat capacity (1500 $J \cdot kg^{-1} \cdot K^{-1}$- 2300 $J \cdot kg^{-1} \cdot K^{-1}$) such as water, rocks, concrete, sand, soil, and some molten salts.[35] The heat stored can be calculated via; [35]

$$Q = mC_p\Delta T \qquad (1\text{-}1)$$

Where:

- Q is in the energy stored (J).
- m is the mass (kg).
- C_p is the specific heat capacity ($J \cdot kg^{-1} \cdot K^{-1}$).
- ΔT is the temperature change of the material (K).

Latent heat storage: Uses materials that store a large amount of heat during a phase change (typically solid to liquid), typically referred to as phase change materials (PCMs) and include water/ice, paraffin, molten salts, metallic elements, and alloys.[35] This isothermal heat storage is effective for several industrial applications and for use with stirling engines to generate electricity.[33] The energy stored via latent heat can be calculated via; [35]

$$Q = mL \quad (1\text{-}2)$$

Where:

- Q is energy stored (J),
- m is the mass (kg)
- L is the latent heat ($J \cdot kg^{-1}$).

Thermochemical energy storage: Uses a reversible chemical reaction to store energy, typical materials include the decomposition of metal hydrides, metal carbonates or metal oxides.[35] Heat is stored via an endothermic reaction and is released via an exothermic one, the energy stored can be calculated via;[35]

$$Q = m\Delta H a_r \quad (1\text{-}3)$$

Where:

- ΔH is the enthalpy of reaction ($J \cdot kg^{-1}$),
- a_r is the reacted fraction of the material.

Recently Miscibility Gap Alloys (MGA) show much promise, they are a solid composite encapsulating metallic particles that contribute the latent heat, which is further enhanced by the overall sensible heat storage of the material.[36–38]

1.2.5 Comparison of thermal energy storage types

Ultimately the optimal type of thermal energy storage depends on several factors which are compared below (Table 1-1).

Table 1-1: Thermal energy storage comparison of various types[35,36,36,37,39–42]

Technology Type	**Sensible**	**Latent**	**Thermochemical**

Method	Heat is stored by change of temperature	Heat is stored by change of phase	Heat is stored by a reversible chemical reaction
Storage Mediums	Water, Rocks, Air, Concrete, (PCMs), molten salt,	Water/ice, paraffin, molten salt, salt hydrates, metals, MGA	Metal Hydrides, Metal Oxides, Metal Hydroxides, Metal Carbonates
Typical gravimetric energy density ($kJ \cdot kg^{-1}$)	72 - 108	180 – 420	780 - 3600
Advantages	Simple and reliable Easy integration Cheap material cost	High energy density Compact storage material Isothermal heat for industrial applications and stirling engines	Very high energy density High operating temperatures High thermal to electric conversion efficiency
Disadvantages	Low energy density Limited temperature range	Expensive storage material Medium energy density	Complex technology Slow reaction kinetics Poor cyclability

	Relatively low efficiency	Storage material degradation	
Maturity	Commercialised	Pilot Scale	Lab Scale

In order to compare various types of TES materials refer to Desage *et al.*'s recent review which depicts the correlation between maximum operating temperatures and the gravimetric energy density among diverse thermal energy storage (TES) materials (Figure 1-3).[22]

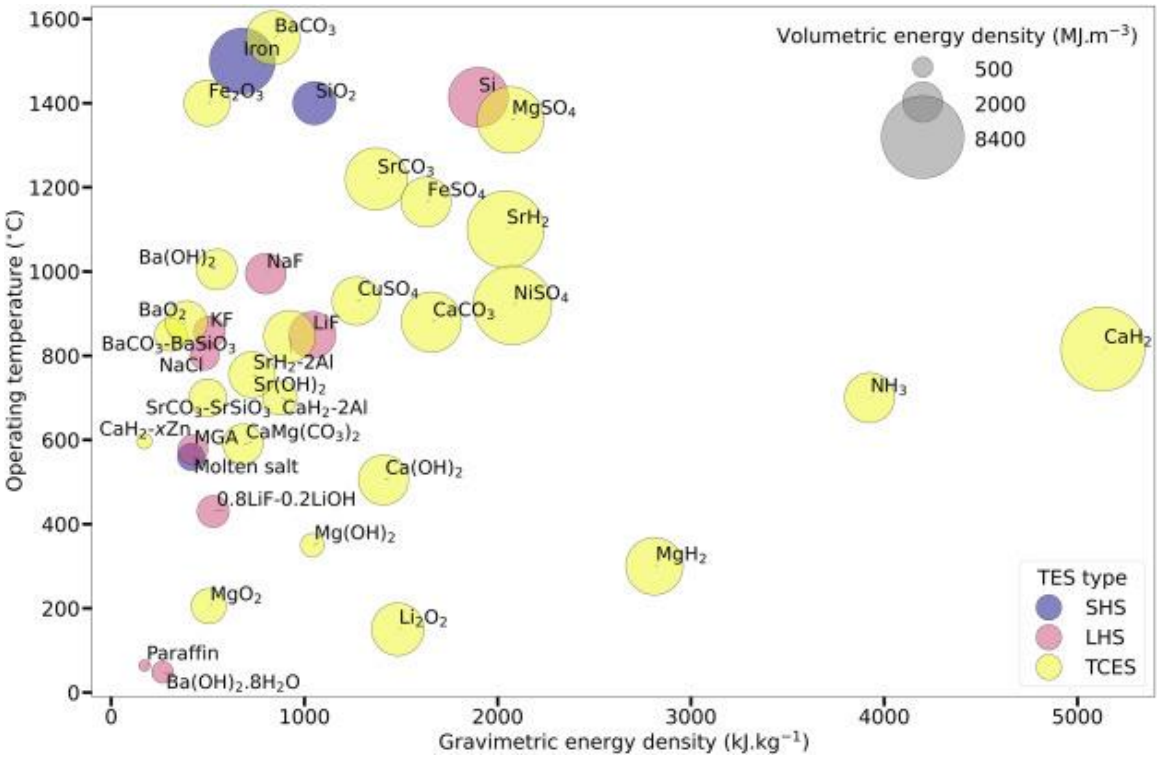

Figure 1-3: Maximum operating temperature of selected TES materials as a function of their gravimetric energy density. The size of the circles is proportional to the volumetric energy density of each material. Latent heat storage (LHS, purple), Sensible Heat Storage (SHS, pink), and Thermochemical Energy Storage (TCES, yellow) materials are indicated by a colour code.[22]

1.2.6 High temperature energy storage (600 - 1500 °C)

High temperature energy storage is beneficial for efficient and cost-effective storage of large amounts of energy from high-temperature sources such as concentrated solar power and high-temperature industrial processes. Heat engines convert thermal energy to electricity and usually operate at 75% of the theoretical maximum efficiency of heat recovery from such processes, which is limited by the Carnot efficiency given by:[43]

$$\eta_{carnot} = 1 - \frac{T_L}{T_H} \quad (1\text{-}4)$$

Where:

- η_{carnot} is the efficiency of the heat engine.
- T_L is the temperature of the low temperature source.
- T_H is the temperature of the high temperature source.

There are several processes that generate or utilise high temperature heat and benefit from thermal energy storage (Figure 1-4);

- The steam Rankine heat engine which uses steam as the working fluid to generate mechanical power and typically operates at temperatures between 350 - 600 °C.[44]
- The super critical carbon dioxide (sCO_2) power cycle utilises carbon dioxide as the working fluid. Due to the high pressures (100 - 300 bar) and high operating temperatures (500 - 800 °C) the CO_2 maintains a supercritical state, which leads to higher thermal efficiencies than the other cycles.[45]
- CO_2 closed Brayton cycle operating at 950 °C uses CO_2 as the working fluid that is compressed, heated and expanded through a turbine to generate mechanical power, it is cooled and compressed again completing the cycle, it has higher efficiencies than typical gas fired turbines.[46]

- The ‘combined cycle’ operates at temperatures above 1450 °C and uses a high temperature gas turbine. Subsequently the waste heat from this process is used to power a lower temperature cycle such as a steam Rankine heat engine.[47,48]
- High-temperature heat can also be used directly in industrial processes (as opposed to converting it to electricity), such as steel making, aluminium production, and cement manufacturing, which are typically difficult to decarbonise. By reusing industrial waste heat from batch processing and purchasing energy at a surplus and utilising it at times of peak demand, the process can operate round the clock.[49]
- Direct thermochemical production of hydrogen which uses a multistep thermochemical cycle to split water, operating in the range of approximately 1000 – 1500 °C.[50]

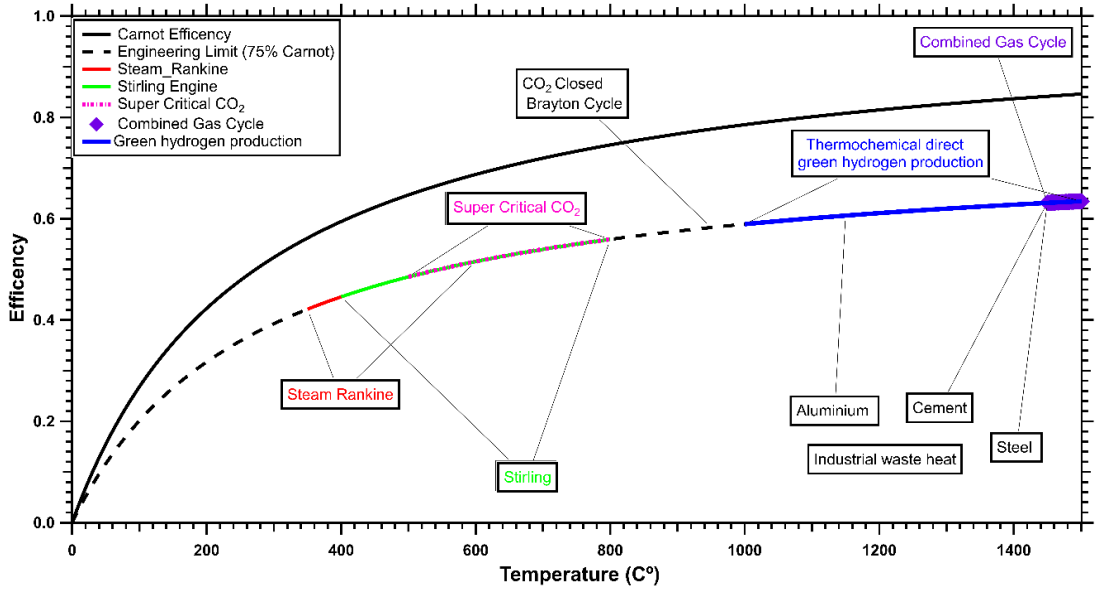

Figure 1-4: Carnot efficiency vs practical engineering limit as well as various sources and consumers of thermal energy.

1.2.7 Concentrated solar power

Concentrated solar power (CSP) uses mirrors or lenses to focus sunlight onto a receiver to generate thermal energy, which can then be converted to electrical energy using a heat engine. There are four main types of CSP;

1. Parabolic trough collectors (300 - 550 °C), which reflect sunlight onto a focal line using a parabolic mirror.[51,52]
2. Linear Fresnel reflectors (250 - 500 °C), which use flat or slightly curved mirrors to focus sunlight onto a linear receiver.[51,53]
3. Parabolic dish collectors (500 - 750 °C), which focus solar energy onto a focal point of each dish.[54]
4. Solar power towers (400 - 1500 °C), such as solar towers and dish systems, use heliostats or mirrors to focus sunlight onto a central receiver, which can generate temperatures up to 1500 °C for electricity production.[54]

CSP plants pair perfectly with TES as it provides load smoothing and grid stability, addressing the intermittent nature of renewable energy.[55,56] Modern CSP plants use sensible heat to store energy using molten salts made up of sodium nitrate:potassium nitrate (60:40 wt.%) at temperatures of 290 - 565 °C, with thermal to electric conversion efficiencies of up to 18%.[57] These tanks have the advantage that molten salt can also be used as the heat transfer fluid, however major projects have suffered from leaking due to ruptured tanks.[58] Thermochemical energy storage (TCES) allows CSP to store energy at much higher temperatures, providing access to more efficient heat engine cycles and improving overall efficiency by up to 60%.[59–61]

1.3 Thermochemical energy storage

1.3.1 Introduction

Thermochemical energy storage relies on reversible chemical reactions. During the charging step, heat (ΔH) is added, and an endothermic reaction occurs where a reactant (A) is converted into products (B and C). The products are then reused in the reverse

process, converting the products (B and C) back into the reactant (A) through an exothermic reaction (energy release) see (Figure 1-5).[62]

$$A + \Delta H \rightleftharpoons B + C \qquad (1\text{-}5)$$

Where:

- A is the reactant.
- B & C are the products
- ΔH is the enthalpy of reaction ($J \cdot kg^{-1}$).

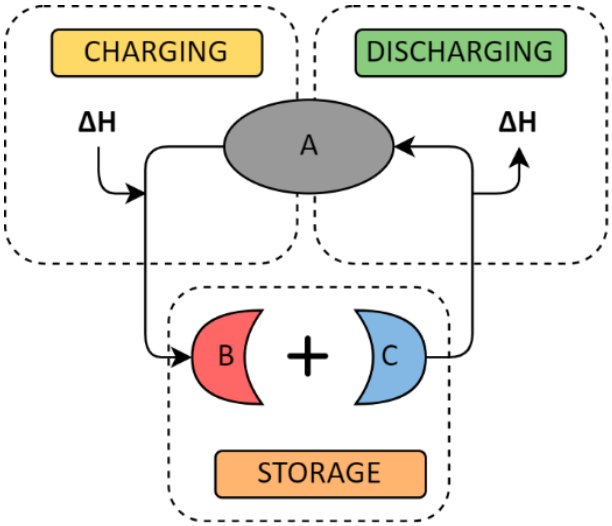

Figure 1-5: Schematic of thermochemical energy storage cycle.[22]

1.3.2 History

The first known mention of the storage of solar energy via reversible chemical reactions was by Dr Martin Goldstein in 1955. He presented a paper at the Rome conference on Solar Energy utilisation, where he highlighted the characteristics of an ideal thermochemical energy storage material. He noted that the material should have the highest possible temperature equilibrium reaction and high entropy changes, and that gaseous products would have the highest entropy changes, despite having a lower volume-based density due to gas storage requirements.[63] In another seminal paper in

1977, Dr Guy Ervin emphasised that energy storage is an energy consumer, not an energy source, with a consumption equal to its inefficiency. The value of energy storage lies in utilising wasted energy or shifting from a limited energy source to a more abundant one.[64]

In the 1970s, several materials for thermochemical energy storage were identified and summarised by Wentworth and Chen.[65] These included gas-gas reactions involving the decomposition of methane and water, as well as the solid-gas decomposition of ammonium salts, (Group I+II) sulphates, (Group I+II) carbonates, and (Group I+II) hydroxides.[65]

Although research into thermochemical energy storage dwindled over the 1980s and 1990s, in the last two decades, there has been a significant increase in the quantity of research, with over 200 publications per year with keywords related to TCES. This renewed interest in TCES research is due to the growing demand for sustainable energy solutions and the need to reduce dependence on fossil fuels.

1.3.3 Desired characteristics and properties

The early research into the chemical storage of energy outlined several criteria which are still true today for selecting a thermochemical storage material.

1. High enthalpy of reaction: Enthalpy dictates the heat stored within a reversible chemical reaction.
2. Operating temperature: Materials should be selected for their desired applications, for energy storage purposes however higher temperatures allow for higher efficiency heat engines (See Section 1.2.6).
3. Reversibility: The reaction should be completely reversible with no significant side reactions or changes of reaction rate with time. The material should perform multiple cycles with little to no degradation of the material.
4. Reaction rates: These must be high enough to absorb all the available energy and to provide it at the required rate. This requires a low activation energy, which

could be reduced by the addition of a catalyst. This is also affected by the morphology of the material.

5. Controllability: The reaction should be simply controlled by a catalyst or by controlling the pressure or temperature.
6. Ease of storage: The reactants and products should be easily stored, for gases this can cause several problems; either large volume requirements, energy for compressing the gas, expensive pressure vessels or the use of a secondary gas storage material.
7. High abundance and low cost of material: By using widely available materials thermochemical batteries can compete with other energy storage methods.
8. Recyclability and lifecycle of the material: Materials with low environmental impact that can be reused or repurposed will be favoured.

1.3.4 High temperature thermochemical reactions

Most materials studied for TCES can be separated into three main categories by the reactants-products, these are solid-gas, liquid-gas and gas-gas. For this study we will focus on solid-gas reactions (> 500 °C).[66,67]

1.3.4.1 Metal Oxides

Involves the reduction of a pure or mixed metal oxide to metal and oxygen gas via the following reaction:[68]

$$2M_xO_{y(s)} + \Delta H \rightleftharpoons 2M_xO_{y-1(s)} + O_{2(g)} \quad (1\text{-}6)$$

Where:

- M is a metal.
- ΔH is the heat of reaction ($J \cdot kg^{-1}$).

Metal oxide TCES systems are particularly promising as they permit working with air (low partial pressures of O_2), which can be used as the heat transfer medium as well as the

reactant, and there is no need to store gas separately.[68] The most prominently studied pure metal oxides are cobalt oxide,[69–74] manganese oxide,[71,73–78] barium oxide[79–83] and copper oxide.[84–92] Each of these metal oxides in the pure state has distinct advantages and disadvantages (see Table 1-2), none of them reach all the criteria for thermochemical energy storage materials outlined previously (see 1.3.3).

Recent work on combining mixed metal oxides has yielded promising results, the introduction of iron to Co_3O_4 and Mn_2O_3 can raise their equilibrium temperature and gaps, depending on the mixture.[74] Meanwhile, the inclusion of Cu in Co_3O_4 can lower the equilibrium temperature from ~ 865 °C to ~ 815 °C.[61]

Table 1-2: Various parameters for the most prominent metal oxides for thermochemical energy storage.

Metal Oxide	T_{eq}	**Energy Density**		**Cost**[93]	**Pros**	**Cons**
	°C	$kJ \cdot mol^{-1}$	$kJ \cdot kg^{-1}$	$US \cdot ton^{-1}$		
Co_3O_4/CoO [69–72,81,94,95]	870-935	196 - 202	816 - 901	250,000	High enthalpy, good kinetics, no side reactions	Expensive, toxic, carcinogenic, sintering
Mn_2O_3/Mn_3O_4 [61,71,78,94]	500 - 530	90	110 - 230	100,000	Inexpensive and abundant	Incomplete redox reaction, slow kinetics, sintering

BaO_2/BaO[79,82,83]	960 - 880	75 - 77	104 - 390	10,000 - 50,000[96]	Inexpensive, low toxicity, abundant, no side reactions	Poor cyclability, few experimental studies,
CuO/Cu_2O [61,84,84,89]	958 - 1045	80	1009 - 1042	60,000	Abundant, (high solar radiation areas), fast reduction.	Melting point close to redox sintering.

1.3.4.2 Metal Hydrides

Metal hydrides are an attractive possibility for TCES applications due to their high energy density (~ 900 $kJ \cdot kg^{-1}$ up to ~ 5000 $kJ \cdot kg^{-1}$).[97] They store energy via the reduction of a metal hydride to metal and hydrogen gas via the following: [98]

$$2MH_{x(s)} + \Delta H \rightleftharpoons 2M_{(s)} + xH_{2(g)} \quad (1\text{-}7)$$

Where:

- M is a metal
- ΔH is the heat of reaction ($J \cdot kg^{-1}$),

For high temperature applications (> 500 °C) there are multiple candidates, several of which are outlined below (See Table 1-3).

Table 1-3:Various parameters for the most prominent metal hydrides for thermochemical energy storage.

Metal hydride	T_{eq}	Energy Density		Cost	Pros	Cons
	°C	kJ·mol^{-1}	kJ·kg^{-1}	$US·ton^{-1}		
$CaH_2/Ca+H_2$[97,99,100]	947	216	5131	6000	High volumetric energy density, low cost	Highly corrosive, melting of products and reactants
CaH_2+4Al/Al_4Ca+H_2[97,99]	700	83	735	3631	Excellent reversibility, low-cost elements	Low energy density
$SrH_2+2Al/SrAl_2+H_2$[97,101,102]	846	132	923	4375	High energy density,	Low energy density, slight capacity loss over cycles

1.3.5 Metal carbonates

Metal carbonates are attractive because of their low costs(as little as US$60 a tonne for $CaCO_3$) and abundance, as well as their relatively high energy densities(~ 1000 kJ·kg^{-1} up to ~ 1500 kJ·kg^{-1}.[22] They store energy via the calcination of a metal carbonate via:[98]

$$MCO_{3(s)} + \Delta H \rightleftharpoons MO_{(s)} + CO_{2(g)} \quad (1\text{-}8)$$

Where:

- M is a metal
- ΔH is the heat of reaction (J·kg^{-1})

As the focus of this thesis, I will go into greater detail on the current state of materials research on metal carbonates and for convenience some of their properties are listed in Table 1-4.

Table 1-4: Various parameters for the most prominent metal carbonates for thermochemical energy storage.

Metal carbonate	T_{eq}	**Energy Density**		**Cost**	**Pros**	**Cons**
	°C	**kJ·mol^{-1}**	**kJ·kg^{-1}**	**$USD·ton^{-1}**		
$CaCO_3/CaO+CO_2$[65,95,100,103]	837	178	1657	60	High gravimetric and volumetric energy. Extremely cost effective.	Capacity loss over multiple cycles. Grain growth and agglomeration.
$SrCO_3/SrO+CO_2$[65,95,100,103]	1175	242	1389	700	High gravimetric and volumetric energy. High operating temperature.	Capacity loss over multiple cycles. Grain growth and agglomeration.
$BaCO_3/BaO+CO_2$[65,95,100,103]	1297	273	1040	300	High gravimetric and volumetric energy densities. High thermal conductivity. Environmentally friendly.	Slow reaction kinetics. Operating temperature too high for practical use. Melts at high temperatures

						causing sintering.

1.3.5.1 Calcium Carbonate

Calcium carbonate is highly attractive as a TCES material because of the extremely low material cost and abundance of limestone ~60US/tonne. It also has a high gravimetric energy density of 1657 $kJ \cdot kg^{-1}$ and a high operating temperature of ~800 - 900 °C, however it has the significant drawback of suffering from rapid cyclic capacity loss due to sintering.[103,104]

Most studies on the calcium carbonate-calcium oxide reaction focus on calcium looping (CaL) as a carbon capture and utilisation technology. CaL uses calcium oxide (CaO) to react with and capture CO_2 from exhaust gas in a 'carbonator' (this is to extract CO_2 from other exhaust gases). Then in a separate 'calciner' the CO_2 is released from $CaCO_3$ and can be stored or used in other processes, the process has been covered in several reviews in the last two decades.[105–110] There have been several studies exploring the feasibility of incorporating CaL with CSP, which can be done with current technology from the cement industry.[111–113]

Calcium carbonate was first investigated as a TCES material by Barker. He performed over 40 CO_2 sorption cycles at 866 °C and observed a significant decrease in the rate of the absorption reaction over each cycle.[114] He observed two distinct regimes during the back reaction (absorption of CO_2); (i) a fast reaction to a distinct break off point, (ii) a further much slower back reaction. The two steps were attributed to firstly a loss of pore volume in the oxide and secondly sintering of the carbonate which Barker concluded could be mitigated by the reduction of particle size to less than 44 nm.[114] Further research by Barker using ~ 10 nm sized calcium oxide showed a reversible capacity of 93 % over several cycles (24 hour absorption times).[115]

Additional technological challenges with $CaCO_3$ as a TCES mainly are concerned with the multicyclic carbonation performance loss due to sintering.[116] The Tanmann temperature (T_t), of a material is the temperature where agglomeration occurs due to increased particle mobility throughout the bulk material. The sintering of $CaCO_3$ (T_t = 533 °C) results in particle size growth and pore plugging which hinders CO_2 desorption and future absorption cycles [103–105,115–118]. This can be mitigated by the addition of sorbents such as AlOOH,[119] Al_2O_3,[120–122] $Ca_3Al_2O_6$,[120,123] CeO_2,[124] Li_2SO_4,[125] SiO_2.[126–128] resulting in a higher Tanmann temperature to increase resistance to sintering (see Table 1-5).

Table 1-5: Tanmann temperature of various metal carbonates, oxides, and additives commonly used for TCES applications. [129–133]

Compound	T_t **(°C)**
CaO	1170
$CaCO_3$	533
$BaCO_3$	730
$SrCO_3$	610
Al_2O_3	891
MgO	1276
TiO_2	785

When operating TCES-CSP (i.e., carbonation under high pressures and temperatures and calcination under low-temperature CO_2 pressures) the reaction temperatures increase causing sintering, which forms a layer of $CaCO_3$ thicker than 100 nm. The pores inside the

CaO skeleton usually have a size smaller than 50 nm, resulting in the blocking of pores due to the large $CaCO_3$ layer, affecting the coarse CaO particles.[111,117,134,135] For larger scale systems, small initial particle size cause problems such as severe agglomeration, poor gas/solid contact and mass heat transfer issues.[136]

Another method $CaCO_3$ multicyclic capacity can be improved is by hydrating the carbonate (see (1-9).[108,137–139] The hydroxide has an increased molar volume (CaO = 16.9 $cm^3 \cdot mol^{-1}$; $Ca(OH)_2$ = 33.7 $cm^3 \cdot mol^{-1}$) and a lower density (CaO = 3.32 $g \cdot cm^{-3}$; $Ca(OH)_2$ = 2.20 $g \cdot cm^{-3}$) which causes fractures within the material resulting in increased porosity and surface area and thus improved CO_2 diffusion[108].

$$CaO_{(s)} + H_2O_{(g)} \rightleftharpoons Ca(OH)_{2(s)} \quad (1\text{-}9)$$

In conclusion, calcium carbonate has been extensively studied as a potential material for TCES, and it shows promise due to its high enthalpy and thus high volumetric and gravimetric energy density, but above all else its cost effectiveness. However, technological challenges such as multicyclic performance loss due to sintering, particle size growth, and pore plugging hinder its practical application. The addition of sorbents, hydration, or particle size control can improve CO_2 diffusion and have been proposed as effective solutions to overcome these issues. Despite the multitude of studies further research is required to optimise the performance of calcium carbonate as a TCES material.

1.3.5.2 Strontium Carbonate

Strontium is the 15th most abundant element on earth and as a carbonate is relatively inexpensive.[96,140] The higher 1 bar equilibrium temperature (1108 °C) leads to a higher thermal to electric conversion efficiency compared to $CaCO_3$, and the gravimetric energy

density is higher (2340 kJ·kg^{-1}). It is also well suited to high temperature (> 1000 °C) applications (See Figure 1-4).

$SrCO_3$ was first proposed as a TCES combined with CSP by Wentworth and Chen in 1976,[65] since then, studies have shown that it suffers from the same multi cycle decrease in capacity as $CaCO_3$.[103,141–143] In the last few years it has been patented as an energy storage method in 2010 (patent expired 2013),[144] and studied as a carbon capture material.[141,145]

Further studies on $SrCO_3$ are mainly concerned with various methods to increase the cyclic capacity retention. MgO has been used to great success by Gigantino *et al.* resulting in 60% capacity retention over 100 cycles when SrO is combined with 60 wt.%. MgO.[146] In a similar experiment André & Abanades demonstrated a 96 % capacity retention over 4 cycles with a 32 wt.% MgO addition.[103] More recently, Ammendola *et al.* showed that adding 34 wt.% Al_2O_3 worked as an effective sintering and agglomeration inhibitor in a fluidised bed TCES system over 7 cycles.[142,147] In another study, Bagherisereshki *et al.* found that altering the particle size had no effect on cyclic stability and that by the addition of 25 wt.% $Sr_3(PO_4)_2$ resulted in a stable cycling capacity of 500 kJ·kg^{-1}.[148] Finally, Amghar *et al.* compared the multicycle stability of $SrCO_3$ by the addition of various oxides, namely, ZrO_2, SiO_2 and MgO and found that via the addition of SiO_2 the cyclic stability could be stabilised to 22% of the theoretical maximum after 30 cycles.[149]

$SrCO_3$ is a viable TCES material for ultra-high temperature applications due to its high energy density, ideal operating temperature, low cost and abundance of materials. Further work on improving the cyclic stability without sacrificing energy density is recommended.

The present author has published work using $SrSiO_3$ to destabilise the reaction of $SrCO_3$ reducing the operating temperature to ~700 °C, the cyclic capacity retention was also improved using a eutectic mixture of NaCl : $MgCl_2$ (0.44 : 0.56 molar ratio) as a catalyst to enhance cyclic capacity retention to a stable 80 % over 17 cycles (See appendix B)

1.3.5.3 Barium Carbonate

There have been few studies on barium carbonate as a thermochemical energy storage material due to its high equilibrium temperature of 1297 °C, which is considered too high for most applications.[95] Additionally, it suffers from the same sintering and agglomeration problems as other metal carbonates.[103,143]

Prior to the publication of the present author's work, there have only been two studies where the potential of $BaCO_3$ as a TCES material has been experimentally validated. André and Abanades studied the potential of $BaCO_3$ as a TCES material, although complete calcination of pure $BaCO_3$ was achieved it could not completely reabsorb the lost CO_2. [103] However, the addition of MgO to $BaCO_3$ was found to partially mitigate this problem even though the material was found to lose significant carbonation capacity (~ 10%) over each cycle. [103]

The present author has published a recent study on the utilisation of barium carbonate as a TCES, in which the operating temperature was lowered by > 350 °C by the addition of $BaSiO_3$. This reduces sintering and agglomeration and ultimately improves the cyclic capacity to over 25 cycles at over 60% of the theoretical capacity (See appendix A).

1.4 Challenges and opportunities

TCES is a promising technology for storing and releasing thermal energy, it is also a cost-competitive method to store excess electrical energy. Here are some challenges and opportunities associated with this technology:

Opportunities

- Thermochemical energy storage can be integrated with renewable energy sources such as concentrated solar power and industrial waste heat.
- The availability of dispatchable energy on demand provides grid flexibility.

- Thermochemical energy storage has high energy density compared to other competing technologies, which makes it ideal for applications where space is limited.
- Operating temperatures can be reduced, and the kinetics and morphology can be modified by the addition of various additives.

Challenges

- Limited research on materials with suitable thermochemical properties for energy storage.
- Gas storage is expensive and/or requires large volumes.
- There is a high capital cost for initial installation. Additionally, maintenance costs can also be significant.
- The storage materials have limited durability and can degrade over time due to repeated thermal cycling.

1.5 Thesis Aims and Objectives

The main aim of this thesis is to identify and characterise new TCES composites which consist of barium or strontium carbonate combined with various additives. The details are summarised as follows.

1. Refine the selection of composite materials by considering their decomposition temperature, cost, and desorption kinetics.
2. Enhance the operational efficiency of TCES composites by destabilising the reaction of barium carbonate or strontium carbonate through the incorporation of diverse additives.
3. Characterise the thermodynamic properties of metal carbonates using sieverts apparatus and the van 't Hoff technique.

4. Evaluate the cycling capacity of TCES materials using thermogravimetric analysis and sieverts apparatus. Then improve and evaluate additives effects on the cycling capacity.
5. Conduct a comprehensive analysis of the material cost associated with composites comprising barium or strontium carbonate and additives.

1.6 Thesis outline

The initial chapter of the thesis serves as an introduction, providing a concise overview of the relevant background information. The subsequent chapter provides a summary of the materials, methodologies, and experimental procedures employed throughout the study. The subsequent 3 chapters consist of papers that are either published or in press. Finally, chapter 6 consist of conclusions and directions for future work.

Chapter 3: - **Thermochemical energy storage properties of a barium based reactive carbonate composite.**

Chapter 3 is a peer reviewed publication in Physical Chemistry Chemical Physics that introduces the first metal carbonate destabilised by a pure metal oxide for TCES applications. The chapter describes the thermodynamic properties of the reaction and utilised synchrotron powder X-ray diffraction to distinguish two co-existing phases of $BaCO_3$ and their reaction two-step with Fe_2O_3 . Furthermore, the cost and viability of this composite as a TCES system was explored.

Chapter 4 - Barium carbonate and barium titanate for ultra-high temperature thermochemical energy storage

Chapter 4 has been submitted for publication in the journal of energy storage and is currently undergoing review. In this chapter $BaCO_3$ is destabilised by the addition of TiO_2 which forms $BaTiO_3$ to reversibly store chemical energy at 1100 °C. In this paper thermodynamic properties were determined for the reaction. A nickel additive was used to mitigate cycling capacity loss with no discernible loss of capacity over more than 100

cycles. A material cost analysis was performed and the potential of this material for TCES was assessed.

Chapter 5 - **Thermochemical energy storage in $SrCO_3$ composites with $SrTiO_3$ or $SrZrO_3$**

Currently in press, chapter 5 explores the effects of two different additives to improve the cyclic capacity of $SrCO_3$. $SrTiO_3$ and $SrZrO_3$ both have potential to eliminate the cyclic CO_2 capacity loss of $SrCO_3$ when studied via thermogravimetric analysis. Various ratios of $SrZrO_3$ were used to discover an optimal quantity however when scaled up from a mg to a gram scale experiment the $SrZrO_3$ lost capacity rapidly while $SrTIO_3$ maintained significant cyclic performance. The viability of these composite TCES materials was compared in terms of cost and potential cyclic stability.

Chapter 6: Conclusions and future recommendations

This final chapter summarises the main conclusions from the research and outlines future research directions.

Appendix – A: Thermochemical energy storage properties of a barium based reactive carbonate composite

This work has been published as a peer reviewed paper in the Journal of Materials Chemistry - A. A new reactive carbonate composite consisting of $BaSiO_3$ and $BaCO_3$ is assessed for cyclic stability which ultimately was enhanced by the addition of $CaCO_3$. It operates at 850 °C and cycles at 60% of the theoretical maximum operating capacity over 25 cycles.

The authors major contributions involved experimental work and analysis of the data, particularly in the solid-state synthesis of $BaSiO_3$ and measurements involving the synthesised $BaSiO_3$.

Appendix – B: A new strontium based reactive carbonate composite for thermochemical energy storage.

This work was also published as a peer reviewed paper in the Journal of Materials Chemistry – A. This explores a reactive carbonate composite consisting of $SrSiO_3$ and $SrCO_3$ operating at 700 °C. The cyclic stability was realised at 80% capacity over 17 cycles by the addition of eutectic mixture of salts as a catalyst.

The authors major contributions initial conception and planning of the experiment, experimental measurements and analysis and processing of data.

Appendix – C: Supplementary information

Appendix – D: Permission from copyright owners

Appendix – E: Co-author attribution Statements

1.7 References

(1) *The global energy crisis – World Energy Outlook 2022 – Analysis*. IEA. https://www.iea.org/reports/world-energy-outlook-2022/the-global-energy-crisis (accessed 2023-02-16).

(2) *Data & Statistics*. IEA. https://www.iea.org/data-and-statistics (accessed 2020-02-24).

(3) COP28: Global Renewables And Energy Efficiency Pledge. https://www.cop28.com/en/global-renewables-and-energy-efficiency-pledge (accessed 2023-12-07)

(4) Younesi, A.; Shayeghi, H.; Wang, Z.; Siano, P.; Mehrizi-Sani, A.; Safari, A. Trends in Modern Power Systems Resilience: State-of-the-Art Review. *Renew. Sustain. Energy Rev.* **2022**, *162*, 112397. https://doi.org/10.1016/j.rser.2022.112397.

(5) *IEA, Total renewable electricity capacity additions, 2001-2027*. IEA. https://www.iea.org/data-and-statistics/charts/total-renewable-electricity-capacity-additions-2001-2027 (accessed 2023-02-17).

(6) Liu, J.; Jian, L.; Wang, W.; Qiu, Z.; Zhang, J.; Dastbaz, P. The Role of Energy Storage Systems in Resilience Enhancement of Health Care Centers with Critical Loads. *J. Energy Storage* **2021**, *33*, 102086. https://doi.org/10.1016/j.est.2020.102086.

(7) Lagrange, A.; de Simón-Martín, M.; González-Martínez, A.; Bracco, S.; Rosales-Asensio, E. Sustainable Microgrids with Energy Storage as a Means to Increase Power Resilience in Critical Facilities: An Application to a Hospital. *Int. J. Electr. Power Energy Syst.* **2020**, *119*, 105865. https://doi.org/10.1016/j.ijepes.2020.105865.

(8) Tan, Y.; Meegahapola, L.; Muttaqi, K. M. A Review of Technical Challenges in Planning and Operation of Remote Area Power Supply Systems. *Renew. Sustain. Energy Rev.* **2014**, *38*, 876–889. https://doi.org/10.1016/j.rser.2014.07.034.

(9) AL Shaqsi, A. Z.; Sopian, K.; Al-Hinai, A. Review of Energy Storage Services, Applications, Limitations, and Benefits. *Energy Rep.* **2020**, *6*, 288–306. https://doi.org/10.1016/j.egyr.2020.07.028.

(10) Krishan, O.; Suhag, S. Techno-Economic Analysis of a Hybrid Renewable Energy System for an Energy Poor Rural Community. *J. Energy Storage* **2019**, *23*, 305–319. https://doi.org/10.1016/j.est.2019.04.002.

(11) Kalair, A.; Abas, N.; Saleem, M. S.; Kalair, A. R.; Khan, N. Role of Energy Storage Systems in Energy Transition from Fossil Fuels to Renewables. *Energy Storage* **2021**, *3* (1), e135. https://doi.org/10.1002/est2.135.

(12) Valentine, S. V. Emerging Symbiosis: Renewable Energy and Energy Security. *Renew. Sustain. Energy Rev.* **2011**, *15* (9), 4572–4578. https://doi.org/10.1016/j.rser.2011.07.095.

(13) Gökgöz, F.; Güvercin, M. T. Energy Security and Renewable Energy Efficiency in EU. *Renew. Sustain. Energy Rev.* **2018**, *96*, 226–239. https://doi.org/10.1016/j.rser.2018.07.046.

(14) *Global EV Outlook 2022 – Analysis*. IEA. https://www.iea.org/reports/global-ev-outlook-2022 (accessed 2023-03-10).

(15) Wu, W.; Lin, B. Benefits of Electric Vehicles Integrating into Power Grid. *Energy* **2021**, *224*, 120108. https://doi.org/10.1016/j.energy.2021.120108.

(16) Tavakoli, A.; Saha, S.; Arif, M. T.; Haque, M. E.; Mendis, N.; Oo, A. M. T. Impacts of Grid Integration of Solar PV and Electric Vehicle on Grid Stability, Power Quality and Energy Economics: A Review. *IET Energy Syst. Integr.* **2020**, *2* (3), 243–260. https://doi.org/10.1049/iet-esi.2019.0047.

(17) Moon, H.; Park, S. Y.; Jeong, C.; Lee, J. Forecasting Electricity Demand of Electric Vehicles by Analyzing Consumers' Charging Patterns. *Transp. Res. Part Transp. Environ.* **2018**, *62*, 64–79. https://doi.org/10.1016/j.trd.2018.02.009.

(18) *Electric Vehicles – Analysis*. IEA. https://www.iea.org/reports/electric-vehicles (accessed 2023-02-17).

(19) *World Energy Outlook 2022 – Analysis*. IEA. https://www.iea.org/reports/world-energy-outlook-2022 (accessed 2023-02-16).

(20) Abbas, Q.; Mirzaeian, M.; Hunt, M. R. C.; Hall, P.; Raza, R. Current State and Future Prospects for Electrochemical Energy Storage and Conversion Systems. *Energies* **2020**, *13* (21), 5847. https://doi.org/10.3390/en13215847.

(21) Zhou, G.; Chen, H.; Cui, Y. Formulating Energy Density for Designing Practical Lithium–Sulfur Batteries. *Nat. Energy* **2022**, *7* (4), 312–319. https://doi.org/10.1038/s41560-022-01001-0.

(22) Desage, L.; McCabe, E.; Vieira, A. P.; Humphries, T. D.; Paskevicius, M.; Buckley, C. E. Thermochemical Batteries Using Metal Carbonates: A Review of Heat Storage and Extraction. *J. Energy Storage* **2023**, *71*, 107901. https://doi.org/10.1016/j.est.2023.107901.

(23) Chen, T.; Jin, Y.; Lv, H.; Yang, A.; Liu, M.; Chen, B.; Xie, Y.; Chen, Q. Applications of Lithium-Ion Batteries in Grid-Scale Energy Storage Systems. *Trans. Tianjin Univ.* **2020**, *26* (3), 208–217. https://doi.org/10.1007/s12209-020-00236-w.

(24) Kalantzakos, S. The Race for Critical Minerals in an Era of Geopolitical Realignments. *Int. Spect.* **2020**, *55* (3), 1–16. https://doi.org/10.1080/03932729.2020.1786926.

(25) *The Role of Critical Minerals in Clean Energy Transitions – Analysis*. IEA. https://www.iea.org/reports/the-role-of-critical-minerals-in-clean-energy-transitions (accessed 2023-05-16).

(26) Chen, Y.; Kang, Y.; Zhao, Y.; Wang, L.; Liu, J.; Li, Y.; Liang, Z.; He, X.; Li, X.; Tavajohi, N.; Li, B. A Review of Lithium-Ion Battery Safety Concerns: The Issues, Strategies, and Testing Standards. *J. Energy Chem.* **2021**, *59*, 83–99. https://doi.org/10.1016/j.jechem.2020.10.017.

(27) Duan, J.; Tang, X.; Dai, H.; Yang, Y.; Wu, W.; Wei, X.; Huang, Y. Building Safe Lithium-Ion Batteries for Electric Vehicles: A Review. *Electrochem. Energy Rev.* **2020**, *3* (1), 1–42. https://doi.org/10.1007/s41918-019-00060-4.

(28) Hales, T. A.; Møller, K. T.; Humphries, T. D.; D'Angelo, A. M.; Buckley, C. E.; Paskevicius, M. Investigating the Potential of Alkali Metal Plumba-Closo-Dodecaborate (B11H11Pb2–) Salts as Solid-State Battery Electrolytes. *J. Phys. Chem. C* **2023**, *127* (2), 949–957. https://doi.org/10.1021/acs.jpcc.2c07226.

(29) Whitby, R. D. Mechanical Batteries. *Tribol. Lubr. Technol.* **2021**, *77* (9), 88.

(30) Ansorena Ruiz, R.; de Vilder, L. H.; Prasasti, E. B.; Aouad, M.; De Luca, A.; Geisseler, B.; Terheiden, K.; Scanu, S.; Miccoli, A.; Roeber, V.; Marence, M.; Moll, R.; Bricker, J. D.; Goseberg, N. Low-Head Pumped Hydro Storage: A Review on Civil Structure Designs, Legal and Environmental Aspects to Make Its Realization Feasible in Seawater. *Renew. Sustain. Energy Rev.* **2022**, *160*, 112281. https://doi.org/10.1016/j.rser.2022.112281.

(31) Amiryar, M. E.; Pullen, K. R. A Review of Flywheel Energy Storage System Technologies and Their Applications. *Appl. Sci.* **2017**, *7* (3), 286. https://doi.org/10.3390/app7030286.

(32) Awadallah, M. A.; Venkatesh, B. Energy Storage in Flywheels: An Overview. *Can. J. Electr. Comput. Eng.* **2015**, *38* (2), 183–193. https://doi.org/10.1109/CJECE.2015.2420995.

(33) International Renewable Energy AgencyIRENA. *Innovation Outlook: Thermal Energy Storage*; International Renewable Energy Agency, Abu Dhabi, 2020. /-/media/Files/IRENA/Agency/Publication/2020/Nov/IRENA_Innovation_Outlook_TES_2020.pdf?rev=6950b7b9792344b5ab28d58e18209926 (accessed 2023-03-10).

(34) Cabeza, L. F.; de Gracia, A.; Zsembinszki, G.; Borri, E. Perspectives on Thermal Energy Storage Research. *Energy* **2021**, *231*, 120943. https://doi.org/10.1016/j.energy.2021.120943.

(35) Bauer, T.; Steinmann, W.-D.; Laing, D.; Tamme, R. THERMAL ENERGY STORAGE MATERIALS AND SYSTEMS. *Annu. Rev. Heat Transf.* **2012**, *15* (15), 131–177. https://doi.org/10.1615/AnnualRevHeatTransfer.2012004651.

(36) Copus, M.; Fraser, B.; Reece, R.; Hands, S.; Cuskelly, D.; Sugo, H.; Reed, S.; Bradley, J.; Post, A.; Kisi, E. On-Sun Testing of Miscibility Gap Alloy Thermal Storage. *Sol. Energy* **2019**, *177*, 657–664. https://doi.org/10.1016/j.solener.2018.11.048.

(37) Cuskelly, D.; Fraser, B.; Reed, S.; Post, A.; Copus, M.; Kisi, E. Thermal Storage for CSP with Miscibility Gap Alloys. *AIP Conf. Proc.* **2019**, *2126* (1), 200013. https://doi.org/10.1063/1.5117728.

(38) Reed, S.; Kisi, E. Miscibility Gap Alloys with a Ceramic Matrix for Thermal Energy Storage. *SN Appl. Sci.* **2020**, *2* (12), 2148. https://doi.org/10.1007/s42452-020-03942-1.

(39) Zhang, H.; Baeyens, J.; Cáceres, G.; Degrève, J.; Lv, Y. Thermal Energy Storage: Recent Developments and Practical Aspects. *Prog. Energy Combust. Sci.* **2016**, *53*, 1–40. https://doi.org/10.1016/j.pecs.2015.10.003.

(40) Koohi-Fayegh, S.; Rosen, M. A. A Review of Energy Storage Types, Applications and Recent Developments. *J. Energy Storage* **2020**, *27*, 101047. https://doi.org/10.1016/j.est.2019.101047.

(41) Sadeghi, G. Energy Storage on Demand: Thermal Energy Storage Development, Materials, Design, and Integration Challenges. *Energy Storage Mater.* **2022**, *46*, 192–222. https://doi.org/10.1016/j.ensm.2022.01.017.

(42) Palacios, A.; Barreneche, C.; Navarro, M. E.; Ding, Y. Thermal Energy Storage Technologies for Concentrated Solar Power – A Review from a Materials Perspective. *Renew. Energy* **2020**, *156*, 1244–1265. https://doi.org/10.1016/j.renene.2019.10.127.

(43) Steinfeld, A.; Palumbo, R. Solar Thermochemical Process Technology. In *Encyclopedia of Physical Science and Technology (Third Edition)*; Meyers, R. A., Ed.;

Academic Press: New York, 2003; pp 237–256. https://doi.org/10.1016/B0-12-227410-5/00698-0.

(44) Karni, J. Solar-Thermal Power Generation. *Annu. Rev. Heat Transf.* **2012**, *15*, 37–92. https://doi.org/10.1615/AnnualRevHeatTransfer.2012004925.

(45) Turchi, C. S.; Ma, Z.; Neises, T. W.; Wagner, M. J. Thermodynamic Study of Advanced Supercritical Carbon Dioxide Power Cycles for Concentrating Solar Power Systems. *J. Sol. Energy Eng.* **2013**, *135* (4). https://doi.org/10.1115/1.4024030.

(46) Ortiz, C.; Chacartegui, R.; Valverde, J. M.; Alovisio, A.; Becerra, J. A. Power Cycles Integration in Concentrated Solar Power Plants with Energy Storage Based on Calcium Looping. *Energy Convers. Manag.* **2017**, *149*, 815–829. https://doi.org/10.1016/j.enconman.2017.03.029.

(47) Henry, A.; Prasher, R. The Prospect of High Temperature Solid State Energy Conversion to Reduce the Cost of Concentrated Solar Power. *Energy Environ. Sci.* **2014**, *7* (6), 1819–1828. https://doi.org/10.1039/C4EE00288A.

(48) Thermal Energy Storage for CSP Hybrid Gas Turbine Systems: Dynamic Modelling and Experimental Validation. *Appl. Energy* **2018**, *212*, 1240–1251. https://doi.org/10.1016/j.apenergy.2017.12.130.

(49) Miró, L.; Gasia, J.; Cabeza, L. F. Thermal Energy Storage (TES) for Industrial Waste Heat (IWH) Recovery: A Review. *Appl. Energy* **2016**, *179*, 284–301. https://doi.org/10.1016/j.apenergy.2016.06.147.

(50) Kodama, T.; Gokon, N. Thermochemical Cycles for High-Temperature Solar Hydrogen Production. *Chem. Rev.* **2007**, *107* (10), 4048–4077. https://doi.org/10.1021/cr050188a.

(51) Borunda, M.; Jaramillo, O. A.; Dorantes, R.; Reyes, A. Organic Rankine Cycle Coupling with a Parabolic Trough Solar Power Plant for Cogeneration and Industrial Processes. *Renew. Energy* **2016**, *86*, 651–663. https://doi.org/10.1016/j.renene.2015.08.041.

(52) Fernández-García, A.; Zarza, E.; Valenzuela, L.; Pérez, M. Parabolic-Trough Solar Collectors and Their Applications. *Renew. Sustain. Energy Rev.* **2010**, *14* (7), 1695–1721. https://doi.org/10.1016/j.rser.2010.03.012.

(53) Romero, M.; Steinfeld, A. Concentrating Solar Thermal Power and Thermochemical Fuels. *Energy Environ. Sci.* **2012**, *5* (11), 9234. https://doi.org/10.1039/c2ee21275g.

(54) Dev, D. R.; Harison, D. S. A Review on Concentrated Solar Power (CSP) and Emerging Technology. -*Manag. J. Electr. Eng.* **2022**, *16* (1), 38–44. https://doi.org/10.26634/jee.16.1.19196.

(55) Lovegrove, K.; Stein, W. *Concentrating Solar Power Technology: Principles, Developments and Applications*; Elsevier Science & Technology: Cambridge, UNITED KINGDOM, 2012.

(56) Forrester, J. The Value of CSP with Thermal Energy Storage in Providing Grid Stability. *Energy Procedia* **2014**, *49*, 1632–1641. https://doi.org/10.1016/j.egypro.2014.03.172.

(57) Liu, M.; Steven Tay, N. H.; Bell, S.; Belusko, M.; Jacob, R.; Will, G.; Saman, W.; Bruno, F. Review on Concentrating Solar Power Plants and New Developments in High Temperature Thermal Energy Storage Technologies. *Renew. Sustain. Energy Rev.* **2016**, *53*, 1411–1432. https://doi.org/10.1016/j.rser.2015.09.026.

(58) Zhou, H.; Shi, H.; Lai, Z.; Zuo, Y.; Hu, S.; Zhou, M. Migration and Phase Change Study of Leaking Molten Salt in Tank Foundation Material. *Appl. Therm. Eng.* **2020**, *170*, 114968. https://doi.org/10.1016/j.applthermaleng.2020.114968.

(59) Prieto, C.; Cooper, P.; Fernández, A. I.; Cabeza, L. F. Review of Technology: Thermochemical Energy Storage for Concentrated Solar Power Plants. *Renew. Sustain. Energy Rev.* **2016**, *60*, 909–929. https://doi.org/10.1016/j.rser.2015.12.364.

(60) Thermochemical Energy Storage by Consecutive Reactions for Higher Efficient Concentrated Solar Power Plants (CSP): Proof of Concept. *Appl. Energy* **2017**, *185*, 836–845. https://doi.org/10.1016/j.apenergy.2016.10.093.

(61) Dizaji, H. B.; Hosseini, H. A Review of Material Screening in Pure and Mixed-Metal Oxide Thermochemical Energy Storage (TCES) Systems for Concentrated Solar Power (CSP) Applications. *Renew. Sustain. Energy Rev.* **2018**, *98*, 9–26. https://doi.org/10.1016/j.rser.2018.09.004.

(62) Garg, H. P.; Mullick, S. C.; Bhargava, A. K. Chemical Energy Storage. In *Solar Thermal Energy Storage*; Garg, H. P., Mullick, S. C., Bhargava, A. K., Eds.; Springer Netherlands: Dordrecht, 1985; pp 292–427. https://doi.org/10.1007/978-94-009-5301-7_4.

(63) Goldstein, M. Some Physical Chemical Aspects of Heat Storage. **1961**.

(64) Ervin, G. Solar Heat Storage Using Chemical Reactions. *J. Solid State Chem.* **1977**, *22* (1), 51–61. https://doi.org/10.1016/0022-4596(77)90188-8.

(65) Wentworth, W. E.; Chen, E. Simple Thermal Decomposition Reactions for Storage of Solar Thermal Energy. *Sol. Energy* **1976**, *18* (3), 205–214. https://doi.org/10.1016/0038-092X(76)90019-0.

(66) Bauer, T. Chapter 1 - Fundamentals of High-Temperature Thermal Energy Storage, Transfer, and Conversion. In *Ultra-High Temperature Thermal Energy Storage, Transfer and Conversion*; Datas, A., Ed.; Woodhead Publishing Series in Energy; Woodhead Publishing, 2021; pp 1–34. https://doi.org/10.1016/B978-0-12-819955-8.00001-6.

(67) Pardo, P.; Deydier, A.; Anxionnaz-Minvielle, Z.; Rougé, S.; Cabassud, M.; Cognet, P. A Review on High Temperature Thermochemical Heat Energy Storage. *Renew. Sustain. Energy Rev.* **2014**, *32*, 591–610. https://doi.org/10.1016/j.rser.2013.12.014.

(68) Wu, S.; Zhou, C.; Doroodchi, E.; Nellore, R.; Moghtaderi, B. A Review on High-Temperature Thermochemical Energy Storage Based on Metal Oxides Redox Cycle. *Energy Convers. Manag.* **2018**, *168*, 421–453. https://doi.org/10.1016/j.enconman.2018.05.017.

(69) Wu, R.; Huang, H.; Deng, L.; Kubota, M.; Kobayashi, N. Influence of CuO Doping on Cobalt Oxide for Thermochemical Energy Storage. *Sol. Energy Mater. Sol. Cells* **2023**, *253*, 112211. https://doi.org/10.1016/j.solmat.2023.112211.

(70) Pagkoura, C.; Karagiannakis, G.; Zygogianni, A.; Lorentzou, S.; Kostoglou, M.; Konstandopoulos, A. G.; Rattenburry, M.; Woodhead, J. W. Cobalt Oxide Based Structured Bodies as Redox Thermochemical Heat Storage Medium for Future CSP Plants. *Sol. Energy* **2014**, *108*, 146–163. https://doi.org/10.1016/j.solener.2014.06.034.

(71) Carrillo, A. J.; Moya, J.; Bayón, A.; Jana, P.; de la Peña O'Shea, V. A.; Romero, M.; Gonzalez-Aguilar, J.; Serrano, D. P.; Pizarro, P.; Coronado, J. M. Thermochemical Energy Storage at High Temperature via Redox Cycles of Mn and Co Oxides: Pure Oxides versus Mixed Ones. *Sol. Energy Mater. Sol. Cells* **2014**, *123*, 47–57. https://doi.org/10.1016/j.solmat.2013.12.018.

(72) Neises, M.; Tescari, S.; de Oliveira, L.; Roeb, M.; Sattler, C.; Wong, B. Solar-Heated Rotary Kiln for Thermochemical Energy Storage. *Sol. Energy* **2012**, *86* (10), 3040–3048. https://doi.org/10.1016/j.solener.2012.07.012.

(73) Karagiannakis, G.; Pagkoura, C.; Zygogianni, A.; Lorentzou, S.; Konstandopoulos, A. G. Monolithic Ceramic Redox Materials for Thermochemical Heat Storage Applications in CSP Plants. *Energy Procedia* **2014**, *49*, 820–829. https://doi.org/10.1016/j.egypro.2014.03.089.

(74) Liu, J.; Baeyens, J.; Deng, Y.; Wang, X.; Zhang, H. High Temperature Mn2O3/Mn3O4 and Co3O4/CoO Systems for Thermo-Chemical Energy Storage. *J. Environ. Manage.* **2020**, *267*, 110582. https://doi.org/10.1016/j.jenvman.2020.110582.

(75) Müller, D.; Knoll, C.; Artner, W.; Harasek, M.; Gierl-Mayer, C.; Welch, J. M.; Werner, A.; Weinberger, P. Combining In-Situ X-Ray Diffraction with Thermogravimetry and Differential Scanning Calorimetry – An Investigation of Co3O4, MnO2 and PbO2 for Thermochemical Energy Storage. *Sol. Energy* **2017**, *153*, 11–24. https://doi.org/10.1016/j.solener.2017.05.037.

(76) Bielsa, D.; Zaki, A.; Arias, P. L.; Faik, A. Improving the Redox Performance of Mn2O3/Mn3O4 Pair by Si Doping to Be Used as Thermochemical Energy Storage for Concentrated Solar Power Plants. *Sol. Energy* **2020**, *204*, 144–154. https://doi.org/10.1016/j.solener.2020.04.073.

(77) Bielsa, D.; Oregui, M.; Arias, P. L. New Insights into Mn2O3 Based Metal Oxide Granulation Technique with Enhanced Chemical and Mechanical Stability for Thermochemical Energy Storage in Packed Bed Reactors. *Sol. Energy* **2022**, *241*, 248–261. https://doi.org/10.1016/j.solener.2022.06.010.

(78) Carrillo, A. J.; Pizarro, P.; Coronado, J. M. Assessing Cr Incorporation in Mn2O3/Mn3O4 Redox Materials for Thermochemical Heat Storage Applications. *J. Energy Storage* **2021**, *33*, 102028. https://doi.org/10.1016/j.est.2020.102028.

(79) Bowrey, R. G.; Jutsen, J. Energy Storage Using the Reversible Oxidation of Barium Oxide. *Sol. Energy* **1978**, *21* (6), 523–525. https://doi.org/10.1016/0038-092X(78)90078-6.

(80) Fahim, M. A.; Ford, J. D. Energy Storage Using the BaO2⇌BaO Reaction Cycle. *Chem. Eng. J.* **1983**, *27* (1), 21–28. https://doi.org/10.1016/0300-9467(83)80042-2.

(81) Agrafiotis, C.; Roeb, M.; Sattler, C. Exploitation of Thermochemical Cycles Based on Solid Oxide Redox Systems for Thermochemical Storage of Solar Heat. Part 4: Screening of Oxides for Use in Cascaded Thermochemical Storage Concepts. *Sol. Energy* **2016**, *139*, 695–710. https://doi.org/10.1016/j.solener.2016.04.034.

(82) Carrillo, A. J.; Sastre, D.; Serrano, D. P.; Pizarro, P.; Coronado, J. M. Revisiting the BaO2/BaO Redox Cycle for Solar Thermochemical Energy Storage. *Phys. Chem. Chem. Phys.* **2016**, *18* (11), 8039–8048. https://doi.org/10.1039/C5CP07777J.

(83) Lei, F.; Dyall, A.; AuYeung, N. An In-Depth Investigation of BaO2/BaO Redox Oxides for Reversible Solar Thermochemical Energy Storage. *Sol. Energy Mater. Sol. Cells* **2021**, *223*, 110957. https://doi.org/10.1016/j.solmat.2021.110957.

(84) Alonso, E.; Pérez-Rábago, C.; Licurgo, J.; Fuentealba, E.; Estrada, C. A. First Experimental Studies of Solar Redox Reactions of Copper Oxides for Thermochemical Energy Storage. *Sol. Energy* **2015**, *115*, 297–305. https://doi.org/10.1016/j.solener.2015.03.005.

(85) Alonso, E.; Gallo, A.; Pérez-Rábago, C.; Fuentealba, E. Thermodynamic Study of CuO/Cu2O and Co3O4/CoO Redox Pairs for Solar Energy Thermochemical Storage. *AIP Conf. Proc.* **2016**, *1734* (1), 050004. https://doi.org/10.1063/1.4949102.

(86) Deutsch, M.; Horvath, F.; Knoll, C.; Lager, D.; Gierl-Mayer, C.; Weinberger, P.; Winter, F. High-Temperature Energy Storage: Kinetic Investigations of the CuO/Cu2O Reaction Cycle. *Energy Fuels* **2017**, *31* (3), 2324–2334. https://doi.org/10.1021/acs.energyfuels.6b02343.

(87) Setoodeh Jahromy, S.; Birkelbach, F.; Jordan, C.; Huber, C.; Harasek, M.; Werner, A.; Winter, F. Impact of Partial Pressure, Conversion, and Temperature on the Oxidation Reaction Kinetics of Cu2O to CuO in Thermochemical Energy Storage. *Energies* **2019**, *12* (3), 508. https://doi.org/10.3390/en12030508.

(88) Gigantino, M.; Sas Brunser, S.; Steinfeld, A. High-Temperature Thermochemical Heat Storage via the CuO/Cu2O Redox Cycle: From Material Synthesis to Packed-Bed Reactor Engineering and Cyclic Operation. *Energy Fuels* **2020**, *34* (12), 16772–16782. https://doi.org/10.1021/acs.energyfuels.0c02572.

(89) Yilmaz, D.; Darwish, E.; Leion, H. Thermochemical Energy Storage Performance of Copper Oxides: Effect of Support Materials. *J. Energy Storage* **2020**, *32*, 102012. https://doi.org/10.1016/j.est.2020.102012.

(90) Xiang, D.; Gu, C.; Xu, H.; Deng, J.; Zhu, P.; Xiao, G. Al-Modified CuO/Cu2O for High-Temperature Thermochemical Energy Storage: From Reaction Performance to Modification Mechanism. *ACS Appl. Mater. Interfaces* **2021**, *13* (48), 57274–57284. https://doi.org/10.1021/acsami.1c17592.

(91) Deng, J.; Gu, C.; Xu, H.; Xiao, G. MgCr2O4-Modified CuO/Cu2O for High-Temperature Thermochemical Energy Storage with High Redox Activity and Sintering Resistance. *ACS Appl. Mater. Interfaces* **2022**, *14* (38), 43151–43162. https://doi.org/10.1021/acsami.2c09519.

(92) Imtiaz, Q.; Armutlulu, A.; Donat, F.; Müller, C. CuO-Based Materials for Thermochemical Redox Cycles: The Influence of the Formation of a CuO Percolation Network on Oxygen Release and Oxidation Kinetics. *Discov. Chem. Eng.* **2022**, *2* (1), 6. https://doi.org/10.1007/s43938-022-00013-2.

(93) Block, T.; Schmücker, M. Metal Oxides for Thermochemical Energy Storage: A Comparison of Several Metal Oxide Systems. *Sol. Energy* **2016**, *126*, 195–207. https://doi.org/10.1016/j.solener.2015.12.032.

(94) André, L.; Abanades, S.; Flamant, G. Screening of Thermochemical Systems Based on Solid-Gas Reversible Reactions for High Temperature Solar Thermal Energy Storage. *Renew. Sustain. Energy Rev.* **2016**, *64*, 703–715. https://doi.org/10.1016/j.rser.2016.06.043.

(95) Roine, A. HSC Chemistry® [Software], 2018. Software available at www.outotec.com/HSC.

(96) National Minerals Information Center. U.S. Geological Survey Mineral Commodity Summaries 2022 Data Release, 2022. https://doi.org/10.5066/P9KKMCP4.

(97) Sunku Prasad, J.; Muthukumar, P.; Desai, F.; Basu, D. N.; Rahman, M. M. A Critical Review of High-Temperature Reversible Thermochemical Energy Storage Systems. *Appl. Energy* **2019**, *254*, 113733. https://doi.org/10.1016/j.apenergy.2019.113733.

(98) Carrillo, A. J.; González-Aguilar, J.; Romero, M.; Coronado, J. M. Solar Energy on Demand: A Review on High Temperature Thermochemical Heat Storage Systems and Materials. *Chem. Rev.* **2019**, *119* (7), 4777–4816. https://doi.org/10.1021/acs.chemrev.8b00315.

(99) Balakrishnan, S.; Sofianos, M. V.; Paskevicius, M.; Rowles, M. R.; Buckley, C. E. Destabilized Calcium Hydride as a Promising High-Temperature Thermal Battery. *J. Phys. Chem. C* **2020**, *124* (32), 17512–17519. https://doi.org/10.1021/acs.jpcc.0c04754.

(100) Humphries, T. D.; Møller, K. T.; Rickard, W. D. A.; Sofianos, M. V.; Liu, S.; Buckley, C. E.; Paskevicius, M. Dolomite: A Low Cost Thermochemical Energy Storage Material. *J. Mater. Chem. A* **2019**, *7* (3), 1206–1215. https://doi.org/10.1039/C8TA07254J.

(101) Humphries, T. D.; Paskevicius, M.; Alamri, A.; Buckley, C. E. Thermodynamic Destablization of SrH2 Using Al for the next Generation of High Temperature

Thermal Batteries. *J. Alloys Compd.* **2022**, *894*, 162404. https://doi.org/10.1016/j.jallcom.2021.162404.

(102) Peterson, D. T.; Nelson, S. O. Equilibrium Hydrogen Pressures in the Strontium-Hydrogen System. *J. Common Met.* **1980**, *72* (2), 251–256. https://doi.org/10.1016/0022-5088(80)90144-7.

(103) André, L.; Abanades, S. Evaluation and Performances Comparison of Calcium, Strontium and Barium Carbonates during Calcination/Carbonation Reactions for Solar Thermochemical Energy Storage. *J. Energy Storage* **2017**, *13*, 193–205. https://doi.org/10.1016/j.est.2017.07.014.

(104) H. Borgwardt, R. Sintering of Nascent Calcium Oxide. *Chem. Eng. Sci.* **1989**, *44* (1), 53–60. https://doi.org/10.1016/0009-2509(89)85232-7.

(105) Han, R.; Wang, Y.; Xing, S.; Pang, C.; Hao, Y.; Song, C.; Liu, Q. Progress in Reducing Calcination Reaction Temperature of Calcium-Looping CO2 Capture Technology: A Critical Review. *Chem. Eng. J.* **2022**, *450*, 137952. https://doi.org/10.1016/j.cej.2022.137952.

(106) Chen, J.; Duan, L.; Sun, Z. Review on the Development of Sorbents for Calcium Looping. *Energy Fuels* **2020**, *34* (7), 7806–7836. https://doi.org/10.1021/acs.energyfuels.0c00682.

(107) Sun, H.; Wu, C.; Shen, B.; Zhang, X.; Zhang, Y.; Huang, J. Progress in the Development and Application of CaO-Based Adsorbents for CO2 Capture—a Review. *Mater. Today Sustain.* **2018**, *1–2*, 1–27. https://doi.org/10.1016/j.mtsust.2018.08.001.

(108) Salaudeen, S. A.; Acharya, B.; Dutta, A. CaO-Based CO2 Sorbents: A Review on Screening, Enhancement, Cyclic Stability, Regeneration and Kinetics Modelling. *J. CO2 Util.* **2018**, *23*, 179–199. https://doi.org/10.1016/j.jcou.2017.11.012.

(109) Hanak, D. P.; Michalski, S.; Manovic, V. From Post-Combustion Carbon Capture to Sorption-Enhanced Hydrogen Production: A State-of-the-Art Review of Carbonate Looping Process Feasibility. *Energy Convers. Manag.* **2018**, *177*, 428–452. https://doi.org/10.1016/j.enconman.2018.09.058.

(110) Perejón, A.; Romeo, L. M.; Lara, Y.; Lisbona, P.; Martínez, A.; Valverde, J. M. The Calcium-Looping Technology for CO2 Capture: On the Important Roles of Energy Integration and Sorbent Behavior. *Appl. Energy* **2016**, *162*, 787–807. https://doi.org/10.1016/j.apenergy.2015.10.121.

(111) Ortiz, C.; Valverde, J. M.; Chacartegui, R.; Perez-Maqueda, L. A.; Giménez, P. The Calcium-Looping (CaCO3/CaO) Process for Thermochemical Energy Storage in Concentrating Solar Power Plants. *Renew. Sustain. Energy Rev.* **2019**, *113*, 109252. https://doi.org/10.1016/j.rser.2019.109252.

(112) Ortiz, C.; Romano, M. C.; Valverde, J. M.; Binotti, M.; Chacartegui, R. Process Integration of Calcium-Looping Thermochemical Energy Storage System in

Concentrating Solar Power Plants. *Energy* **2018**, *155*, 535–551. https://doi.org/10.1016/j.energy.2018.04.180.

(113) Alovisio, A.; Chacartegui, R.; Ortiz, C.; Valverde, J. M.; Verda, V. Optimizing the CSP-Calcium Looping Integration for Thermochemical Energy Storage. *Energy Convers. Manag.* **2017**, *136*, 85–98. https://doi.org/10.1016/j.enconman.2016.12.093.

(114) Barker, R. The Reversibility of the Reaction CaCO3 ⇄ CaO+CO2. *J. Appl. Chem. Biotechnol.* **1973**, *23* (10), 733–742. https://doi.org/10.1002/jctb.5020231005.

(115) Barker, R. The Reactivity of Calcium Oxide towards Carbon Dioxide and Its Use for Energy Storage. *J. Appl. Chem. Biotechnol.* **1974**, *24* (4–5), 221–227. https://doi.org/10.1002/jctb.2720240405.

(116) Khosa, A. A.; Xu, T.; Xia, B. Q.; Yan, J.; Zhao, C. Y. Technological Challenges and Industrial Applications of CaCO3/CaO Based Thermal Energy Storage System – A Review. *Sol. Energy* **2019**, *193*, 618–636. https://doi.org/10.1016/j.solener.2019.10.003.

(117) Durán-Martín, J. D.; Sánchez Jimenez, P. E.; Valverde, J. M.; Perejón, A.; Arcenegui-Troya, J.; García Triñanes, P.; Pérez Maqueda, L. A. Role of Particle Size on the Multicycle Calcium Looping Activity of Limestone for Thermochemical Energy Storage. *J. Adv. Res.* **2020**, *22*, 67–76. https://doi.org/10.1016/j.jare.2019.10.008.

(118) Yin, J.; Lv, X.; Xiang, S.; Bai, C.; Yu, B. Influence of CaO Source on the Formation Behavior of Calcium Ferrite in Solid State. *ISIJ Int.* **2013**, *53* (9), 1571–1579. https://doi.org/10.2355/isijinternational.53.1571.

(119) Jin, D.; Yu, X.; Yue, L.; Wang, L. Decomposition Kinetics Study of AlOOH Coated Calcium Carbonate. *Mater. Chem. Phys.* **2009**, *115* (1), 418–422. https://doi.org/10.1016/j.matchemphys.2008.12.013.

(120) Møller, K. T.; Ibrahim, A.; Buckley, C. E.; Paskevicius, M. Inexpensive Thermochemical Energy Storage Utilising Additive Enhanced Limestone. *J. Mater. Chem. A* **2020**, *8* (19), 9646–9653. https://doi.org/10.1039/D0TA03080E.

(121) Benitez-Guerrero, M.; Valverde, J. M.; Sanchez-Jimenez, P. E.; Perejon, A.; Perez-Maqueda, L. A. Calcium-Looping Performance of Mechanically Modified Al2O3-CaO Composites for Energy Storage and CO2 Capture. *Chem. Eng. J.* **2018**, *334*, 2343–2355. https://doi.org/10.1016/j.cej.2017.11.183.

(122) Wu, S. F.; Li, Q. H.; Kim, J. N.; Yi, K. B. Properties of a Nano CaO/Al2O3 CO2 Sorbent. *Ind. Eng. Chem. Res.* **2008**, *47* (1), 180–184. https://doi.org/10.1021/ie0704748.

(123) Jing, J.; Li, T.; Zhang, X.; Wang, S.; Feng, J.; Turmel, W. A.; Li, W. Enhanced CO2 Sorption Performance of CaO/Ca3Al2O6 Sorbents and Its Sintering-Resistance Mechanism. *Appl. Energy* **2017**, *199*, 225–233. https://doi.org/10.1016/j.apenergy.2017.03.131.

(124) Yanase, I.; Maeda, T.; Kobayashi, H. The Effect of Addition of a Large Amount of CeO2 on the CO2 Adsorption Properties of CaO Powder. *Chem. Eng. J.* **2017**, *327*, 548–554. https://doi.org/10.1016/j.cej.2017.06.140.

(125) Lu, S.; Wu, S. Calcination–Carbonation Durability of Nano CaCO3 Doped with Li2SO4. *Chem. Eng. J.* **2016**, *294*, 22–29. https://doi.org/10.1016/j.cej.2016.02.100.

(126) Chen, X.; Jin, X.; Liu, Z.; Ling, X.; Wang, Y. Experimental Investigation on the CaO/CaCO3 Thermochemical Energy Storage with SiO2 Doping. *Energy* **2018**, *155*, 128–138. https://doi.org/10.1016/j.energy.2018.05.016.

(127) Shui, M.; Yue, L.; Hua, Y.; Xu, Z. The Decomposition Kinetics of the SiO2 Coated Nano-Scale Calcium Carbonate. *Thermochim. Acta* **2002**, *386* (1), 43–49. https://doi.org/10.1016/S0040-6031(01)00723-7.

(128) Kumar, D.; Maiti, S. C.; Ghoroi, C. Decomposition Kinetics of CaCO3 Dry Coated with Nano-Silica. *Thermochim. Acta* **2016**, *624*, 35–46. https://doi.org/10.1016/j.tca.2015.11.019.

(129) Zhao, M.; Shi, J.; Zhong, X.; Tian, S.; Blamey, J.; Jiang, J.; Fennell, P. S. A Novel Calcium Looping Absorbent Incorporated with Polymorphic Spacers for Hydrogen Production and CO2 Capture. *Energy Environ. Sci.* **2014**, *7* (10), 3291–3295. https://doi.org/10.1039/C4EE01281J.

(130) Willie; Tuttle Of. The System CaO-CO2-H2O and the Origin of Carbonatites.

(131) CRC Handbook of Chemistry and Physics, 86th Edition Edited by David R. Lide (National Institute of Standards and Technology). CRC Press (an Imprint of Taylor and Francis Group): Boca Raton, FL. 2005. 2544 Pp. $125.96. ISBN 0-8493-0486-5. *J. Am. Chem. Soc.* **2006**, *128* (16), 5585–5585. https://doi.org/10.1021/ja059868l.

(132) Beretka, J.; J. Ridge, M.; Brown, T. Reaction between Finely Divided Iron(III) Oxide and Barium Carbonate, in Vacuo. *Trans. Faraday Soc.* **1971**, *67* (0), 1453–1458. https://doi.org/10.1039/TF9716701453.

(133) Beretka, J.; Brown, T. Studies on the Reaction between Strontium Carbonate and Iron(III) Oxide. *Aust. J. Chem.* **1971**, *24* (2), 237–242. https://doi.org/10.1071/ch9710237.

(134) Benitez-Guerrero, M.; Valverde, J. M.; Sanchez-Jimenez, P. E.; Perejon, A.; Perez-Maqueda, L. A. Multicycle Activity of Natural CaCO3 Minerals for Thermochemical Energy Storage in Concentrated Solar Power Plants. *Sol. Energy* **2017**, *153*, 188–199. https://doi.org/10.1016/j.solener.2017.05.068.

(135) Sarrion, B.; Valverde, J. M.; Perejon, A.; Perez-Maqueda, L.; Sanchez-Jimenez, P. E. On the Multicycle Activity of Natural Limestone/Dolomite for Thermochemical Energy Storage of Concentrated Solar Power. *Energy Technol.* **2016**, *4* (8), 1013–1019. https://doi.org/10.1002/ente.201600068.

(136) Raganati, F.; Chirone, R.; Ammendola, P. Gas–Solid Fluidization of Cohesive Powders. *Chem. Eng. Res. Des.* **2018**, *133*, 347–387. https://doi.org/10.1016/j.cherd.2018.03.034.

(137) Arias, B.; Grasa, G. S.; Abanades, J. C. Effect of Sorbent Hydration on the Average Activity of CaO in a Ca-Looping System. *Chem. Eng. J.* **2010**, *163* (3), 324–330. https://doi.org/10.1016/j.cej.2010.08.009.

(138) Martínez, I.; Grasa, G.; Murillo, R.; Arias, B.; Abanades, J. C. Evaluation of CO2 Carrying Capacity of Reactivated CaO by Hydration. *Energy Fuels* **2011**, *25* (3), 1294–1301. https://doi.org/10.1021/ef1015582.

(139) Wang, K.; Guo, X.; Zhao, P.; Zhang, L.; Zheng, C. CO2 Capture of Limestone Modified by Hydration–Dehydration Technology for Carbonation/Calcination Looping. *Chem. Eng. J.* **2011**, *173* (1), 158–163. https://doi.org/10.1016/j.cej.2011.07.057.

(140) Vieira, A. P.; Williamson, K.; Humphries, T. D.; Paskevicius, M.; Buckley, C. E. A New Strontium Based Reactive Carbonate Composite for Thermochemical Energy Storage. *J. Mater. Chem. A* **2021**, *9* (36), 20585–20594. https://doi.org/10.1039/D1TA04363C.

(141) Zare Ghorbaei, S.; Ale Ebrahim, H. Carbonation Reaction of Strontium Oxide for Thermochemical Energy Storage and CO2 Removal Applications: Kinetic Study and Reactor Performance Prediction. *Appl. Energy* **2020**, *277*, 115604. https://doi.org/10.1016/j.apenergy.2020.115604.

(142) Ammendola, P.; Raganati, F.; Miccio, F.; Murri, A. N.; Landi, E. Insights into Utilization of Strontium Carbonate for Thermochemical Energy Storage. *Renew. Energy* **2020**, *157*, 769–781. https://doi.org/10.1016/j.renene.2020.05.048.

(143) Fedunik-Hofman, L.; Bayon, A.; Donne, S. Calcium, Strontium and Barium Carbonate Mixtures for Calcination-Carbonation Thermochemical Energy Storage. *AIP Conf. Proc.* **2019**, *2126* (1), 210002. https://doi.org/10.1063/1.5117751.

(144) Peter, P. D. W.; Wolfgang, P. D.-I. A. Storing and Transporting Energy, Comprises e.g. Using One-Component System of A and B in a Chemical Reaction under Heat Absorption and Removal of Carbon Dioxide to Form an Energy-Rich Compound B. DE102010009543A1, September 1, 2011. https://patents.google.com/patent/DE102010009543A1/en (accessed 2023-05-11).

(145) Miccio, F.; Murri, A. N.; Landi, E. High-Temperature Capture of CO2 by Strontium Oxide Sorbents. *Ind. Eng. Chem. Res.* **2016**, *55* (23), 6696–6707. https://doi.org/10.1021/acs.iecr.6b00184.

(146) Gigantino, M.; Kiwic, D.; Steinfeld, A. Thermochemical Energy Storage via Isothermal Carbonation-Calcination Cycles of MgO-Stabilized SrO in the Range of 1000–1100 °C. *Sol. Energy* **2019**, *188*, 720–729. https://doi.org/10.1016/j.solener.2019.06.046.

(147) Ammendola, P.; Raganati, F.; Landi, E.; Natali Murri, A.; Miccio, F. Kinetics of the Carbonation Reaction of an SrO-Al2O3 Composite for Thermochemical Energy Storage. *Chem. Eng. J.* **2021**, *420*, 129618. https://doi.org/10.1016/j.cej.2021.129618.

(148) Bagherisereshki, E.; Tran, J.; Lei, F.; AuYeung, N. Investigation into SrO/SrCO3 for High Temperature Thermochemical Energy Storage. *Sol. Energy* **2018**, *160*, 85–93. https://doi.org/10.1016/j.solener.2017.11.073.

(149) Amghar, N.; Ortiz, C.; Perejón, A.; Valverde, J. M.; Maqueda, L. P.; Sánchez Jiménez, P. E. The SrCO3/SrO System for Thermochemical Energy Storage at Ultra-High Temperature. *Sol. Energy Mater. Sol. Cells* **2022**, *238*, 111632. https://doi.org/10.1016/j.solmat.2022.111632.

Chapter 2

Experimental

“It doesn't matter how beautiful your theory is ... If it doesn't agree with experiment, it's wrong.”

— Richard Feynman

2.1 Introduction

In this chapter, the various methods employed for the synthesis and characterisation of TCES materials are described. These methods have undergone consistent revision and refinement over the course of this PhD. The chapter will provide a brief historical background and working principles of each technique. Furthermore, it will focus on the parameters and modifications made to these techniques to suit the specific laboratory requirements and research objectives. It is worth noting that some of these techniques and parameters evolved over the timeframe of this PhD as new instrumentation was purchased, developed, upgraded and/or constructed.

The majority of this work was undertaken in the Hydrogen Storage Laboratory at Curtin University in the department of Physics and Astronomy. Prior to commencing experimental procedures, a thorough analysis of all starting materials and potential reactants was conducted, including a review of the corresponding safety data sheets (SDS). Additionally, comprehensive risk assessments were performed to ensure the safe handling and management of all experimental processes.

2.2 Materials

While metal carbonates and oxides are typically unreactive in air, nickel was handled within an argon-filled glovebox (Unilab Glovebox, MBraun, Germany) to minimise contact with moisture and oxygen and prevent oxidation. The glovebox H_2O/O_2 levels were below one ppm using an automated argon gas purifier. The following starting materials were used in the course of the PhD.

Table 2-1: List of starting materials including purity and supplier.

Name	Formula	State	Purity	Supplier

Barium carbonate	$BaCO_3$	Powder	≥ 99.0 %	Sigma-Aldrich
Barium silicon oxide	$BaSiO_3$	Powder	Unlisted	Alfa Aesar
Strontium carbonate	$SrCO_3$	Powder	≥ 99.9 %	Sigma-Aldrich
Silicon dioxide	SiO_2	Nano Powder < 20 nm	> 99.5 %	Sigma-Aldrich
Sodium chloride	NaCl	Powder	≥ 99.0%	Sigma-Aldrich
Magnesium chloride	$MgCl_2$	Powder	≥ 98.0%	Sigma-Aldrich
Titanium dioxide (anatase)	TiO_2	Powder	≥ 99.9 %	Sigma-Aldrich
Iron (iii) oxide	Fe_2O_3	Powder	≥ 94.0 %	Chem-Supply
Aluminium oxide	Al_2O_3	Powder	> 98	Sigma-Aldrich
Zinc oxide	ZnO	Powder	> 99	Sigma-Aldrich
Manganese oxide	MnO	Powder	> 94	Chem-supply
Copper oxide	CuO	Powder	> 99	Sigma-Aldrich
Nickel oxide	NiO	Powder	> 99.9	Sigma-Aldrich
Zirconium dioxide	ZrO_2	Powder, < 100 nm	≥ 99.9 %	Sigma-Aldrich
Nickel	Ni	Powder, < 1 mm	> 99.7%	Sigma-Aldrich
Argon	Ar	Gas	≥ 99.995%	Coregas
Carbon Dioxide	CO_2	Gas	≥ 99.995%	Coregas

2.3 Synthesis

2.3.1 Ball milling

Ball milling, as it is commonly referred to, is a widely used technique in material science to produce a homogenous mixture of powders and enhance their properties. The process involves placing one or more materials in a cylindrical container filled with balls and applying a centrifugal force, thus causing high energy collisions between the balls, the powder, and the side of the container resulting in a reduction of particle size and an increase in defects such as dislocations and vacancies.[1,2]

Ball milling was employed to ensure homogenous mixing of materials and reduce the average particle size, thereby increasing the surface area of reactants. Characterisation through X-ray diffraction was utilised to confirm that no unintended reactions occurred during the process. To preserve consistency, all samples were ball milled under similar conditions. Mixtures of powders totalling 3 - 6 g were milled using an Across International Planetary Ball Mill (PQ-N04.) Samples were ball milled at 200 rpm for 1 - 6 h (bi-directional 20-minute segments with 1-minute breaks) in sealed (under air or 99.995% argon) 100 mL stainless steel (SS 304, inner diameter = 52 mm depth = 52mm, outer diameter = 64mm) vials with stainless steel balls (SS 316, o.d. 8 mm, ball-to-powder mass ratio of 10 : 1) (see Figure 2-1).

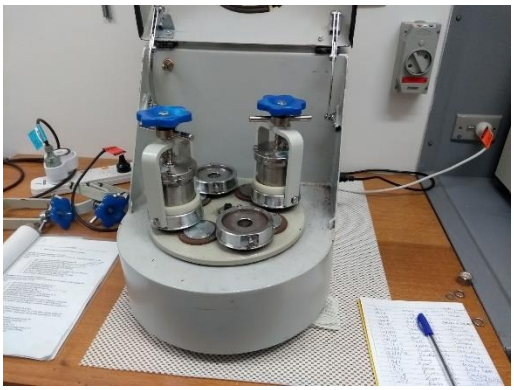

Figure 2-1: Ball milling sample vials with stainless steel balls (left), ball mills loaded for milling.

The following procedure was used to clean the ball mill and balls between runs:

1. Washing with water and then ethanol separately.
2. Milling with a mixture of ethanol and NaCl for one hour.
3. Washing with water and then ethanol.
4. Milling with ethanol for 1 hour.
5. Visual inspection of mall and bills either repeat steps 2-4 or dry with compressed air.
6. Replacement of balls on any sign of damage or discolouration.

2.3.2 Solid State Thermochemical Synthesis

Solid state thermochemical synthesis involves mixing reactants and heating them to a high temperature in a furnace to promote chemical reactions between the reactants. Solid state synthesis has several advantages over other synthesis methods, it produces high quality materials, avoids the use of solvents, and allows the synthesis of otherwise difficult to obtain materials.[3]

Milled mixtures were placed in an alumina boat (length = 100 mm, depth = 18 mm, width = 14 mm, thickness = 2 mm) that was placed in a FB1310M furnace (ThermoFisher Scientific) (see Figure 2-2). A heating rate of ($\Delta T/\Delta t$) = 10 °C min^{-1}, was selected and the reactants were held isothermally for periods of 3 or 6 h, under air. The furnace was placed in a fume hood to prevent human exposure to unwanted gases produced during the process.

Figure 2-2: Alumina boats used in solid state synthesis (left) FB1310M (ThermoFisher Scientific) furnace used for solid state synthesis (right).

After synthesis, the products were allowed to cool naturally and then carefully transferred to sample vials, while X-ray diffraction was employed to verify the success of the synthesis procedures. Table 2-2 lists the selected synthesis parameters. The synthesised products were all milled before heating under the conditions outlined above (see section 2.3.1).

Table 2-2: List of conditions used in solid state synthesis.

Reactants	Product	Temperature	Notes
$SrCO_3$ + TiO_2	$SrTiO_3$	1100 °C	3 hours isothermal
$SrCO_3$ + ZrO_2	$SrZrO_3$	1100 °C	3 hours isothermal
$BaCO_3$ + SiO_2	$BaSiO_3$	1000 °C	1:1.17 molar ratio 6 hours isothermal
$SrCO_3$ + SiO_2	$SrSiO_3$	1000 °C	1:1.1 molar ratio $SrCO_3$ & SiO_2 heated separately for 3 hrs at 600 °C to remove moisture. Ball milled before heating for 16 hours, Isothermal for 3 hours

2.4 Characterisation

2.4.1 TGA-DSC

Thermogravimetric analysis (TGA) coupled with differential scanning calorimetry (DSC) is a powerful technique employed in material science to study the thermal behaviour of materials. TGA measures the weight change of materials using a finely tuned balance while DSC simultaneously measures the heat flow from the sample. The combination of these two techniques provides complementary information about the sample which can be used to determine a wide range of characteristics including thermal decomposition, phase changes, activation energy of materials, kinetics of decomposition and specific heat capacity.[4]

Thermogravimetric analysis (TGA) was employed to investigate the behaviour of materials under different gas flows. This analytical technique allowed for the measurement of temperature and mass change for calcination and carbonation at various partial gas

pressures. In particular, the intermittent introduction of CO_2 or argon gas flow enabled the measurement of cyclic uptake and release of carbon dioxide.

The experiments were conducted using a Netzsch STA 449 F3 Jupiter instrument.[5] For TGA-DSC experiments, samples weighing between 10 – 30 mg were gently pressed into Al_2O_3 crucibles (85 µl, CS Ceramics) equipped with a lid and a pinhole to facilitate gas flow. All samples (due to their inert nature) were loaded under an air atmosphere except for those which contain nickel which were loaded under argon in a glove box to prevent oxidation. The heating and cooling rates employed during most experiments were $\Delta T/\Delta t$ = 10 °C·min^{-1} unless otherwise mentioned. A protective flow of argon (Coregas, 99.995%, 20 mL·min^{-1}) was used at all times to protect the Pt furnace. The DSC was calibrated using In, Zn, Al, Ag, and Au reference materials, and the scale was calibrated using an internal mass, resulting in an overall accuracy of ± 0.2 °C for temperature and ± 20 µg for the balance.

2.4.2 Activation energy – the Kissinger method

Activation energy is important in chemical kinetics as it quantifies the energy barrier that reactants must overcome to form products in a chemical reaction. The Kissinger method can be used to determine activation energy by using TGA-DSC to analyse corresponding peak reaction temperatures as a function of heating rate. The Kissinger equation is expressed as follows:[6]

$$\ln[\beta/T_p^2] = -E_a/RT_p + \ln[AR/E_a] \quad (2\text{-}1)$$

Where:

- β is the heating rate (K·s^{-1})
- T_p is the DSC peak temperature for calcination (K)
- E_a is the activation energy (kJ·mol^{-1})
- R is the gas constant (8.3145 J·(K·mol)$^{-1}$)
- A is a reaction species constant (s^{-1})

The process for determining the activation energy (E_a) from the Kissinger plot involves the following steps:

1. Conduct DSC experiments using various heating rates.
2. Identify the temperature (T_p)* at which the DSC curve reaches its peak for the reaction in question.
3. Calculate the natural logarithm of the ratio ($\ln(\beta/T_p^2)$)
4. Plot $\ln(\beta/T_p^2)$ against $1000/T_p$ and use linear regression to find the gradient of the data.
5. Determine the activation energy (E_a) by multiplying the absolute value of the gradient by the gas constant (R) and 1000, as follows: $E_a = |\text{gradient}| \times R \times 1000$.

*Note that this method applies to single step reactions and does not consider thermal inertia, this is negligible to the final result in most cases.

2.4.3 TGA CO_2 absorption-desorption experiments

To measure CO_2 absorption and desorption the Netzsch STA 449 F3 Jupiter was utilised using a different sample carrier. The Pt DSC sensor (C_p Type-S) in the TGA-DSC can corrode due to the formation of CO from CO_2 due to the Boudouard reaction at temperatures > 800°C.[5] To avoid this corrosion a TGA sample carrier (TGA, Type S, pin, NETZCH) was utilised when using CO_2 flows in experiments.

The samples were placed in Al_2O_3 crucibles (85 µl, CS Ceramics) and a protective flow of argon (Coregas, 99.995%, 20 mL·min^{-1}) was used at all times. For both calcination and carbonation, a flow rate of argon (Coregas, 99.995%, 20 mL·min^{-1}) was utilised to protect the Pt furnace. However, for carbonation a CO_2 (Coregas, 99.995%, 80 mL·min^{-1}) flow was introduced. This is equivalent to a partial pressure of $p(CO_2)$ = 0.8 bar for carbonation and $p(CO_2)$ = 0 bar for calcination.

2.4.4 Laboratory Powder XRD

X-ray diffraction (XRD) is a technique used to study the structure of materials at the atomic level. A beam of X-rays is directed at a crystalline material, which are diffracted by the atoms in a crystalline structure, forming a characteristic pattern on a detector. The angle between the beam source and the scattering plane is defined by 2θ. To determine the distance between atomic layers within the structure we can use Braggs law:[8]

$$n\lambda = 2d_{hkl}\sin\vartheta \qquad (2\text{-}2)$$

Where:

- n = an integer
- λ = is the wavelength of the incident X-ray beam
- d = the interatomic distance between layers
- 2ϑ = the angle of incidence between the beam path and the scattering planes
- h, k and l = the miller indices of the crystalline plane.

Miller indices define the spacing between a particular crystal plane of atoms and determine the peak position as a function of 2ϑ in the diffraction profile, which is almost unique for each crystal structure and can therefore be identified.

Two laboratory-based diffractometers were utilised. The Bruker D8 Advance diffractometer uses a Cu K_α wavelength radiation (λ = 1.5418 Å, 40 kV, 40 mA) and the Bruker D8 Discover diffractometer with Co K_α radiation (λ = 1.7890 Å, 35 kV, 30 mA). The diffractometers were calibrated and instrument parameters defined using a NIST Al_2O_3 plate (SRM 1976c). Both diffractometers were operated using a Bragg-Bretano geometry. In this configuration, the incident divergent X-ray beam strikes the sample surface at a specific angle, and the diffracted beams are collected at the same angle on the opposite side. The majority of samples were measured using the D8 Advance, which utilises Cu K_α radiation, this is because it is the standard in material science because of its relatively high intensity and suitable wavelength. However, when studying materials that contain iron, a

phenomenon known as florescence can occur when using a Cu X-ray source.[9] X-ray fluorescence can create a high background that also may mask low intensity diffraction peaks, so should be avoided. Further parameters and a summary are listed below (see Table 2-3):

Table 2-3 XRD instrument parameters.

Parameter	D8 Advance XRD	D8 Discover XRD
Radiation wavelength (Å)	Cu (1.5418)	Co (1.789)
Operating Voltage (kV)	40	35
Operating current (mA)	40	30
Detector	Linear PSD lynxeye (2.94°- 2ϑ)	Linear PSD lynxeye (3.4° - 2ϑ)
Goniometer radii	250	217
Fixed divergence slit angle	0.3	0.3
Primary Soller slit angle (°)	2.5	2.5
Secondary Soller slit angle (°)	2.5	2.5

Samples were ground in a mortar and pestle and placed in low background sample holders constructed from polymethylmethacrylate with a single-crystal silicon wafer, with a small cavity (diameter = 10 mm, depth = 1 mm) housing the sample (see Figure 2-3). The samples were side-packed against a glass slide to minimise preferential orientation.

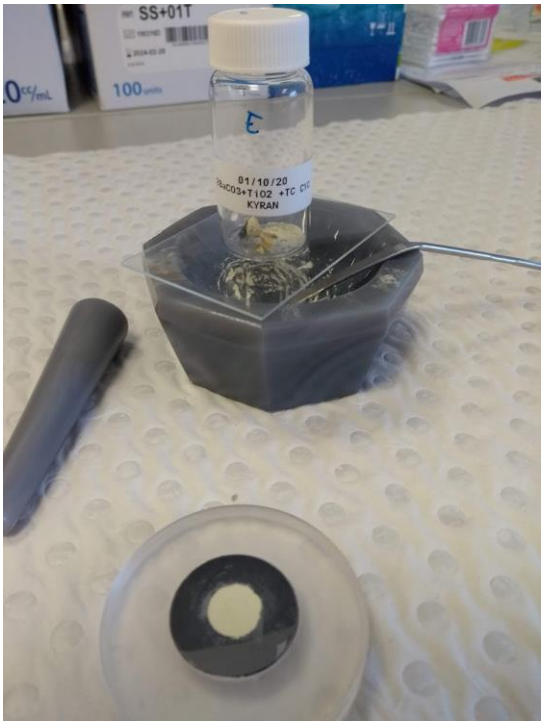

Figure 2-3: Prepared sample for X-ray diffraction in a low background sample holder.

All diffraction peaks were identified by Phase-ID using the software package Match! (Crystal Impact) which utilises two primary databases: the International Centre for Diffraction Data (ICDD) - Powder Diffraction File Database (PDF2) and Crystallography Open Database (COD). Other diffraction patterns were sourced from the literature.[10]

2.4.5 Synchrotron powder X-ray diffraction

In-situ Synchrotron powder X-ray diffraction (SR-PXD) is a powerful technique for investigating the structural properties of crystalline materials in an evolving environment. The Australian synchrotron in Melbourne was accessed via competitive merit-based grants to undertake several experiments. A Synchrotron is a particle accelerator that uses electromagnetic fields to produce a beam of high energy electrons that are boosted to close to the speed of light. The path of these electrons are deflected by magnets, which causes them to emit synchrotron light that is channelled to various end stations.[11,12] The

powder diffraction (PD) beamline was accessed with the help of beamline scientist Dr Anita D'Angelo. Synchrotron radiation has a number of advantages over traditional lab-based diffraction.

1. High flux: Synchrotron radiation sources provide much higher intensity X-rays than laboratory-based sources. This allows for faster data collection and higher quality data.

2. High resolution: The high intensity of synchrotron radiation sources allows for higher resolution data collection, leading to more accurate and detailed structural information.

3. Time-resolved studies: Synchrotron radiation sources allow for time-resolved studies, which can reveal structural changes in a material over time.

4. Allows for non-ambient and non-conventional sample environments.

At the Australian synchrotron, two types of experiments were performed due to various sample requirements. Both experiments utilised the same custom-built gas manifold but featured distinct sample stage configurations.

2.4.5.1 SR-XRD Experimental setup

The SR-XRD experiments in this study utilised a wavelength of λ = 0.775227(5) Å or 0.825040(5) Å. The instrument function was defined and the wavelength refined against a LaB6 660c standard. The data was captured using a Mythen microstrip detector at two different positions, each with a 30-second acquisition time, before being combined into a single dataset using in-house powder diffraction software package "PD-VIPER".[13]

Lower temperature samples (< 1000 °C) were packed in quartz capillaries (o.d. 0.7 mm, wall thickness 0.05 mm) and mounted in a custom gas fitting sealed with rubber o-rings using transmission geometry (see Figure 2-4). The samples were continuously oscillated over 90° to improve powder averaging during data acquisition. The capillaries were

heated using a hot air blower (Cyberstar) at $\Delta T/\Delta t$ = 6 °C min^{-1} to the desired temperature. Temperature measurements were calibrated against the thermal expansion of an Ag standard. [14–16]

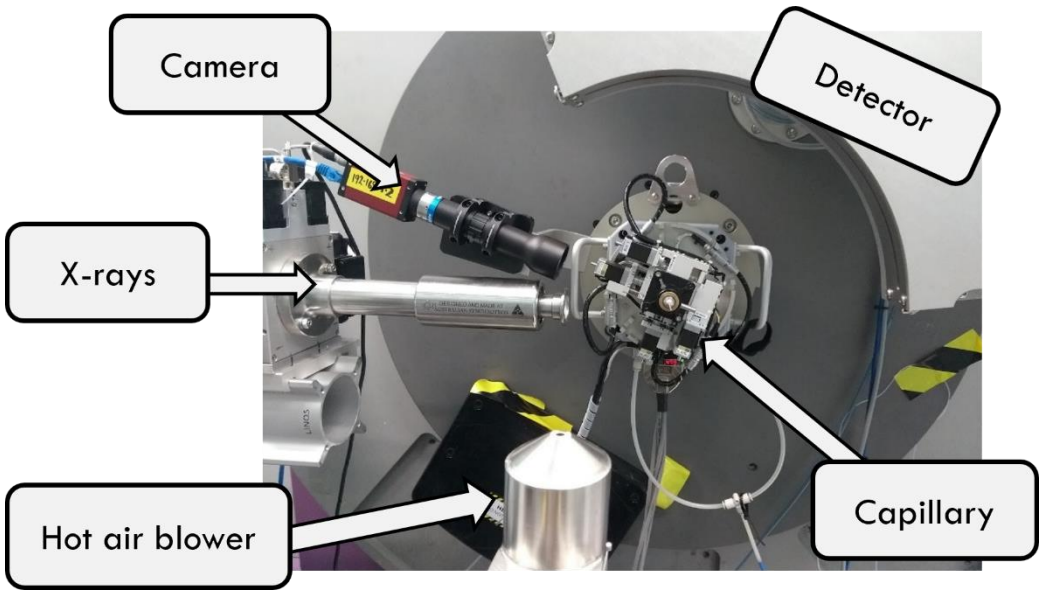

Figure 2-4: Photo of experimental set up for quartz capillary samples at the Australian synchrotron.

Due to safety requirements, there is a working temperature limit of 1000 °C for capillary samples at the Australian Synchrotron. The high temperature (> 1000 °C) powder samples were housed within an Anton Paar HTK 2000 strip furnace (using a Pt strip), in flat-plate geometry, and were heated from room temperature to 1100 °C at $\Delta T/\Delta t$ = 6 °C·min^{-1} on a pre-stressed Pt strip with a thermocouple (Type S, 90% Pt: 10% Rh, ± 1%) spot-welded to the heating strip(See Figure 2-5).

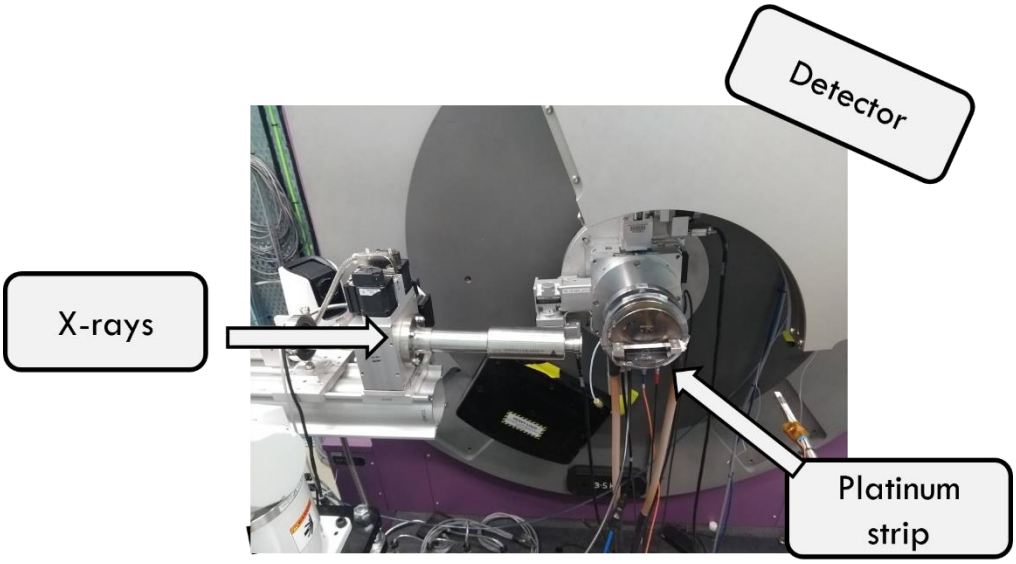

Figure 2-5: Photo of experimental set up at Australian synchrotron for flat plate samples.

To apply CO_2 pressure or vacuum on the sample a custom gas manifold was built from Swagelok parts (Figure 2-6). A pressure gauge (0 - 10 bar, Swagelok) and a vacuum pump (Pfeiffer, Hicube 80 eco turbo pumping station, ultimate pressure: $< 1 \times 10^{-7}$ mbar) were then connected to a gas manifold that provided vacuum or various CO_2 (BOC Gas, 99.99%) pressure on the samples (Figure 2-6).

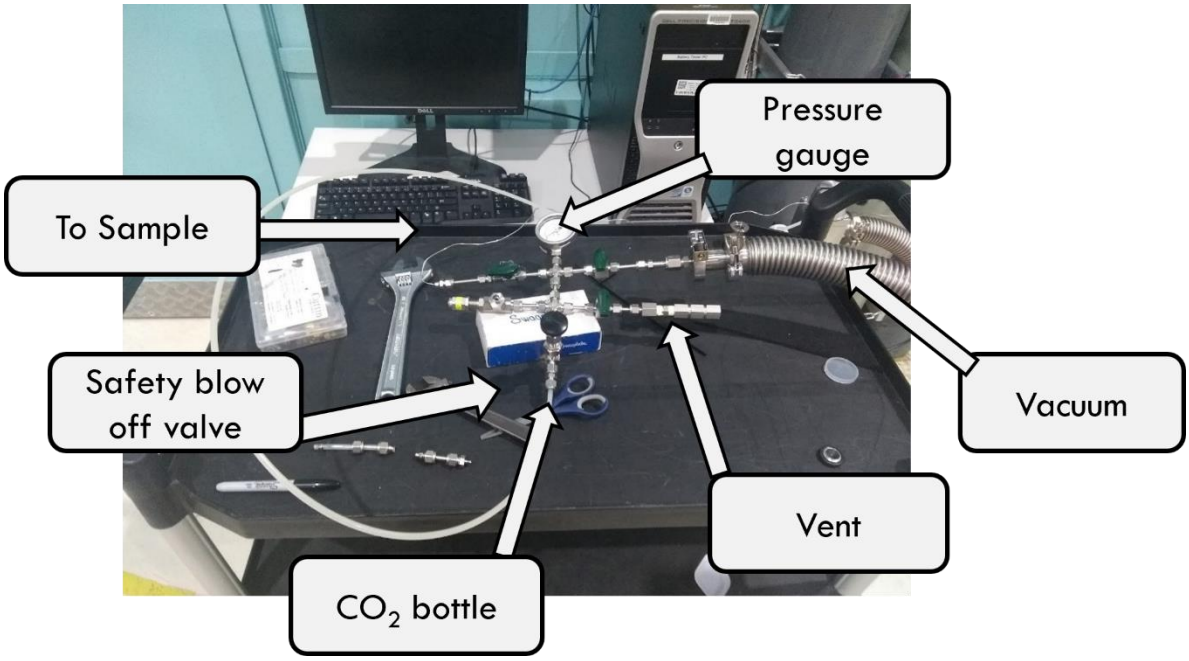

Figure 2-6: Gas manifold used to apply CO_2 and vacuum to the measurement of TCES samples at the Australian synchrotron.

2.4.6 Quantitative phase analysis using the Rietveld refinement method

The X-ray diffraction patterns of selected samples were quantitatively analysed using the Rietveld refinement method with TOPAS V.5 software from Bruker AXS.[17] The Rietveld refinement technique utilises a non-linear least squares method to fit a model which that describes the entire XRD profile (in a selected 2ϑ range). The model is iteratively refined for factors such as the background, crystallite size, lattice parameters, the weight percentage of each compound, preferred orientation, densities, accounting for uncertainties. The software can determine the intrinsic parameters and give a relative wt.% of each phase present within an uncertainty of approximately 2%. Rietveld refinement can be applied to SR-XRD data to demonstrate the evolution of phases as a compound is heated or subjected to various gas pressures.

2.4.7 SEM

Scanning electron microscopy (SEM) is a versatile imaging technique that uses a focused beam of electrons to generate high resolution images down to the nanometer scale. This provides valuable information about the morphology, composition, and surface of a material.

SEM was performed using a Neon Dual-Beam FESEM (Zesis, Germany) and Tescan Mira3 (see Figure 2-7). Both SEMs are equipped with electron backscattered diffraction/energy-dispersive X-ray spectroscopy (EBSD/EDS) oxford instrument detectors. The SEM were controlled, and data were analysed using Aztec version 5 and version 6.1 (Oxford Instruments).[18]

Figure 2-7: Neon Dual-Beam FESEM (left) and Mira VP-FESEM (right).

The SEM analyses involved a range of parameters tailored to each material. Accelerating voltages spanned 5 kV to 20 kV, aperture sizes varied from 30 µm to 60 µm, and working distances ranged from 2.5 mm to 10 mm. The samples were prepared by distributing a small amount of the powdered sample onto carbon tape, which was placed on an aluminium stub and then sputter coated with a 10 nm layer of conductive carbon. Magnetic samples can be damaging to the instrumentation, so Fe-rich samples were

prepared by embedding powder in an epoxy resin that was polished using colloidal silica, these were then sputter coated with a 10 nm thick carbon layer before analysis. The SEM-EDS was used for qualitive measurements and was not calibrated for these experiments. Further parameters are summarised below (see Table 2-4) and further details of the instruments can be found on Curtin university John de Laeter website.[19,20]

Table 2-4 SEM parameters and sample preparation across investigated materials.

Material	SEM Instrument	Accelerating Voltage	Aperture Size	Working Distance	Sample Preparation
$BaSiO_3$	Zeiss Neon 40EsB	5 kV (SEM), 20 kV (EDS)	30 µm	2.5 – 7 mm	Embed powdered samples in epoxy resin, polish with colloidal silica, sputter coat with 10 nm carbon layer
$SrCO_3$-$SrSiO_3$	Tescan Mira3	5 kV (SEM), 20 kV (EDS)	10 µm	5 mm	Sputter-coat with 3 nm Pt
$BaCO_3$- Fe_2O_3 (non-magnetic)	Zeiss Neon 40EsB	20 kV	60 µm	9.9 mm	Distribute sample on carbon tape, coat with 10 nm carbon layer
$BaCO_3$ -Fe_2O_3 (magnetic)	Tescan Mira3	20 kV	10 µm	2–10 mm	Embed powdered samples in epoxy resin, sputter coat with 10 nm carbon layer

$2BaCO_3$ -TiO_2	Tescan Mira3	5 kV	10 µm	5 mm	Distribute sample powder on carbon tape, sputter-coat with 3 nm Pt
$SrCO_3$ $SrZrO_3$	Tescan Clara	15 kV(SEM and EDS)	30 µm	2 – 10 mm	Sprinkle powder samples on carbon tape, coat with 20 nm conductive carbon layer

2.4.8 EDS

Energy dispersive X-ray spectroscopy is a complementary technique used within the SEM, it is commonly used in material science and analytical chemistry.[21] EDS operates by bombarding the sample with a focused electron beam, which excites electrons ejecting them from inner shells creating an electron hole. When an electron from a higher-energy electron shell drops to fill this void, characteristic X-rays corresponding to the difference in energy are released. These X-rays correspond to the characteristic difference in energy level between the shells, which can be matched to the element in question. This allows us to map corresponding elements across an SEM image.

2.5 SIEVERTS APPARTUS

2.5.1 Introduction

A Sieverts apparatus is an experimental tool for the precise measurement of gas absorption and desorption in materials (Figure 2-8).[22] It is named after the German chemist Adolf Ferdinand Sieverts who developed the instrument in the early 20th century.[23–25] It is based on the principle of manometric analysis where a pressure change is measured in a closed system in response to a change in initial conditions (pressure, volume or temperature).[22]

The Sieverts apparatus was built from Swagelok parts made from SS316 and consists of several volumes separated by pneumatic valves, the interconnections are sealed with Swagelok VCR fittings and filters/silver-plated stainless-steel gaskets. It is equipped with a Rosemount 3051S pressure transducer with an accuracy of ±0.02 % and uses K-type thermocouples (Omega engineering) with an accuracy of ±1.5 °C and RTD sensors (Omega engineering) with an accuracy of ±1 °C. Three Sieverts apparatus have been previously constructed at Curtin University for hydrogen storage measurements and further details of their build and the calculations which provide the gas volume etc are detailed here.[26–28]

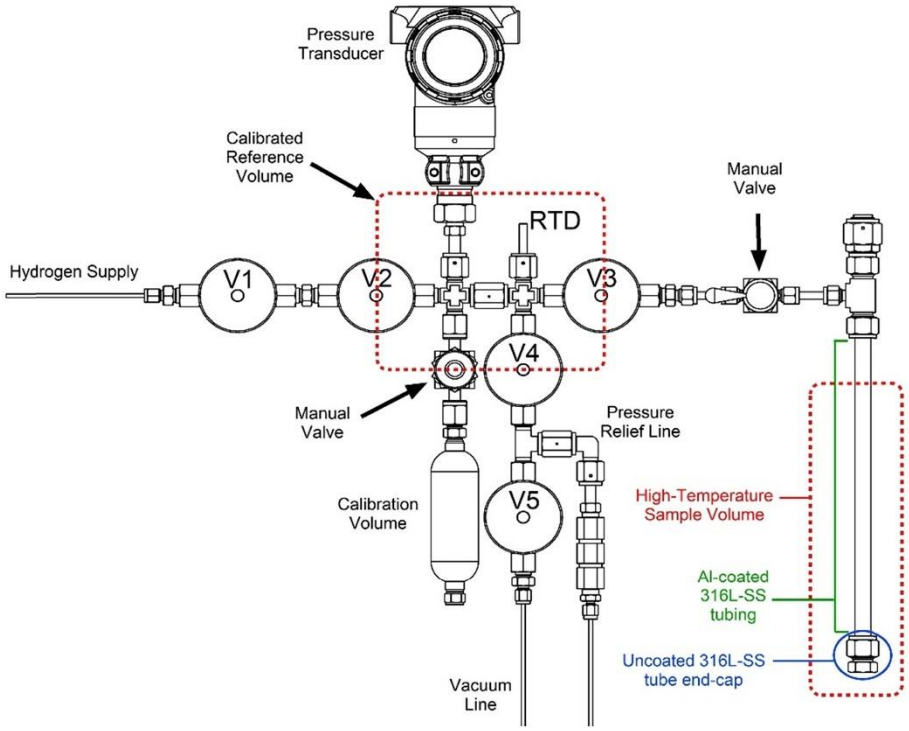

Figure 2-8: Sieverts apparatus schematic for hydrogen storage, in this project the sample cell and gas supply were modified for CO_2 applications.[22]

To perform CO_2 measurements an almost identical Sieverts apparatus was constructed by the author in collaboration with A/Prof Mark Paskevicius and Sruthy Balakrishnan with two additional modifications (see Figure 2-9).

1. The addition of a 150.3 cm^3 stainless steel ballast volume below V2 with a separate automatic valve V6. This was used to optionally increase the volume of the reference side from 37.2 cm^3 to 187.5 cm^3, which allows the system to reach different pressures on the reference and/or sample side.
2. The attachment of CO_2 as opposed to H_2 left of V1, (the corresponding LabVIEW control software was modified to account for the compressibility of CO_2).

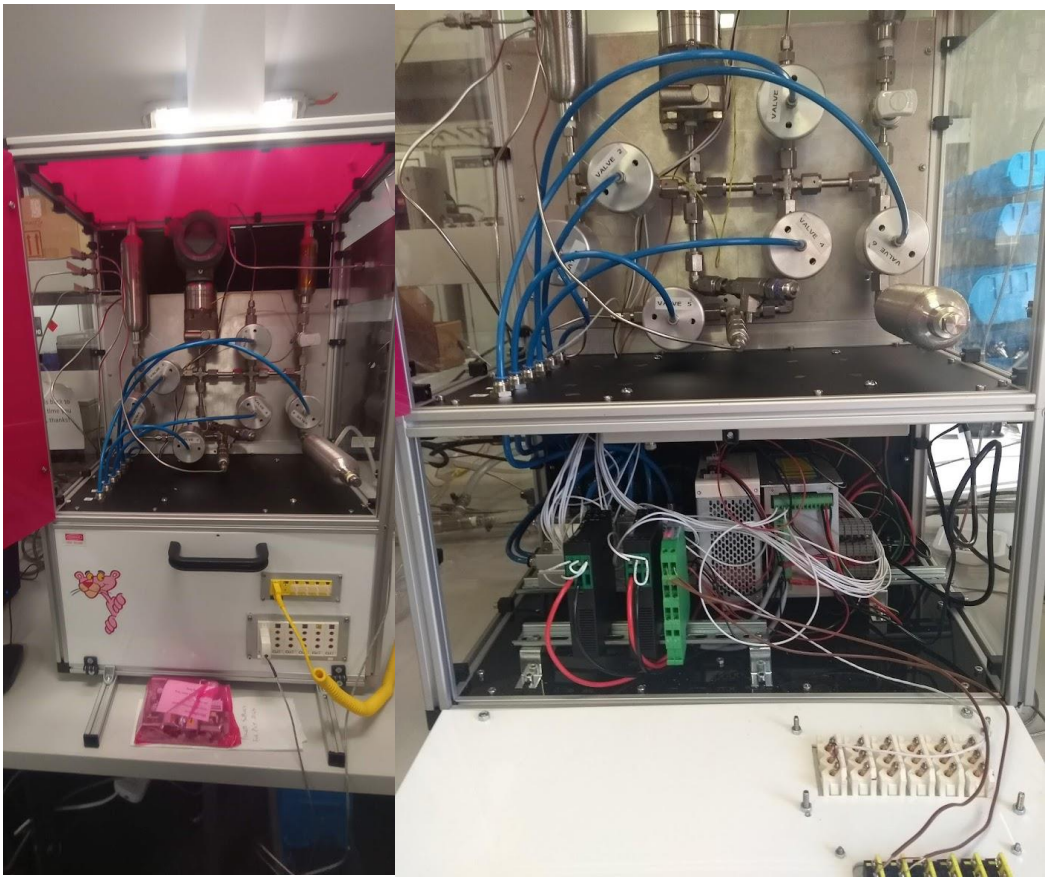

Figure 2-9: Sieverts apparatus "Pink Panther", fascade and volumetric section (left) close up of electronics (right).

In addition, a sample cell that is resistant to the high temperature reaction between stainless steel and CO_2 was constructed (Figure 2-10).[22] The sample cell consists of SS316 Swagelok parts including a pressure safety release valve set to 25 bar (Swagelok) and a manual valve (Swagelok). This was connected to a sample holder built from a single-ended silicon carbide tube (SiC, Saint-Gobain, France) with a length of 450 mm, an outer diameter of 16.2 mm, a wall thickness of 2.9 mm and an inner diameter of 10.4 mm

(specified with grain size < 10 µm and > 98 % theoretical density). The silicon carbide was connected to SS316 tubing via a Teflon ferrule and adequate measures were taken to reduce the heat to the ferrule which started to soften and melt at temperatures (> 100 °C). These included the use of a cooling fan, thermal paste and an aluminium radial heatsink on the outer surface of the SiC.

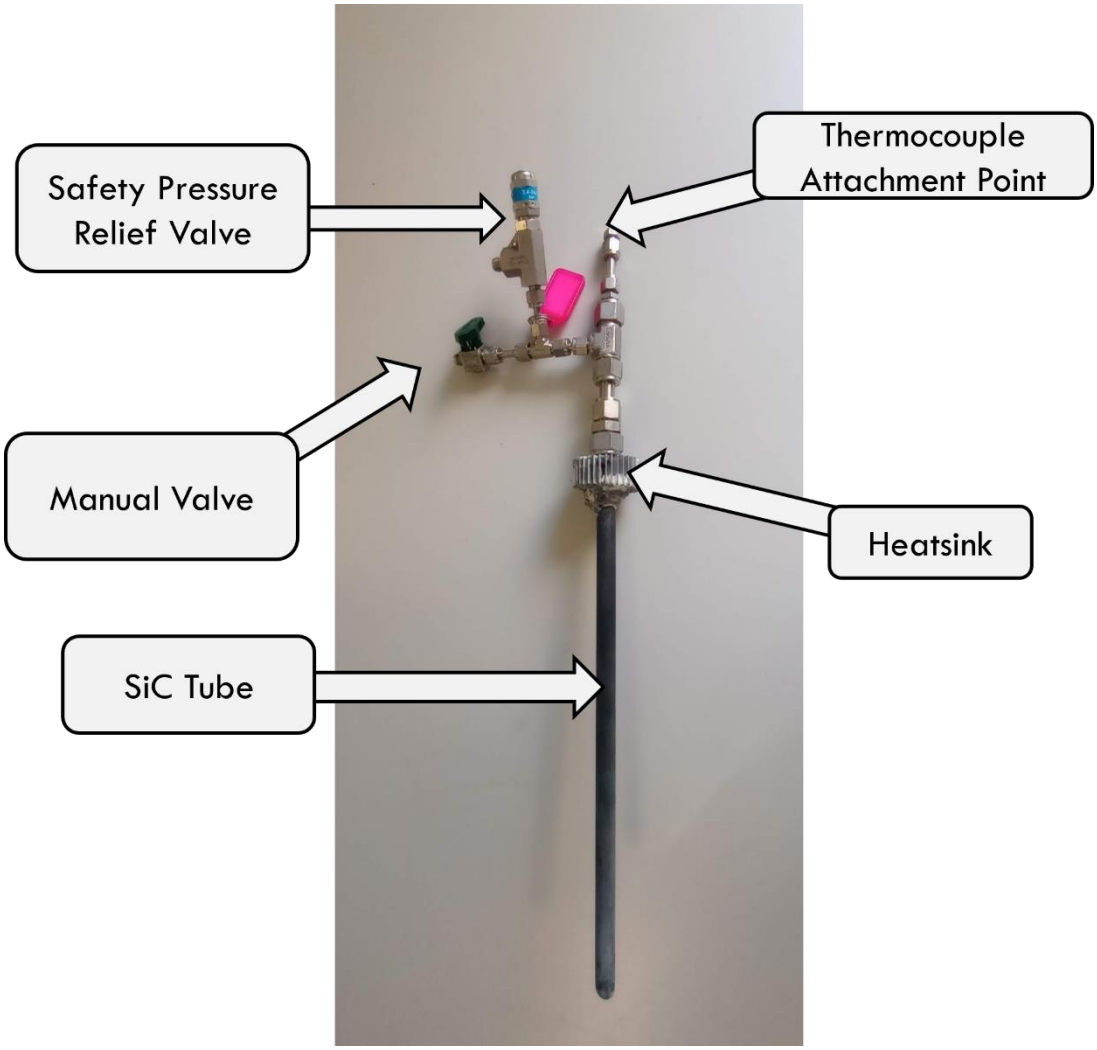

Figure 2-10: Sample cell of Sieverts apparatus for high temperature CO_2 measurements.

The sample cell was loaded with samples of ~ 0.3 - 3 g and heated with a vertical tube furnace (GSL 1100-X, MTI corporation). K-type thermocouples were placed through the top of the sample cell and resided in the powder at the bottom of the SiC tube. A Perspex

blast shield was used around the sample cell, in case of ceramic fracture of the SiC tube during gas pressure excursions (see Figure 2-11).

Figure 2-11: Perspex blast shield around the furnace heating the sample cell of the Sieverts apparatus.

For higher temperature measurements (above 950 °C) another furnace was used (LABEC VTHTF40/15, maximum temperature of 1400 °C) (Figure 2-12). Preliminary measurements at temperatures > 1000 °C found unreliable readings from the K-type thermocouple, which was degrading due to corrosion by CO_2, leading to drifting readings.[29] To circumvent this problem, the Sieverts apparatus was connected to the furnace's internal B-type

thermocouple, through a signal module with thermocouple input and voltage output, and the resulting temperature difference between the furnace thermocouple and the internal cell temperature was calibrated using an internal K-type thermocouple.

Figure 2-12: Labec VTHTF40/15 high temperature furnace in operation.

2.6 Pressure composition isotherms (PCI)

The thermodynamics of a gas–solid reaction can be calculated using the van't Hoff equation. At a constant temperature and pressure the change in Gibbs free energy is defined as:[30]

$$\Delta G = \Delta H - T\Delta S \quad (2\text{-}3)$$

Where:

- ΔG is the change in Gibbs free energy ($kJ \cdot mol^{-1}$)
- ΔH is the change in enthalpy ($kJ \cdot mol^{-1}$)
- T is the temperature (K)
- ΔS is the change in entropy ($J \cdot K^{-1}$)

Combined with the Gibbs free energy isotherm equation;[31]

$$\Delta G = -R\,T\,\ln(K) \quad 2\text{-}36 \quad (2\text{-}4)$$

Where:

- R is 8.31446 is the universal gas constant ($J \cdot K^{-1} \cdot mol^{-1}$)
- K is the thermodynamic equilibrium constant

This gives the van't Hoff equation which relates the equilibrium constant (K) of the reaction to the change in enthalpy (ΔH) and entropy (ΔS) temperature (T) using the following equation.[22]

$$\ln(K) = \ln(P_{eq}/P_0) = \Delta H/RT - \Delta S/R \quad (2\text{-}5)$$

Where:

- P_{eq} is the measured equilibrium pressure

- P_0 = 1 bar

When Δ*H* and Δ*S* are constant we obtain the linear form of the van't Hoff equation which gives ln(*K*) as a function of 1/*T*.

The Sieverts apparatus is used to heat a sample under gas pressure, maintaining a state above the thermodynamic gas equilibrium pressure and temperature of the reaction. Subsequently, the gas pressure is gradually decreased in decrements of ~ 0.1 - 1 bar, initiating the gas desorption reaction from the material, which results in a pressure plateau as a function of gas content, indicating the equilibrium pressure for the reaction at a given temperature. The pressure can then be further reduced in steps until the reaction is complete. This process should be repeated for several temperatures, each corresponding to different equilibrium pressures for the desorption reaction.

By conducting at least three equilibrium measurements over this temperature range, we can obtain a straight-line graph, from which the gradient and intercept can be determined:

$$\text{Gradient} = -\Delta H/R \qquad \text{Intercept} = \Delta S/R \tag{2-6}$$

Where:

- Δ*H* is the change in enthalpy ($kJ \cdot mol^{-1}$)
- Δ*S* is the change in entropy ($J \cdot K^{-1}$)
- *R* is 8.31446 is the universal gas constant ($J \cdot K^{-1} \cdot mol^{-1}$)

An example of pressure composition isotherms and corresponding van't Hoff plot are given below (see Figure 2-13).

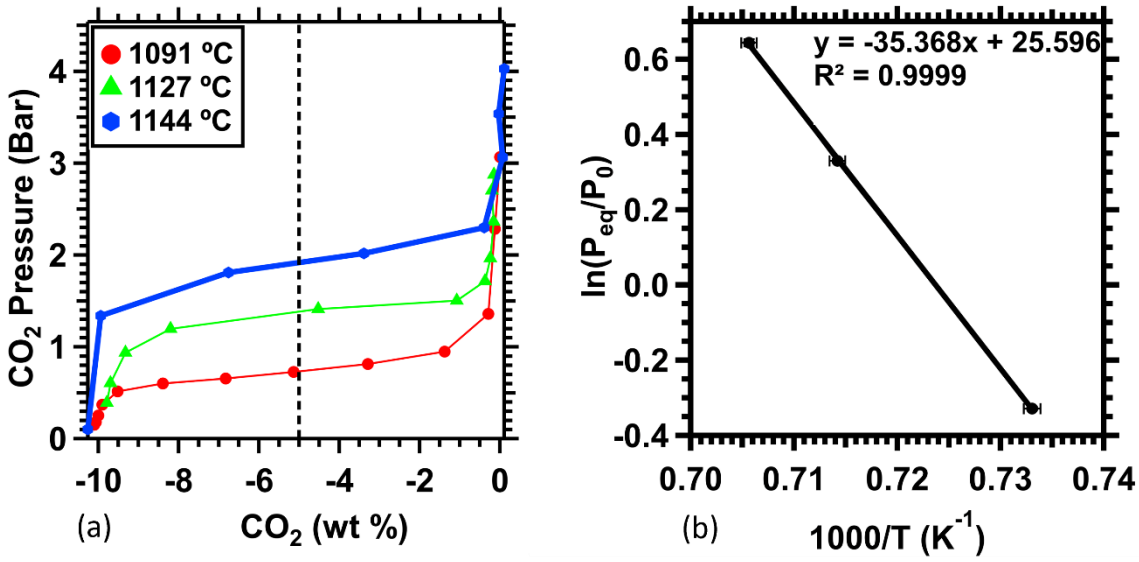

Figure 2-13: (Example plot) (a) Pressure-composition-temperature (PCT) measurements of the CO_2 release from $BaCO_3$:$BaTiO_3$. Each sample is isothermal and 48 h pressure steps (each data point) were undertaken (step size $p(CO_2$ = 0.2 - 0.5 bar) to reach equilibrium. Equilibrium pressures were taken at the midpoint of the reaction (dashed line), wt% is the loss due to CO_2 desorption. (b) Corresponding van't Hoff plot generated from taking the center point of each desorption isotherm.

2.7 PCI considerations for metal carbonates

PCI measurements are commonly employed to assess the hydrogen storage potential of metal hydride materials.[32,33] However, when using metal carbonates and CO_2, certain additional considerations should be taken into account:

- Metal carbonates undergo extremely slow reactions, sometimes taking up to 24 hours per step. Therefore, careful consideration should be given to the time period allowed for each desorption step.
- The kinetics of desorption steps should be inspected to ensure that it reaches completion, and that the material truly reaches equilibrium.
- As many metal carbonates are prone to sintering, which may significantly increase the duration of desorption, measurements should be conducted at temperatures that typically have low equilibrium pressures.

- It is advisable to use small pressure step sizes of 0.1 - 0.2 bar in close proximity to the equilibrium reaction for more precise results.

One additional point is that this Sieverts apparatus could be applied in other fields including carbon capture and storage.

2.8 Material screening and selection

In the initial stages of the project several materials were screened for their potential as thermochemical energy storage materials. This was initially performed using TGA by comparing their desorption profiles, later when the capabilities of the lab were upgraded (CO_2 integrated into TGA) their capability to re-absorb CO_2 was also considered. Each material was ball milled in a 1:1 molar ratio and heated using TGA ($\Delta T/\Delta t$) = 10 °C min^{-1} under a protective argon gas flow of 20 mL·min^{-1}. These preliminary screening results are presented in appendix C.

Materials were selected for further study based on a combination of the following.

- Desorption temperature.
- Desorption kinetics (slope of the desorption curve)
- Carbonate and additive cost[34–37]

2.9 References

(1) Zhang, D. L. Processing of Advanced Materials Using High-Energy Mechanical Milling. *Prog. Mater. Sci.* **2004**, *49* (3), 537–560. https://doi.org/10.1016/S0079-6425(03)00034-3.

(2) Manikandan, M.; Venkateswaran, C. Effect of High Energy Milling on the Synthesis Temperature, Magnetic and Electrical Properties of Barium Hexagonal Ferrite. *J. Magn. Magn. Mater.* **2014**, *358–359*, 82–86. https://doi.org/10.1016/j.jmmm.2014.01.041.

(3) Aykol, M.; Montoya, J. H.; Hummelshøj, J. Rational Solid-State Synthesis Routes for Inorganic Materials. *J. Am. Chem. Soc.* **2021**, *143* (24), 9244–9259. https://doi.org/10.1021/jacs.1c04888.

(4) Saadatkhah, N.; Carillo Garcia, A.; Ackermann, S.; Leclerc, P.; Latifi, M.; Samih, S.; Patience, G. S.; Chaouki, J. Experimental Methods in Chemical Engineering: Thermogravimetric Analysis—TGA. *Can. J. Chem. Eng.* **2020**, *98* (1), 34–43. https://doi.org/10.1002/cjce.23673.

(5) *STA 449 F3 Jupiter*. NETZSCH - Analyzing and Testing. Leading in Thermal Analysis, Rheology and Fire Testing. https://analyzing-testing.netzsch.com/en-AU/products/simultaneous-thermogravimetry-differential-scanning-calorimetry-sta-tg-dsc/sta-449-f3-jupiter (accessed 2023-06-26).

(6) Kissinger, H. E. Variation of Peak Temperature with Heating Rate in Differential Thermal Analysis. *J Res Natl Bur Stand* **1956**, *57* (4), 217–221.

(7) Vyazovkin, S. Kissinger Method in Kinetics of Materials: Things to Beware and Be Aware Of. Molecules 2020, 25 (12), 2813. https://doi.org/10.3390/molecules25122813.

(8) Warren, B. E. X-Ray Diffraction Methods. *J. Appl. Phys.* **2004**, *12* (5), 375–384. https://doi.org/10.1063/1.1712915.

(9) Mos, Y. M.; Vermeulen, A. C.; Buisman, C. J. N.; Weijma, J. X-Ray Diffraction of Iron Containing Samples: The Importance of a Suitable Configuration. *Geomicrobiol. J.* **2018**, *35* (6), 511–517. https://doi.org/10.1080/01490451.2017.1401183.

(10) *SpringerMaterials – properties of materials*. https://materials.springer.com/ (accessed 2023-06-26).

(11) Wallwork, K. S.; Kennedy, B. J.; Wang, D. The High Resolution Powder Diffraction Beamline for the Australian Synchrotron. *AIP Conf. Proc.* **2007**, *879* (1), 879–882. https://doi.org/10.1063/1.2436201.

(12) Boldeman, J. W.; Einfeld, D. The Physics Design of the Australian Synchrotron Storage Ring. *Nucl. Instrum. Methods Phys. Res. Sect. Accel. Spectrometers Detect. Assoc. Equip.* **2004**, *521* (2), 306–317. https://doi.org/10.1016/j.nima.2003.11.191.

(13) *PDViPeR*. http://archive.synchrotron.org.au/aussyncbeamlines/powder-diffraction/pdviper (accessed 2023-07-20).

(14) Bergamaschi, A.; Cervellino, A.; Dinapoli, R.; Gozzo, F.; Henrich, B.; Johnson, I.; Kraft, P.; Mozzanica, A.; Schmitt, B.; Shi, X. The MYTHEN Detector for X-Ray Powder Diffraction Experiments at the Swiss Light Source. *J. Synchrotron Radiat.* **2010**, *17* (5), 653–668. https://doi.org/10.1107/S0909049510026051.

(15) Huntley, J.; Brand, H.; Aubert, M.; Morwood, M. J. The First Australian Synchrotron Powder Diffraction Analysis of Pigment from a Wandjina Motif in the Kimberley, Western Australia. *Aust. Archaeol.* **2014**, *78*, 33–38.

(16) Wallwork, K. S.; Kennedy, B. J.; Wang, D. The High Resolution Powder Diffraction Beamline for the Australian Synchrotron. In *AIP Conference Proceedings*; AIP: Daegu (Korea), 2007; Vol. 879, pp 879–882. https://doi.org/10.1063/1.2436201.

(17) Rietveld, H. M. A Profile Refinement Method for Nuclear and Magnetic Structures. *J. Appl. Crystallogr.* **1969**, *2* (2). https://doi.org/10.1107/S0021889869006558.

(18) *AZtecLive - Nanoanalysis - Oxford Instruments*. https://nano.oxinst.com/products/azteclive (accessed 2023-08-09).

(19) Gumina, T. *Neon Dual-Beam FESEM. instrument, John de Laeter Centre | Curtin University, Perth, Western Australia*. John de Laeter Research Centre. https://jdlc.curtin.edu.au/instruments/neon-dual-beam-fesem/ (accessed 2023-07-21).

(20) Gumina, T. *MIRA VP-FESEM, instruments, John de Laeter Centre | Curtin University, Perth, Western Australia*. John de Laeter Research Centre. https://jdlc.curtin.edu.au/instruments/mira-vp-fesem/ (accessed 2023-07-21).

(21) Allen, L. J.; D'Alfonso, A. J.; Freitag, B.; Klenov, D. O. Chemical Mapping at Atomic Resolution Using Energy-Dispersive x-Ray Spectroscopy. *MRS Bull.* **2012**, *37* (1), 47–52. https://doi.org/10.1557/mrs.2011.331.

(22) Sheppard, D. A.; Paskevicius, M.; Javadian, P.; Davies, I. J.; Buckley, C. E. Methods for Accurate High-Temperature Sieverts-Type Hydrogen Measurements of Metal Hydrides. *J. Alloys Compd.* **2019**, *787*, 1225–1237. https://doi.org/10.1016/j.jallcom.2019.02.067.

(23) Sieverts, A. Z. *Phys Chem Leipz.* **1908**, No. 129, 60.

(24) Langmuir, I. Theory of Adsorption. *Phys Rev* **1915**, *6* (1), 79–80.

(25) Brunauer, S.; Emmett, P. H.; Teller, E. Adsorption of Gases in Multimolecular Layers. *J. Am. Chem. Soc.* **1938**, *60* (2), 309–319. https://doi.org/10.1021/ja01269a023.

(26) Balakrishnan, S. High-Temperature Materials for Thermochemical Energy Storage in Concentrated Solar Power Plants. Thesis, Curtin University, 2022. https://espace.curtin.edu.au/handle/20.500.11937/88828 (accessed 2023-07-20).

(27) *(19) (PDF) The development of metal hydrides using as concentrating solar thermal storage materials*. ResearchGate. https://www.researchgate.net/publication/282425719_The_development_of_metal_hydrides_using_as_concentrating_solar_thermal_storage_materials (accessed 2020-03-04).

(28) Paskevicius, M. A Nanostructural Investigation of Mechanochemically Synthesised Hydrogen Storage Materials. Thesis, Curtin University, 2009. https://espace.curtin.edu.au/handle/20.500.11937/254 (accessed 2023-07-20).

(29) Abdelaziz, Y.; Hammam, M.; Megahed, F.; Qamar, E. Characterizing Drift Behavior in Type K and N Thermocouples After High Temperature Thermal Exposures. *J. Adv. Res. Fluid Mech. Therm. Sci.* **2022**, *97* (1), 62–74. https://doi.org/10.37934/arfmts.97.1.6274.

(30) Gibbs, J. W. *Graphical Methods in the Thermodynamics of Fluids*; Connecticut Academy, 1873.

(31) Dickerson, R. E.; Geis, I. *Chemistry, Matter, and the Universe: An Integrated Approach to General Chemistry*; W. A. Benjamin, 1976.

(32) Broom, D. P. Gas Sorption Measurement Techniques. In *Hydrogen Storage Materials: The Characterisation of Their Storage Properties*; Broom, D. P., Ed.; Green Energy and Technology; Springer: London, 2011; pp 117–139. https://doi.org/10.1007/978-0-85729-221-6_4.

(33) Hirscher, M.; Yartys, V. A.; Baricco, M.; Bellosta von Colbe, J.; Blanchard, D.; Bowman, R. C.; Broom, D. P.; Buckley, C. E.; Chang, F.; Chen, P.; Cho, Y. W.; Crivello, J.-C.; Cuevas, F.; David, W. I. F.; de Jongh, P. E.; Denys, R. V.; Dornheim, M.; Felderhoff, M.; Filinchuk, Y.; Froudakis, G. E.; Grant, D. M.; Gray, E. MacA.; Hauback, B. C.; He, T.; Humphries, T. D.; Jensen, T. R.; Kim, S.; Kojima, Y.; Latroche, M.; Li, H.-W.; Lototskyy, M. V.; Makepeace, J. W.; Møller, K. T.; Naheed, L.; Ngene, P.; Noréus, D.; Nygård, M. M.; Orimo, S.; Paskevicius, M.; Pasquini, L.; Ravnsbæk, D. B.; Veronica Sofianos, M.; Udovic, T. J.; Vegge, T.; Walker, G. S.; Webb, C. J.; Weidenthaler, C.; Zlotea, C. Materials for Hydrogen-Based Energy Storage – Past, Recent Progress and Future Outlook. *J. Alloys Compd.* **2020**, *827*, 153548. https://doi.org/10.1016/j.jallcom.2019.153548.

(34) National Minerals Information Center. U.S. Geological Survey Mineral Commodity Summaries 2022 Data Release, 2022. https://doi.org/10.5066/P9KKMCP4.

(35) Møller, K. T.; Williamson, K.; Buckley, C. E.; Paskevicius, M. Thermochemical Energy Storage Properties of a Barium Based Reactive Carbonate Composite. *J. Mater. Chem. A* **2020**, *8* (21), 10935–10942. https://doi.org/10.1039/D0TA03671D.

(36) Vieira, A. P.; Williamson, K.; Humphries, T. D.; Paskevicius, M.; Buckley, C. E. A New Strontium Based Reactive Carbonate Composite for Thermochemical Energy Storage. *J. Mater. Chem. A* **2021**, *9* (36), 20585–20594. https://doi.org/10.1039/D1TA04363C.

(37) Humphries, T. D.; Møller, K. T.; Rickard, W. D. A.; Sofianos, M. V.; Liu, S.; Buckley, C. E.; Paskevicius, M. Dolomite: A Low Cost Thermochemical Energy Storage Material. *J. Mater. Chem. A* **2019**, *7* (3), 1206–1215. https://doi.org/10.1039/C8TA07254J.

Chapter 3

Thermochemical Energy Storage in Barium Carbonate Enhanced by Iron(III) Oxide

K.Williamson, K.T. Møller, A.M D'Angelo T.D. Humphries M. Paskevicius, and C.E. Buckley, Thermochemical Energy Storage in Barium Carbonate Enhanced by Iron(III) Oxide. *Phys. Chem. Chem. Phys.* **2023**, *25* (10), 7268–7277. https://doi.org/10.1039/D2CP05745J.

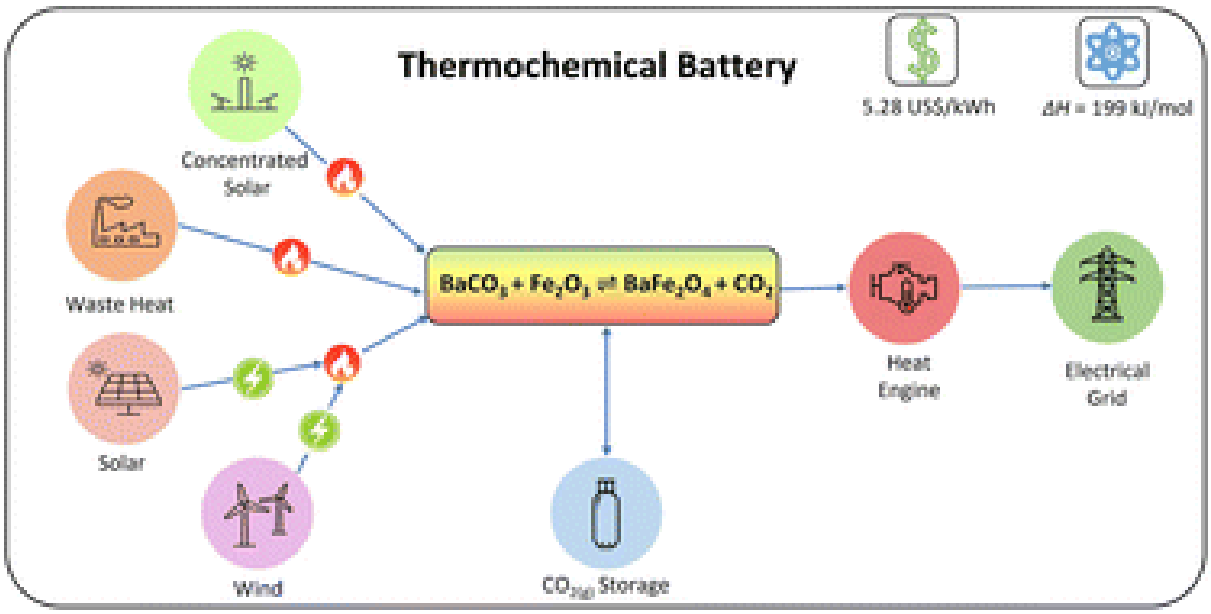

Abstract

Renewable energy requires cost effective and reliable storage to compete with fossil fuels. This study introduces a new reactive carbonate composite (RCC) where Fe_2O_3 is used to thermodynamically destabilise $BaCO_3$ and reduce its decomposition temperature from 1400 °C to 850 °C, which is more suitable for thermal energy storage applications. Fe_2O_3 is consumed on heating to form $BaFe_{12}O_{19}$, which is a stable Fe source for promoting reversible CO_2 reactions. Two reversible reaction steps were observed that corresponded to, first, the reaction between β-$BaCO_3$ and with $BaFe_{12}O_{19}$, and second, between γ-$BaCO_3$ with $BaFe_{12}O_{19}$. The thermodynamic parameters were determined to be ΔH = 199 ± 6 kJ·mol^{-1} of CO_2, ΔS = 180 ± 6 J·K^{-1}mol^{-1} of CO_2 and ΔH = 212 ± 6 kJ·mol^{-1} of CO_2 ΔS = 185 ± 7 J·K^{-1}mol^{-1} of CO_2, respectively for the two reactions. Due to the low-cost and high gravimetric and volumetric energy density, the RCC is demonstrated to be a promising candidate for next generation thermal energy storage.

3.1 Introduction

Concentrating solar thermal power (CSP) is an emerging technology which aims to replace our dependence on fossil-fuel-based energy sources with renewable solar energy. Over the last decade, the number of CSP installations have increased by almost 750% and there is currently more than 6.2 GW of installed capacity worldwide.[1,2] Modern CSP plants utilise a 40% KNO_3/60% $NaNO_3$ molten salt for thermal energy storage to provide 24/7 electrical power generation.[3] However, due to the low energy storage density of the molten salt (413 kJ kg^{-1}), a large quantity of salt is required for thermal energy storage. This means that the salt cost accounts for 10 – 20 % of the overall plant cost, whilst the operating temperature of 265 - 565 °C is also on the low side of what is desired due to the inefficient heat-to-electricity conversion ($\eta_{\text{theoretical(265 °C)}}$ = 25 %).[3] Thus, by developing alternative thermal energy storage technology there is potential to significantly improve CSP plants. The next generation of CSP plants may utilise thermochemical energy storage (TCES),

which stores energy in an endothermic chemical reaction and releases it in an exothermic reaction,[4] as follows for a metal carbonate:

$$MCO_3(s) + \Delta H \rightleftharpoons MO(s) + CO_2(g) \quad (3\text{-}1)$$

Where *M* represents a metal and Δ*H* is the enthalpy of reaction. Metal carbonates offer several advantages as TCES materials over state-of-the-art sensible heat storage systems: (*i*) Higher energy densities (837 - 1657 kJ kg^{-1}) compared to 427 kJ kg^{-1} for the molten salts (when operating between *T* = 270 - 565 °C).[5] (*ii*) Lower overall material costs \$2 - \$4/MJ compared to \$6.55/MJ for molten salts.[5] (*iii*) Higher heat-to-electricity generation efficiency and thus a potential decreased cost of electricity through higher operating temperatures (700 °C - 1000 °C).[6] On the other hand they pose several challenges such as complexity of system design, and often poor cycling capacity retention.[7] The use of low-cost materials may widen the utilization of thermal energy storage to areas other than CSP plants, for example waste heat,[8] wind power,[9] photovoltaics,[10] or nuclear energy.[11]

The calcium oxide–carbon dioxide reaction was first proposed as a method to store energy by Barker in 1974.[12] Although other alkaline earth metal carbonates were studied in the 1970s for this purpose,[13] there has been growing interest over the last two decades, particularly in using metal carbonates for CO_2 sequestration[14] and in the 'calcium looping' process.[15,16] As of now, there are several studies on calcium carbonate and the calcium looping (CaL) process for TCES,[15–17] which suffer from cycling capacity issues. $CaCO_3$ can be operated at 950 °C over 500 cycles but loses 92% of its effective CO_2 capacity (equivalent to the energy storage capacity through reaction scheme (1)).[15,17,18] In Spain the largest CaL TCES prototype to date is being constructed, with an output power of 1 $MW_{th.}$[19] However, it is based on the CaL process and thus may require constant replacement of the limestone ($CaCO_3$) due to its limited cyclability.[20] Recent work shows that TCES in either the dolomite ($CaMg(CO_3)_2$) or limestone systems show that cycling stability can be improved by naturally occurring impurities .[5,21–23] Additionally, the cyclic capacity loss issue can also be overcome by the addition of additives, particularly either ZrO_2 or Al_2O_3.[24]

Due to their high operating temperature, $SrCO_3$ (850 °C) and $BaCO_3$ (1200 °C) have been investigated as TCES materials, but they have poor cyclic CO_2 capacity in their raw form due to sintering at high temperatures.[25] However, the loss of capacity for $SrCO_3$ can be reduced to only 92% of its initial capacity over several cycles by the addition of MgO.[25] In a similar manner, Rhodes *et al.* significantly reduced the cyclic CO_2 capacity loss to 80% over 45 cycles with the addition of $SrZrO_3$ thereby reducing the sintering of the $SrCO_3$ particles.[26]

The concept of a reactive carbonate composite (RCC) was introduced in previous research through a stoichiometric $BaCO_3$-$BaSiO_3$ composite, which retained ~ 95% of the theoretical maximum CO_2 capacity over 20 cycles with addition of $CaCO_3$:[27]

$$BaCO_3(s) + BaSiO_3(s) \rightleftharpoons Ba_2SiO_4(s) + CO_2(g) \qquad (3\text{-}2)$$

$$\Delta H_{850\,^\circ C} = 126.9 \text{ kJ mol}^{-1} \text{ of } CO_2$$

A new RCC, which consists of a 1:1 molar ratio of $BaCO_3$:Fe_2O_3 was chosen to be studied herein as Fe_2O_3 is widely available[28] and has a favourable enthalpy of 168 kJ mol^{-1} CO_2 and predicted operating temperature (> 850 °C) through the following reaction:[29]

$$BaCO_3 (s) + Fe_2O_3(s) \rightleftharpoons BaFe_2O_4(s) + CO_2(g) \qquad (3\text{-}3)$$

$$\Delta H_{850\,^\circ C} = 168 \text{ kJ mol}^{-1} \text{ of } CO_2$$

$BaFe_2O_4$ is usually reported as an intermediate in the formation of $BaFe_{12}O_{19}$, which has been studied extensively due to its commercial applications as a magnetic material.[30] Recent studies suggest three stable phases of barium and iron containing compounds are formed during the solid state reaction between $BaCO_3$ and Fe_2O_3 : $Ba_2Fe_2O_5$, $BaFe_2O_4$, and $BaFe_{12}O_{19}$.[31] However, there are several contradictory reports concerning the conditions and ratios of the starting reagents that cause each phase (or others) to form.[30] Additionally, the solid-state reaction between $BaCO_3$ – Fe_2O_3 to form $BaFe_{12}O_{19}$ is rarely

studied under a CO_2 atmosphere.[32] Perhaps the impact of CO_2 pressure on these reactions could also provide insight into the formation of $BaFe_2O_4$ in the manufacture of $BaFe_{12}O_{19}$, which is an important industrial process in the magnetic film industry.[30,33–35]

3.2 Experimental

3.2.1 Sample Preparation

$BaCO_3$ (Sigma-Aldrich, ≥99 %) and Fe_2O_3 (Chem-Supply, >94 %) were ball-milled for at 2000 rpm for 1 hour (three bidirectional 20-minute segments with 1-minute breaks) in a 1:1 molar ratio in 80 mL stainless steel vials with stainless steel balls (o.d. 8 mm, ball-to-powder mass ratio of 10:1) using an Across International Planetary Ball Mill (PQ-N04). Pristine $BaCO_3$, without the addition of Fe_2O_3, was ball milled in an identical manner.

3.2.2 Powder X-ray Diffraction

Ex-situ powder X-ray diffraction (PXRD) data were collected on a Bruker D8 Discovery equipped with a cobalt X-ray source (Co 6.9257 keV, λ = 1.7902 Å) in flat plate geometry mode. Data were collected over a 2θ range of 5 – 80° on a Lynxeye PSD detector.

3.2.3 In-situ synchrotron radiation powder X-ray diffraction

In-situ time-resolved synchrotron radiation powder X-ray diffraction (SR-PXD) data was collected at the Australian Synchrotron, Melbourne, Australia using the Powder Diffraction (PD) beamline.[36] A wavelength of λ = 0.775227(5) Å or 0.825040(5) Å were selected for the various experiments, both of which were calibrated using NIST 660b LaB_6. Data was collected on a Mythen microstrip detector in two different positions with a data acquisition time of 30 s in each position, before being merged into a single data set. Samples were packed in quartz capillaries (o.d. 0.7 mm, wall thickness 0.05 mm) and mounted in a custom gas fitting sealed with rubber o-rings. A pressure and vacuum gauge were then connected to a gas manifold that provided vacuum or various CO_2 (BOC Gas, 99.99%) pressures on the samples. During data acquisition, the samples were

continuously oscillated over 90° to provide improved powder averaging. Finally, the samples were heated with a hot air blower (Cyberstar) at $\Delta T/\Delta t$ = 6 °C min^{-1} to the desired temperature. This heating rate was the maximum rate possible. Temperature measurements were calibrated against the thermal expansion of an Ag standard.[37] Diffraction patterns were quantitatively analysed using the Rietveld method in the software TOPAS V.5 (Bruker-AXS). [38]

3.2.4 Thermal Analysis

Simultaneous differential scanning calorimetry and thermogravimetric analysis (DSC-TGA) was performed on a Netzsch STA 449 F3 Jupiter instrument by heating several samples of ~ 15 mg of $BaCO_3$-Fe_2O_3 in Al_2O_3 crucibles covered with an Al_2O_3 lid with a pin hole, under flowing argon atmosphere (20 mL min^{-1}), from 40 to 1200 °C at $\Delta T/\Delta t$ = 10, 20, and 25 °C min^{-1}. The temperature and sensitivity of the DSC was calibrated using In, Zn, Al, Ag and Au reference materials, resulting in a temperature accuracy of ± 0.2 °C, while the balance has an accuracy of ± 20 µg.

3.2.5 Sieverts Measurements

Cyclic CO_2 (Coregas, 99.995%) capacity measurements were performed on a custom-made Sieverts/manometric instrument utilising a custom-made SiC sample holder (Saint-Gobain) to withstand high temperature.[39] Approximately 1 g of $BaCO_3$-Fe_2O_3 was heated under vacuum to 850 °C at $\Delta T/\Delta t$ ~ 10 °C min^{-1} in a tube furnace and kept isothermal at 850 °C throughout the measurements. The Sieverts apparatus was equipped with RTD thermistors (± 0.1 °C) and K-type thermocouples (± 1.5 °C) and a pressure gauge (Rosemount 3051S, ± 14 mbar). CO_2 cycling was performed between calcination at $p(CO_2)$ ~ 1 bar for 3 hours and carbonation at $p(CO_2)$ ~ 6.5 bar for 3 hours. The compressibility of CO_2 was calculated using the NIST Reference Fluid Thermodynamic and Transport Properties Database 23 (REFPROP).[40]

Pressure Composition Temperature (PCT) measurements were performed on the same instrumental setup as above using ~ 1 g of $BaCO_3$-Fe_2O_3 at selected isothermal temperatures between 820 °C – 930 °C. The CO_2 pressure was initiated at > 3 bar, which was then reduced in 0.5 - 1 bar steps for timespans of 6 – 18 hours to collect a complete decomposition isotherm.

3.2.6 Scanning Electron Microscopy and Energy Dispersive X-ray Spectroscopy

Scanning electron microscopy (SEM) was performed using a Zeiss Neon 40EsB equipped with a field emission gun. The SEM image was obtained using an accelerating voltage of 20 kV, an aperture size of 60 µm, and a working distance of 9.9 mm. The sample was prepared by distributing a small amount of sample on carbon tape attached to an aluminium stub and coated with a 10 nm carbon layer. Two additional images were captured using a Tescan Mira 3 field emission microscope coupled with secondary electron (SE) and backscattered electron (BSE) detectors. The samples were prepared by embedding powdered samples in an epoxy resin that was polished using colloidal silica, which were then sputter coated with a 10 nm thick carbon layer before analysis. The images were collected using an accelerating voltage of 20 kV, aperture size 10 mm, and a working distance between 2 - 10 mm.

3.3 Results and Discussion

A sample of $BaCO_3$ was ball milled, as was a 1:1 mixture of $BaCO_3$-Fe_2O_3 to ensure adequate mixing and a reduction in particle size. TGA analysis of the milled $BaCO_3$ sample shows a weight loss of 19 % due to the release of CO_2 that begins at a temperature of ~ 1000 °C and by 1200 °C it has almost decomposed entirely with an expected theoretical 23 wt.% (See Figure 3-1). The milled $BaCO_3$-Fe_2O_3 sample reveals a significant reduction in the decomposition temperature, with an onset temperature of ~ 650 °C. The reduced decomposition temperature is assigned to altered thermodynamics of the expected decomposition reaction (3-3) than for pure $BaCO_3$. The $BaCO_3$-Fe_2O_3 sample loses 12.9 wt.%, which matches the theoretical maximum CO_2 release of 12.3 wt.%. In comparison

with the recently investigated $BaCO_3$-$BaSiO_3$ RCC, the onset of decomposition for the $BaCO_3$-Fe_2O_3 RCC is in the same temperature range, but mass loss occurs more rapidly in $BaCO_3$-Fe_2O_3. It is evident CO_2 is completely desorbed from $BaCO_3$-Fe_2O_3 at 960 °C (as indicated by the plateau in wt. % loss), this is slightly earlier than 1015 °C for $BaCO_3$-$BaSiO_3$.[27]

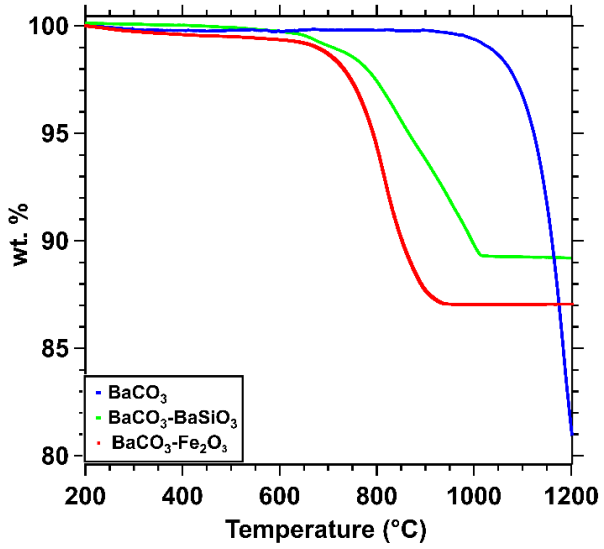

Figure 3-1: TGA measurements comparing the decomposition of pristine $BaCO_3$ (blue), $BaCO_3$-Fe_2O_3 (red), and $BaCO_3$-$BaSiO_3$ (green)[27] heated from room temperature to 1200 °C at $\Delta T/\Delta t$ = 10 °C min^{-1} under an argon flow of 20 mL min^{-1}

The cyclic energy storage capacity of $BaCO_3$-Fe_2O_3 was evaluated by Sieverts measurements, through its cyclic CO_2 sorption, by multiple steps of either low (~ 1 bar) or high (~ 6.5 bar) CO_2 pressure at a constant temperature, see Figure 3-2. The sample was initially decomposed by heating to 900 °C under static vacuum. The first CO_2 absorption rapidly reaches 60 % of the maximum theoretical CO_2 capacity in ~ 5 minutes and 75 % by the end of the first 3-hour absorption step.

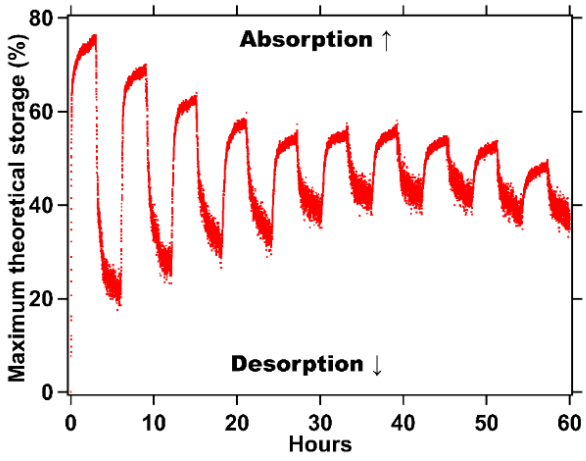

Figure 3-2: Cyclic Sieverts experiments for $BaCO_3$-Fe_2O_3 highlighting the decreasing CO_2 capacity over 16 cycles at T = 850 °C ($t_{abs/des}$ = 3 hours, initial pressures p_{abs} ~ 6.5 bar, p_{des} ~ 1 bar). Maximum storage capacity is calculated from the maximum theoretical capacity of CO_2 for (3-3).

The subsequent desorption only reaches ~ 55 % after 3 hours, indicating that there is a kinetic barrier hindering the reaction. The $BaCO_3$-Fe_2O_3 system loses CO_2 capacity throughout the subsequent cycles but begins to stabilise at ~ 10 - 12 % capacity after the 5th cycle. It is clear that the $BaCO_3$-Fe_2O_3 system does not perform sufficiently for long-term energy storage purposes in its current form due to this capacity loss. Therefore, insight into the reaction mechanisms, composition, and morphological evolution are of great interest in better understanding the system with the hope of optimising it.

Two samples of the $BaCO_3$-Fe_2O_3 RCC weighing ~ 1g were heated in a sealed volume using Sieverts equipment from 25 °C to 900 °C ($\Delta T/\Delta t$= 10 °C min^{-1}) in two different volumes: 53.27 cm^3 and 203.6 cm^3 (Figure S-6-16).

The data shows the evolution of pressure in the closed volume as a function of time and temperature, giving an indication of the pressure-dependent reaction kinetics of CO_2 release. An intermediate step or pressure plateau was observed in the sample heated in the smaller volume (53.27 cm^3), which obtained a higher final CO_2 pressure (1.5 bar) compared to the sample heated in a larger volume (0.4 bar). The pressure plateau that is only observed during decomposition under an increased back-pressure is an indication of

a two-step reaction pathway with pressure dependence. This two-step behaviour is later confirmed using pressure composition isotherm measurements below.

SR-PXD combined with Rietveld refinement was used to identify the decomposition steps under varying CO_2 pressure conditions. The RCC $BaCO_3$–Fe_2O_3 was heated from room temperature to 900 °C ($\Delta T/\Delta t$= 6 °C min^{-1}) in a quartz capillary under dynamic vacuum (Figure 3-3). The initial composition of the sample consisted of orthorhombic *γ*-$BaCO_3$ (green (*Pnma*)) and trigonal Fe_2O_3 (red (*R*-3*c*)) with no other detectable phases, which suggests that no reactions occurred during ball milling. On initial heating there was a noticeable shift in Bragg reflections to lower angles due to thermal expansion. The formation of *γ*-$BaFe_2O_4$ (purple ($Cmc2_1$)) was observed from 645 °C in a slow, but predominantly single-step reaction, which complies with the observation of CO_2 release at ~ 650 °C by TGA (Figure 3-1). At 782 °C, 92% of the *γ*-$BaCO_3$ has been consumed in its reaction to form *γ*-$BaFe_2O_4$, but the remaining $BaCO_3$ undergoes a polymorphic phase transition from *γ*-$BaCO_3$ to *β*-$BaCO_3$ (teal (*R-3m*)), which is marginally lower than the reported temperature of 811 °C.[41] At 884 °C both $BaCO_3$ and Fe_2O_3 are completely consumed, forming predominantly *γ*-$BaFe_2O_4$, but also a fraction of the metastable orthogonal *β*-$BaFe_2O_4$ (pink (*Pnma*)).[42] *β*-$BaFe_2O_4$ undergoes a polymorphic phase transition on cooling at 554 °C to form *γ*-$BaFe_2O_4$. The overall reaction progresses without any observable intermediate step (Equation (3-3)). Additionally, there is also the formation of a minor amount of $Ba_2Fe_2O_5$ (yellow ($P2_1/c$)) at a temperature of 888 °C, which could be caused by the excess $BaCO_3$ reacting with as-formed $BaFe_2O_4$ as follows:[43]

$$BaCO_3(s) + BaFe_2O_4(s) \rightleftharpoons Ba_2Fe_2O_5(s) + CO_2(g) \quad (3\text{-}4)$$

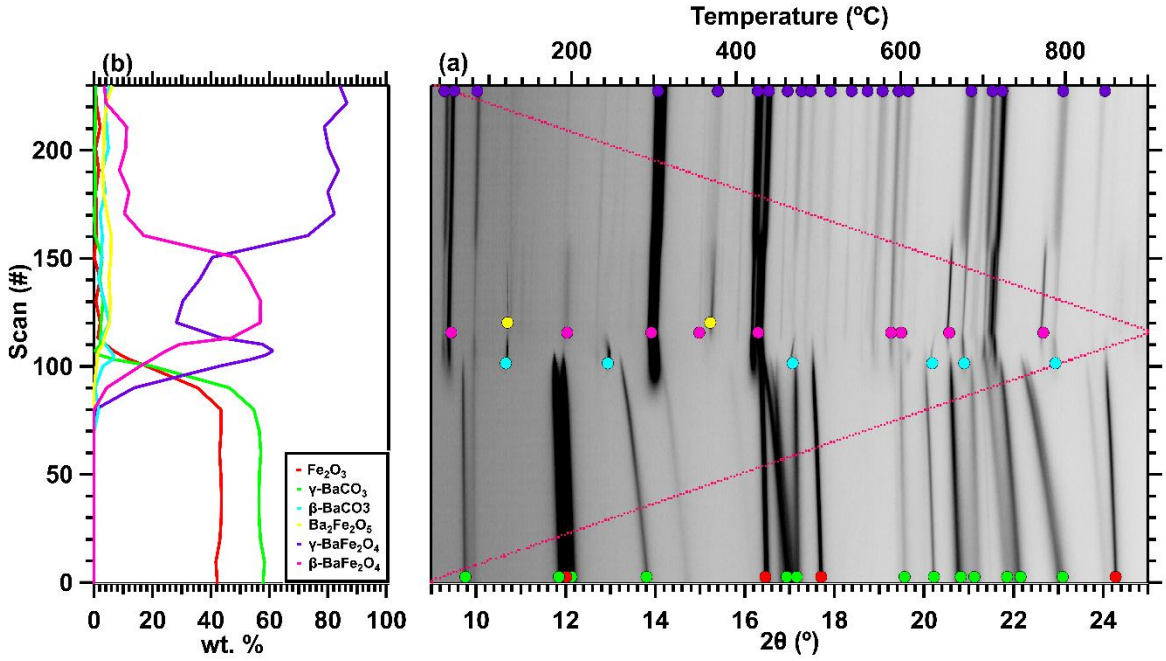

Figure 3-3: **(a)** SR-PXD data of ball milled $BaCO_3$-Fe_2O_3 heated from room temperature (red line) to 900 °C and then cooled to room temperature ($\Delta T/\Delta t$ = 6 °C min^{-1}, λ = 0.775227(5) Å, scan time = 1 min) under dynamic vacuum, $p(CO_2) \leq 10^{-2}$ bar. **(b)** Quantitative phase analysis using the Rietveld method. Colour code: Fe_2O_3 – red, *γ*-$BaCO_3$ – green, *β*-$BaCO_3$ - light blue, $Ba_2Fe_2O_5$ - yellow, *γ*-$BaFe_2O_4$ –purple, *β*-$BaFe_2O_4$ -pink.

In a second experiment, the RCC $BaCO_3$ – Fe_2O_3 was heated from room temperature to 850 °C ($\Delta T/\Delta t$= 6 °C min^{-1}) in a quartz capillary under 7 bar of CO_2 pressure (Figure 3-4). Furthermore, the sample was held isothermally at 850 °C and CO_2 pressure was reduced in a stepwise fashion to investigate the formation of pressure dependent reaction intermediates. The initial reactants, γ-$BaCO_3$ and Fe_2O_3, underwent thermal expansion on heating with no observable reaction below 775 °C under 7 bar CO_2. $BaCO_3$ transforms from orthorhombic γ-$BaCO_3$ (Pnma) to its high temperature trigonal polymorph (β-$BaCO_3$, *R*3*m*) at ~ 775 °C, which coincides with the same event seen in the measurements conducted under vacuum (Figure 3-3). The proportion of γ-$BaCO_3$ decreases from ~ 53 wt.% to ~ 20 wt.% while the proportion of β-$BaCO_3$ increases to 32 wt.% until the sample is held isothermally at 850 °C. Both $BaCO_3$ polymorphs coexist, and the polymorphic ratio remains constant until the formation of β-$BaFe_2O_4$ begins when the CO_2 pressure is decreased. The coexistence of both $BaCO_3$ polymorphs at an isothermal temperature is unexpected. It may be possible that morphological differences, such as the particle size

distribution from ball milling,[44] influences the polymorphic transition temperature, which has been shown in other research to be a function of particle size.[45] It is interesting to see that there is a difference in the reaction pathway observed under 7 bar CO_2 pressure in contrast to measurements under vacuum. At 826 °C the formation of $BaFe_{12}O_{19}$ is observed under 7 bar CO_2, which is reported to form at temperatures as low as 793 °C when the components are ball milled:[46]

$$6BaCO_3(s) + 6Fe_2O_3(s) \rightleftharpoons BaFe_{12}O_{19}(s) + CO_2 + 5BaCO_3(g) \quad (3\text{-}5)$$

However, $BaFe_{12}O_{19}$ is only a minor phase in the sample, and a large quantity of $BaCO_3$ and Fe_2O_3 coexist. While the sample was held isothermally at 850 °C, the CO_2 pressure was reduced in steps to observe the onset of the major CO_2 release event. When the pressure was reduced from 2.5 bar to 2.0 bar (at P_4 in Figure 3-4) the formation of β-$BaFe_2O_4$ can be observed, which formed even more rapidly at lower pressures. β-$BaFe_2O_4$ was the same final reaction product as observed in the thermal ramp under vacuum. From the Rietveld results, it appears as though γ-$BaCO_3$ is consumed before β-$BaCO_3$, which is most apparent at scan 280 in Figure 3-4.

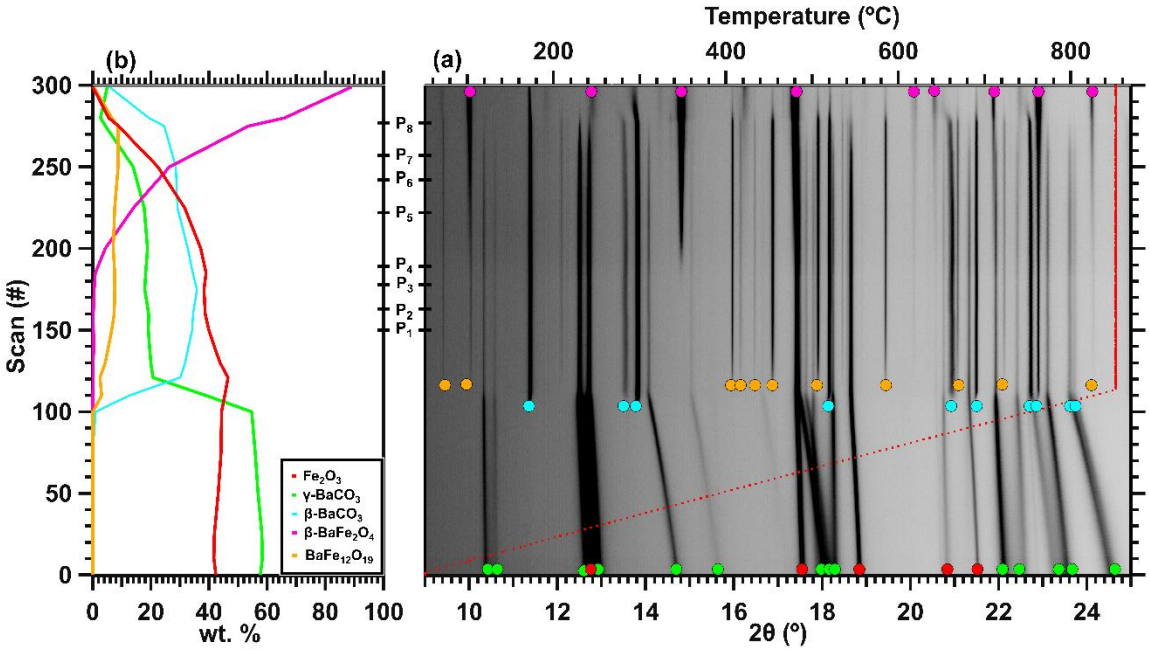

Figure 3-4: **(a)** SR-PXD data of ball milled $BaCO_3$-Fe_2O_3 heated from room temperature (red line) to 850 °C temperature ($\Delta T/\Delta t$ = 6 °C min^{-1}, λ = 0.825040(5) Å, scan time = 1 min). $p(CO_2)$ = 7 bar on heating and reduced as follows $P_{1\text{-}8}(CO_2)$ = 5.0, 4.0, 3.0, 2.5, 2.0, 1.7, 1.0, 0.0 bar); **(b)** Quantitative phase analysis using the Rietveld method. Colour code: Fe_2O_3 – red, *γ*-$BaCO_3$ – green, *β*-$BaCO_3$ - teal, $BaFe_{12}O_{19}$ – orange, *β*-$BaFe_2O_4$ -pink.

The thermodynamics of a gas-solid reaction can be calculated using the van't Hoff technique (3-6) to provide insight into the reaction steps in the $BaCO_3$ – Fe_2O_3 system.[39]

$$\ln(P_{eq}/P_0) = \Delta H/RT - \Delta S/R \qquad (3\text{-}6)$$

Where P_{eq} (bar CO_2) is the pressure of equilibrium, P_0 (bar CO_2) is the reference pressure of 1 bar, T is temperature (K), R is the universal gas constant and ΔH (kJ mol^{-1}) is enthalpy and ΔS (J·Kmol^{-1}) is the reaction entropy.

By studying the reaction using a Sieverts apparatus it is possible to isolate the pressure dependent reactions of *γ*-$BaCO_3$ + $BaFe_{12}O_{19}$ and *β*-$BaCO_3$ + $BaFe_{12}O_{19}$ as two individual steps and quantify their enthalpy and entropy (Figure 3-5). Three separate samples of ball milled $BaCO_3$-Fe_2O_3 (~ 0.3 g) were heated at ($\Delta T/\Delta t$ = 10 °C min^{-1}) to various temperatures

under a $p(CO_2)$ > 4.0 bar then kept isothermal for a time period of at least 24 hours until desorption ceased.[39] Utilising this heating and isothermal step ensured complete transformation of Fe_2O_3 to $BaFe_{12}O_{19}$ occurred (3-5) with the expected wt.% loss of ~ 2% being desorbed (Figure S-6-17). Shorter isothermal time (< 3 hours) did not allow for full conversion, as seen in the SR-PXD data (Figure 3-4).

The subsequent pressure equilibrium plateaus were measured by decreasing the CO_2 pressure in 0.5 - 1 bar steps after 6 – 24 hour wait times on each step to ensure CO_2 was completely desorbed (Figure 3-5). From these experiments it is evident that there are two desorption pressure plateaus, which in total represent a release of CO_2 equivalent to ~ 10 wt.%, matching the theoretical 10.2 wt.% CO_2 loss expected from (3-7)

van't Hoff plots (Figure 3-5b) based on the pressure equilibrium data were used to extract thermodynamic parameters for each of the desorption steps and thus determine Δ*H* and Δ*S* through the van't Hoff equation:[47] The higher pressure ((3-8) and lower pressure (3-9) desorption steps likely correspond to the reaction of γ-$BaCO_3$ and β-$BaCO_3$, respectively. These results are slightly higher than those in the literature.[32]

According to known thermodynamic data $\Delta H_{806\,^\circ C}$(*γ*-$BaCO_3$) = −1124 kJ mol^{-1} and $\Delta H_{806\,^\circ C}$ (*β*-$BaCO_3$) = −1107 kJ mol^{-1}.[29] The difference between these two polymorphs is Δ*H* = 17 kJ mol^{-1} which corresponds to the measured difference of Δ*H* = 13 ± 6 kJ mol^{-1}.

$$BaFe_{12}O_{19}(s) + 5BaCO_3(s) \rightleftharpoons 6BaFe_2O_4(s) + 5CO_2(g) \quad (3\text{-}7)$$

$$xBaFe_{12}O_{19}(s) + (5x)\gamma\text{-}BaCO_3(s) \rightleftharpoons (6x)BaFe_2O_4 + (5x)CO_2(g) \quad (3\text{-}8)$$

ΔH = 199 ± 6 kJ·mol^{-1} of CO_2, ΔS = 180 ± 6 J· K^{-1}mol^{-1} of CO_2

$$(1\text{-}x)BaFe_{12}O_{19}(s) + 5(1-x)\beta\text{-}BaCO_3(s) \rightleftharpoons 6(1\text{-}x)BaFe_2O_4(s) + 5(1-x)CO_2(g)$$

$$\Delta H = 212 \pm 6 \text{ kJ·mol}^{-1} \text{ of } CO_2, \qquad (3\text{-}9)$$

$$\Delta S = 185 \pm 7 \text{ J·K}^{-1}\text{mol}^{-1} \text{ of } CO_2$$

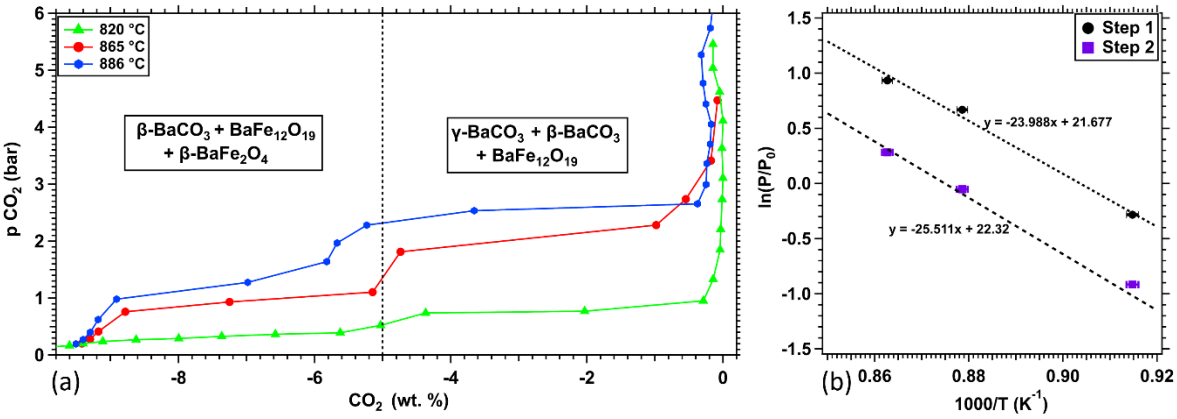

Figure 3-5: **(a)** Pressure composition temperature measurements of the RCC $BaCO_3$-Fe_2O_3 heated under $p(CO_2)$ 3 - 6 bar, ($\Delta T/\Delta t$= 10 °C min^{-1}) until isothermal, the pressure is reduced in steps $p(CO_2)$ = 0.5 − 1 bar, t_{step} = 6 − 24 hours (until desorption ceases). Colour code: green = 820 °C, red = 865 °C, blue = 886 °C. **(b)** Vant' Hoff plots constructed from pressure composition temperature measurements where each point is the centre point of each plateau taken from Figure 3-5a, step 1 is the higher-pressure desorption step and step 2 is the lower one.

To quantify the compounds formed in absorption and desorption over single and multiple cycles PXRD measurements (Figure 3-6) and quantitative analysis using Rietveld refinement were performed (Table 3-1). $BaCO_3$ and Fe_2O_3 are observed in their original ratio (Figure 3-6a), illustrating that no reaction occurred during ball milling and confirms the SR-PXD data (Figure 3-3 and Figure 3-4). The RCC was heated to 886 °C and cooled after the initial minor desorption step, on cooling the presence of $BaFe_7O_{11}$ (52 wt. %) was observed, along with the distinct absence of $BaFe_{12}O_{19}$ that was observed in SPXD data (Figure 3-4). To date, there have not been any reports in the literature that $BaFe_{12}O_{19}$ could transition into $BaFe_7O_{11}$ on cooling, which is especially interesting due to the unexpected composition change, raising some doubts on the validity of one of these compositions. When a pressure composition measurement was performed at 930 °C to

fully decompose the sample (Figure 3-6c), PXRD shows *γ*-$BaFe_2O_4$, which was also observed in the SR-PXD data at 900 °C (Figure 3-3). However, after repeated pressure cycling, stabilisation of β-$BaFe_2O_4$ was observed (Figure 3-6d), which has been reported to form when cooling between 800 - 1000 °C.[42,48] As a side note, Figure 3-6d shows a sample that was cooled under its own desorption pressure (~ 1 bar) creating minor amounts of $BaCO_3$ and Fe_2O_3 from reabsorption of CO_2. Samples that have been pressure cycled and cooled in the absorbed state (Figure 3-6e) again show the presence of $BaFe_7O_{11}$ instead of the expected $BaFe_{12}O_{19}$ which was observed during *in-situ* SR-XRD studies.[49] $BaFe_7O_{11}$ is reportedly composed of both divalent and trivalent Fe as $Ba_2Fe^{2+}{}_2Fe^{3+}{}_{12}O_{22}$,[50] which could suggest that during cooling there is an unknown reduction process occurring as $BaFe_{12}O_{19}$ only contains Fe^{3+}. However, there is limited data on the synthesis and analysis of $BaFe_7O_{11}$ and it is possible that the composition of this compound identified by XRD is in fact a different Ba:Fe:O composition.[49–51] The inability for reduction of Fe^{3+} to Fe^{2+} during cooling in this study suggests that previous XRD data for $BaFe_7O_{11}$ may actually be a new polymorph of $BaFe_{12}O_{19}$ (or another composition containing only Fe^{3+}),[49] although further research must be undertaken to ascertain this.

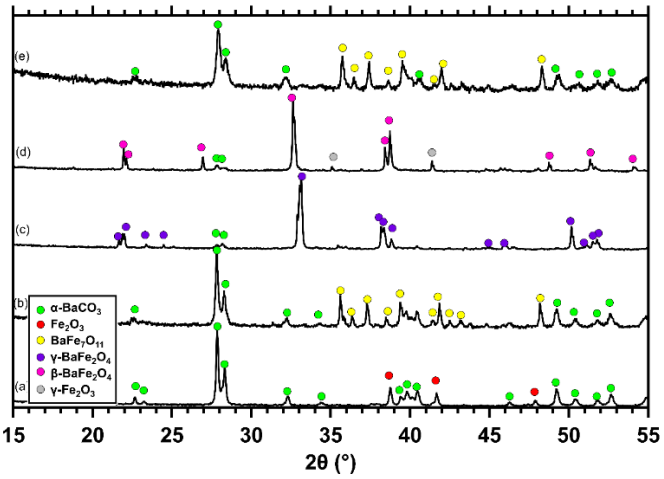

Figure 3-6: *Ex-situ* PXD data (*λ* = 1.7902 Å) of **(a)** ball milled $BaCO_3$–Fe_2O_3; **(b)** $BaCO_3$-Fe_2O_3 heated to 883 °C under $p(CO_2)$ = 8 bar and then decomposed under $p(CO_2)$ ~ 1.5 bar before being cooled; **(c)** $BaCO_3$-Fe_2O_3 heated to 930 °C under $p(CO_2)$ ~ 8.8 bar, followed by 1 bar steps down in pressure until $p(CO_2)$ ~ 2 mbar, allowing a complete desorption before cooling; **(d)** pressure cycled at 940 °C from desorption to absorption, before being cooled in the desorbed state; **(e)** pressure cycled at 880 °C and cooled in

the absorbed state. Colour code: Fe_2O_3 – red, α-$BaCO_3$ –green, β-$BaFe_2O_4$ -pink, $BaFe_7O_{11}$-yellow, γ-Fe_2O_3-grey.

Table 3-1: Quantitative composition of the crystalline components (wt.% ± 2 %) provided from X-ray diffraction-based Rietveld analysis of data represented in Figure 3-6. The symbol colour from Figure 3-6 is also provided.

Phase	α-$BaCO_3$	Fe_2O_3	$BaFe_7O_{11}$	γ-$BaFe_2O_4$	β-$BaFe_2O_4$	γ-Fe_2O_3	Notes
Symbol colour	Green	Red	Yellow	Purple	Pink	Grey	
Space group	*Pnma*	*R*–3*c*	*R*–3*m*	*Cmc*2$_1$	*Pnma*	*Fd*–3*m*	
(a)	55%	45%	0	0	0	0	Ball milled
(b)	43%	5%	52%	0	0	0	883 °C - semi decomposed
(c)	2%	1%	0	97%	0	0	930 °C - decomposed PCT
(d)	8%	0%	0	0	79%	13%	940 °C - cycled and cooled after desorption
(e)	42%	0	58%	0	0	0	880 °C - cycled and cooled after absorption

To gain insight into the kinetics of CO_2 release from the $BaCO_3$-Fe_2O_3 system, the activation energy was determined by the Kissinger method from multiple thermal analysis measurements (3-10).[52,53] Three samples of as-milled $BaCO_3$-Fe_2O_3 were heated at different thermal ramp rates ($\Delta T/\Delta t$ = 10, 20, and 25 K min^{-1}) under flowing argon, and endothermic peaks from CO_2 release were found at 790, 812, and 818 °C, respectively (Figure 3-7a). The additional peaks at 1004 - 1012 °C indicate the high temperature polymorphic transition of $BaFe_2O_4$ (β -> α)).[42] The Kissinger plot of this data is represented in Figure 3-7b.[52,53]

$$ln[\beta/T_p^2] = -E_a/RT_P + A \qquad (3\text{-}10)$$

Where β is the heating rate (K min^{-1}), T_p is the DSC peak temperature for desorption (K), E_a is the activation energy, R is the ideal gas constant (8.3144 Jmol^{-1}K^{-1}) and A is a reaction specific constant. The formation of $BaFe_2O_4$ from $BaCO_3$ and Fe_2O_3 (Equations 3) was

found to have an activation energy of 292 ± 5 kJ mol^{-1}. Pristine $BaCO_3$ has been reported to have an activation energy between 283 kJ mol^{-1} or 305 kJ mol^{-1},[54,55] whereas the RCC $BaCO_3$-$BaSiO_3$ in the milled state is reported to have an activation energy of 195 kJ mol^{-1},[27] thus significantly lower than for the Fe_2O_3 containing system. This indicates that the decomposition reaction is kinetically slower than the $BaCO_3$-$BaSiO_3$ system on the first thermal cycle, which may be improved by the addition of a catalyst or a sintering inhibitor.

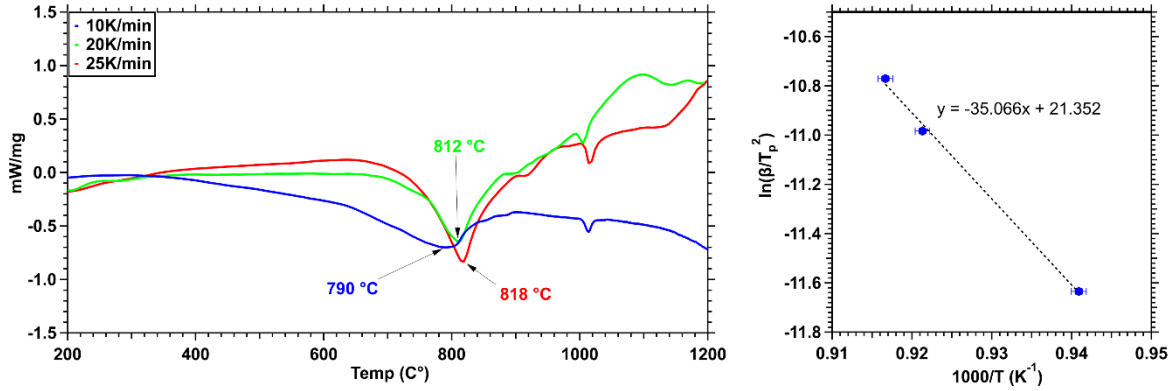

Figure 3-7: (a) Differential scanning calorimetry measurements performed on 3 separate samples of ball milled $BaCO_3$-Fe_2O_3. The samples were heated from 25 °C to 1200 °C at $\Delta T/\Delta t$ = 10, 20, and 25 °C min^{-1}, under flowing argon (20 mL min^{-1}) and (b) the corresponding Kissinger plot. The DSC peak used to construct the Kissinger plot is indicated for each heating rate.

The $BaCO_3$-Fe_2O_3 RCC was also investigated for morphological changes that could cause capacity loss as seen in the CO_2 cycling measurements illustrated in Figure 3-2. Scanning electron microscopy images for $BaCO_3$-Fe_2O_3 after milling, after a single decomposition and after 20 CO_2 desorption/absorption cycles are presented in Figure 3-8. The as milled sample (Figure 3-8a) reveals the presence of large particles with high surface areas. After a single CO_2 desorption, it is possible to observe sintering (Figure 3-8b), which increases after several cycles (Figure 3-8c). Increased sintering indicates a loss of surface area and consequently a loss of available reaction sites, which could explain the CO_2 desorption/absorption capacity loss over multiple cycles (Figure 3-2).[18,26,27,58] It is clear that a sintering inhibitor would enhance the cycling performance of the $BaCO_3$-Fe_2O_3 system if a suitable material could be determined.

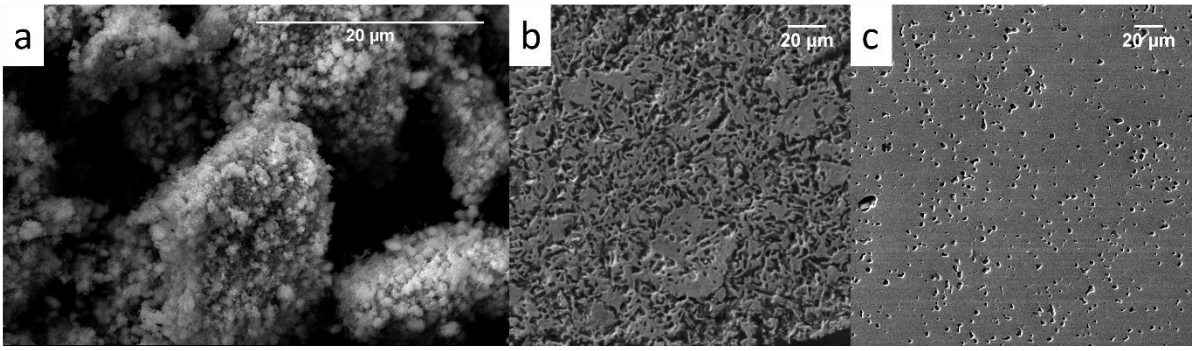

Figure 3-8: SEM for RCC $BaCO_3$-Fe_2O_3 secondary electron images (a) as milled (b) after CO_2 desorption, (c) after 20 CO_2 absorption-desorption cycles. Images B and C were embedded in resin due to their magnetic nature being potentially damaging for the instrument.

A raw materials cost comparison used in previous studies is presented in Table 3-2 with the addition of the RCC $BaCO_3$-Fe_2O_3.[5,27,56] The raw materials cost to store electrical energy was found to be 1.5 US$ MJ_e^{-1}, which is a significant improvement on the previously reported 3.3 US$ MJ_e^{-1} for the $BaCO_3$-$BaSiO_3$ system and $2.3 US$ MJ_e^{-1} for $SrSiO_3$-$SrCO_3$ system.[56] It is also considerably cheaper from a materials standpoint than molten salts (5.7 US$ MJ_e^{-1}), however this does not include the separate storage for CO_2 and auxiliary equipment costs which can be significant.[7] Additionally due to the high enthalpy of the RCC (199 - 212 kJ mol^{-1}) and high gravimetric energy density (2632 MJ m^{-3}) it could reduce the container size of a thermal battery and further lower the cost.[59] Further technoeconomic modelling must be undertaken to understand the complexities associated with complete system design for a TCES battery based on each of these materials.

Table 3-2: Comparison of thermochemical properties, system variables, and cost parameters for select energy storage materials to store 1TJ of electrical energy. [5,27,56,57]

	$BaFe_{12}O_{19}$+5$BaCO_3$ ⇌ 6$BaFe_2O_4$ + 5CO_2	**$BaCO_3$+$BaSiO_3$ ⇌ Ba_2SiO_4 + CO_2**	**$SrCO_3$+$SrSiO_3$ ⇌ Sr_2SiO_4 + CO_2**	**Molten salt (40$NaNO_3$:60KNO_3)**
Enthalpy Δ*H* (kJ mol^{-1} of CO_2)	199	126.9	155.7	39
Molar Mass (g mol^{-1})	357	411	311	94.6

[a,b]Density (g cm^{-3})	4.7	[a]4.4	[a]3.75	2.17
CO_2 Capacity (wt.%)	10.3	10.7	14.1	-
Gravimetric Energy Density (kJ kg^{-1})	560	309	500	413
[d] Volumetric Energy Density (MJ m^{-3})	2632	1359	1878	895
Operating Temperature (°C)	850	850	700	290 - 565
Operating CO_2 Pressure (bar)	1 - 6	5 - 25	0.1 - 6.0	-
[c]Theoretical Carnot Efficiency (%)	73	73	69	46
[d]Estimated Practical Efficiency (%)	48	48	45	27
[e] Mass Required (tonnes)	3714	6903	[g]4700	9100
[e] Volume Required (m^3)	790	1569	[g]1711	4194
[e]Materials Cost (US$ tonne^{-1})	400	[g]495	[g]480	630
[e,f,g] Total Materials Cost Required (US$)	1,485,000	3,410,000	2,258,099	5,730,000

[a]Applies to the mixture MCO_3-$MSiO_3$. [b]Based on crystalline data. [c]Lower temperature. [d]Thermal to electrical energy conversion [e]To generate 1 TJ of electrical energy. [f] 80wt% $SrSiCO_3$:$SrCO_3$ + 20wt% NaCl:$MgCl_2$. [g]Based entirely on the cost of M_xCO_3, as this is also the starting reagent for M_xSiO_3 (M = Sr or Ba).

3.4 Conclusions

An innovative RCC consisting of barium carbonate and iron oxide was investigated as a potential material for thermochemical energy storage, the materials are both readily available and cost effective. The operating temperature was lowered from ~ 1350 °C to 850 °C while still maintaining a high enthalpy of over 199 kJ·mol^{-1} of CO_2 demonstrating metal oxides could potentially be used to destabilize metal carbonates while still

maintaining high energy density. SR-PXD was used to investigate the reaction of $BaCO_3$ and Fe_2O_3 under vacuum and CO_2 pressure where the coexistence and subsequent reaction of two phases of $BaCO_3$ (β- and γ-$BaCO_3$) were observed, hence care with thermodynamic measurements near the boundary of phase changes should be undertaken. The thermodynamics of the reaction of $BaFe_{12}O_{19}$ with each phase β-$BaCO_3$ were measured using sievert apparatus, demonstrating that this method could be applied to characterise other thermochemical energy storage materials. As it stands, to be viable as a thermal energy storage material, the CO_2 cyclic capacity of the RCC must be improved. Scanning electron imaging demonstrated particle agglomeration during cycling, which is the likely cause of CO_2 cyclic degradation. This could be inhibited by the addition of agglomeration inhibitors and/or a catalyst. If the cycling capacity were to be improved, this system would be suitable for scale-up into a thermal battery prototype. Additionally, information about the formation of $BaFe_{12}O_{19}$ under CO_2 pressure and the formation of $BaFe_7O_{11}$ on cooling would also provide useful information for other fields of research including ferromagnetism and ceramics.

Further research should be conducted to examine the impact of incorporating other metal carbonates, such as $CaCO_3$, $SrCO_3$, $PbCO_3$, and $MgCO_3$ with metal oxides. It is anticipated that the addition of metal oxides could result in the destabilisation of these other metal carbonates. Of particular interest is $SrCO_3$, which possesses a similar structure to $BaCO_3$ and holds potential to be reduced to practical operating temperatures in the range of 800 °C to 1000 °C, from its current temperature of 1100 °C.

3.5 Acknowledgements

KW acknowledge the Australian Government for an Australian Government Research Training Program Scholarship. C.E. Buckley,, M. Paskevicius and T. D. Humphries acknowledge the Australian Research Council for DP200102301 and the Australian Government for Global Innovation Linkage project (GIL73589). Part of this research was

undertaken using the SEM/XRD instrumentation (ARC LE0775553 and LE0775551) at the John de Laeter Centre, Curtin University. K.T.M. acknowledges The Independent Research Fund Denmark for International Postdoctoral (grant 8028-00009B) and the Carlsberg Foundation for a Reintegration Fellowship (grant CF19-0465). This research was supported by an AINSE Ltd. Postgraduate Research Award (PGRA). The authors would like to acknowledge A. Patel and A. P. Viera for their assistance in obtaining the SEM images.

3.6 References

(1) *CSP Projects Around the World*. SolarPACES. https://www.solarpaces.org/csp-technologies/csp-projects-around-the-world/ (accessed 2022-11-24).

(2) Hahn Menacho, A. J.; Rodrigues, J. F. D.; Behrens, P. A Triple Bottom Line Assessment of Concentrated Solar Power Generation in China and Europe 2020–2050. *Renew. Sustain. Energy Rev.* **2022**, *167*, 112677. https://doi.org/10.1016/j.rser.2022.112677.

(3) González-Roubaud, E.; Pérez-Osorio, D.; Prieto, C. Review of Commercial Thermal Energy Storage in Concentrated Solar Power Plants: Steam vs. Molten Salts. *Renew. Sustain. Energy Rev.* **2017**, *80*, 133–148. https://doi.org/10.1016/j.rser.2017.05.084.

(4) Carrillo, A. J.; González-Aguilar, J.; Romero, M.; Coronado, J. M. Solar Energy on Demand: A Review on High Temperature Thermochemical Heat Storage Systems and Materials. *Chem. Rev.* **2019**, *119* (7), 4777–4816. https://doi.org/10.1021/acs.chemrev.8b00315.

(5) Humphries, T. D.; Møller, K. T.; Rickard, W. D. A.; Sofianos, M. V.; Liu, S.; Buckley, C. E.; Paskevicius, M. Dolomite: A Low Cost Thermochemical Energy Storage Material. *J. Mater. Chem. A* **2019**, *7* (3), 1206–1215. https://doi.org/10.1039/C8TA07254J.

(6) Liu, M.; Steven Tay, N. H.; Bell, S.; Belusko, M.; Jacob, R.; Will, G.; Saman, W.; Bruno, F. Review on Concentrating Solar Power Plants and New Developments in High

Temperature Thermal Energy Storage Technologies. *Renew. Sustain. Energy Rev.* **2016**, *53*, 1411–1432. https://doi.org/10.1016/j.rser.2015.09.026.

(7) Bayon, A.; Bader, R.; Jafarian, M.; Fedunik-Hofman, L.; Sun, Y.; Hinkley, J.; Miller, S.; Lipiński, W. Techno-Economic Assessment of Solid–Gas Thermochemical Energy Storage Systems for Solar Thermal Power Applications. *Energy* **2018**, *149*, 473–484. https://doi.org/10.1016/j.energy.2017.11.084.

(8) Ortega-Fernández, I.; Rodríguez-Aseguinolaza, J. Thermal Energy Storage for Waste Heat Recovery in the Steelworks: The Case Study of the REslag Project. *Appl. Energy* **2019**, *237*, 708–719. https://doi.org/10.1016/j.apenergy.2019.01.007.

(9) Liu, C.; Cheng, M.-S.; Zhao, B.-C.; Dai, Z.-M. A Wind Power Plant with Thermal Energy Storage for Improving the Utilization of Wind Energy. *Energies* **2017**, *10* (12), 2126. https://doi.org/10.3390/en10122126.

(10) Fernández, R.; Ortiz, C.; Chacartegui, R.; Valverde, J. M.; Becerra, J. A. Dispatchability of Solar Photovoltaics from Thermochemical Energy Storage. *Energy Convers. Manag.* **2019**, *191*, 237–246. https://doi.org/10.1016/j.enconman.2019.03.074.

(11) Denholm, P.; King, J. C.; Kutcher, C. F.; Wilson, P. P. H. Decarbonizing the Electric Sector: Combining Renewable and Nuclear Energy Using Thermal Storage. *Energy Policy* **2012**, *44*, 301–311. https://doi.org/10.1016/j.enpol.2012.01.055.

(12) Barker, R. The Reactivity of Calcium Oxide towards Carbon Dioxide and Its Use for Energy Storage. *J. Appl. Chem. Biotechnol.* **1974**, *24* (4–5), 221–227. https://doi.org/10.1002/jctb.2720240405.

(13) Ervin, G. Solar Heat Storage Using Chemical Reactions. *J. Solid State Chem.* **1977**, *22* (1), 51–61. https://doi.org/10.1016/0022-4596(77)90188-8.

(14) Sanna, A.; Uibu, M.; Caramanna, G.; Kuusik, R.; Maroto-Valer, M. M. A Review of Mineral Carbonation Technologies to Sequester CO2. *Chem. Soc. Rev.* **2014**, *43* (23), 8049–8080. https://doi.org/10.1039/C4CS00035H.

(15) Edwards, S. E. B.; Materić, V. Calcium Looping in Solar Power Generation Plants. *Sol. Energy* **2012**, *86* (9), 2494–2503. https://doi.org/10.1016/j.solener.2012.05.019.

(16) Yuan, Y.; Li, Y.; Zhao, J. Development on Thermochemical Energy Storage Based on CaO-Based Materials: A Review. *Sustainability* **2018**, *10* (8), 2660. https://doi.org/10.3390/su10082660.

(17) Ortiz, C.; Valverde, J. M.; Chacartegui, R.; Perez-Maqueda, L. A.; Giménez, P. The Calcium-Looping (CaCO3/CaO) Process for Thermochemical Energy Storage in Concentrating Solar Power Plants. *Renew. Sustain. Energy Rev.* **2019**, *113*, 109252. https://doi.org/10.1016/j.rser.2019.109252.

(18) Manovic, V.; Anthony, E. J. Sintering and Formation of a Nonporous Carbonate Shell at the Surface of CaO-Based Sorbent Particles during CO2-Capture Cycles. *Energy Fuels* **2010**, *24* (10), 5790–5796. https://doi.org/10.1021/ef100931v.

(19) Hritz, S.; Eusha, M.; Mir, F.; Schories, G. Life Cycle Analysis of the Solar Thermochemical Energy Storage Scheme SOCRATCES [Version 1; Peer Review: 2 Approved with Reservations]. *Open Res. Eur.* **2022**, *2* (14). https://doi.org/10.12688/openreseurope.14386.1.

(20) Chacartegui, R.; Alovisio, A.; Ortiz, C.; Valverde, J. M.; Verda, V.; Becerra, J. A. Thermochemical Energy Storage of Concentrated Solar Power by Integration of the Calcium Looping Process and a CO2 Power Cycle. *Appl. Energy* **2016**, *173*, 589–605. https://doi.org/10.1016/j.apenergy.2016.04.053.

(21) Sarrion, B.; Valverde, J. M.; Perejon, A.; Perez-Maqueda, L.; Sanchez-Jimenez, P. E. On the Multicycle Activity of Natural Limestone/Dolomite for Thermochemical Energy

Storage of Concentrated Solar Power. *Energy Technol.* **2016**, *4* (8), 1013–1019. https://doi.org/10.1002/ente.201600068.

(22) Benitez-Guerrero, M.; Sarrion, B.; Perejon, A.; Sanchez-Jimenez, P. E.; Perez-Maqueda, L. A.; Manuel Valverde, J. Large-Scale High-Temperature Solar Energy Storage Using Natural Minerals. *Sol. Energy Mater. Sol. Cells* **2017**, *168*, 14–21. https://doi.org/10.1016/j.solmat.2017.04.013.

(23) Sarrión, B.; Perejón, A.; Sánchez-Jiménez, P. E.; Pérez-Maqueda, L. A.; Valverde, J. M. Role of Calcium Looping Conditions on the Performance of Natural and Synthetic Ca-Based Materials for Energy Storage. *J. CO2 Util.* **2018**, *28*, 374–384. https://doi.org/10.1016/j.jcou.2018.10.018.

(24) Møller, K. T.; Ibrahim, A.; Buckley, C. E.; Paskevicius, M. Inexpensive Thermochemical Energy Storage Utilising Additive Enhanced Limestone. *J. Mater. Chem. A* **2020**, *8* (19), 9646–9653. https://doi.org/10.1039/D0TA03080E.

(25) André, L.; Abanades, S. Evaluation and Performances Comparison of Calcium, Strontium and Barium Carbonates during Calcination/Carbonation Reactions for Solar Thermochemical Energy Storage. *J. Energy Storage* **2017**, *13*, 193–205. https://doi.org/10.1016/j.est.2017.07.014.

(26) Rhodes, N. R.; Barde, A.; Randhir, K.; Li, L.; Hahn, D. W.; Mei, R.; Klausner, J. F.; AuYeung, N. Solar Thermochemical Energy Storage Through Carbonation Cycles of SrCO3/SrO Supported on SrZrO3. *ChemSusChem* **2015**, *8* (22), 3793–3798. https://doi.org/10.1002/cssc.201501023.

(27) Møller, K. T.; Williamson, K.; Buckley, C. E.; Paskevicius, M. Thermochemical Energy Storage Properties of a Barium Based Reactive Carbonate Composite. *J. Mater. Chem. A* **2020**, *8* (21), 10935–10942. https://doi.org/10.1039/D0TA03671D.

(28) *Iron Ore Statistics and Information | U.S. Geological Survey*. https://www.usgs.gov/centers/national-minerals-information-center/iron-ore-statistics-and-information (accessed 2022-11-24).

(29) Roine, A. HSC Chemistry® [Software], 2018. Software available at www.outotec.com/HSC.

(30) Pullar, R. C. Hexagonal Ferrites: A Review of the Synthesis, Properties and Applications of Hexaferrite Ceramics. *Prog. Mater. Sci.* **2012**, *57* (7), 1191–1334. https://doi.org/10.1016/j.pmatsci.2012.04.001.

(31) Rakshit, S. K.; Parida, S. C.; Singh, Z.; Prasad, R.; Venugopal, V. Thermodynamic Properties of Ternary Oxides in the System Ba–Fe–O Using Solid-State Electrochemical Cells with Oxide and Fluoride Ion Conducting Electrolytes. *J. Solid State Chem.* **2004**, *177* (4), 1146–1156. https://doi.org/10.1016/j.jssc.2003.10.021.

(32) Pouillard, G.; Alam, M. S.; MC, T. D.; P, P. The binary system barium oxide-iron(iii) oxide (Bao-Fe_2O_3): phase diagram and thermodynamic properties. *bin. syst. barium oxide-ironiii oxide BaO-Fe_2O_3 phase Diagr. Thermodyn. Prop.* **1981**.

(33) Singh, V. P.; Jasrotia, R.; Kumar, R.; Raizada, P.; Thakur, S.; Batoo, K. M.; Singh, M. A Current Review on the Synthesis and Magnetic Properties of M-Type Hexaferrites Material. *World J. Condens. Matter Phys.* **2018**, *08* (02), 36. https://doi.org/10.4236/wjcmp.2018.82004.

(34) Srivastava, R.; Yadav, B. C. Ferrite Materials: Introduction, Synthesis Techniques, and Applications as Sensors. *Int. J. Green Nanotechnol.* **2012**, *4* (2), 141–154. https://doi.org/10.1080/19430892.2012.676918.

(35) Tolani, S. C.; Golhar, A. R.; Rewatkar, K. G. A Review of Morphological, Structural Behaviour and Technological Applications of Ferrites. *AIP Conf. Proc.* **2019**, *2104* (1), 030032. https://doi.org/10.1063/1.5100459.

(36) Huntley, J.; Brand, H.; Aubert, M.; Morwood, M. J. The First Australian Synchrotron Powder Diffraction Analysis of Pigment from a Wandjina Motif in the Kimberley, Western Australia. *Aust. Archaeol.* **2014**, *78*, 33–38.

(37) Suh, I.-K.; Ohta, H.; Waseda, Y. High-Temperature Thermal Expansion of Six Metallic Elements Measured by Dilatation Method and X-Ray Diffraction. *J. Mater. Sci.* **1988**, *23* (2), 757–760. https://doi.org/10.1007/BF01174717.

(38) Rietveld, H. M. The Rietveld Method. *Phys. Scr.* **2014**, *89* (9), 098002. https://doi.org/10.1088/0031-8949/89/9/098002.

(39) Sheppard, D. A.; Paskevicius, M.; Javadian, P.; Davies, I. J.; Buckley, C. E. Methods for Accurate High-Temperature Sieverts-Type Hydrogen Measurements of Metal Hydrides. *J. Alloys Compd.* **2019**, *787*, 1225–1237. https://doi.org/10.1016/j.jallcom.2019.02.067.

(40) Lemmon, E.; Huber, M.; McLinden, M. NIST Standard Reference Database 23: Reference Fluid Thermodynamic and Transport Properties-REFPROP, Version 9.1, 2013. https://tsapps.nist.gov/publication/get_pdf.cfm?pub_id=912382.

(41) Antao, S.; Hassan, I. BaCO3: High-Temperature Crystal Structures and the Pmcn → R3m Phase Transition at 811 Celius. *Phys. Chem. Miner.* **2007**, *34*. https://doi.org/10.1007/s00269-007-0172-8.

(42) Meriani, S. Polymorphism of Barium Monoferrite, BaFe2O4. *Acta Crystallogr. B* **1972**, *28* (4), 1241–1243. https://doi.org/10.1107/S0567740872004030.

(43) Fujishiro, F.; Fukasawa, K.; Hashimoto, T. CO2 Absorption and Desorption Properties of Single Phase Ba2Fe2O5 and Analysis of Their Mechanism Using Thermodynamic Calculation. *J. Am. Ceram. Soc.* **2011**, *94* (11), 3675–3678. https://doi.org/10.1111/j.1551-2916.2011.04842.x.

(44) Dudhaiya, A.; Santos, R. M. How Characterization of Particle Size Distribution Pre- and Post-Reaction Provides Mechanistic Insights into Mineral Carbonation. *Geosciences* **2018**, *8* (7), 260. https://doi.org/10.3390/geosciences8070260.

(45) Ayyappan, S.; Panneerselvam, G.; Antony, M. P.; Rama Rao, N. V.; Thirumurugan, N.; Bharathi, A.; Philip, J. Effect of Initial Particle Size on Phase Transformation Temperature of Surfactant Capped Fe3O4 Nanoparticles. *J. Appl. Phys.* **2011**, *109* (8), 084303. https://doi.org/10.1063/1.3564964.

(46) Yamaguchi, T.; Matsumura, K.; Kuno, H. Effects of Ball Milling on the Kinetics and Mechanism of Solid State Reaction between $BaCO_3$ and Sio_2. *Nippon Kagaku Kaishi* **1974**, *1974* (1), 17–21. https://doi.org/10.1246/nikkashi.1974.17.

(47) Lima, E. C.; Gomes, A. A.; Tran, H. N. Comparison of the Nonlinear and Linear Forms of the van't Hoff Equation for Calculation of Adsorption Thermodynamic Parameters (ΔS° and ΔH°). *J. Mol. Liq.* **2020**, *311*, 113315. https://doi.org/10.1016/j.molliq.2020.113315.

(48) Leib, W.; Müller-Buschbaum, H. Zur Verbindungsbildung MO : M2O3 Eine neue From von BaFe2O4 mit aufgefüllter Tridymitstruktur. *Z. Für Anorg. Allg. Chem.* **1986**, *538* (7), 71–77. https://doi.org/10.1002/zaac.19865380708.

(49) Villars, P.; Cenzual, K. *Ba2Fe14O22 (BaFe7O11) Crystal Structure: Datasheet from "PAULING FILE Multinaries Edition – 2012" in SpringerMaterials*. https://materials.springer.com/isp/crystallographic/docs/sd_0312621.

(50) Zhang, X.; Zhang, J. Synthesis and Magnetic Properties of Ba2Fe14O22 Y-Type Hexaferrite. *Mater. Lett.* **2020**, *269*, 127642. https://doi.org/10.1016/j.matlet.2020.127642.

(51) Hadj Farhat, M. A.; Joubert, J. C. Hydrothermal Synthesis and Characterisation of the Hexagonal Ferrite Fe2-Y. *J. Magn. Magn. Mater.* **1986**, *62* (2), 353–358. https://doi.org/10.1016/0304-8853(86)90165-4.

(52) Kissinger, H. E. Variation of Peak Temperature with Heating Rate in Differential Thermal Analysis. *J Res Natl Bur Stand* **1956**, *57* (4), 217–221.

(53) Kissinger, H. E. Reaction Kinetics in Differential Thermal Analysis. *Anal. Chem.* **1957**, *29* (11), 1702–1706. https://doi.org/10.1021/ac60131a045.

(54) Judd, M. D.; Pope, M. I. Energy of Activation for the Decomposition of the Alkaline-Earth Carbonates from Thermogravimetric Data. *J. Therm. Anal.* **1972**, *4* (1), 31–38. https://doi.org/10.1007/BF02100947.

(55) Arvanitidis, I.; Siche, Du.; Seetharaman, S. A Study of the Thermal Decomposition of BaCO3. *Metall. Mater. Trans. B* **1996**, *27* (3), 409–416. https://doi.org/10.1007/BF02914905.

(56) Pires Vieira, A.; Williamson, K.; Humphries, T.; Paskevicius, M.; Buckley, C. A New Strontium Based Reactive Carbonate Composite for Thermochemical Energy Storage. *J. Mater. Chem. A* **2021**, *9*. https://doi.org/10.1039/D1TA04363C.

(57) National Minerals Information Center. U.S. Geological Survey Mineral Commodity Summaries 2022 Data Release, 2022. https://doi.org/10.5066/P9KKMCP4.

(58) Valverde, J. M.; Sanchez-Jimenez, P. E.; Perez-Maqueda, L. A. Limestone Calcination Nearby Equilibrium: Kinetics, CaO Crystal Structure, Sintering and Reactivity. *J. Phys. Chem. C* **2015**, *119* (4), 1623–1641. https://doi.org/10.1021/jp508745u.

(59) Gur, I.; Sawyer, K.; Prasher, R. Searching for a Better Thermal Battery. *Science* **2012**, *335* (6075), 1454. https://doi.org/10.1126/science.1218761.

Chapter 4

Barium carbonate and barium titanate for ultra-high temperature thermochemical energy storage

The work in this chapter has been submitted for publication.

K.Williamson, A.M D'Angelo, T.D. Humphries, M. Paskevicius, and C.E. Buckley, Barium carbonate and barium titanate for ultra-high temperature thermochemical energy storage. *[in press]*

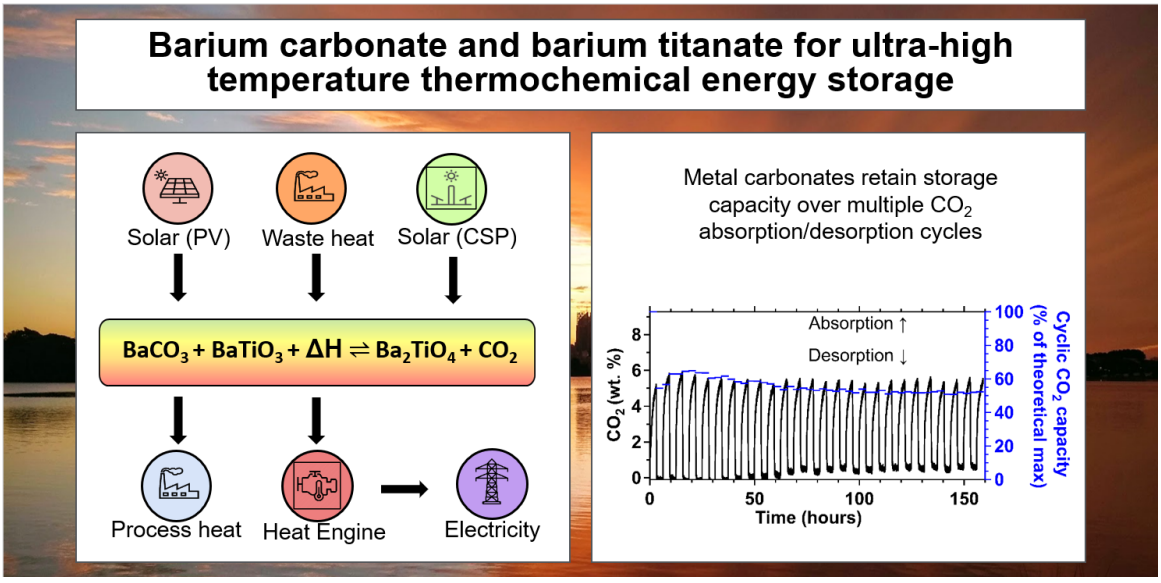

Abstract

The significance of energy storage should not be underestimated in enabling the growth of renewables on the path towards decarbonisation. In this research, a novel ultra-high temperature reactive carbonate composite, $2BaCO_3$:TiO_2, is introduced. Upon heating, the composite initially forms a mixture of $BaCO_3$:$BaTiO_3$, which on further heating reacts to form Ba_2TiO_4 and CO_2 in a reversible thermochemical reaction. The enthalpy and entropy of the carbonation reaction involving Ba_2TiO_4 were determined manometrically to be ΔH = 295 ± 9 kJ·mol^{-1} of CO_2 and ΔS = 214 ± 7 J·K^{-1}·mol^{-1} of CO_2, respectively. The CO_2 cycling capacity of the composite was evaluated using a Sieverts apparatus and thermogravimetric analysis, and sintering was identified as a potential cause of capacity loss. The addition of nickel was employed to mitigate the effect of sintering, resulting in a stable reversible capacity of up to 50 % of the theoretical maximum. The composite's cyclic capacity retention, low cost, and high energy storage density make it a promising candidate for energy storage applications at ≈ 1100 °C, although improvement to the cyclic capacity would lead to a more favourable application potential.

4.1 Introduction

Thermochemical energy storage (TCES) is an efficient method to bridge the gap between the intermittent supply and variable demand of energy.[1] TCES pairs perfectly with thermal energy sources such as Concentrating Solar Thermal Power (CSP), which is an emerging technology that aims to lower the cost of large-scale solar facilities. Over the last decade, the number of CSP installations has increased dramatically and there is currently over 9.6 GW of installed capacity worldwide.[2] The energy collection process uses mirror arrays to focus sunlight and generate heat in a fluid or a gas within a receiver that is then used to run a steam turbine to produce electricity.[3]

State-of-the-art CSP plants operate by using ‘sensible heat storage’ that is based on raising the temperature of molten salts to store heat and provide that thermal energy to a heat engine during night-time, providing 24/7 electrical power from the sun.[3] Despite their low

cost per unit mass, molten salts have a low gravimetric energy density and over 38,000 tonnes of salt are currently used to store 7 h of full load (1050 MWh) power at Noor III CSP project, Morocco, at the cost of ~ $180M USD.[4,5]

TCES materials offer much higher energy densities (1000 - 8000 $kJ \cdot kg^{-1}$) compared to 'sensible heat' storage systems (*i.e.* molten salts with a specific heat capacity of 427 $kJ \cdot kg^{-1}$).[6,7] TCES can be performed through a range of chemical reactions, including those with ammonia, hydrocarbons, sulphur, metal hydroxides, redox pairs, metal hydrides or metal carbonates.[8] An ideal TCES material is fully reversible over multiple cycles, has high energy storage density, fast reaction kinetics, long-term stability of materials, is cost-competitive, non-toxic, has zero unwanted by-products, and operates in a desired temperature window to maximise thermal to electrical conversion efficiencies.[9]

Metal carbonates are cost-effective TCES materials that can be thermally decomposed into a metal oxide and carbon dioxide gas. They also have a high energy density (i.e. reaction enthalpy per unit mass) and are safer than many other TCES alternatives.[6,10,11] High operating temperatures (1000 °C – 1200 °C) allow high-efficiency Brayton or combined cycle thermal-electrical energy conversion, which promise potent solar capture and thermal to electric conversion rates.[12,13] Additionally, TCES materials can also be integrated into high-temperature industrial processes such as steel making, cement manufacture and advanced solar fuel synthesis, to store and supply heat on demand.[12,14–16]

Barium carbonate ($BaCO_3$) has previously been investigated as a TCES material, although as a pure carbonate the operational temperature is typically too high for most current applications. As such, the calcination reaction of $BaCO_3$ has been thermodynamically destabilised by the addition of iron(ii) oxide (Fe_2O_3) to reduce its decomposition temperature from ~ 1300 °C to ~ 850 °C.[17]

$$BaCO_3 + Fe_2O_3 \rightleftharpoons BaFe_2O_4 + CO_2 \quad (4\text{-}1)$$

$\Delta H_{832\,°C}$ = 199 kJ·mol^{-1} CO_2, $\Delta S_{832\,°C}$ = 180 J·K^{-1}·mol^{-1} CO_2

Thermodynamic destabilisation of $BaCO_3$ has also been achieved using a $BaSiO_3$ additive to form Ba_2SiO_4, which can operate near 850 °C.[18] Similarly, $BaCO_3$ can be thermodynamically destabilised by the addition of $BaTiO_3$. This reaction was experimentally determined by Suyama and Kato to have a 1 bar (CO_2) equilibrium temperature of 1145 °C, which makes it a promising candidate for TCES applications in a higher temperature window than other $BaCO_3$ composites.[19]

$$BaCO_3 + BaTiO_3 \rightleftharpoons Ba_2TiO_4 + CO_2 \quad (4\text{-}2)$$

$\Delta H_{1145\,°C}$ = 210 kJ·mol^{-1} CO_2, $\Delta S_{1145\,°C}$ = 148 J·K^{-1}·mol^{-1} CO_2

Barium titanate ($BaTiO_3$) is a ceramic that has gained much attention due to its ferroelectric, pyroelectric and piezoelectric properties. It is used in applications as transducers, sensors and capacitors, as well as in optical phase-modulation.[20–23] Barium orthotitanate (Ba_2TiO_4) is typically formed as a side-product, or impurity, in the formation of $BaTiO_3$ from the solid-state reaction between $BaCO_3$ and TiO_2.[24–26]

The formation of Ba_2TiO_4 from TiO_2 and $BaCO_3$ in air has been studied over the last half-century. Initially, it was proposed by Tzebiatowski *et al.* [25] to be formed directly by reaction (4-3).

$$2BaCO_3 + TiO_2 \rightarrow Ba_2TiO_4 + 2CO_2 \quad (4\text{-}3)$$

$\Delta H_{718\,°C}$ = 326 kJ·mol^{-1} CO_2, $\Delta S_{718\,°C}$ = 329 J·K^{-1}·mol^{-1} CO_2[27]

However, Kubo[28] (using rutile) and Suyama and Koto[29] (using anatase) found the formation of Ba_2TiO_4 occurs via intermediate reaction (4-4) and then proceeds via reaction (4-2).

$$BaCO_3 + TiO_2 \rightarrow BaTiO_3 + CO_2 \quad (4\text{-}4)$$

$\Delta H_{391\,°C}$ = 103 kJ·mol^{-1} CO_2, $\Delta S_{391\,°C}$ = 155 J·K^{-1}·mol^{-1} CO_2[27]

Further studies indicate that the calcination reaction products are highly dependent on the partial pressures of either air or CO_2. Templeton and Pask experimentally determined that under 1 atmosphere of CO_2 the formation of Ba_2TiO_4 is suppressed up to a temperature between 1100 °C and 1150 °C, compared to 750 °C under air.[30] Additional studies of the solid state reaction when under vacuum (10^{-3} mbar) were undertaken by Beaugar *et al.* where they proposed reaction schemes involving BaO intermediates.[31,32]

Most of the research in the Ba-Ti-O literature focuses on the suppression of Ba_2TiO_4 formation in the manufacture of $BaTiO_3$, for example Hennings *et al.* established that by regulating the particle size of $BaCO_3$ (average diameter of 0.17 µm) and TiO_2 (average diameter of 0.2 µm), Ba_2TiO_4 formation can be prevented.[26] Meanwhile, Buscagali *et al*. discovered that no detectable Ba_2TiO_4 was produced when nanocrystalline TiO_2 (with a size of 70 nm) was reacted with $BaCO_3$ (with sizes of 650, 140, and 50 nm) at 740 °C under 1 bar of air.[33] However, when the pressure was lowered to 40 mbar of air, Ba_2TiO_4 was formed.

Based on the above findings, it was concluded that the formation of Ba_2TiO_4 is affected by various factors, such as the gas pressure (whether air or CO_2), the particle size of reactants, the annealing temperature, and the geometrical arrangement of the initial particles, and there is much dispute over the order of reactions under various conditions.[34]

Additionally, Ba_2TiO_4 has been studied for its viability as a CO_2 sequestration material, due to its ability to reversibly ab/desorb CO_2 over multiple cycles.[35,36] In a recent study, Ba_2TiO_4 was investigated using thermogravimetric analysis (TGA) for its ability to absorb and desorb CO_2 in a cyclic manner via reaction (4-2). Marusawa and Saito determined there was a 90 % cyclic capacity loss after 10 cycles, which was improved to a negligible quantity for up to 100 cycles by the addition of 1.5 wt.% Ni.[35]

The reversible cyclic capacity of Reaction (4-2) has previously only been explored through thermogravimetric analysis (TGA) utilizing sample sizes of approximately 20 mg and low

CO_2 pressures (0 – 1 bar).[35] In the present study, the cyclic capacity of both TGA samples (~20 mg) and larger samples (0.3 - 1 g) using Sieverts apparatus are investigated. This investigation is of particular significance because larger sample sizes can be influenced by additional factors such as heat transfer limitations, bulk kinetics of calcination and carbonation, as well as bulk sintering, that are likely to have a notable impact in larger industrial applications. Additionally, the Sieverts apparatus can be used to accurately determine the thermodynamic properties (enthalpy and entropy) of a thermochemical reaction by using the van't Hoff method.[37] Finally, *in-situ* time-resolved synchrotron radiation powder X-ray diffraction (SR-PXD) was used to elucidate the reaction pathway given the complexity outlined in the literature.

4.2 Materials and methods

$BaCO_3$ (Sigma-Aldrich, ACS reagent, ≥ 99 %) and TiO_2 (Sigma-Aldrich, ACS reagent, anatase ≥ 99 %), in a molar ratio of $BaCO_3$:TiO_2 2:1, were added to 80 mL 316 stainless steel vials with 316 stainless steel balls (8 mm diameter, in a ball-to-powder mass ratio of 10:1) and were ball-milled at 200 rpm for 1 hour (three 20 minute segments with 1 minute breaks) in air using an Across International planetary ball mill (PQ-N04). Pristine $BaCO_3$ was ball milled under the same conditions. An additional sample of $2BaCO_3$:TiO_2 was ball milled with 18.6 wt.% Ni (Sigma-Aldrich, powder, < 150 µm, 99.99 % trace metals basis) under argon using the same parameters but was handled in an argon-filled glove box (MBraun, Germany, < 1 ppm H_2O & O_2).

Simultaneous differential scanning calorimetry and thermogravimetric analysis (DSC-TGA) were measured on a STA 449 Jupiter using samples of 10 - 20 mg contained within Al_2O_3 crucibles. A protective gas flow of argon (Coregas, 99.995%, 20 mL·min^{-1}) was always utilised. For calcination a flow rate of argon 20 mL·min^{-1} was used. and for carbonation a flow rate of 80 mL·min^{-1} CO_2 (Coregas, 99.995%) mixed with a flow rate of argon (20 mL·min^{-1}) was used. The DSC-TGA temperature and heat flow were calibrated using In, Zn, Al, Ag, and Au reference materials resulting in an overall accuracy of ± 0.2 °C for

temperature and ± 20 μg for the balance. Heating and cooling rates of $\Delta T/\Delta t$ = 10 °C·min^{-1} were used.

A Bruker D8 Advance ((λ = 1.54187 ,2ϑ = 5 - 80°) was utilised for *ex-situ* Powder X-ray Diffraction (PXD) measurements in Bragg-Brentano geometry. Measurements were undertaken in air over a 2ϑ range of 5 – 80° using a Lynxeye position sensitive detector.

SR-PXD data was obtained at the Australian Synchrotron (ANSTO) in Melbourne, Australia, using the Powder Diffraction (PD) beamline. The experiments utilised a wavelength of 0.82504(1) Å, which was determined using NIST 660b LaB_6. The data were gathered using a Mythen II microstrip detector at two different positions, each with a 30-second acquisition time, before being combined into a single dataset. In one configuration the powder sample was housed within an Anton Paar HTK 2000 strip furnace (using a Pt strip), in flat-plate geometry, and was heated from room temperature to 1100 °C at $\Delta T/\Delta t$ = 6 °C·min^{-1} on a pre-stressed Pt strip with a thermocouple (type-S 90% Pt: 10% Rh, ± 1%) spot welded to the heating strip. In a second configuration, the sample was housed in a quartz capillary in transmission geometry, and sealed inside a custom gas fitting using rubber O-rings. During data collection, the capillary sample was continuously oscillated over 90° for improved powder averaging and heated using a hot air blower (Cyberstar) at a rate of $\Delta T/\Delta t$ = 6 °C·min^{-1} to reach the desired temperature. The temperature measurements were calibrated using the thermal expansion of a Ag standard.[38] Both configurations were connected to a custom-built gas manifold to provide vacuum (Pfeiffer HICUBE 80 eco turbo pumping station, 10^{-4} mbar) or CO_2 pressure ($p(CO_2)$ = 0.5 bar) as desired.

Cyclic CO_2 capacity and pressure-composition (PCT) measurements were performed on a custom-made Sieverts/volumetric instrument utilising a custom-made SiC sample holder, which was utilised to avoid corrosion at high temperature.[37] The reference volume was 22.85 ± 0.03 cm^3, the sample-side volume was 44.98 ± 0.05 cm^3, and the apparatus was equipped with RTD thermistors (± 0.1 °C), K-type thermocouples (± 1.5 °C) and a pressure gauge (Rosemount 3051S, ± 14 mbar). A vertical tube furnace (LABEC VTHTF40/15) was used to heat approximately 1 g of material to various temperatures ~ 1000 °C – 1150 °C

at $\Delta T/\Delta t$ ~ 10 °C·min^{-1} then kept isothermal. Calcination and carbonation were performed isothermally over a range of pressures between 0.2 - 2 bar CO_2 for varying lengths of time (1 - 24 hours).

Morphological studies were undertaken using a Tescan Mira3 field emission scanning electron microscope (SEM) coupled with secondary electron (SE) and backscattered electron (BSE) detectors. Images were collected using an accelerating voltage of 5 kV, an aperture size of 10 mm, and a working distance of 5 mm. Samples were prepared by distributing the sample powder on carbon tape, which was placed on aluminium stubs then sputter-coated with 3 nm of Pt.

4.3 Results and discussion

To reduce the particle size and homogeneously mix the chemicals, the composite ($2BaCO_3$:TiO_2) was ball milled for 1 hour under air. X-ray diffraction peaks assigned to $BaCO_3$ and TiO_2 are observed (Figure 4-1a), which suggests no reaction occurs during milling.

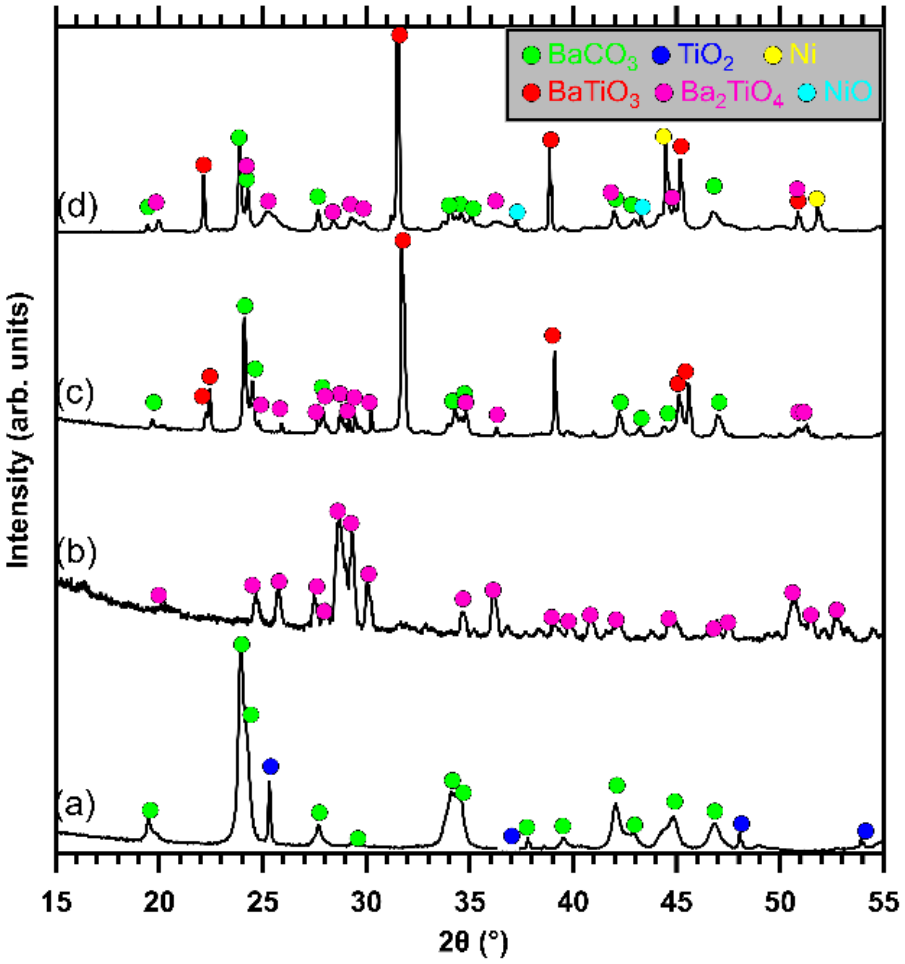

Figure 4-1: Ex-situ PXD data (λ = 1.54187 Å); (a) $2BaCO_3$:TiO_2 as milled ; (b) $2BaCO_3$:TiO_2 heated to 1144 °C under p(CO_2) = 4 bar and then decomposed by reducing pressure (CO_2) ~ 0 bar, allowing complete desorption before being cooled; (c) $2BaCO_3$:TiO_2 heated to 1085 °C then absorption/desorption cycled (45 times) and cooled in the absorbed state from 2.4 bar CO_2; (d) $2BaCO_3$:TiO_2:(18.6 wt.%)Ni heated to 1072 °C followed by 75 absorption/desorption cycles, then cooled in the absorbed state from p(CO_2) = 0.74 bar. y-axis is arbitrary intensity.

The decomposition and thermal evolution of barium carbonate as well as its mixture with titanium dioxide were both investigated to understand the behaviour of the systems under an inert atmosphere. In two separate DSC-TGA experiments, ~ 10 mg samples of ball milled $BaCO_3$ and ball milled $2BaCO_3$:TiO_2 were heated from room temperature to 1200 °C at $\Delta T/\Delta t$ = 10 °C·min^{-1} with an argon flow rate of 20 mL·min $^{-1}$ (Figure 4-2). TGA data (Figure 4-2a) shows that the decomposition and CO_2 release from $BaCO_3$ occurs

significantly above 1000 °C and has been destabilised to ~ 750 °C for the $2BaCO_3$:TiO_2 composite. From TGA data, both reactions appear to occur in single-step processes under these conditions. The total mass loss from the $2BaCO_3$:TiO_2 composite was 18.7 %, which is consistent with the expected 18.5 % in theoretical reaction scheme (3). Additionally, in the DSC data (Figure 4-2b) endothermic peaks corresponding to polymorphic phase changes in pristine $BaCO_3$ were observed at 814 °C and 973 °C that correspond to the expected polymorphic phase changes of the α (*Pmcn*) polymorph to β (*R*-3*m*) and β (*R*-3*m*) to γ (*Fm*-3*m*), respectively.[39] The α to β phase change of $BaCO_3$ is also observed in the $2BaCO_3$:TiO_2 sample at 825 °C (this shift in transformation temperature is likely caused by a hysteresis effect caused by the slower thermal conductivity of the mixed composite),[30] whilst the second larger endothermic peak in the $2BaCO_3$:TiO_2 composite at 975°C is attributed to the endothermic formation of Ba_2TiO_4.

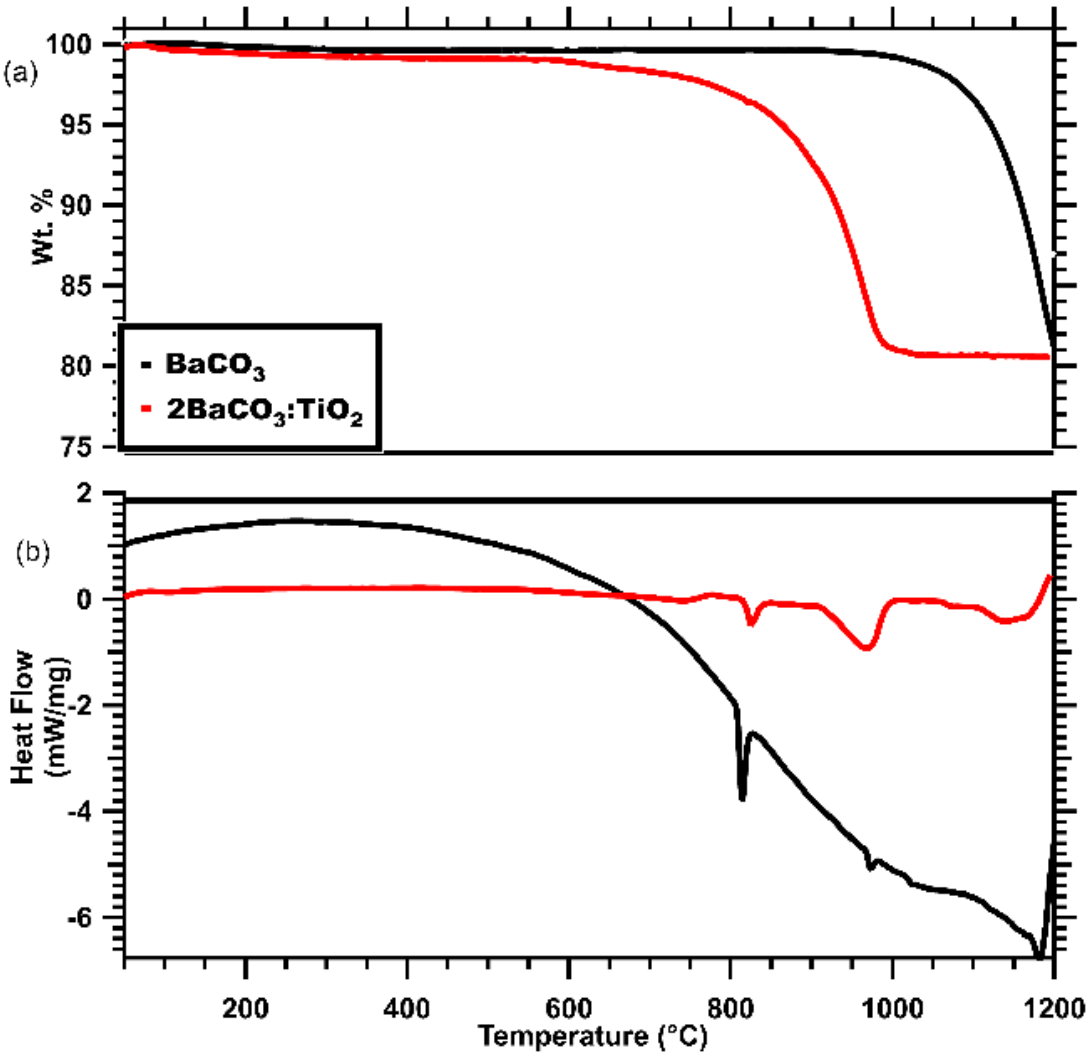

Figure 4-2: (a) TGA and corresponding (b) DSC measurements comparing the decomposition of ball milled $BaCO_3$, (black) and ball milled $2BaCO_3$:TiO_2 (red) heated from room temperature to 1200 °C at $\Delta T/\Delta t$ = 10 °C·min^{-1} under an argon flow of 20 mL·min^{-1}.

To evaluate the behaviour of $2BaCO_3$:TiO_2 under atmospheres of either CO_2 or argon, four separate TGA experiments were undertaken (Figure 4-3). When heated under an argon atmosphere to 1200 °C ($\Delta T/\Delta t$ = 10 °C·min^{-1}), $2BaCO_3$:TiO_2 (Figure 4-3a) initiates CO_2 desorption at 615 °C and desorbs 18.4 wt.% of gas by 1200 °C, which corresponds with the data represented in Figure 4-2. On application of a CO_2 flow (80 mL·min^{-1}) at 1200 °C no absorption is detected (no mass gain). CO_2 absorption initiates on cooling at 1095 °C and the mass gain observed reaches 7.2 wt.% as it cools to 690 °C. The kinetics of CO_2

absorption are not particularly rapid (see supplementary information Figure S-20), so CO_2 is not absorbed below 690 °C despite the reaction being thermodynamically favorable. We can deduce that reaction (4-3) is not completely reversible under these conditions and it is likely that CO_2 is absorbed via reaction (4-2).

When heated ($\Delta T/\Delta t$ = 10 °C·min^{-1}) under a CO_2 flow of 80 mL·min^{-1} $2BaCO_3$:TiO_2 initiates CO_2 desorption at 684 °C (Figure 4-3b), at a higher temperature than when heated under argon. Upon reaching 1100 °C a 9.1 wt.% loss is observed, this is close to the expected loss of 9.3 wt.% forming $BaTiO_3$ (reaction (4-4)). The reaction between $BaTiO_3$ and remaining $BaCO_3$ proceeds slowly at 1100 °C until the CO_2 flow is stopped (only argon flow), this gas change results in an almost instantaneous mass loss corresponding to 18.1 total wt.%, which corresponds to the theoretical reaction wt.% loss of 18.5 % for the complete production of Ba_2TiO_4 (reaction (4-4) then reaction (4-2). This result demonstrates that the desorption reaction proceeds in two steps, which can be controlled using a CO_2 back pressure.

To test cyclic CO_2 capacity, the $2BaCO_3$:TiO_2 sample was heated up to 1050 °C under argon, resulting in an expected loss of 18.3 wt.% when forming Ba_2TiO_4 (Figure 4-3c). After application of CO_2 flow (0.8 bar, 80 mL·min^{-1}) a rapid mass gain of 7.7 wt.% occurred at 1050 °C over 30 minutes, this is less than expected from complete reversibility of reaction 2(83 % of theoretical maximum). The sample rapidly decreases back to an 18.7 wt.% loss on removal of CO_2 pressure (argon flow = 20 mL·min^{-1}) within 14 minutes. Subsequent CO_2 absorption steps only recover 3.9 wt.% (42% of maximum theoretical capacity) in 30 minutes, suggesting a kinetic barrier to CO_2 absorption, despite CO_2 desorption remaining rapid.

Nickel has been utilised in another study as a sintering inhibitor to increase the cyclic CO_2 sorption capacity retention of Ba_2TiO_4.[35] $2BaCO_3$:TiO_2:18.6 wt.% Ni was ball milled under an argon atmosphere, and on removal from the glove box it was rapidly transferred to undergo TGA analysis (Figure 4-3d). The nickel enhanced sample was measured via TGA and showed a 14.4 wt.% loss (which is below the expected maximum of 15.0 wt.%) on

heating ($\Delta T/\Delta t$ = 10 °C·min^{-1}) to 1050 °C (argon flow = 80 mL·min^{-1}). On subsequent CO_2 absorption a mass increase of 8.6 wt.% is observed compared to a theoretically expected 7.5 wt.% from reaction 2. The additional 0.9 wt.% gained is in-fact due to the partial conversion of metallic nickel to nickel oxide under CO_2, which was also observed by Marusawa and Saito.[35] On subsequent cycles, the amount of CO_2 absorbed decreases slightly on each cycle (7.4, 7.2, 7.2, 6.8 and 6.4 wt.%) and there is also a slight overall increase in sample mass (0.2 - 0.3 wt.% per cycle) on each plateau after absorption, which could be attributed to further conversion of nickel to nickel oxide. A significant improvement to the cyclic CO_2 capacity retention in comparison to the sample without nickel is observed (Figure 4-3d).

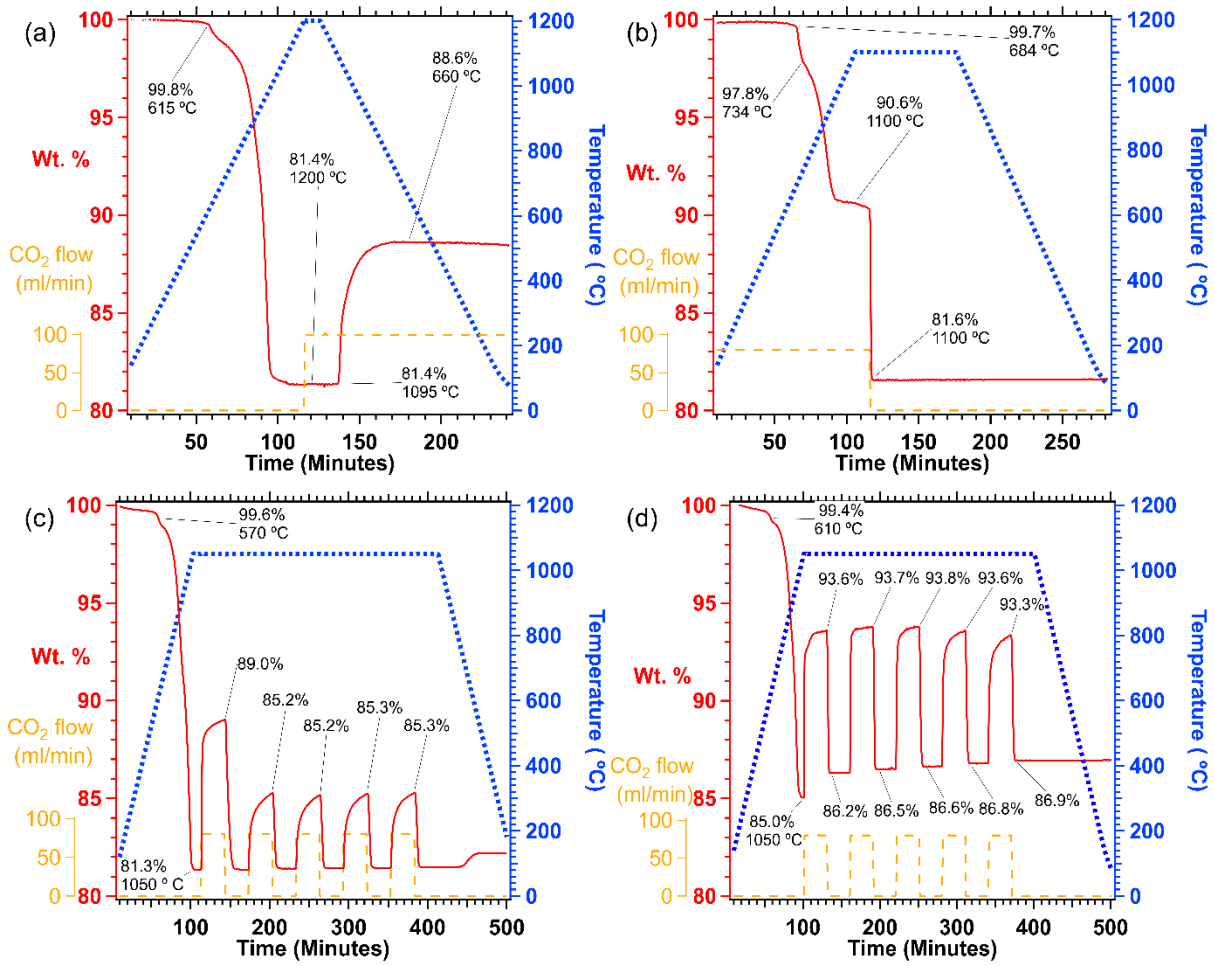

Figure 4-3: TGA (red) measurements of 4 samples of $2BaCO_3$:TiO_2 (a,b,c) and $2BaCO_3$:TiO_2:(18.6wt.%Ni) (d), heated ($\Delta T/\Delta t$= 10°C·min^{-1}) and cooled ($\Delta T/\Delta t$= -10°C·min^{-1}) (blue) in an Al_2O_3 crucible with an intermittent gas flow rate (orange) of CO_2 (0 or 80 mL·min^{-1}) and a constant flow of argon (20 mL·min^{-1}).

The thermodynamic properties of a gas-solid reaction can be determined using the van 't Hoff method, which is based on the measurement of the gas pressure at chemical equilibrium during the reaction under isothermal conditions. The thermodynamic properties are important for understanding the energy storage capacity of reversible chemical reactions.[37,40] The reaction enthalpy and entropy can be calculated using the following equation:

$$\ln(P_{eq}/P_0) = \Delta H/RT - \Delta S/R \qquad (4\text{-}5)$$

Where:

- P_{eq} is the measured pressure at equilibrium (half-way through the reaction) (bar).
- P_0 is the reference pressure (1 bar).
- T is temperature (K).
- R is the universal gas constant (8.3144 $kJ \cdot mol^{-1}K^{-1}$).
- ΔH is reaction enthalpy ($kJ \cdot mol^{-1}$).
- ΔS is the reaction entropy ($J \cdot K^{-1} \cdot mol^{-1}$).

In order to measure the thermodynamics of reaction (4-2), three samples of $2BaCO_3$:TiO_2, weighing 1.07 g, 0.42 g and 0.30 g, were heated ($\Delta T/\Delta t$ = 10°C·min^{-1}) up to temperatures of 1091 °C, 1127 °C, and 1144 °C then held isothermally for 12 hours prior to undertaking Sieverts measurements. The initial heating of samples was carried out under a minimum back pressure ($P(CO_2)$ > 3 bar) to prevent premature progress of reaction (4-2), but allowing reaction (4-4) to proceed, thus producing a $BaCO_3$:$BaTiO_3$ composite ready for analysis. As a result, the samples underwent a single-step release of CO_2 ((4-4)) that was equivalent to ~ 9.4 wt.%, which corresponds to the expected 9.3 wt.% (See sample desorption in supplementary information(see Figure S-18).

Pressure-Composition-Temperature (PCT) measurements were then conducted on each of the $BaCO_3$:$BaTiO_3$ samples at a given temperature (Figure 4-4a). It was observed that $BaCO_3$ has an unusually slow reaction rate with $BaTiO_3$ when the system gas pressure is close to equilibrium, which can result in misleading thermodynamic measurement unless ample time is allowed for the system to reach true equilibrium. This can make it difficult to accurately determine the thermodynamic properties of these materials. To address this issue, the system CO_2 pressure was decreased in increments of 0.2 - 1 bar until CO_2 desorption first began before waiting up to 48 hours to allow for the completion of each CO_2 release step to reach an equilibrium pressure. The complete desorption of each sample resulted in a 10.2(5) wt.% change in composition, corresponding to an expected 10.2 wt.% loss from reaction (4-2).

A van't Hoff plot was constructed by taking the central pressure reading of each equilibrium plateau (Figure 4-4b), where a reaction enthalpy value of ΔH = 295 ± 9 kJ·mol^{-1} of CO_2 and entropy of ΔS = 214 ± 7 J·K^{-1}mol^{-1} of CO_2 were determined. These are significantly higher than the literature values of ΔH = 210 kJ·mol^{-1} of CO_2 and ΔS = 148 J·K^{-1}mol^{-1} of CO_2.[19] It is believed that previous thermodynamic measurements could have been underestimated due to the rapid 30 minute wait time per PCT data point.[19] After cooling at the end of PCT measurements, PXD was performed (Figure 4-1b) where only Ba_2TiO_4 was observed, suggesting the sample was completely desorbed of CO_2 in two steps via reaction (4-4) then reaction (4-2).

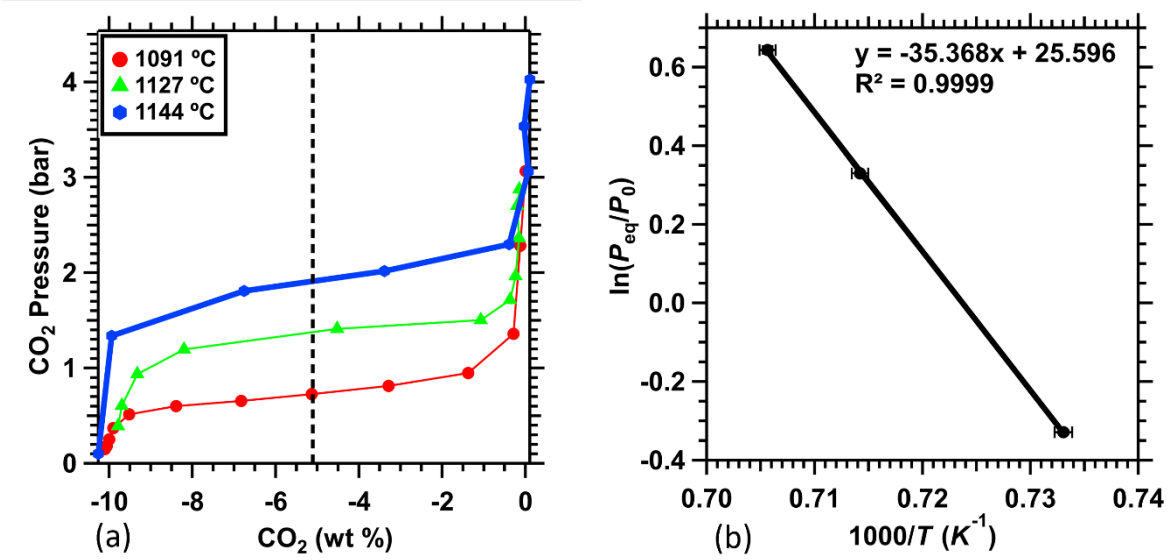

Figure 4-4: (a) Pressure-composition-temperature (PCT) measurements of the CO_2 release from $BaCO_3$:$BaTiO_3$. Each sample is isothermal and 48 h pressure steps were undertaken (step size $p(CO_2$ = 0.2 - 0.5 bar) to reach equilibrium. Equilibrium pressures were taken at the midpoint of the reaction (dashed line). (b) Corresponding van't Hoff plot generated from taking the center point of each desorption isotherm.

SR-PXD was utilised during heating and pressure steps on $2BaCO_3$:TiO_2 to identify crystalline compounds (Figure 4-5). An initial room temperature scan shows both $BaCO_3$ and TiO_2 as expected. The sample was heated ($\Delta T/\Delta t$ = 6 °C·min^{-1}) to 1100 °C under a carbon dioxide atmosphere ($p(CO_2)$ = 0.5 bar). During heating, characteristic shifts in diffraction peaks towards lower diffraction angle were observed due to thermal expansion of the respective crystal lattices. $BaCO_3$ was observed to undergo two polymorphic phase changes at 812 °C and 975 °C: α (*Pmcn*) to β (*R*-3*m*) then β (*R*-3*m*) to γ (*Fm*-3*m*), which correspond well to the literature (811 °C and 982 °C).[41] At a temperature of 657 °C the formation of $BaTiO_3$ was observed along with the consumption of some TiO_2 and $BaCO_3$. This is lower than the 685 °C reaction observed in the TGA experiment under $p(CO_2)$ = 0.8 bar (Figure 4-3). Ba_2TiO_4 begins to form at 1056 °C and γ-$BaCO_3$ is quickly consumed, which is as expected for $p(CO_2)$= 0.5 bar (where the 1 bar equilibrium temperature for the reaction would be 1108 °C based on thermodynamics).

By 1094 °C, $BaTiO_3$ and $BaCO_3$ were completely consumed leaving only Ba_2TiO_4. Minor splitting of the Ba_2TiO_4 Bragg peaks was observed at this temperature, which is believed to be an artefact. This peak splitting may result from observed reflections from two different sample heights that could occur due to cracking of the flat powder sample as the CO_2 is released rapidly. This may also explain the disappearance of the Pt sample holder peaks at scan 160 (2ϑ = 20.7°), which may be masked by movement of the powder. On cooling to 1050 °C (under 0.5 bar CO_2) an immediate reabsorption of CO_2 occurred as Ba_2TiO_4 converts back into $BaCO_3$ and $BaTiO_3$, with a minor amount of Ba_2TiO_4 remaining. These results demonstrate that the order of reaction under $p(CO_2)$ = 0.5 bar is primarily the complete consumption of TiO_2 to form $BaTiO_3$ as per reaction (4-4) followed by the formation of Ba_2TiO_4 shown in reaction (4-2).

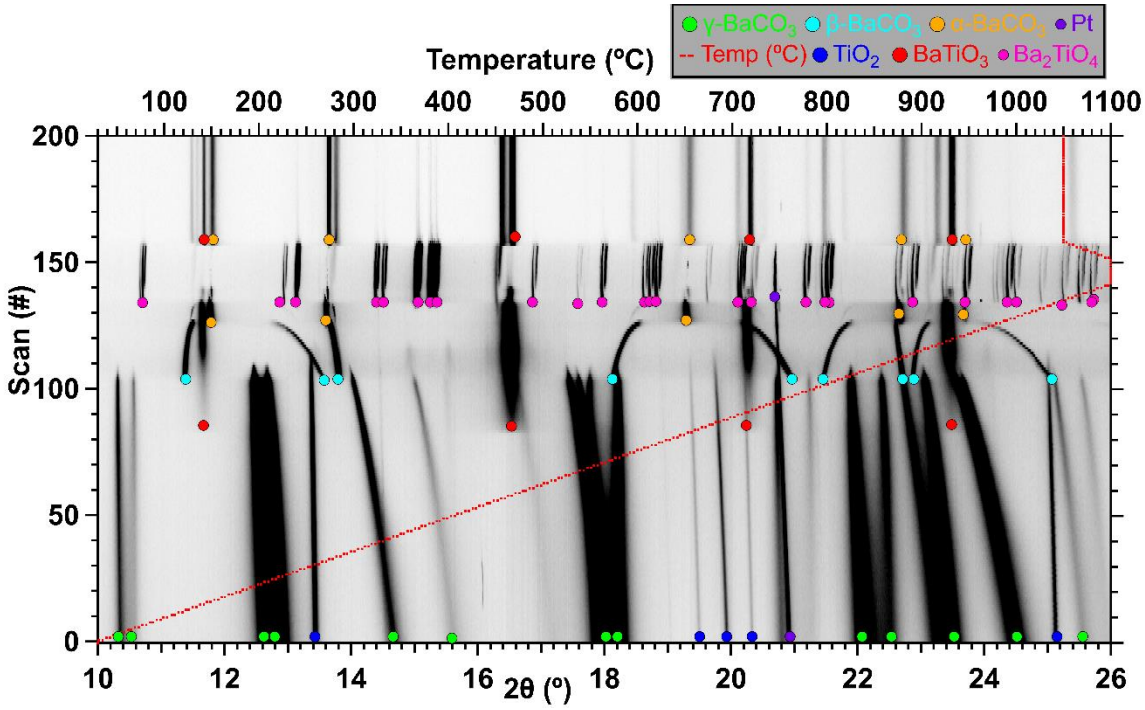

Figure 4-5: SR-PXD data of ball milled $2BaCO_3$:TiO_2, heating and cooling rate ($\Delta T/\Delta t$ = 6 °C·min), λ = 0.825094(5) Å, scan time = 1 min. p(CO_2) = 0.5 bar on heating, reduced to 0 bar at scan 182;. Colour code: Temperature - dashed red line, TiO_2 – blue, γ-$BaCO_3$ – green, β-$BaCO_3$ - teal, α- $BaCO_3$ - orange, $BaTiO_3$ – red, Ba_2TiO_4 – pink, Pt – purple.

In a subsequent experiment utilising SR-PXD, a sample of $2BaCO_3$:TiO_2 was heated from room temperature to 968 °C ($\Delta T/\Delta t$ = 6 °C·min^{-1}) under dynamic vacuum ($p(CO_2) \leq 10^{-4}$ bar) in a quartz capillary (Figure 4-6). Observations were consistent with those from heating under CO_2 (Figure 4-5) with a shift in the reaction temperatures, as observed by TGA. Specifically, $BaTiO_3$ was observed to form at 642 °C, as opposed to 657 °C when under CO_2. The formation of Ba_2TiO_4 was also observed at a temperature of 100 °C lower whilst under vacuum, at 951 °C.

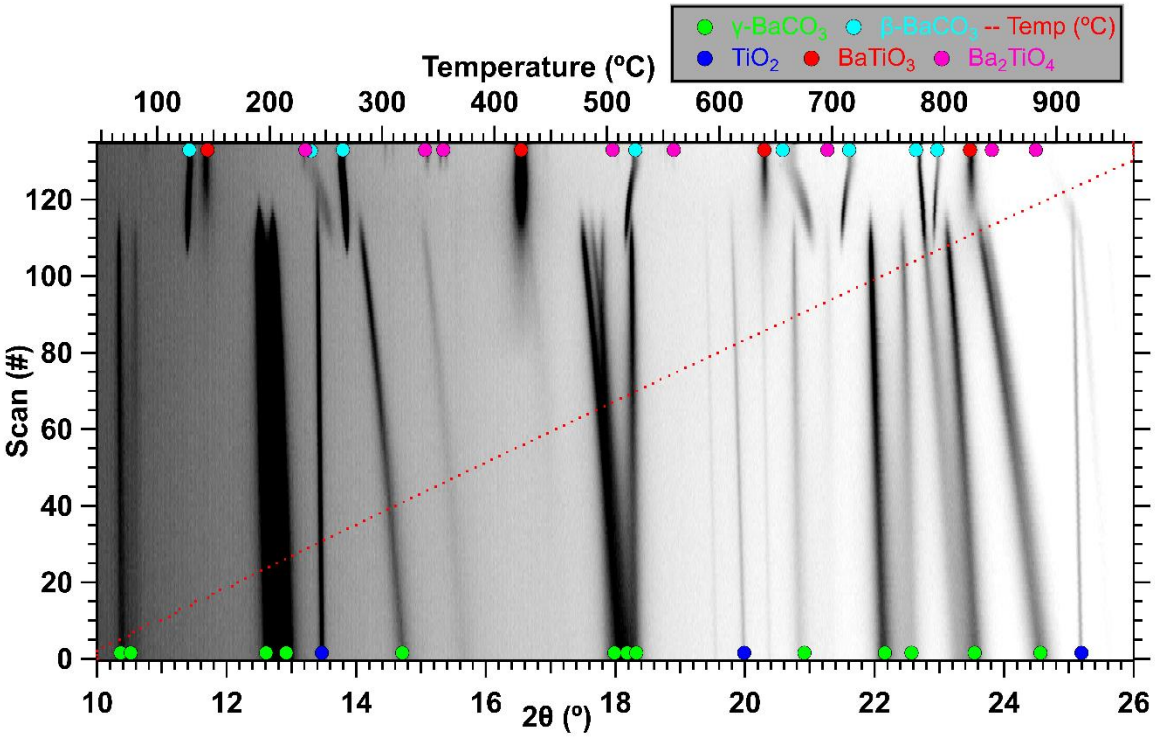

Figure 4-6: SR-PXD data of ball milled $2BaCO_3$:TiO_2, heating and cooling rate ($\Delta T/\Delta t$ = 6 °C·min^{-1}, λ = 0.82509(1) Å, scan time = 1 min). p(CO_2) = 0 bar. Colour code: Temperature - dashed red line, TiO_2 – blue, γ-$BaCO_3$ – green, β-$BaCO_3$ - teal, $BaTiO_3$ –red, Ba_2TiO_4 – pink.

The cyclic energy storage capacity of $2BaCO_3$:TiO_2 was evaluated through an absorption/desorption experiment on the transformation between $BaCO_3$/$BaTiO_3$ and Ba_2TiO_4/CO_2(g) (reaction 2) using Sieverts-type equipment.[37] 1.12 g of $2BaCO_3$:TiO_2 was heated under static vacuum from room temperature to 1085 °C in a total closed volume of 195.30 cm^3 (See supplementary information Figure S-19). The sample released CO_2 equivalent to 18.8 wt.% (theoretical maximum = 18.6 wt .%), as expected for the complete reaction (4-3), where two clear steps are observable, assigned to reaction (4-4) then reaction (4-2).

The sample was then subjected to a series of CO_2 pressure cycles comprising of CO_2 absorption (2.1 bar) and desorption (0.35 bar) steps, each lasting 3 hours (Figure 4-7). The initial CO_2 absorption capacity was found to be 5.2 wt.% on the first absorption and 5.9

wt.% on the second absorption, which is below the theoretical maximum of 9.27 wt.%. This capacity may be improved by extending the duration of the absorption steps, but this was left constant for consistency. The theoretical CO_2 equilibrium pressure at 1085 °C is 0.51 bar,[42] and as the system gas pressure approaches this thermodynamic pressure limit desorption kinetics appear to be sluggish.

Additionally, it was observed the CO_2 capacity gradually decreased over progressive cycles, reducing from 65 % to 52% of the maximum capacity after 25 cycles this is likely due to a decrease in kinetics of absorption (see supplementary information Figure S-20). The capacity retention is a significant improvement over the cycled TGA sample (Figure 4-3c), which could be due to the higher pressure of absorption driving the calcination of the sample as well as longer absorption times. After the final CO_2 absorption step the sample was cooled ($\Delta T/\Delta t$ = -10 °C·min^{-1}), PXD was performed (Figure 4-1c), and the presence of $BaTiO_3$ and $BaCO_3$ were observed, as well as a small unreacted portion of Ba_2TiO_4 that supports that CO_2 absorption was not progressing to completion.

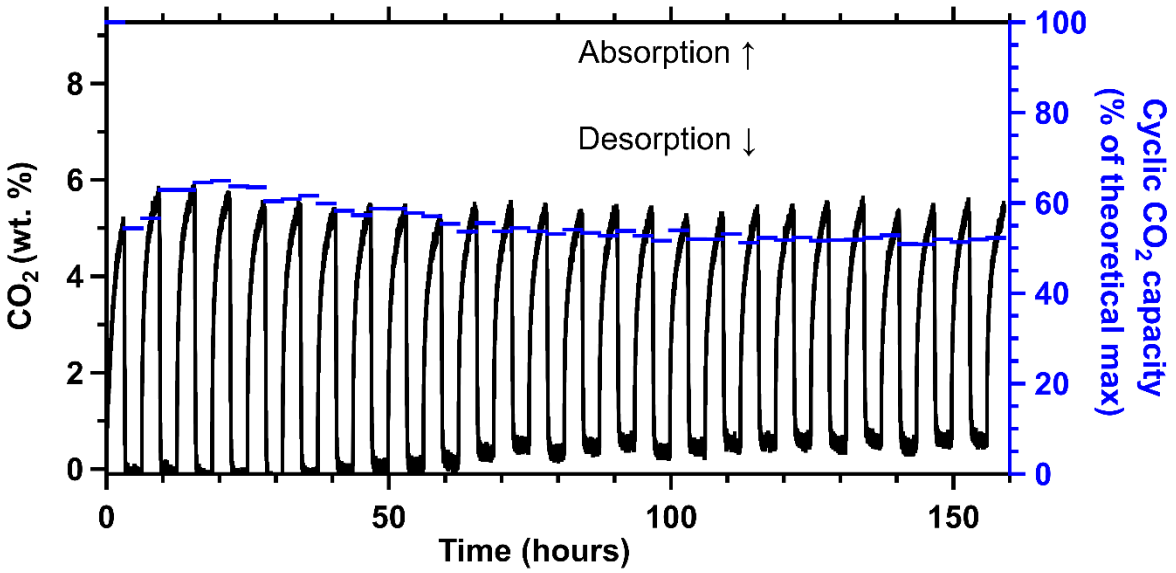

Figure 4-7: Sieverts pressure cycling, 1.12(5) g of $2BaCO_3$:TiO_2, T = 1085 °C, $t_{abs/des}$ = 3 hours, initial pressures p_{abs} = 2.15 bar, p_{des} = 0.35 bar)

To improve the cyclic CO_2 capacity further, a 0.75 g sample of $2BaCO_3$:TiO_2:(18.6 wt.%)Ni was heated in a Sieverts type apparatus from room temperature to 1072 °C at a rate of 10 °C·min^{-1} before being pressure cycled under various conditions (Figure 4-8). Here, the initial CO_2 absorption and desorption pressures and times were adjusted to provide insight into the potential of short and long charge and discharge cycles to accommodate kinetic factors. The first observation is that the cyclic storage capacity is improved by the addition of nickel (~ 70 %, rather than ~ 50 % of theoretical capacity), the second is that the capacity loss over multiple cycles is negligible. Additionally due to the rapid initial sorption period followed by a plateau the charge and discharge time has little effect on the capacity.

The sample was cooled ($\Delta T/\Delta t$ = -10 °C·min^{-1}) in the absorbed state and then subsequently underwent PXD analysis (Figure 4-1d). Bragg peaks corresponding to $BaTiO_3$, $BaCO_3$ and Ba_2TiO_4 and the absence of TiO_2 indicate successful cycling via reaction (4-2). Additionally, there is the presence of Ni and a minor presence of NiO, which explains the minor wt.% gain observed in the TGA CO_2 cycling study presented in Figure 4-3d.

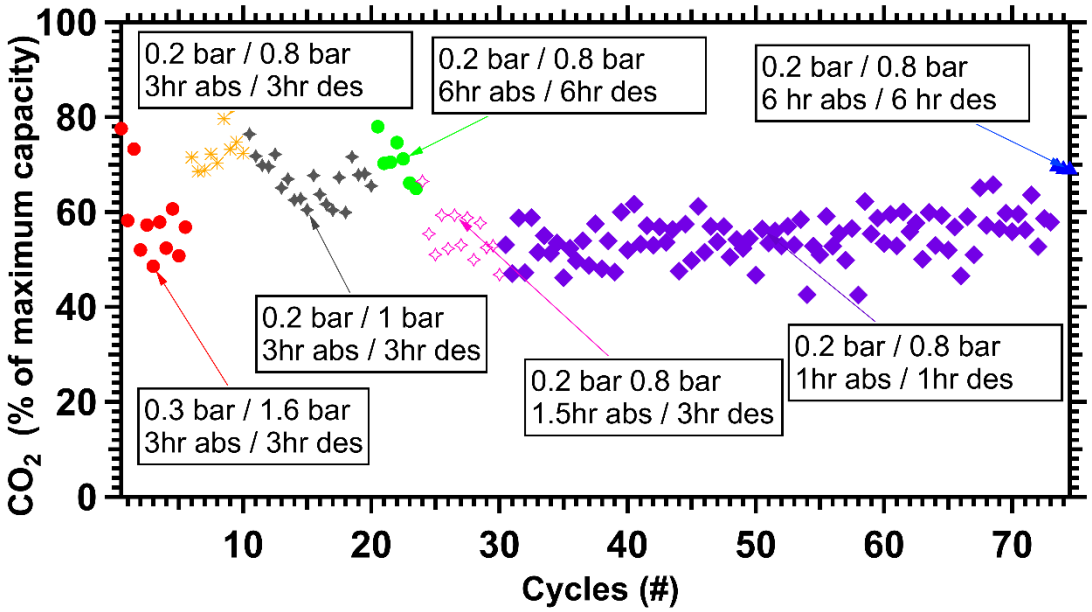

Figure 4-8: Sieverts CO_2 pressure cycling of 0.87(5) g of $2BaCO_3$:TiO_2:(18.6 wt.%)Ni, T = 1072 °C, initial sorption CO_2 pressure and step times as indicated.

The morphology of $2BaCO_3$:TiO_2 after milling and Sieverts cycling was investigated using scanning electron microscopy (SEM) (Figure 4-9). The as-milled $2BaCO_3$:TiO_2 sample (Figure 4-9a) exhibited signs of homogeneous mixing, characterized by a fluffy texture suggesting a high surface area with multiple channels between small particles (50 – 500 nm), which are favourable for CO_2 sorption. After 25 CO_2 absorption-desorption cycles at 1085 °C the sample was cooled in the absorbed state (see Figure 4-7), and the formation of larger sintered particles is observed (> 2000 nm), which results in a reduction in surface area. This possibly hinders the passage of CO_2 and phase segregation, resulting in a reduced CO_2 capacity (Figure 4-9b). The addition of nickel to the sample before cycling 75 times (see Figure 4-8) results in the cycled sample (1072 °C) having an increased surface area and smaller particle size (200 – 1000 nm), as evidenced by a rougher overall surface with more channels for CO_2 sorption (Figure 4-9c). This indicates that the addition of nickel significantly reduces sintering of the sample, preventing the formation of large particles, which is beneficial for maintaining cyclic CO_2 sorption capacity.

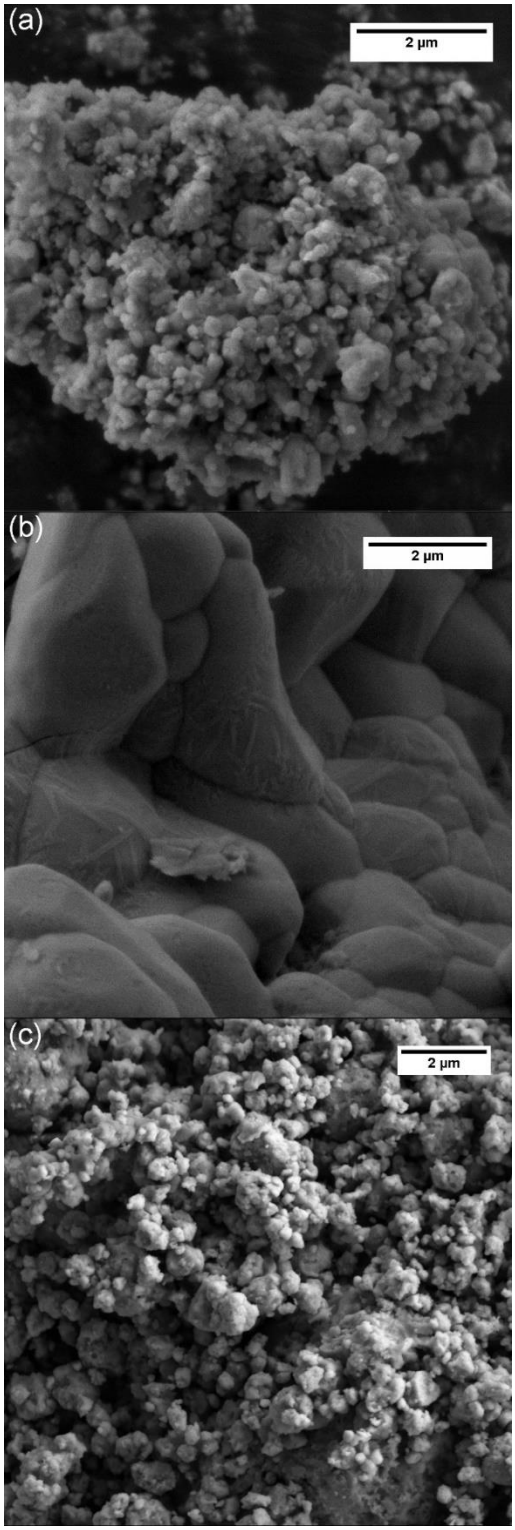

Figure 4-9: Secondary electron SEM micrographs for $2BaCO_3$:TiO_2 (a) as-milled (b) after 25 CO_2 absorption-desorption cycles (cooled in the absorbed state) (c) $2BaCO_3$:TiO_2:(18.6 wt.%) Ni, after 75 absorption-desorption cycles (cooled in the absorbed state).

4.4 Cost analysis

A material cost comparison used in previous studies has been extended to include the $2BaCO_3$:TiO_2 composite.[6,18,44] The cost of raw materials used to store electrical energy from $2BaCO_3$:TiO_2 was determined to cost 2.40 US$/$MJ_e$, which is more cost effective than 3.3 US$/$MJ_e$ for the $BaCO_3$-$BaSiO_3$ system, but is slightly more expensive than the 2.30 US$/$MJ_e$ for the $SrSiO_3$-$SrCO_3$ system. However, $2BaCO_3$:TiO_2 is more cost-effective on a raw materials basis than molten salts, which cost 5.7 US$/$MJ_e$. Importantly, the cost analysis does not account for CO_2 storage and other auxiliary equipment, which can add significant expenses. The $2BaCO_3$:TiO_2 system possesses high reaction enthalpy (295 ± 9 kJ·mol^{-1}) and high gravimetric energy density (620 kJ kg^{-1}), potentially reducing the size of a thermal battery and further lowering costs. Further technoeconomic modelling is necessary to fully understand the complexities involved in designing a TCES battery based on these materials. Finally, nickel is not a viable additive to mitigate the cycling capacity loss because even a 10% (by mass) addition increases the price per tonne of storage material from $774 to $2,604. Other additives or a lower amount of nickel should be considered to further reduce costs.[45,46]

Table 4-1: Comparison of thermochemical properties, system variables, and cost parameters for select energy storage materials to store 1TJ of electrical energy.[6,18,44,44,47]

	$BaCO_3 + BaTiO_3 \rightleftharpoons Ba_2TiO_4 + CO_2$	**$BaCO_3$+$BaSiO_3 \rightleftharpoons Ba_2SiO_4 + CO_2$**	**$SrCO_3$+$SrSiO_3 \rightleftharpoons Sr_2SiO_4 + CO_2$**	**Molten salt ($40NaNO_3$:$60KNO_3$)**
Enthalpy Δ*H* (kJ mol^{-1} of CO_2)	295	126.9	155.7	39
Molar Mass (g mol^{-1}) (CO_2 loaded material)	357	411	311	94.6
[a,b]Density (g cm^{-3})	5.2	[a]4.4	[a]3.75	2.17

CO_2 Capacity (wt.%)	9.3	10.7	14.1	-
Gravimetric Energy Density (kJ kg^{-1})	620	309	500	413
[d] Volumetric Energy Density (MJ m^{-3})	3221	1359	1878	895
Operating Temperature (°C)	1050	850	700	290 - 565
Operating CO_2 Pressure (bar)	0.5-1.5	5 - 25	0.1 - 6.0	-
[c] Theoretical Carnot Efficiency (%)	77.1	73	69	46
[d]Estimated Practical Efficiency (%)	52.1	48	45	27
[e] Mass Required (tonnes)	3095	6903	[g]4700	9100
[e] Volume Required (m^3)	595	1569	[g]1711	4194
[e]Materials Cost (US$ $tonne^{-1}$)	[g]774	[g]495	[g]480	630
[e,f,g] Total Materials Cost Required (US$)	2,400,000	3,410,000	2,258,099	5,730,000

[a]Applies to the mixture $\boldsymbol{M}CO_3$-$\boldsymbol{M}SiO_3$. [b]Based on crystalline data. [c]Lower temperature. [d]Thermal to electrical energy conversion [e]To generate 1 TJ of electrical energy. [f] 80 wt.% $SrSiCO_3$:$SrCO_3$ + 20 wt.% NaCl:$MgCl_2$. [g]Based entirely on the cost of $\boldsymbol{M}_xCO_3$, as this is also the starting reagent for $\boldsymbol{M}_xSiO_3$ (***M*** = Sr or Ba).

4.5 Conclusions

This study highlights the potential of a thermochemical battery composed of inexpensive and abundant materials to address the growing demand for high-temperature thermal energy storage. The energy storage capacity of the $2BaCO_3$:TiO_2 composite was successfully measured, demonstrating promising energy storage capabilities in the ultra-high temperature range. To improve the cycling capacity of the system, future research should investigate the optimal quantity of nickel or the incorporation of other materials to reduce sintering. This research represents a starting point for exploring the use of metal carbonates and metal oxides composites as energy storage materials. Moreover, the use of Sieverts apparatus offers a promising avenue for studying cycling capacity of metal carbonates on a larger scale than through traditional thermogravimetric analysis, bringing us one step closer to upscaling prototypes. Additionally, future studies on the thermodynamic properties of these reactions are needed, as predictions based on thermochemical properties from tables can be outdated or unreliable when extrapolated to high-temperature conditions.

4.6 Declaration of Competing Interest

The authors declare that they have no known competing financial interests or personal relationships that could have appeared to influence the work reported in this paper.

4.7 Acknowledgments

KW acknowledge the Australian Government for an Australian Government Research Training Program Scholarship. C.E. Buckley, M. Paskevicius and T. D. Humphries acknowledge the Australian Research Council for DP200102301 and the Australian Government for Global Innovation Linkage project (GIL73589). Part of this research was undertaken using the SEM/XRD instrumentation (ARC LE0775553 and LE0775551) at the John de Laeter Centre, Curtin University. This research was supported by an AINSE Ltd. Postgraduate Research Award (PGRA).

4.8 References

(1) André, L.; Abanades, S. Recent Advances in Thermochemical Energy Storage via Solid–Gas Reversible Reactions at High Temperature. *Energies* **2020**, *13* (22), 5859. https://doi.org/10.3390/en13225859.

(2) *CSP Projects Around the World - SolarPACES*. https://www.solarpaces.org/csp-technologies/csp-projects-around-the-world/ (accessed 2019-10-23).

(3) Lovegrove, K.; Stein, W. *Concentrating Solar Power Technology: Principles, Developments and Applications*; Elsevier Science & Technology: Cambridge, UNITED KINGDOM, 2012.

(4) *NOOR III | Concentrating Solar Power Projects | NREL*. https://solarpaces.nrel.gov/project/noor-iii (accessed 2023-05-05).

(5) *ACWA POWER | Nooro III CSP IPP*. https://acwapower.com/en/projects/nooro-iii-csp-ipp/ (accessed 2023-05-05).

(6) Humphries, T. D.; Møller, K. T.; Rickard, W. D. A.; Sofianos, M. V.; Liu, S.; Buckley, C. E.; Paskevicius, M. Dolomite: A Low Cost Thermochemical Energy Storage Material. *J. Mater. Chem. A* **2019**, *7* (3), 1206–1215. https://doi.org/10.1039/C8TA07254J.

(7) Adams, M.; Buckley, C. E.; Busch, M.; Bunzel, R.; Felderhoff, M.; Heo, T. W.; Humphries, T. D.; Jensen, T. R.; Klug, J.; Klug, K. H.; Møller, K. T.; Paskevicius, M.; Peil, S.; Peinecke, K.; Sheppard, D. A.; Stuart, A. D.; Urbanczyk, R.; Wang, F.; Walker, G. S.; Wood, B. C.; Weiss, D.; Grant, D. M. Hydride-Based Thermal Energy Storage. *Prog. Energy* **2022**, *4* (3), 032008. https://doi.org/10.1088/2516-1083/ac72ea.

(8) Carrillo, A. J.; González-Aguilar, J.; Romero, M.; Coronado, J. M. Solar Energy on Demand: A Review on High Temperature Thermochemical Heat Storage Systems and Materials. *Chem. Rev.* **2019**, *119* (7), 4777–4816. https://doi.org/10.1021/acs.chemrev.8b00315.

(9) André, L.; Abanades, S.; Flamant, G. Screening of Thermochemical Systems Based on Solid-Gas Reversible Reactions for High Temperature Solar Thermal Energy Storage. *Renew. Sustain. Energy Rev.* **2016**, *64*, 703–715. https://doi.org/10.1016/j.rser.2016.06.043.

(10) André, L.; Abanades, S. Investigation of Metal Oxides, Mixed Oxides, Perovskites and Alkaline Earth Carbonates/Hydroxides as Suitable Candidate Materials for High-Temperature Thermochemical Energy Storage Using Reversible Solid-Gas Reactions. *Mater. Today Energy* **2018**, *10*, 48–61. https://doi.org/10.1016/j.mtener.2018.08.007.

(11) Jarimi, H.; Aydin, D.; Yanan, Z.; Ozankaya, G.; Chen, X.; Riffat, S. Review on the Recent Progress of Thermochemical Materials and Processes for Solar Thermal Energy Storage and Industrial Waste Heat Recovery. *Int. J. Low-Carbon Technol.* **2019**, *14* (1), 44–69. https://doi.org/10.1093/ijlct/cty052.

(12) Romero, M.; Steinfeld, A. Concentrating Solar Thermal Power and Thermochemical Fuels. *Energy Environ. Sci.* **2012**, *5* (11), 9234. https://doi.org/10.1039/c2ee21275g.

(13) Bayon, A.; Bader, R.; Jafarian, M.; Fedunik-Hofman, L.; Sun, Y.; Hinkley, J.; Miller, S.; Lipiński, W. Techno-Economic Assessment of Solid–Gas Thermochemical Energy Storage Systems for Solar Thermal Power Applications. *Energy* **2018**, *149*, 473–484. https://doi.org/10.1016/j.energy.2017.11.084.

(14) Ortega-Fernández, I.; Rodríguez-Aseguinolaza, J. Thermal Energy Storage for Waste Heat Recovery in the Steelworks: The Case Study of the REslag Project. *Appl. Energy* **2019**, *237*, 708–719. https://doi.org/10.1016/j.apenergy.2019.01.007.

(15) Fernández, A. I.; Barreneche, C.; Miró, L.; Brückner, S.; Cabeza, L. F. 19 - Thermal Energy Storage (TES) Systems Using Heat from Waste. In *Advances in Thermal Energy Storage Systems*; Cabeza, L. F., Ed.; Woodhead Publishing Series in Energy; Woodhead Publishing, 2015; pp 479–492. https://doi.org/10.1533/9781782420965.4.479.

(16) Barati, M.; Esfahani, S.; Utigard, T. A. Energy Recovery from High Temperature Slags. *Energy* **2011**, *36* (9), 5440–5449. https://doi.org/10.1016/j.energy.2011.07.007.

(17) Williamson, K.; Møller, K. T.; D'Angelo, A. M.; Humphries, T. D.; Paskevicius, M.; Buckley, C. E. Thermochemical Energy Storage in Barium Carbonate Enhanced by Iron(III) Oxide. *Phys. Chem. Chem. Phys.* **2023**, *25* (10), 7268–7277. https://doi.org/10.1039/D2CP05745J.

(18) Møller, K. T.; Williamson, K.; Buckley, C. E.; Paskevicius, M. Thermochemical Energy Storage Properties of a Barium Based Reactive Carbonate Composite. *J. Mater. Chem. A* **2020**, *8* (21), 10935–10942. https://doi.org/10.1039/D0TA03671D.

(19) Suyama, Y.; Kato, A. A Comment on the Chemical Equilibrium in the BaCO3 - TiO2 System. *Ceramurg. Int.* **1975**, *1* (3), 123–126. https://doi.org/10.1016/0390-5519(75)90045-9.

(20) Roberts, S. Dielectric and Piezoelectric Properties of Barium Titanate. *Phys. Rev.* **1947**, *71* (12), 890–895. https://doi.org/10.1103/PhysRev.71.890.

(21) Ansaree, J.; Upadhyay, S. Study of Phase Evolution and Dielectric Properties of Sn-Doped Barium Titanate. *Emerg. Mater. Res.* **2017**, *6*, 1–28. https://doi.org/10.1680/jemmr.16.00013.

(22) Acosta, M.; Novak, N.; Rojas, V.; Patel, S.; Vaish, R.; Koruza, J.; Rossetti, G. A.; Rödel, J. BaTiO3-Based Piezoelectrics: Fundamentals, Current Status, and Perspectives. *Appl. Phys. Rev.* **2017**, *4* (4), 041305. https://doi.org/10.1063/1.4990046.

(23) Kaminow, I. P. Barium Titanate Light Phase Modulator. *Appl. Phys. Lett.* **1965**, *7* (5), 123–125. https://doi.org/10.1063/1.1754337.

(24) Rase, D. E.; Roy, R. Phase Equilibria in the System BaO–TiO2. *J. Am. Ceram. Soc.* **1955**, *38* (3), 102–113. https://doi.org/10.1111/j.1151-2916.1955.tb14585.x.

(25) Templeton, L. K.; Pask, J. A. Formation of BaTiO3 from BaCO3 and TiO2 in Air and in CO2. *J. Am. Ceram. Soc.* **1959**, *42* (5), 212–216. https://doi.org/10.1111/j.1151-2916.1959.tb15455.x.

(26) Hennings, D. F. K.; Schreinemacher, B. S.; Schreinemacher, H. Solid-State Preparation of BaTiO3-Based Dielectrics, Using Ultrafine Raw Materials. *J. Am. Ceram. Soc.* **2001**, *84* (12), 2777–2782. https://doi.org/10.1111/j.1151-2916.2001.tb01094.x.

(27) BARIN, I. Thermochemical Data of Pure Substances. *VCH* **1989**.

(28) Kubo, T.; Shinriki, K. Synthesis of BaTiO3 by Chemical Reaction in the Solid State; VII, Rate of Solid Phase Reaction of BaCO3–TiO2 System. *J Chem Soc Jpn Ind Chem Sect* **1954**, *57*, 621–623.

(29) Suyama, Y.; Kato, A. Reactivity of Ultrafine-TiO2 (Anatase) Powders with BaCO3. *Ceramurg. Int.* **1975**, *1* (1), 5–9. https://doi.org/10.1016/0390-5519(75)90031-9.

(30) Templeton, L. K.; Pask, J. A. Formation of BaTiO3 from BaCO3 and TiO2 in Air and in CO2. *J. Am. Ceram. Soc.* **1959**, *42* (5), 212–216. https://doi.org/10.1111/j.1151-2916.1959.tb15455.x.

(31) Beauger, A.; Mutin, J. C.; Niepce, J. C. Synthesis Reaction of Metatitanate BaTiO3. *J. Mater. Sci.* **1983**, *18* (10), 3041–3046. https://doi.org/10.1007/BF00700786.

(32) Beauger, A.; Mutin, J. C.; Niepce, J. C. Synthesis Reaction of Metatitanate BaTiO3. *J. Mater. Sci.* **1983**, *18* (12), 3543–3550. https://doi.org/10.1007/BF00540726.

(33) Buscaglia, M. T.; Bassoli, M.; Buscaglia, V.; Alessio, R. Solid-State Synthesis of Ultrafine BaTiO3 Powders from Nanocrystalline BaCO3 and TiO2. *J. Am. Ceram. Soc.* **2005**, *88* (9), 2374–2379. https://doi.org/10.1111/j.1551-2916.2005.00451.x.

(34) Lotnyk, A.; Senz, S.; Hesse, D. Formation of BaTiO3 Thin Films from (110) TiO2 Rutile Single Crystals and BaCO3 by Solid State Reactions. *Solid State Ion.* **2006**, *177* (5), 429–436. https://doi.org/10.1016/j.ssi.2005.12.027.

(35) Marusawa, H.; Saito, Y. *CO2 Absorption Properties of Barium Orthotitanate under Continuous Operation*. Key Engineering Materials. https://doi.org/10.4028/www.scientific.net/KEM.350.143.

(36) Saito, Y.; Sakabe, Y. Development of CO2 Absorbent with Barium Orthotitanate Ceramics. *Fuel Cell* **2005**, *5* (2).

(37) Sheppard, D. A.; Paskevicius, M.; Javadian, P.; Davies, I. J.; Buckley, C. E. Methods for Accurate High-Temperature Sieverts-Type Hydrogen Measurements of Metal Hydrides. *J. Alloys Compd.* **2019**, *787*, 1225–1237. https://doi.org/10.1016/j.jallcom.2019.02.067.

(38) Suh, I.-K.; Ohta, H.; Waseda, Y. High-Temperature Thermal Expansion of Six Metallic Elements Measured by Dilatation Method and X-Ray Diffraction. *J. Mater. Sci.* **1988**, *23* (2), 757–760. https://doi.org/10.1007/BF01174717.

(39) Arvanitidis, I.; Siche, Du.; Seetharaman, S. A Study of the Thermal Decomposition of BaCO3. *Metall. Mater. Trans. B* **1996**, *27* (3), 409–416. https://doi.org/10.1007/BF02914905.

(40) Lima, E. C.; Gomes, A. A.; Tran, H. N. Comparison of the Nonlinear and Linear Forms of the van't Hoff Equation for Calculation of Adsorption Thermodynamic Parameters (ΔS° and ΔH°). *J. Mol. Liq.* **2020**, *311*, 113315. https://doi.org/10.1016/j.molliq.2020.113315.

(41) Hodgman, C. Handbook of Chemistry Andphysics. *Clevel. Ohio Chem. Rubber Co.* **1958**.

(42) Roine, A. HSC Chemistry® [Software], 2018. Software available at www.outotec.com/HSC.

(43) Humphries, T. D.; Møller, K. T.; Rickard, W. D. A.; Sofianos, M. V.; Liu, S.; Buckley, C. E.; Paskevicius, M. Dolomite: A Low Cost Thermochemical Energy Storage Material. *J Mater Chem A* **2019**, *7* (3), 1206–1215. https://doi.org/10.1039/C8TA07254J.

(44) Pires Vieira, A.; Williamson, K.; Humphries, T.; Paskevicius, M.; Buckley, C. A New Strontium Based Reactive Carbonate Composite for Thermochemical Energy Storage. *J. Mater. Chem. A* **2021**, *9*. https://doi.org/10.1039/D1TA04363C.

(45) Marusawa, H.; Saito, Y. CO2 Absorption Properties of Barium Orthotitanate under Continuous Operation. *Key Eng. Mater.* **2007**, *350*, 143–146. https://doi.org/10.4028/www.scientific.net/KEM.350.143.

(46) Møller, K. T.; Ibrahim, A.; Buckley, C. E.; Paskevicius, M. Inexpensive Thermochemical Energy Storage Utilising Additive Enhanced Limestone. *J. Mater. Chem. A* **2020**, *8* (19), 9646–9653. https://doi.org/10.1039/D0TA03080E.

(47) National Minerals Information Center. U.S. Geological Survey Mineral Commodity Summaries 2022 Data Release, 2022. https://doi.org/10.5066/P9KKMCP4.

CHAPTER 5

Thermochemical energy storage in $SrCO_3$ composites with $SrTiO_3$ or $SrZrO_3$

The work in this chapter has been submitted for publication.

K.Williamson, Y Liu, A.M D'Angelo, T.D. Humphries, M. Paskevicius, and C.E. Buckley, Thermochemical energy storage in $SrCO_3$ composites with $SrTiO_3$ or $SrZrO_3$ *[in press]*

Abstract

Thermochemical energy storage offers a cost-effective and efficient approach for storing thermal energy at high temperature (~ 1100 °C) for concentrated solar power and large-scale long duration energy storage. $SrCO_3$ is a potential candidate as a thermal energy storage material due to its high energy density of 205 kJ/mol of CO_2 during reversible CO_2 release and absorption. However, it loses cyclic capacity rapidly due to sintering. This study determined that the cyclic capacity of $SrCO_3$ was enhanced by the addition of either reactive $SrTiO_3$ or inert $SrZrO_3$. Thermogravimetric analysis over 15 CO_2 sorption cycles demonstrated that both materials retained ~80% of their maximum cyclic capacity on the milli gram scale. Repeated measurements using gram scale samples revealed a decrease in maximum capacity to 11% using $SrZrO_3$ additives over 50 cycles, while the use of $SrTiO_3$ additives allowed for the retention of 80% maximum capacity over 50 cycles. The improved performance of the titanate system can be attributed to the formation of a metastable intermediate, $Sr_3Ti_2O_7$, as confirmed by synchrotron powder X-ray diffraction. The material costs for the $SrTiO_3$-enhanced and $SrZrO_3$-enhanced $SrCO_3$ were estimated to be 17.70 and 9.90 US$/kWh, respectively. These findings highlight the potential of reactive additives in enhancing the performance of thermochemical energy storage systems, while providing valuable insights for the development of cost-effective materials.

5.1 Introduction

In the pursuit of a sustainable future, the global energy system is transforming to be largely based on renewable energy. Solar energy represents a major component of the renewable energy mix[1]. One of the most promising technologies to achieve the efficient use of solar energy is concentrated solar power (CSP) integrated with thermal energy storage (TES)[2]. During the hours of sunlight, the excess heat produced through the CSP systems is stored in the TES systems. At times of energy demand, the stored heat is released to generate electricity via a heat engine or steam turbine. In this way, a reduction of peak demand and continuous power supply is achieved[3].

There are three types of TES systems: sensible heat storage, latent heat storage, and thermochemical heat storage[3]. Sensible heat storage is based on the temperature change of a liquid or solid storage medium (e.g., water, sand, and molten salts) during heating or cooling. Sensible heat storage using molten salts is currently the only commercially available technology in CSP plants. However, the disadvantage of this technology is its low energy storage density (413 kJ/kg) and restricted operating temperature (290 – 565 °C)[3,4]. Latent heat storage is based on the absorption and release of heat from a storage material (e.g., miscibility gap alloy) when it undergoes a phase transition from solid to liquid, or liquid to gas[5,6]. Latent heat storage systems using phase change materials with high energy densities have the potential to achieve high efficiency as heat transfer takes place almost isothermally in the process. The development of latent heat storage systems for CSP plant is promising in lower temperature ranges, if the low thermal conductivity of most phase change materials can be overcome[6]. Thermochemical energy storage (TCES) is based on the storage and release of heat through reversible endothermic/exothermic reaction processes[7]. Among the three TES technologies, TCES is at an early stage of maturity for large-scale CSP applications. Nonetheless, there has been growing interests in investigating TCES as it has the advantages of higher energy density and higher operating temperatures over most sensible or latent heat storage systems[8] and is considered to be particularly suitable for medium and long-term storage[4,9].

In TCES systems that may be combined with CSP plants, solar heat is used to promote the endothermic battery charging step whereby a reactant A is dissociated into products B and C, as shown in Eq. 1. During the reverse discharging step, heat is released from the exothermic reaction between products B and C when they are mixed together[10].

$$\mathrm{A} + \Delta H_{\mathrm{r}} \rightleftharpoons \leftrightarrow \mathrm{B} + \mathrm{C} \qquad (5\text{-}1)$$

Where ΔH_{r} is the reaction enthalpy.

Extensive studies have been carried out on screening of potential TCES materials including metal hydrides[11–14], metal oxides[4], carbonates[15–19], hydroxides[6] and ammonia[3,4]. Among

these materials, alkaline earth metal carbonate-oxide systems (MCO_3/MO, with M = Ca, Sr, Ba) are especially attractive due to their abundance, low cost, and non-toxicity. Carbonate-oxide systems also present the advantageous features of high energy density and working temperatures[18–21]. Carbonate-oxide systems are based on the cyclic carbonation/calcination process. During the endothermic reaction (calcination), the carbonate (MCO_3) is decomposed into a metal oxide (MO) and CO_2 gas. The reverse exothermic reaction between MO and CO_2 is the carbonation process.

The $CaCO_3$/CaO system has been heavily investigated for both energy storage[16,17,19,22] and carbon capture applications[23,24]. The $SrCO_3$/SrO system recently gained attention due to its high decomposition temperature (ΔG = 0 kJ/mol at 1175 °C), allowing an increased operating temperature (~ 1200°C) than the $CaCO_3$/CaO system (900°C)[10]. Its high operating temperature also matches the combined Brayton-Rankine cycle, which may be key to increasing overall energy efficiency of the power plants[4,18,25,26]. Moreover, $SrCO_3$ has a high volumetric energy density ($4\ \mathrm{GJ\ m}^{-3}_{SrCO_3}$), which leads to a reduction in feedstock and therefore a cost decrease in the storage vessel[4]. Despite these favourable features, this system also faces the thermal sintering problems at high temperature that the $CaCO_3$/CaO system has also suffered from[27,28]. The sintering and agglomeration of particles at high temperatures causes morphological changes in the material, hindering the absorption of CO_2 by SrO for a further carbonation reaction. As a result, the sorption capacity decreases with increasing cycle number. Adding sintering-resistant inert additives such as $SrSiO_3$[18], Al_2O_3[29], MgO[30], ZrO_2[20] have proven to be an effective approach to improve the cyclic stability of the $SrCO_3$/SrO system.

There is one previous study on SrO supported by $SrZrO_3$ for thermochemical energy storage[26]. Rhodes *et al.* used a mass ratio of 2:3 of SrO/$SrZrO_3$ and cycled between carbonation (1150 °C, $p(CO_2)$ = 1 bar) and calcination (1235 °C, $p(CO_2)$ = 0.1 bar) using thermogravimetric analysis (TGA), however the sample only stabilised at 24% of the maximum theoretical CO_2 capacity[26].

In this study, we introduce alternative $SrCO_3$/SrO systems supported by either $SrTiO_3$ or $SrZrO_3$, which retain high capacity and cyclic stability at high temperature. The energy storage performance of the proposed system was experimentally assessed at 1100 °C using thermogravimeter analyser (TGA) as well as a custom-made Sieverts apparatus[31]. The effect of varying ratios of $SrZrO_3$ additives on the CO_2 absorption capacity of SrO was also investigated.

5.2 Experimental

5.2.1 Synthesis of $SrTiO_3$ and $SrZrO_3$

$SrTiO_3$ and $SrZrO_3$ were prepared through solid state reaction between $SrCO_3$ (Sigma-Aldrich, > 99%) and TiO_2 (GPR RECTAPUR, ≥ 99%) or $SrCO_3$ and ZrO_2 (Aldrich, > 99%). A mixture of $SrCO_3$ and TiO_2 or ZrO_2 in stoichiometric amounts according to Eq. 2 and Eq. 3 were mixed by ball milling for 2 hours (six bidirectional 20 minute segments with 1 minute breaks) in a planetary type mill (PQ-N04) employing stainless steel (316) milling vials (80 mL) and balls (8 mm in diameter) with a ball to powder mass ratio of 10:1. The powder mixture was then placed in an Al_2O_3 boat in a (Thermo-FB1310M) furnace and subjected to calcination in an air atmosphere by heating to 1100 °C ($\Delta T/\Delta t$ = 10 °C/min) then held isothermally for 3 h to obtain $SrTiO_3$ and $SrZrO_3$.

$$\mathrm{SrCO_{3(s)} + TiO_{2(s)} \rightarrow SrTiO_{3(s)} + CO_{2(g)}} \quad \text{(5-2)}$$

$\mathrm{SrCO_{3(s)} + ZrO_{2(s)} \rightarrow SrZrO_{3(s)} + CO_{2(g)}}$	(5-3)

5.2.2 Preparation of SrCO3–SrTiO3 and SrCO3-SrZrO3 samples

The $SrCO_3$–$SrTiO_3$ and $SrCO_3$-$SrZrO_3$ composites were prepared by ball milling $SrCO_3$ with synthesised $SrTiO_3$ or $SrZrO_3$ for 1 hour (three bidirectional 20-minute segments with 1-minute breaks) using the aforementioned parameters. Composites with various molar

ratios of $SrCO_3$ and $SrZrO_3$, e.g. $SrCO_3$-0.5M $SrZrO_3$ correspond to a sample with a $SrCO_3$ and $SrZrO_3$ molar ratio of 1:0.5 respectively (See Table 5-1).

Table 5-1. Details of prepared samples.

Samples	$SrCO_3$:$SrTiO_3$/$SrZrO_3$ molar ratio	Theoretical CO_2 wt%
$SrCO_3$	1	29.81
$SrCO_3$ - 1M $SrTiO_3$	1: 1	13.29
$SrCO_3$ - 1M $SrZrO_3$	1: 1	11.75
$SrCO_3$ - 0.5M $SrZrO_3$	1: 0.5	16.85
$SrCO_3$ - 0.25M $SrZrO_3$	1: 0.25	21.53
$SrCO_3$ - 0.125M $SrZrO_3$	1: 0.125	25.00

5.2.3 Thermogravimetric analysis (TGA)

Thermogravimetric analysis (TGA) was performed on a Netzsch STA 449 F3 Jupiter instrument. The samples (15 – 20 mg) were measured inside Al_2O_3 crucibles with pierced lids and were heated from room temperature to 1200 °C ($\Delta T/\Delta t$ = 10 °C/min) under a flowing argon (Coregas, 99.995%, 20 mL·min^{-1}) atmosphere (20 mL/min). The temperature was calibrated using In, Zn, Al, Ag and Au reference materials, resulting in a temperature accuracy of ± 0.2 °C, while the balance has an accuracy of ± 20 µg.

5.2.4 CO_2 cyclic capacity measurements

An initial assessment of the carbonation/calcination cyclic capacity was performed by TGA (Netzsch STA 449) with calibration details as listed above. Approximately 18 mg of sample was placed into an Al_2O_3 crucible with a pierced lid and heated at $\Delta T/\Delta t$ = 10 °C/min in a flowing mixture of CO_2 (Coregas, 99.995%, 80 mL/min, $p(CO_2) \sim 0.8$ bar) and protective Ar gas (Coregas, 99.995%, 20 mL/min, p(Ar) ~ 0.2 bar) mixture up to 1100 °C. The sample was then held isothermal for 30 minutes before undergoing consecutive calcination and carbonation steps of 30 min at the same temperature. CO_2 flow (80 mL/min, $p(CO_2)$ = 0.8 bar) was employed during carbonation and Ar (20 mL/min) was used for calcination, for a total of 15 cyclic steps.

The cyclic CO_2 absorption/desorption performance of selected samples were further assessed utilising a custom-made Sieverts-type instrument for CO_2 measurements. Details of the instrument and the measurement method can be found in previous studies[15,19,31]. The volumes used were 46.2 cm^3 for the sample side volume, 23.4 cm^3 for the non-ambient volume, and 20.4 cm^3 for the reference volume. Pressure was measured using a Rosemount 3051S pressure transducer (±35 mbar, range 0 to 140 bar) and temperatures were recorded using a B-type thermocouple (+- 5°C). An equation of state for CO_2 was used in molar calculations from the NIST Refprop database[32]. Samples (0.6 - 0.8 g) were loaded into a SiC reactor and heated to 1100 °C ($\Delta T/\Delta t$ = 10 °C/min) by a vertical tube furnace (LABEC VTHTF40/15) under a CO_2 backpressure $p(CO_2) \sim 5$ bar. Samples were held isothermally for 1 hour before conducting the first CO_2 desorption step. Desorption was carried out under dynamic vacuum $p(CO_2) \sim 10^{-2}$ bar for 1 hour followed by an absorption step under $p(CO_2) \sim 5$ bar for 1 hour. These measurements were repeated for ~ 50 absorption-desorption cycles.

5.2.5 Sample characterization

Ex-situ Powder X-ray diffraction (XRD) characterisation was performed using a Bruker D8 Advance diffractometer equipped with a copper X-ray source Cu $K_{\alpha1}$ radiation, λ = 1.540593 Å, Cu $K_{\alpha2}$ radiation, λ = 1.544414 Å and a Lynxeye PSD detector in Bragg-

Brentano geometry. Data were collected in the 2θ range from 10° to 80° with a step size of 0.02°. The collected XRD patterns were analysed using Bruker EVA and Bruker TOPAS V.5 software[33].

In-situ synchrotron radiation SR-XRD measurements were conducted at the Powder Diffraction beamline of the Australian Synchrotron, Melbourne, Australia[34]. Data were acquired using a Mythen-II microstrip detector at λ = 0.82504 (1825040() Å. Samples were combined with ethanol and smeared onto a prestressed Pt strip within an Anton Paar HTK 2000 strip furnace, a B-type thermocouple (± 0.5 %) was attached to the sample., The gas pressure was controlled via a manifold to provide vacuum or 1.5 bar CO_2. The sample was heated from room temperature to 800°C at $\Delta T/\Delta t$ = 10°C/min then from 800°C to 1100 °C at $\Delta T/\Delta t$ = 10 at $\Delta T/\Delta t$ = 10 - 15 °C/min.

The morphological and microstructural structure of samples were characterised using scanning electron microscopy (SEM). The SEM and Energy dispersive X-ray spectroscopy (EDS) data were collected using a Tescan Clara equipped with a secondary electron (SE) detector and an accelerating voltage of 15 kV. Prior to the microscopy analysis, the powder samples were sprinkled onto carbon tape attached to an aluminium stub and were coated with a 20 nm thick layer of conductive carbon.

5.3 Results and discussion

The successful synthesis of $SrTiO_3$ and $SrZrO_3$ without any detectable side reactions was confirmed using X-ray diffraction (XRD) (see Figure 5-1A & Figure 5-2A respectively). Furthermore, XRD analysis of the milled samples $SrCO_3$ - 1M $SrTiO_3$ and $SrCO_3$ - 1M $SrZrO_3$, demonstrates the absence of any additional unwanted materials generated during the milling process (Figure 5-1B & Figure 5-2B).

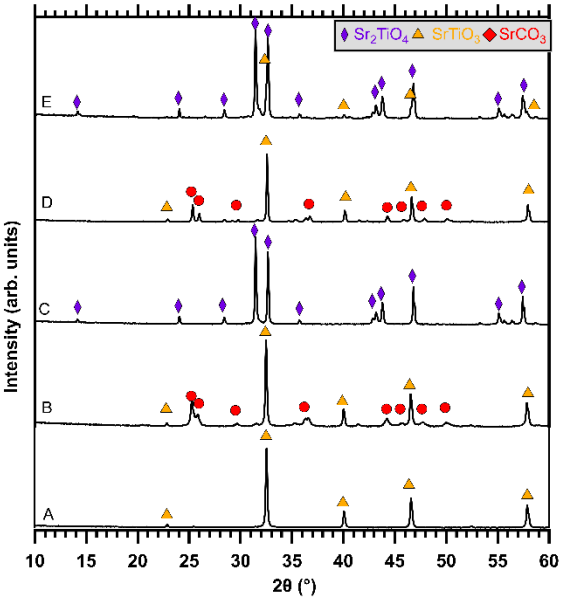

Figure 5-1: XRD data (λ = 1.54056 Å) of (A) synthesised $SrTiO_3$; (B) Ball-milled $SrCO_3$ - 1M $SrTiO_3$; (C) $SrCO_3$ - 1M $SrTiO_3$ after TGA heating to 1200 °C ($\Delta T/\Delta t$ = 10 °C/min); (D) after 15 CO_2 sorption cycles using TGA at T = 1100 °C for $SrCO_3$ - 1M $SrTiO_3$, removed after final absorption step; and (E) $SrCO_3$ - 1M $SrTiO_3$ after Sieverts apparatus measurements for 55 sorption cycles at T = 1100 °C, removed after the final desorption step.

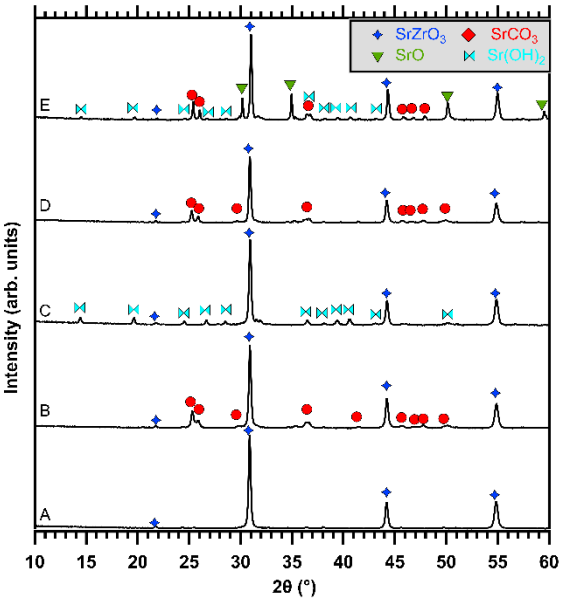

Figure 5-2: XRD data (λ = 1.54056 Å) of (A) synthesised $SrZrO_3$; (B) Ball-milled $SrCO_3$ - 1M $SrZrO_3$; (C) $SrCO_3$ - 1M $SrZrO_3$ after TGA heating to 1200 °C ($\Delta T/\Delta t$ = 10 °C/min); (D) after 15 CO_2 sorption cycles using TGA at T = 1100 °C for $SrCO_3$ - 1M $SrZrO_3$, removed after the final absorption step; and (E) $SrCO_3$ - 1M $SrZrO_3$ after Sieverts apparatus measurements for 52 cycles at T = 1100 °C, removed after the final desorption step.

5.3.1 Thermal behaviour of $SrCO_3$ with $SrTiO_3$ or $SrZrO_3$

From TGA studies (Figure 5-3), the onset of mass loss (CO_2 release) of both $SrCO_3$ - 1M $SrTiO_3$ and $SrCO_3$ – 1M $SrZrO_3$ were detected at a similar temperature compared to pure $SrCO_3$, ~ 900 °C. This suggests that the addition of $SrTiO_3$ or $SrZrO_3$ does not significantly thermodynamically destabilise the CO_2 release from $SrCO_3$ as additives have in other studies[15,16,18]. A final weight loss of 14.9% and 12.9% were observed for $SrCO_3$ – 1M $SrTiO_3$ and $SrCO_3$ - 1M $SrZrO_3$ respectively, which are above the theoretical values of 13.29 wt% and 11.75 wt%. This suggests the initial wt% loss in the region < 100 °C could be due to an impurity (such as moisture) contained in the composite samples.

After thermal treatment, $SrCO_3$ – 1M $SrTiO_3$ was removed from the TGA and subjected to XRD analysis, where Sr_2TiO_4 was observed (Figure 5-1C). This indicates that $SrTiO_3$ reacts with $SrCO_3$ to form Sr_2TiO_4 as per Eq. (5-4).

$$SrCO_{3(s)} + SrTiO_{3(s)} \rightarrow Sr_2TiO_{4(s)} + CO_{2(g)} \quad (5\text{-}4)$$

On the other hand, XRD of $SrCO_3$ – 1M $SrZrO_3$ reveals the presence of two compounds, $SrZrO_3$ and $Sr(OH)_2$(Figure 5-2c) (SrO is known to absorb moisture from the air to form $Sr(OH)_2$)[35]. This suggests that $SrZrO_3$ did not participate as a reactant during CO_2 release and the calcination of $SrCO_3$ occurred via Eq. 5.

$$SrCO_{3(s)} \overset{SrZrO_3}{\leftrightarrows} SrO_{(s)} + CO_{2(g)} \quad (5\text{-}5)$$

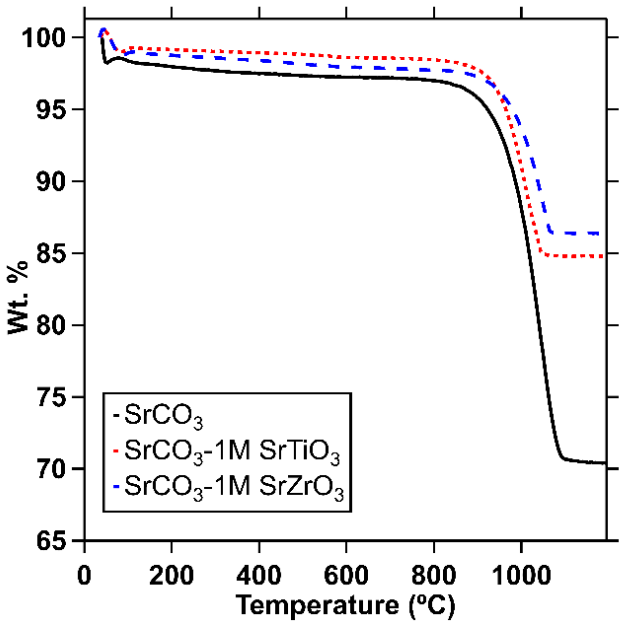

Figure 5-3: TGA data comparing the ball-milled (1 h) $SrCO_3$, $SrCO_3$ – 1M $SrTiO_3$ and $SrCO_3$ – 1M $SrZrO_3$. Measurement conditions: $\Delta T/\Delta t$ = 10 °C/min, argon flow of 20 mL/min.

5.3.2 Cyclic stability and calcination/carbonation of the $SrCO_3$ – 1M $SrTiO_3$ system

The cyclic CO_2 storage stability of two samples, $SrCO_3$ – 1M $SrTiO_3$ and $SrCO_3$ were evaluated using TGA (Figure 5-4). Both samples were heated ($\Delta T/\Delta t$ = 10 °C) up to 1100 °C under a CO_2 atmosphere. They then underwent intermittent calcination and carbonation steps, each lasting for 30 minutes.

For $SrCO_3$, the initial calcination step resulted in slow CO_2 desorption, accounting for 7.4 wt% compared to the theoretical maximum of 29.8 wt%. Sluggish calcination and carbonation reactions are also observed for $SrCO_3$/SrO after the first cycle, which are indicated by the sloping curves that do not reach completion in the allocated time (30 min). Subsequent sorption cycles decreased in overall CO_2 capacity, stabilising at 3.2 wt% for each absorption step and 3.5 wt% for each desorption step, indicating that CO_2 absorption was slower than desorption, but both were unsatisfactory on this timescale.

In contrast, the $SrCO_3$ – 1M $SrTiO_3$ composite exhibited an initial CO_2 desorption capacity at the maximum theoretical value of 13.3 wt%. Subsequent CO_2 absorption cycles showed a rapid reabsorption of the desorbed CO_2, and over 15 cycles, a slight weight gain of approximately 1 wt% was observed. This slight increase in weight suggests the presence of a minor amount of SrO in the initial composite (possibly from trace hydroxide decomposed from the starting material during the initial thermal treatment), which subsequently converts to $SrCO_3$. The cyclic CO_2 capacity stabilises at 11.5 wt% (85% of the theoretical maximum).

After the final CO_2 absorption cycle, the sample was cooled and XRD was performed, where $SrTiO_3$ and $SrCO_3$ were observed ((5-1). This demonstrates that the sample reforms $SrCO_3$ and $SrTiO_3$ after multiple CO_2 cycles and thus Eqn. (5-4) is reversible. The incorporation of $SrTiO_3$ into $SrCO_3$ resulted in a significant enhancement in the cyclic capacity and stability of the composite compared to pristine $SrCO_3$.

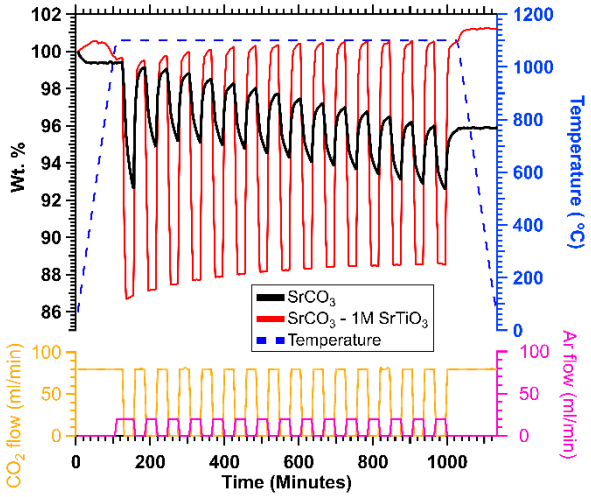

Figure 5-4:TGA cycling measurements of $SrCO_3$ and $SrCO_3$ - 1M $SrTiO_3$ over 15 CO_2 desorption and absorption cycles at 1100 °C.

The cyclic stability of $SrCO_3$ - 1M $SrTiO_3$ was further assessed using CO_2 absorption measurements conducted with a Sieverts type apparatus (Figure 5-5). This employed a

larger sample size of 0.81 g (compared to mg-scale in the TGA) and higher CO_2 absorption pressures ($p(CO_2)$ ~ 5 bar) along with longer sorption times (1 hour absorption and 1 hour desorption steps), aiming to better represent the thermodynamic and cyclic stability/energy capacity under conditions relevant to potential industrial operations[4].

The $SrCO_3$ - 1M $SrTiO_3$ composite consistently maintains a stable CO_2 capacity at approximately 85% of the theoretical maximum throughout 55 cycles, which aligns well with the TGA results on a smaller scale (see Fig. 4). A slight decline in capacity (~ 2% of the theoretical maximum) is observed over the 55 cycles, which can be attributed to morphological changes that will be discussed in detail below. The absorption kinetics of the 1st, 15th and 30th cycle was compared (Figure S-21) revealing little degradation between cycles and a slight improvement after the first cycle.

After the final CO_2 desorption cycle, XRD analysis was conducted to confirm the reaction products, namely Sr_2TiO_4 and a minor trace of $SrTiO_3$ (Figure 5-1E), which confirms the validity of Eqn. 4. These findings highlight the excellent CO_2 cyclic capacity and stability exhibited by $SrCO_3$ - 1M $SrTiO_3$ on a larger scale with elevated CO_2 pressures.

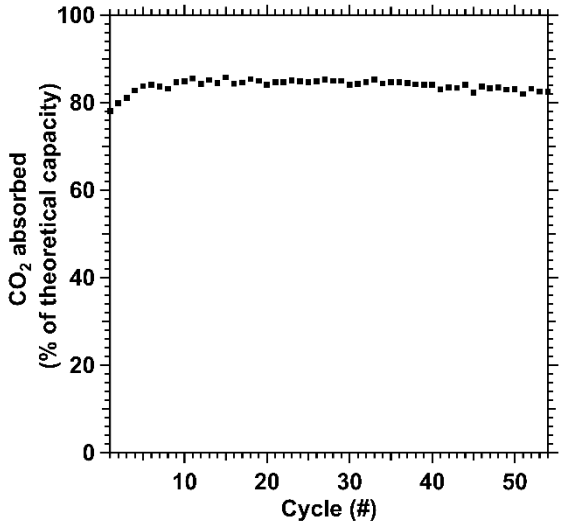

Figure 5-5: CO_2 storage capacity of $SrCO_3$ – 1M $SrTiO_3$ over 55 cycles. Measurements were carried out using Sieverts method at 1100 °C, mass = 0.81 g, abs/desorption $p(CO_2)$ = (5 bar/0 bar), t = (1 hour/1 hour).

In-situ SR-XRD data was collected on ~ 0.2 g of $SrCO_3$ - 1M $SrTiO_3$ heated to 1100 °C under a CO_2 atmosphere ($p(CO_2)$ = 1.5 bar) (Figure 5-6). At 931 °C, $SrCO_3$ undergoes a polymorphic phase transition from (orthorhombic) α to (hexagonal) β phase, as expected to occur in the temperature range of 925 - 933 °C[36]. The sample reached 1100 °C without showing evidence of decomposition, this is expected due to the partial pressure of CO_2 being above the expected equilibrium partial pressure ($p(CO_2$ = 0.62 bar). The CO_2 release reaction was initiated by the application of vacuum ($p(CO_2)$ ~ 0 bar) at 1100 °C, where the reaction of β-$SrCO_3$ and $SrTiO_3$ to form Sr_2TiO_4 was observed. The results support the *ex-situ* XRD data revealing Sr_2TiO_4 is the final solid product from the decomposition of the $SrCO_3$ - 1M $SrTiO_3$ composite. On re-application of CO_2 pressure ($p(CO_2)$ = 1.5 bar) the Bragg peaks of Sr_2TiO_4 disappear completely and β-$SrCO_3$ and $SrTiO_3$ reform.

Additionally, it is interesting to note that a minor amount of a metastable $Sr_3Ti_2O_7$ intermediate is formed during the calcination. The reason that $Sr_3Ti_2O_7$ is not observed from *ex-situ* XRD data could be due to its lower thermal stability than Sr_2TiO_4[37]. As such, the formed $Sr_3Ti_2O_7$ intermediate may revert to Sr_2TiO_4 on cooling. The formation of a $Sr_3Ti_2O_7$ intermediate could contribute greatly to the superior long-term CO_2 cyclic stability of $SrCO_3$-$SrTiO_3$ systems because it may act as a grain-growth inhibitor to prevent sintering.

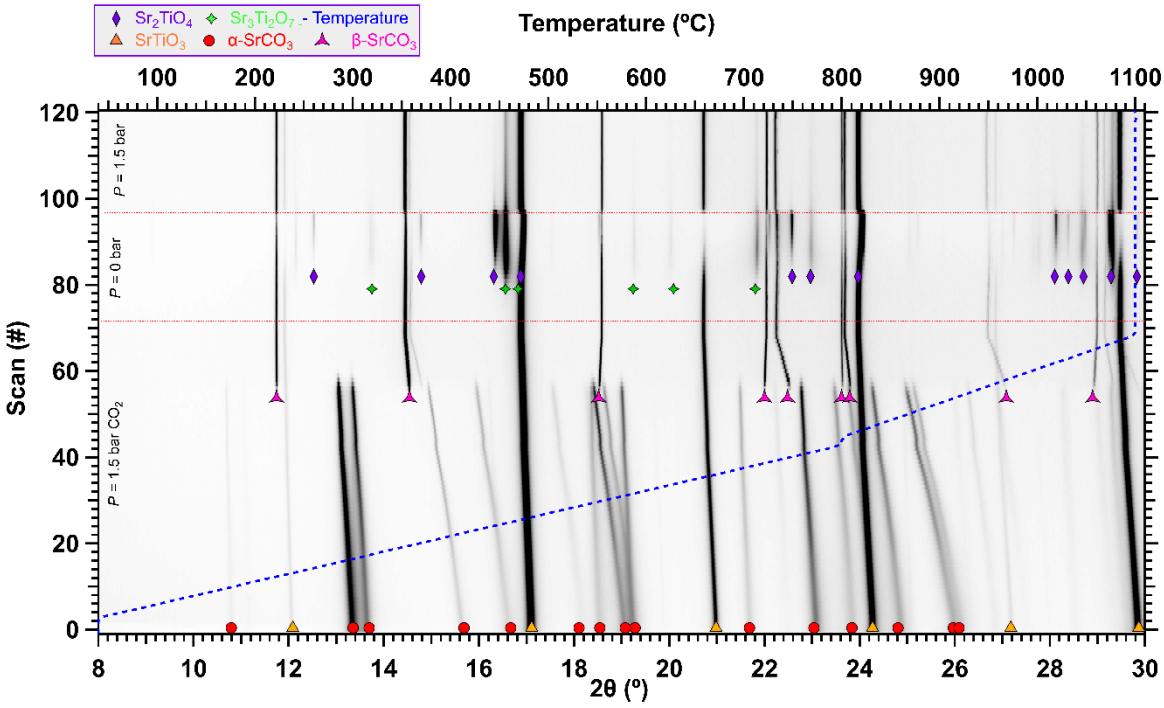

Figure 5-6: *In-situ* SR-XRD data of $SrCO_3$ – 1M $SrTiO_3$ heated from room temperature to 1100 °C ($\Delta T/\Delta t$ = 10 — 15 °C/min; λ = 0.8250 (182504(5) Å, $p(CO_2)$ = 0 or 1.5 bar). The blue dashed line represents the temperature profile.

To investigate the morphological changes occurring during cyclic CO_2 absorption and desorption at high temperature, both milled and cycled samples of $SrCO_3$ - 1M $SrTiO_3$ were analysed using SEM-EDS (Figure 5-7). The milled sample consists of small particles (~ 100 nm) and exhibits an even distribution of Ti and Sr distributed homogenously throughout the composite, indicating a well-mixed sample (Figure 5-7a).

Both the TGA cycled (Figure 5-7b) and Sieverts cycled (Figure 5-7c) samples exhibit larger particles (~ 1 µm) that appear sintered together. The sintering process leads to a reduction in the surface area and porosity of the sample, which is expected given the high operating temperature during cycling. Consequently, the diffusion of CO_2 into the sample may slow down with each additional cycle if particle growth becomes excessive. However, there is evidence of channels within larger agglomerates, which could facilitate CO_2 flow, aligning

with the observed high reactivity towards CO_2. Furthermore, the distribution of Ti and Sr remains uniform in both cycled samples throughout, indicating no obvious phase segregation that could limit reactivity. Under the test conditions in this study, the $SrCO_3$ - 1M $SrTiO_3$ composite maintains a stable cycling capacity of ~ 80% in both TGA and Sieverts experiments (see Figure 5-4 and Figure 5-5) despite the observed grain growth and sintering. This could be attributed to the previously mentioned formation of the intermediate $Sr_3Ti_2O_7$ (see Figure 5-6) and the lack of particles or agglomerates larger than micron-scale.

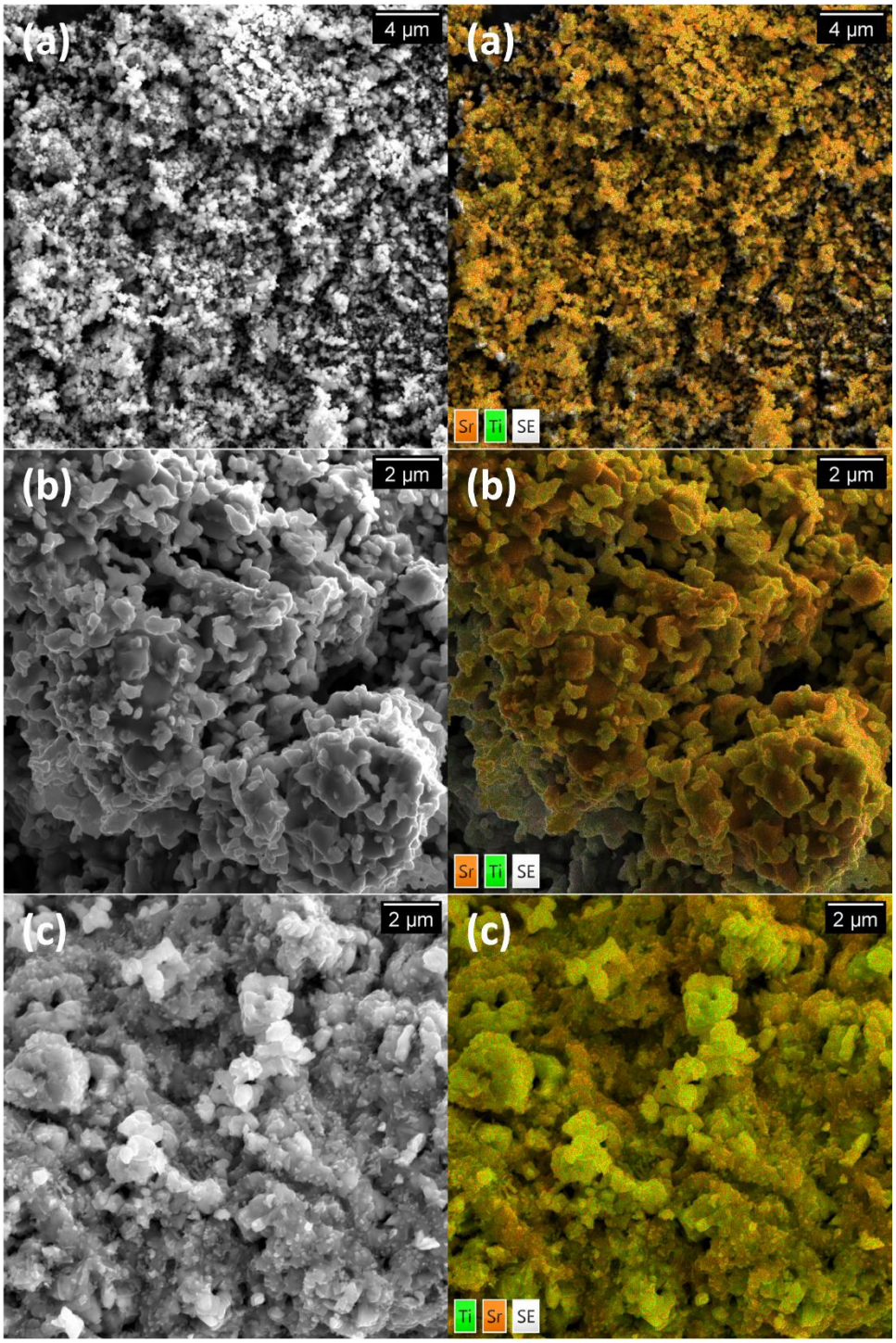

Figure 5-7: SEM (left) and EDS (right) mapping of $SrCO_3$ - 1M $SrTiO_3$ in SE mode, 15 kV: (a) Ball-milled; (b) after 15 cycles at 1100 °C, TGA, removed after CO_2 absorption; and (c) after 55 cycles at 1100 °C, Sieverts apparatus, removed after CO_2 desorption. Colour code: Sr (Orange); Ti (green).

5.3.3 Cyclic stability and calcination/carbonation of the $SrCO_3$–$SrZrO_3$ system

TGA was utilised to compare the mass change profiles between $SrCO_3$ and the $SrCO_3$ - 1M $SrZrO_3$ system during 15 CO_2 sorption cycles (see Figure 5-8a). The $SrCO_3$ - 1M $SrZrO_3$ composite demonstrates exceptional stability in its CO_2 cycling capacity over 15 cycles. Furthermore, the inclusion of $SrZrO_3$ significantly enhances the CO_2 absorption kinetics, as indicated by the steep curves during the carbonation step. In each cycle, the carbonation process occurs rapidly and reaches its maximum theoretical value (11.8 wt%). In contrast, $SrCO_3$ exhibits sluggish kinetics and a diminished cyclic capacity, as discussed earlier (see section 5.2.4). After the final CO_2 absorption cycle, the sample was cooled and XRD was performed, where $SrZrO_3$ and $SrCO_3$ were observed as expected ((5-1).

It was found in section 5.3.1 that the $SrZrO_3$ additive does not participate in a thermochemical reaction with $SrCO_3$ but acts as an inert additive and possible sintering inhibitor. It is beneficial to optimise the content of an inert additive to achieve high energy density and low cost without sacrificing cyclic stability. The effect of the $SrZrO_3$ additive content on the multicycle performance of $SrCO_3$ was further studied using TGA. Figure 5-8b shows the weight change of $SrCO_3$ with various additive content of $SrZrO_3$ during 15 CO_2 desorption and absorption cycles at 1100 °C. The samples with 1M and 0.5M $SrZrO_3$ loading maintain stable capacity throughout the 15 cycles. Whilst the capacity drops gradually after 10 and 5 cycles for the samples with 0.25M and 0.125M loading of $SrZrO_3$, respectively. The carbonation rate also decreases with increasing number of cycles in these samples, this is particularly obvious for the $SrCO_3$-0.125M $SrZrO_3$ sample. Comparing similar samples with differing $SrZrO_3$ content demonstrates that cycling stability decreases as the $SrCO_3$ content exceeds at least 62% by mass (with 0.25M $SrZrO_3$ loading). A low ratio of $SrZrO_3$ loading is unable to maintain high CO_2 cyclic capacity.

It is important to note that the TGA results herein demonstrate a much higher CO_2 capacity than those of Rhodes *et al*[26]. One possible reason is the selected temperature of 1235 °C for carbonation in the previous study is too high for SrO to absorb CO_2, where according

to thermodynamics the equilibrium pressure of the carbonation of SrO is expected to be 1.25 bar, which is higher than the applied pressure of their measurements (0.9 bar)[26,38].

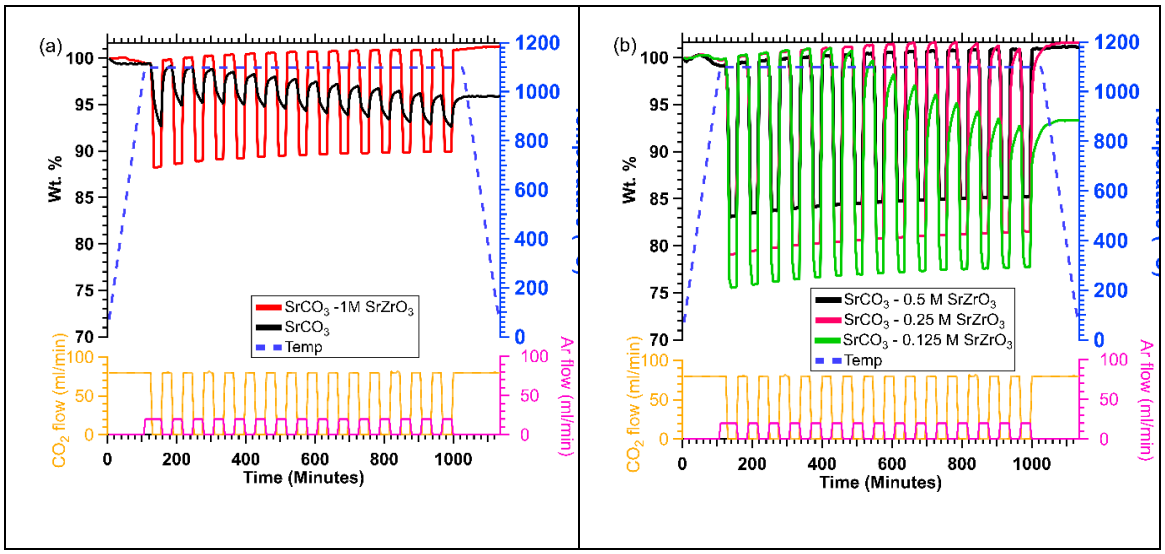

Figure 5-8: TGA measured mass change of (a) $SrCO_3$ – black; $SrCO_3$ – 1M $SrZrO_3$-blue. (b) $SrCO_3$ – 0.5M $SrZrO_3$ - purple; $SrCO_3$ – 0.25M $SrZrO_3$ - teal; $SrCO_3$ – 0.125M $SrZrO_3$ – green, 15 CO_2 desorption and absorption cycles at 1100 °C.

Given that $SrCO_3$-0.5M $SrZrO_3$ (44 wt% $SrZrO_3$) demonstrated excellent cycling stability over 15 cycles in TGA analysis, while maintaining a higher energy density compared to $SrCO_3$-1M $SrZrO_3$ (60 wt% $SrZrO_3$), it was selected for further investigation using the Sieverts apparatus to evaluate its extended capacity. Figure 5-9 shows the CO_2 absorption capacity of $SrCO_3$-0.5M $SrZrO_3$ over 53 cycles.

Interestingly, unlike the results obtained from TGA measurements, the CO_2 absorption capacity declines from 86% during the first cycle to 11% after 53 cycles. The Sieverts measurement provides a more realistic analysis than TGA, as it employs a larger sample size of 0.8 g compared to the small amount (15 - 20 mg) used in TGA measurements. This highlights the inefficiency of testing TCES materials using only TGA as factors such as heat transfer and bulk morphological properties may influence the cyclic capacity[10]. For instance, poor thermal conductivity could result in thermal spikes during CO_2 absorption that could lead to further sintering and degradation of the material.

The observed decrease in capacity implies that the 0.5M $SrZrO_3$ ratio may not be sufficient to overcome the decline in multicycle activity resulted from sintering. Specifically, there is a significant drop from 58% to 41% in CO_2 capacity after 16 cycles, which could be attributed to the rapid growth of particles caused by thermal annealing, leading to a significant reduction in porosity. The absorption kinetics of the 1st, 15th and 30th cycle was compared which show a sudden kinetic barrier hindering absorption on each cycle (Figure S-22).

The sample was removed in the desorbed state after cycling and subjected to XRD where SrO, $SrCO_3$, and $SrZrO_3$ were all observed suggesting the partial carbonation of SrO has occurred (see Figure 5-2E). Additionally, a phase corresponding to $Sr(OH)_2$ was observed in Figure 5-2E just as in Figure 5-2C (SrO absorbs moisture from the air to form $Sr(OH)_2$)[35].

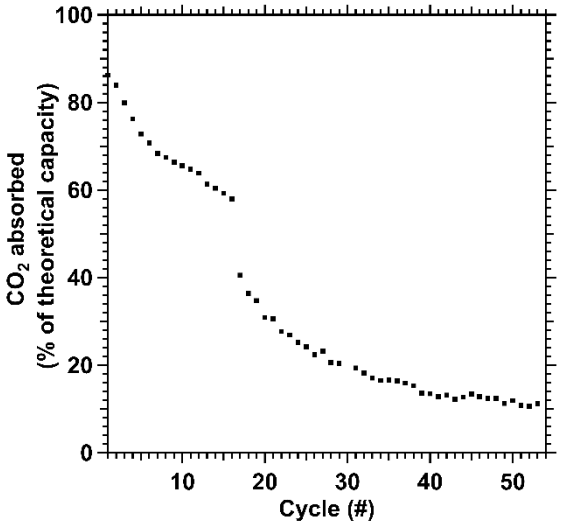

Figure 5-9: CO_2 storage capacity of $SrCO_3$ – 0.5M $SrZrO_3$ over 53 cycles. Measurements were carried out using Sieverts method at 1100 °C, mass = 0.63 g, abs/desorption p(CO_2) = (5 bar/0 bar), t = (1 hour/1 hour).

The particle morphology of the as-milled and CO_2 cycled $SrCO_3$ - 0.5M $SrZrO_3$ samples is shown in Figure 5-10. The milled composite consists of finely mixed small particles < 1 µm (Figure 5-10a) and Sr and Zr are homogeneously dispersed throughout the sample. After the sample is subjected to 15 cycles in the TGA at 1100 ° C (Figure 5-10b), Sr is

concentrated in areas in which the SEM image shows a flat plate-like agglomerate. The large (10's μm) agglomerate results from the substantial sintering of aggregated $SrCO_3$/SrO particles. On the other hand, some Zr is spread away from the $SrCO_3$/SrO clusters, showing some phase segregation. Cycling in Sieverts apparatus causes the $SrCO_3$/SrO to show more substantial sintering (100's μm) while $SrZrO_3$ regions appear separate with some particles possibly trapped in the agglomerated $SrCO_3$ (Figure 5-10c).

It is clear that $SrCO_3$ - 0.5M $SrZrO_3$ has a radically different morphology to $SrCO_3$-1M $SrTiO_3$, which may result in the different cycling performance observed between these two composite systems. Large SrO particles may hinder CO_2 uptake and could limit the cyclic capacity of the $SrCO_3$ - 0.5M $SrZrO_3$ system in TGA and/or Sieverts studies. The large cyclic capacity drop observed in Sieverts measurements indicates that particles larger than 10's of micron in size could be the limit for satisfactory kinetics. In the case of large particles, only part of the SrO reacts with CO_2 to form $SrCO_3$ on the external surface of unreacted SrO[26,39,40]. The $SrCO_3$ external shell formed could in-turn block access of CO_2 to the inner SrO particles. An additional factor affecting the disparity in the cyclic performance could be caused by the differences in thermal conductivity of the additives. $SrTiO_3$ has a higher thermal conductivity of ~ 6 - 12 W/m·K at 1100 °C compared to ~2.3 W/m·K for $SrZrO_3$ at 1100 °C[41,42]. The effect of this sintering may scale with sample size (due to heat dissipation) and may not be as apparent in TGA samples where heat flow and sintering do not play such a large role.

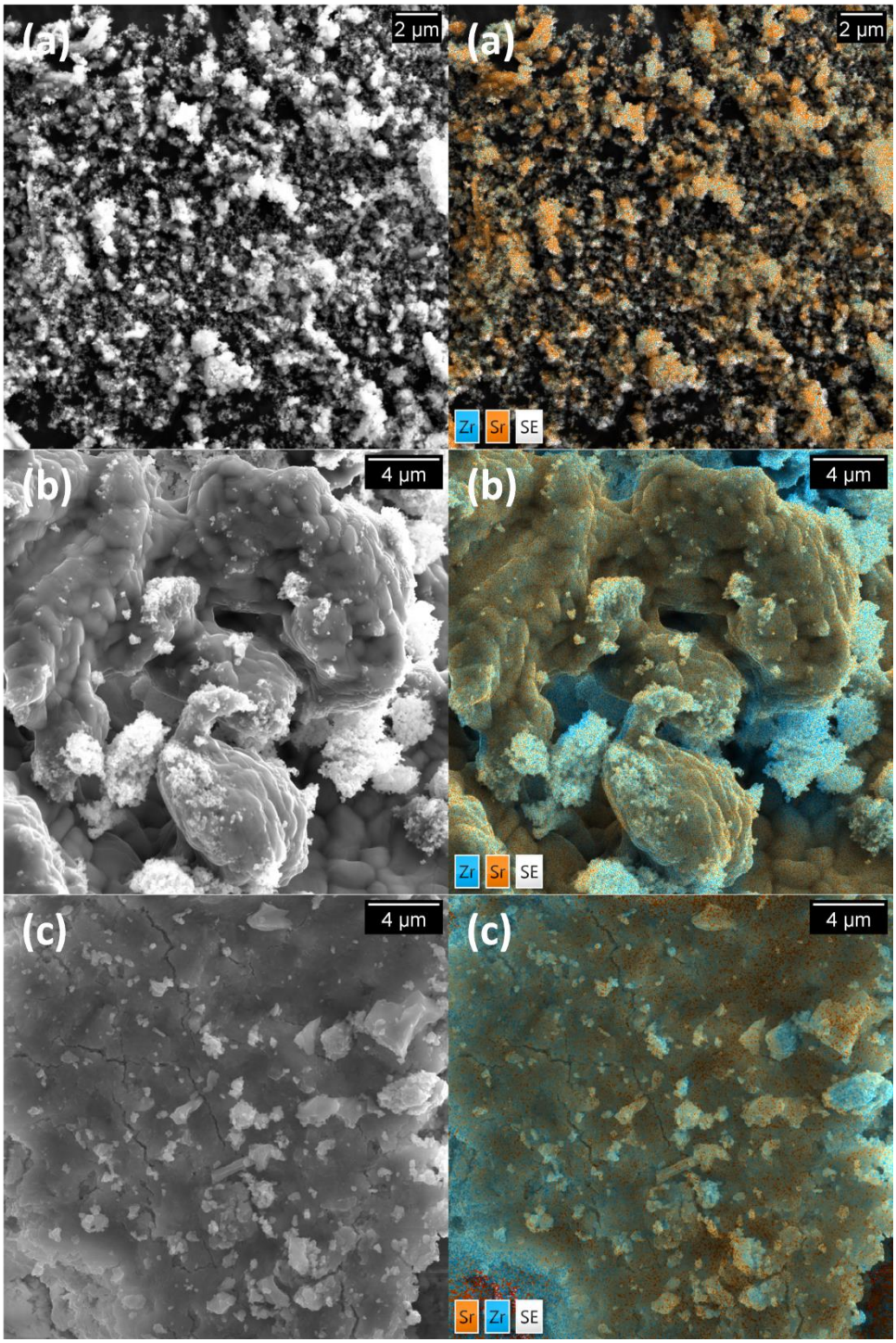

Figure 5-10: SEM (left) and EDS (right) mapping of $SrCO_3$ - 0.5M $SrZrO_3$ at 15 kV: (a) as ball-milled; (b) after 15 cycles at 1100 °C, TGA, removed after CO_2 absorption; (c) after 52 cycles at 1100 °C in the Sieverts apparatus, removed after CO_2 desorption. Colour code: Sr (Orange); Zr (blue).

5.4 Cost analysis

A material cost comparison used in previous studies has been extended to include the composites SrCO3 - 1M $SrTiO_3$ and $SrCO_3$ - 0.5M $SrZrO_3$ (Table 5-2)[15,16,18]. Although the strontium zirconate and titanate additives are competitive from a US$/kWh perspective (9.94 and 17.73 US$/kWh respectively) they are outperformed by the strontium silicate additive (8.13 US$/kWh). They do however have higher volumetric and gravimetric densities and produce more energy per mole of CO2 so will require less CO2 gas storage volume. The zirconate additive has the edge in every category over the titanate additive due to its higher percentage of SrCO3, but unless a method to mitigate the cyclic capacity loss of this material is implemented the titanate will perform better over multiple cycles. This cost analysis is reliable only on a pure material-based comparison, and therefore, additional costs and a complete techno-economic assessment is recommended in future studies[4].

Table 5-2: Comparison of thermochemical properties, system variables, and cost parameters for select energy storage materials to store 1 TJ of electrical energy[16,18,43].

	$SrCO_3 + SrTiO_3 \rightleftharpoons Sr_2TiO_4 + CO_2$ [a]	**$SrCO_3$+0.5$SrZrO_3$ $\rightleftharpoons$ 0.5 $SrZrO_3$+SrO + CO_2** [a]	**$SrCO_3$+$SrSiO_3 \rightleftharpoons Sr_2SiO_4 + CO_2$** [b]	**Molten salt (40$NaNO_3$:60KNO_3)**
Enthalpy Δ*H* (kJ mol^{-1} of CO_2)	176	206	155.7	-
Molar Mass (g mol^{-1}) (CO_2 loaded)	331	261	311	94.6
Density (g cm^{-3})	4.2	4.2	[a]3.75	2.17
CO_2 Capacity (wt.%)	13.3	16.9	14.1	-
Gravimetric Energy Density (kJ kg^{-1})	531	788	500	413

Volumetric Energy Density (MJ m^{-3})[d]	2242	3303	1878	895
Operating Temperature (°C)	1100	1100	700	290 - 565
Operating CO_2 Pressure (bar)	0 - 5	0 - 5	0.1 - 6	-
Theoretical Carnot Efficiency (%)	77.9	77.9	69	46
Estimated Practical Efficiency (%)	53	53	45	27
Mass Required (tonnes) [c]	3554	2392	[g]4700	9100
Volume Required (m^3) [c]	841	570	[g]1711	4194
Materials Cost (US$/tonne) [c]	1372	1301	[g]480	630
Energy Cost (US$/kWh)[d]	17.55	11.20	*8.13*	
Total Materials Cost Required (US$)[c]	4,876,012	3,112,376	2,258,099	5,730,000

[a]Cost based on the price of the corresponding oxide, TiO_2 and ZrO_2 [b,c]80 wt.% $SrSiCO_3$:$SrCO_3$ + 20 wt.% NaCl:$MgCl_2$, [c]To generate 1 TJ of electrical energy [d]Thermal to electrical energy conversion. Assuming 100% cycling capacity.

5.5 Conclusions

It is clear that thermal energy storage is posed to provide heat storage for a range of applications and conditions. The comparison between $SrZrO_3$ and $SrTiO_3$ as additives in to $SrCO_3$ highlights their contrasting characteristics. Notably, $SrTiO_3$ exhibits inherent

resistance to cyclic CO_2 capacity decline on both smaller scale TGA experiments and larger scale experiments using Sieverts apparatus (maintaining over 80% capacity), indicating its potential suitability for upscaling. Whilst the use of $SrZrO_3$ as an additive offers lower material costs relative to $SrTiO_3$(9.94 to 17.73 US$/kWh), it fails to prevent sintering and enhance CO_2 cyclic capacity on a larger scale. The contrast in performance may be due to the ability of $SrTiO_3$ to actively take part in the reaction pathway with $SrCO_3$, whereas $SrZrO_3$ acts as an inert additive and is unable to completely prevent sintering at 1100 °C.

This study emphasizes the significance of studying materials under diverse conditions, as expecting consistent performance from mg-scale TGA to large-scale systems can be unrealistic. Future recommendations involve the exploration of cost-effective additives that undergo morphological changes near the operating temperature of the active metal carbonate, aiming to disrupt the sintering process and improve capacity. Additionally, conducting further studies on TCES materials in larger-scale systems, where bulk effects are more pronounced, would be valuable. Additionally, Sieverts apparatus could be used as an effective steppingstone to test TCES materials on a scale between TGA and benchtop scale prototypes.

5.6 Conflicts of interest

There are no conflicts to declare.

5.7 Acknowledgements

CEB, MP and TDH acknowledge the Global Innovation Linkage project for grant GIL73589. CEB, MP, TDH acknowledge the Australian Research Council for ARC Discovery project grant DP200102301. KW acknowledges the Australian Government for an Australian Government Research Training Program Scholarship. This research was supported by an AINSE Ltd through a Postgraduate Research Award (PGRA) for KW. SEM and XRD research were undertaken using the Tescan Mira3 EM (ARC LE130100053) and the Bruker D8 Advance XRD instrumentation (ARC LE0775551) at the John de Laeter Centre, Curtin

University. ANSTO is acknowledged for providing access to the PD beamline at the Australian Synchrotron, Melbourne, Australia.

5.8 References

(1) IRENA(2019), I. *Global Energy Transformation: A Roadmap to 2050 (2019 Edition)*; 2019. https://www.irena.org/publications/2019/Apr/Global-energy-transformation-A-roadmap-to-2050-2019Edition (accessed 2023-06-08).

(2) Forrester, J. The Value of CSP with Thermal Energy Storage in Providing Grid Stability. *Energy Procedia* **2014**, *49*, 1632–1641. https://doi.org/10.1016/j.egypro.2014.03.172.

(3) Sarbu, I.; Sebarchievici, C. A Comprehensive Review of Thermal Energy Storage. *Sustainability* **2018**, *10* (1), 191. https://doi.org/10.3390/su10010191.

(4) Bayon, A.; Bader, R.; Jafarian, M.; Fedunik-Hofman, L.; Sun, Y.; Hinkley, J.; Miller, S.; Lipiński, W. Techno-Economic Assessment of Solid–Gas Thermochemical Energy Storage Systems for Solar Thermal Power Applications. *Energy* **2018**, *149*, 473–484. https://doi.org/10.1016/j.energy.2017.11.084.

(5) Copus, M.; Fraser, B.; Reece, R.; Hands, S.; Cuskelly, D.; Sugo, H.; Reed, S.; Bradley, J.; Post, A.; Kisi, E. On-Sun Testing of Miscibility Gap Alloy Thermal Storage. *Solar Energy* **2019**, *177*, 657–664. https://doi.org/10.1016/j.solener.2018.11.048.

(6) Steinmann, W.-D. *Thermal Energy Storage for Medium and High Temperatures: Concepts and Applications*; Springer Fachmedien Wiesbaden: Wiesbaden, 2022. https://doi.org/10.1007/978-3-658-02004-0.

(7) Bayon, A.; Carrillo, A. J.; Mastronardo, E.; Coronado, J. M. Chapter Six - Thermochemical Heat Storage at High Temperature. In *Advances in Chemical Engineering*; Lipiński, W., Ed.; Solar Thermochemistry; Academic Press, 2021; Vol. 58, pp 247–295. https://doi.org/10.1016/bs.ache.2021.10.004.

(8) Pardo, P.; Deydier, A.; Anxionnaz-Minvielle, Z.; Rougé, S.; Cabassud, M.; Cognet, P. A Review on High Temperature Thermochemical Heat Energy Storage. *Renewable and Sustainable Energy Reviews* **2014**, *32*, 591–610. https://doi.org/10.1016/j.rser.2013.12.014.

(9) André, L.; Abanades, S. Recent Advances in Thermochemical Energy Storage via Solid–Gas Reversible Reactions at High Temperature. *Energies* **2020**, *13* (22), 5859. https://doi.org/10.3390/en13225859.

(10) Desage, L.; McCabe, E.; Vieira, A. P.; Humphries, T. D.; Paskevicius, M.; Buckley, C. E. Thermochemical Batteries Using Metal Carbonates: A Review of Heat Storage and Extraction. *Journal of Energy Storage* **2023**, *71*, 107901. https://doi.org/10.1016/j.est.2023.107901.

(11) Harries, D. N.; Paskevicius, M.; Sheppard, D. A.; Price, T. E. C.; Buckley, C. E. Concentrating Solar Thermal Heat Storage Using Metal Hydrides. *Proceedings of the IEEE* **2012**, *100* (2), 539–549. https://doi.org/10.1109/JPROC.2011.2158509.

(12) Humphries, T. D.; Paskevicius, M.; Alamri, A.; Buckley, C. E. Thermodynamic Destablization of SrH2 Using Al for the next Generation of High Temperature Thermal Batteries. *Journal of Alloys and Compounds* **2022**, *894*, 162404. https://doi.org/10.1016/j.jallcom.2021.162404.

(13) Poupin, L.; Humphries, T. D.; Paskevicius, M.; Buckley, C. E. A Thermal Energy Storage Prototype Using Sodium Magnesium Hydride. *Sustainable Energy Fuels* **2019**, *3* (4), 985–995. https://doi.org/10.1039/C8SE00596F.

(14) Poupin, L.; Humphries, T. D.; Paskevicius, M.; Buckley, C. E. An Experimental High Temperature Thermal Battery Coupled to a Low Temperature Metal Hydride for Solar Thermal Energy Storage. *Sustainable Energy Fuels* **2020**, *4* (1), 285–292. https://doi.org/10.1039/C9SE00538B.

(15) Møller, K. T.; Williamson, K.; Buckley, C. E.; Paskevicius, M. Thermochemical Energy Storage Properties of a Barium Based Reactive Carbonate Composite. *J. Mater. Chem. A* **2020**, *8* (21), 10935–10942. https://doi.org/10.1039/D0TA03671D.

(16) Humphries, T. D.; Møller, K. T.; Rickard, W. D. A.; Sofianos, M. V.; Liu, S.; Buckley, C. E.; Paskevicius, M. Dolomite: A Low Cost Thermochemical Energy Storage Material. *J. Mater. Chem. A* **2019**, *7* (3), 1206–1215. https://doi.org/10.1039/C8TA07254J.

(17) Møller, K. T.; Humphries, T. D.; Berger, A.; Paskevicius, M.; Buckley, C. E. Thermochemical Energy Storage System Development Utilising Limestone. *Chemical Engineering Journal Advances* **2021**, *8*, 100168. https://doi.org/10.1016/j.ceja.2021.100168.

(18) Pires Vieira, A.; Williamson, K.; Humphries, T.; Paskevicius, M.; Buckley, C. A New Strontium Based Reactive Carbonate Composite for Thermochemical Energy Storage. *Journal of Materials Chemistry A* **2021**, *9*. https://doi.org/10.1039/D1TA04363C.

(19) Møller, K. T.; Ibrahim, A.; Buckley, C. E.; Paskevicius, M. Inexpensive Thermochemical Energy Storage Utilising Additive Enhanced Limestone. *J. Mater. Chem. A* **2020**, *8* (19), 9646–9653. https://doi.org/10.1039/D0TA03080E.

(20) Amghar, N.; Ortiz, C.; Perejón, A.; Valverde, J. M.; Maqueda, L. P.; Sánchez Jiménez, P. E. The SrCO3/SrO System for Thermochemical Energy Storage at Ultra-High Temperature. *Solar Energy Materials and Solar Cells* **2022**, *238*, 111632. https://doi.org/10.1016/j.solmat.2022.111632.

(21) Fedunik-Hofman, L.; Bayon, A.; Donne, S. Calcium, Strontium and Barium Carbonate Mixtures for Calcination-Carbonation Thermochemical Energy Storage. *AIP Conference Proceedings* **2019**, *2126* (1), 210002. https://doi.org/10.1063/1.5117751.

(22) Khosa, A. A.; Zhao, C. Y. Heat Storage and Release Performance Analysis of CaCO3/CaO Thermal Energy Storage System after Doping Nano Silica. *Solar Energy* **2019**, *188*, 619–630. https://doi.org/10.1016/j.solener.2019.06.048.

(23) Zhao, M.; Shi, J.; Zhong, X.; Tian, S.; Blamey, J.; Jiang, J.; Fennell, P. S. A Novel Calcium Looping Absorbent Incorporated with Polymorphic Spacers for Hydrogen Production and CO2 Capture. *Energy Environ. Sci.* **2014**, *7* (10), 3291–3295. https://doi.org/10.1039/C4EE01281J.

(24) Mostafavi, E.; Sedghkerdar, M. H.; Mahinpey, N. Thermodynamic and Kinetic Study of CO2 Capture with Calcium Based Sorbents: Experiments and Modeling. *Ind. Eng. Chem. Res.* **2013**, *52* (13), 4725–4733. https://doi.org/10.1021/ie400297s.

(25) Bagherisereshki, E.; Tran, J.; Lei, F.; AuYeung, N. Investigation into SrO/SrCO3 for High Temperature Thermochemical Energy Storage. *Solar Energy* **2018**, *160*, 85–93. https://doi.org/10.1016/j.solener.2017.11.073.

(26) Rhodes, N. R.; Barde, A.; Randhir, K.; Li, L.; Hahn, D. W.; Mei, R.; Klausner, J. F.; AuYeung, N. Solar Thermochemical Energy Storage Through Carbonation Cycles of SrCO3/SrO Supported on SrZrO3. *ChemSusChem* **2015**, *8* (22), 3793–3798. https://doi.org/10.1002/cssc.201501023.

(27) Maya, J. C.; Chejne, F.; Gómez, C. A.; Bhatia, S. K. Effect of the CaO Sintering on the Calcination Rate of CaCO3 under Atmospheres Containing CO2. *AIChE Journal* **2018**, *64* (10), 3638–3648. https://doi.org/10.1002/aic.16326.

(28) Bogdanović, B.; Reiser, A.; Schlichte, K.; Spliethoff, B.; Tesche, B. Thermodynamics and Dynamics of the Mg–Fe–H System and Its Potential for Thermochemical Thermal Energy Storage. *Journal of Alloys and Compounds* **2002**, *345* (1–2), 77–89. https://doi.org/10.1016/S0925-8388(02)00308-0.

(29) Ammendola, P.; Raganati, F.; Landi, E.; Natali Murri, A.; Miccio, F. Kinetics of the Carbonation Reaction of an SrO-Al2O3 Composite for Thermochemical Energy Storage. *Chemical Engineering Journal* **2021**, *420*, 129618. https://doi.org/10.1016/j.cej.2021.129618.

(30) Gigantino, M.; Kiwic, D.; Steinfeld, A. Thermochemical Energy Storage via Isothermal Carbonation-Calcination Cycles of MgO-Stabilized SrO in the Range of 1000–1100 °C. *Solar Energy* **2019**, *188*, 720–729. https://doi.org/10.1016/j.solener.2019.06.046.

(31) Sheppard, D. A.; Paskevicius, M.; Javadian, P.; Davies, I. J.; Buckley, C. E. Methods for Accurate High-Temperature Sieverts-Type Hydrogen Measurements of Metal Hydrides. *Journal of Alloys and Compounds* **2019**, *787*, 1225–1237. https://doi.org/10.1016/j.jallcom.2019.02.067.

(32) Lemmon, E.; Huber, M.; McLinden, M. NIST Standard Reference Database 23: Reference Fluid Thermodynamic and Transport Properties-REFPROP, Version 9.1, 2013. https://tsapps.nist.gov/publication/get_pdf.cfm?pub_id=912382.

(33) Perl, J.; Shin, J.; Schumann, J.; Faddegon, B.; Paganetti, H. TOPAS: An Innovative Proton Monte Carlo Platform for Research and Clinical Applications. *Med Phys* **2012**, *39* (11), 6818–6837. https://doi.org/10.1118/1.4758060.

(34) Wallwork, K. S.; Kennedy, B. J.; Wang, D. The High Resolution Powder Diffraction Beamline for the Australian Synchrotron. *AIP Conference Proceedings* **2007**, *879* (February 2007), 879–882. https://doi.org/10.1063/1.2436201.

(35) Bagherisereshki, E.; Tran, J.; Lei, F.; AuYeung, N. Investigation into SrO/SrCO3 for High Temperature Thermochemical Energy Storage. *Solar Energy* **2018**, *160* (December 2017), 85–93. https://doi.org/10.1016/j.solener.2017.11.073.

(36) Ptáček, P.; Bartoníčková, E.; Švec, J.; Opravil, T.; Šoukal, F.; Frajkorová, F. The Kinetics and Mechanism of Thermal Decomposition of SrCO3 Polymorphs. *Ceramics International* **2015**, *41* (1, Part A), 115–126. https://doi.org/10.1016/j.ceramint.2014.08.043.

(37) Jacob, K.; Rajitha, G. Thermodynamic Properties of Strontium Titanates: Sr2TiO4, Sr3Ti2O7, Sr4Ti3O10, and SrTiO3. *The Journal of Chemical Thermodynamics* **2011**, *43*, 51–57. https://doi.org/10.1016/j.jct.2010.08.011.

(38) Roine, A. HSC Chemistry® [Software], 2018. Software available at www.outotec.com/HSC.

(39) Carrillo, A. J.; Gonza, J.; Romero, M.; Coronado, J. M. Solar Energy on Demand : A Review on High Temperature Thermochemical Heat Storage Systems and Materials. **2019**. https://doi.org/10.1021/acs.chemrev.8b00315.

(40) Medina-Carrasco, S.; Valverde, J. M. The Calcium Looping Process for Energy Storage: Insights from in Situ XRD Analysis. *Chemical Engineering Journal* **2022**, *429* (June 2021), 132244. https://doi.org/10.1016/j.cej.2021.132244.

(41) Srivastava, D.; Norman, C.; Azough, F.; Schäfer, M. C.; Guilmeau, E.; Freer, R. Improving the Thermoelectric Properties of SrTiO3-Based Ceramics with Metallic Inclusions. *Journal of Alloys and Compounds* **2018**, *731*, 723–730. https://doi.org/10.1016/j.jallcom.2017.10.033.

(42) Fumega, A. O.; Fu, Y.; Pardo, V.; Singh, D. J. Understanding the Lattice Thermal Conductivity of ${\mathrm{SrTiO}}_{3}$ from an Ab Initio Perspective. *Phys. Rev. Mater.* **2020**, *4* (3), 033606. https://doi.org/10.1103/PhysRevMaterials.4.033606.

(43) National Minerals Information Center. U.S. Geological Survey Mineral Commodity Summaries 2022 Data Release, 2022. https://doi.org/10.5066/P9KKMCP4.

Chapter 6

Conclusions

"The strongest arguments prove nothing so long as the conclusions are not verified by experience. Experimental science is the queen of sciences and the goal of all speculation."

-Roger Bacon

In the field of energy storage, thermal energy storage (TES) emerges as a cost-efficient solution. Particularly, thermochemical energy storage (TCES) which offers a promising option for high-energy-density storage, especially for high temperature applications. When combined with modern CSP, it can provide some of the cheapest round the clock power in the world, especially when considering the technology is still in its infancy.

This study is an exploration of novel metal carbonate composites for their potential as TCES materials. Unique to this work, Sievert's methods were used to investigate these highly promising composite materials. It is critical more experimental studies are performed to determine the reaction enthalpies of these systems so that CALPHAD (CALculation of PHAse Diagrams) approach could be used in the future to screen potential materials.

Sieverts apparatus has the capability to handle larger sample sizes and pressures that are unavailable using TGA which is standard in the field. It can also be used to directly measure the thermodynamics of carbonation and calcination reactions. Larger scale measurements provide further insight into the bulk properties of these materials, which are affected by thermal conductivity and sintering, which affects both cycling stability and kinetics.

$CaCO_3$ attracts attention due to its abundance, affordability, and operational temperature of 900 °C. However, $BaCO_3$ and $SrCO_3$ are promising for higher-temperature applications such as next generation CSP (~ 1000 °C), hard-to-decarbonise industrial applications such as steel (~ 1400 °C), cement (~ 1450 °C) and aluminium production (~ 960 °C).

$BaCO_3$, despite its challenging decomposition temperature (~ 1400 °C) and susceptibility to severe sintering, has potential in composite forms. $BaCO_3$:Fe_2O_3 demonstrated reversible CO_2 cycling at 885°C making it ideal for modern day CSP plants. However, the composite experiences cyclic capacity loss, so further research into sintering inhibiting additives is recommended before it can be considered further.

The $2BaCO_3$:TiO_2 composite (which forms $BaTiO_3$:$BaCO_3$ on heating) shows much promise, demonstrating excellent cycling capacity retention and rapid sorption kinetics. Capacity retention was further improved by the addition of nickel which reduced sintering and grain growth. Further studies should focus on optimising nickel additive ratios to see how capacity is affected. Also scaling up of a prototype utilising this material could be effective as nickel hinders sintering while boosting thermal conductivity.

$SrCO_3$, which can reversibly desorb CO_2 at 1100 °C, also suffers from capacity loss challenges due to sintering. $SrTiO_3$ additive and $SrZrO_3$ were compared using TGA and Sievert apparatus. Using TGA the composites were evenly matched at 80 % storage capacity retention. However, using the Sieverts method $SrTiO_3$ performance was superior (~ 80 % retention), while the capacity of $SrZrO_3$ reduced to 12 % over 53 cycles. This large difference shows the benefit of a reactive composite over inert additives, as well as the limitations of TGA when used to study TCES materials.

Further scaling up to kilogram-scale prototypes for both $SrTiO_3$:$SrCO_3$ and $2BaCO_3$:TiO_2 is highly recommended. These composites should be compared to current bulk scale $CaCO_3$ prototypes, where thermal conductivity and capacity retention prove to be major challenges. It must be noted however that building higher temperature prototypes (~ 1100 °C) will require thermally resistant parts and further safety considerations, resulting in additional costs.

Sieverts apparatus is shown as a valuable tool in evaluating metal carbonates due to its capacity for analysing larger sample sizes and directly measuring reaction thermodynamics. The application of Sieverts apparatus should extend to future solid-gas TCES material analysis, and it could be used in complementary studies with TGA to predict larger prototype viability.

Overcoming engineering obstacles, including heat transfer and gas storage are vital for future research. This should be targeted by a combination of both engineering and material science investigation to provide complementary solutions to these problems.

Some potential solutions for gas storage that warrant investigation include using a coupled metal carbonate (a high and low temperature pair) as has been previously used with metal hydrides. A cascaded system which uses a series of carbonates with complementary absorption and desorption temperatures could also provide a novel solution. Another interesting prospect is the development of a composite capable of reacting with CO_2 in ambient air (0.0004 bar), removing the need for separate gas storage requirements and allowing radiative instead of conductive heat transfer. Such a material could also be re-purposed for carbon sequestration or mineral carbonisation purposes.

Appendix A: Thermochemical energy storage of a barium based reactive carbonate composite

Møller, K. T.; Williamson, K.; Buckley, C. E.; Paskevicius, M. Thermochemical Energy Storage Properties of a Barium Based Reactive Carbonate Composite. *J. Mater. Chem. A* **2020**, *8* (21), 10935–10942. https://doi.org/10.1039/D0TA03671D.

Journal of Materials Chemistry A

ROYAL SOCIETY OF CHEMISTRY

PAPER

View Article Online
View Journal | View Issue

Cite this: J. Mater. Chem. A, 2020, 8, 10935

Thermochemical energy storage properties of a barium based reactive carbonate composite†

Kasper T. Møller, * Kyran Williamson, Craig E. Buckley and Mark Paskevicius *

Received 3rd April 2020
Accepted 13th May 2020

DOI: 10.1039/d0ta03671d

rsc.li/materials-a

This study introduces a new concept of reactive carbonate composites (RCCs) for thermochemical energy storage, where a $BaCO_3$–$BaSiO_3$ mixture offers a successful thermodynamic destabilisation of $BaCO_3$ with moderate cyclic stability ~60%, close to the theoretical maximum when considering unreactive impurities. This research presents an alternative to molten salt based energy storage technology that operates at higher temperature (850 °C) and hence maintains a higher Carnot efficiency at a competitive price level, enabling the development of a thermal energy storage system more favourable than state-of-the-art technology. Finally, the addition of catalytic quantities of $CaCO_3$ to the RCC significantly improves the reaction kinetics (one order of magnitude) through the formation of intermediate $Ba_{2-x}Ca_xSiO_4$ compounds, which are hypothesised to facilitate Ba^{2+} and O^{2-} mobility through induced crystal defects.

Introduction

Large-scale storage of renewable energy from solar or wind power is a prerequisite for covering base-load energy demand in the future as these energy sources are intermittent in their nature. Attention is often pointed towards hydrogen as an energy carrier, concentrated solar thermal power, or large-scale lithium battery facilities.[1–5] However, cost is a major issue with these storage options. Concentrated solar thermal power (CSP) plants currently store energy using a KNO_3/$NaNO_3$ (60 : 40) molten salt, which has a low specific heat capacity of 1.53 kJ kg^{-1} K^{-1}, *i.e.* a low energy density ≤ 413 kJ kg^{-1} when $\Delta T \leq 270$ °C, and operates below 550 °C, which leads to a low Carnot efficiency when converting the heat into electricity.[6] Although, most research into metal carbonates is focused on CO_2 sequestration,[7,8] this class of materials have also been identified as promising for thermal energy storage due to their high enthalpy of formation and the low cost.[1,6,9–12] The latter suggest to expand the application of thermal energy storage from CSP plants to a new technology defined as a thermal battery, where the energy input may be concentrated solar, industrial waste heat, energy from wind power, photovoltaics *etc.*, which is stored and released through a chemical reaction.[13]

Witherite, the thermodynamically stable phase of $BaCO_3$, is industrially produced from naturally mined barite ($BaSO_4$) through the reaction with coke, also known as the 'black ash' process, and has a reasonable price of ~$494 USD per metric tonne.[14] However, pristine $BaCO_3$ is thermally stable and decomposes at 1150–1400 °C,[15] which is, perhaps, too high from an application point of view. Thus, thermodynamic destabilisation of the $BaCO_3$ is necessary. A recent study on:

$$Li_2CO_3(s) + Li_2SiO_3(s) \leftrightarrow Li_4SiO_4(s) + CO_2(g) \quad \Delta H_{700°C} = 109.0 \text{ kJ mol}^{-1} \quad (1)$$

suggests a destabilised metal carbonate as a thermochemical energy storage material operating at 700 °C,[16] however, only 5 cycles were performed at low CO_2 pressure (<0.4 bar). A disadvantage of this particular system is that Li is expensive (battery grade, 99.9%, Li_2CO_3 was on average $17 000 USD per metric tonne in 2018, >30 times the price of $BaCO_3$),[17] and thus limits its utilisation in large-scale facilities. This study elaborates on the concept and introduces a new reactive carbonate composite (RCC). The incorporation of barium orthosilicate, $BaSiO_3$, improves the thermodynamics of $BaCO_3$ and thus enables the $BaCO_3$–$BaSiO_3$ system to operate in a suitable temperature range between 700–1000 °C as:

$$BaCO_3(s) + BaSiO_3(s) \leftrightarrow Ba_2SiO_4(s) + CO_2(g) \quad (2)$$

Thermodynamics of the RCC $BaCO_3$–$BaSiO_3$ was evaluated using the software HSC Chemistry.[18] The predicted temperature where the reaction has an equilibrium pressure of 1 bar ($T_{1\ bar}$) was determined to be 670 °C with $\Delta H_{670°C} = 151.9$ kJ mol^{-1} CO_2. However, an increased working temperature of 850 °C was

Department of Imaging and Applied Physics, Fuels and Energy Technology Institute, Curtin University, GPO Box U1987, Perth 6845, WA, Australia. E-mail: kasper.moller@curtin.edu.au; mark.paskevicius@gmail.com

† Electronic supplementary information (ESI) available. See DOI: 10.1039/d0ta03671d

selected, where the thermodynamic predictions are $p_{eq} = 18.1$ bar and $\Delta H_{850°C} = 126.9$ kJ mol^{-1} CO_2.

Experimental

Sample preparation

$BaCO_3$ (Sigma-Aldrich, ACS reagent, ≥99%), $CaCO_3$ (Sigma-Aldrich, ReagentPlus), and $BaSiO_3$ (Alfa Aesar) were used as-purchased. $BaSiO_3$ was synthesised in the laboratory by heating a ball-milled 1 : 1.17 molar mixture of $BaCO_3$ and SiO_2 (Sigma-Aldrich, 99.5%, nanopowder, 10–20 nm particle size) to 1000 °C for six hours in air.

Samples of $BaCO_3$–$BaSiO_3$ were prepared in various molar ratios, see Table 1, and were ball-milled in stainless steel milling vials with stainless steel balls (10 mm diameter, ball-to-powder mass ratio of 11 : 1) using an Across International Planetary Ball Mill (PQ-N04). A sequence of 20 min milling and a 1 min break, which is repeated three times to achieve an accumulated milling time of 1 hour, was applied.

Thermal analysis

Differential scanning calorimetry and thermogravimetric analysis (DSC-TGA) was simultaneously performed on a Mettler Toledo DSC 1 instrument by heating ~15–25 mg of sample in an Al_2O_3 crucible from room temperature to 1200 °C under flowing argon atmosphere (20 mL min^{-1}) at $\Delta T/\Delta t$ = 10, 20, or 30 °C min^{-1}. For comparison, CO_2 cycled samples were first absorbed and then analysed at three heating rates (as above) to construct Kissinger plots and determine their activation energy.

Sievert's measurements

Pressure cycling measurements were performed on a HyEnergy PCTpro E&E using a custom built SiC sample holder.[19] Samples (typical mass ~ 2.4 g) were generally heated to 850 °C ($\Delta T/\Delta t \sim 4$ °C min^{-1}) at $p(CO_2) \sim 1$ bar to avoid decomposition of the $CaCO_3$ catalyst. The temperature was kept isothermal throughout the measurements and CO_2 pressure cycling was initiated between carbonation at $p(CO_2) \sim 21$ bar for 12 hours and decomposition at $p(CO_2) \sim 3$ bar for 12 hours. As reaction kinetics become faster with increasing cycle numbers, the carbonation/decomposition times were adjusted to 1, 3, or 6 hour(s). The samples were cycled from 20–35 carbonation and calcination cycles. At all times, the total gas volume used was 194.06 cm^3 (158.43 cm^3 reference volume and 35.63 cm^3 sample volume) and the non-ambient volume was determined to be between 13.8 to 15.5 cm^3. All data was manually corrected from the PCTPro to include the correct volumes and compressibility factors for gaseous CO_2.[20] The cycling was ceased when the sample was in the absorbed state and cooled under a backpressure of CO_2. However, in some cases, samples were decomposed at 850 °C and analysed to determine the reaction decomposition products.

In-house powder X-ray diffraction

Powder X-ray diffraction data was collected in-house on a Bruker D8 Advance equipped with a Cu X-ray source (Cu $K_{\alpha1}$ radiation, $\lambda = 1.540593$ Å, Cu $K_{\alpha2}$ radiation, $\lambda = 1.544414$ Å) in flat-plate Bragg–Brentano geometry. Data were collected in the 2θ range 5–80° on a Lynxeye PSD detector. The as-synthesised $BaSiO_3$ was further investigated by adding a known 21.2 wt% NIST LaB_6 standard to quantify the amorphous fraction of the sample.

In situ synchrotron radiation powder X-ray diffraction

In situ time-resolved synchrotron radiation powder X-ray diffraction (SR-PXD) data were collected at the Australian Synchrotron, Melbourne, Australia using the Powder Diffraction (PD) beamline.[21] The wavelength was λ = 0.825018 Å and data were collected on a Mythen microstrip detector in two different positions with a data acquisition time of 30 s in each position. Samples were packed in quartz capillaries (o.d. 0.7 mm, wall thickness 0.05 mm) and mounted in a custom gas fitting sealed with rubber rings, which was then connected to a gas manifold that provided vacuum or CO_2. During data acquisition, the samples were continuously oscillated over 90° to prevent preferred orientation of the particles. Finally, the samples were heated with a hot air blower at $\Delta T/\Delta t$ = 6 °C min^{-1}. Diffraction patterns were quantitatively analysed using the Rietveld method in the software TOPAS (Bruker-AXS).

Scanning electron microscopy

Scanning electron microscopy (SEM) and energy dispersive spectroscopy (EDS) were conducted using a Zeiss Neon 40EsB equipped with a field emission gun. The SEM images were collected using an accelerating voltage of 5 kV, an aperture size of 30 µm, and a working distance between 2.5–7 mm. SEM samples were prepared by embedding powdered samples in an epoxy resin that was polished using colloidal

Table 1 Overview of samples discussed in this study

Sample	Compound 1	Compound 2	Compound 3	Molar ratio compound 1 : 2 : 3	mol% $CaCO_3$
S1	$BaCO_3$	$BaSiO_3$ (Alfa Aesar)		1 : 1	0
S2	$BaCO_3$	$BaSiO_3$ (Alfa Aesar)	$CaCO_3$	1 : 1 : 0.052	2.5
S3	$BaCO_3$	$BaSiO_3$ (Alfa Aesar)	$CaCO_3$	1 : 1 : 0.105	5
S4	$BaCO_3$	$BaSiO_3$ (Alfa Aesar)	$CaCO_3$	1 : 1 : 0.224	10
S5	$BaCO_3$	$BaSiO_3$ (as-synthesised)	$CaCO_3$	1 : 1 : 0.105	5

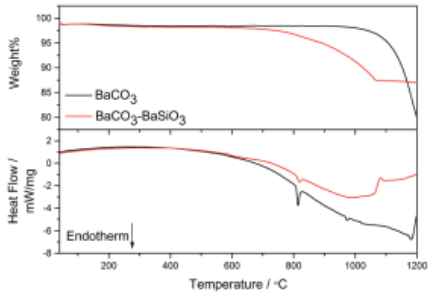

Fig. 1 TG (upper) and DSC (lower) data comparing pristine $BaCO_3$ and the reactive carbonate composite $BaCO_3$–$BaSiO_3$ (S1). $\Delta T/\Delta t$ = 10 K min^{-1}, 20 mL argon flow.

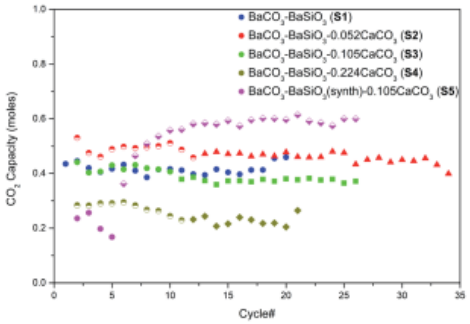

Fig. 2 Comparison of the cyclic CO_2 storage capacity after calcination in each cycle. S1 is the uncatalysed $BaCO_3$–$BaSiO_3$ while S2–S4 are $CaCO_3$ catalysed with various amounts of $CaCO_3$, while S5 is catalysed with 0.105 mol $CaCO_3$ and contains synthesised $BaSiO_3$. Calcination/carbonation times vary and are indicated in the following way: 2 hours (▲); 3 hours (◆); 4 hours (■); 5 hours (⬙); 6 hours (◓); 12 hours (●).

silica, which were then sputter coated with a 10 nm thick carbon layer.

Results & discussion

Destabilisation of $BaCO_3$ utilising $BaSiO_3$

From TG-DSC data it is evident that $BaCO_3$ is destabilised by $BaSiO_3$, see Fig. 1, where a mass loss (CO_2) is detected at lower temperatures. For both pristine $BaCO_3$ and the RCC, $BaCO_3$–$BaSiO_3$ (**S1**), a polymorphic phase transition is observed for $BaCO_3$ at ~815 °C from an orthorhombic (space group *Pmcn*) to a trigonal structure ($R\bar{3}m$),[22] which has previously been reported to occur at ~750 °C and 805 °C.[23–25] A second polymorphic phase transition is observed at ~974 °C from the trigonal to cubic structure ($Fm\bar{3}m$).[24–26] The TG data reveal that pristine $BaCO_3$ decomposes above 1000 °C, whereas the RCC initiates decomposition at ~650 °C, releasing CO_2. Hence, the operational temperature of $BaCO_3$ becomes more favourable for applications when destabilised by $BaSiO_3$. Additional information is provided in Fig. S1–S3.†

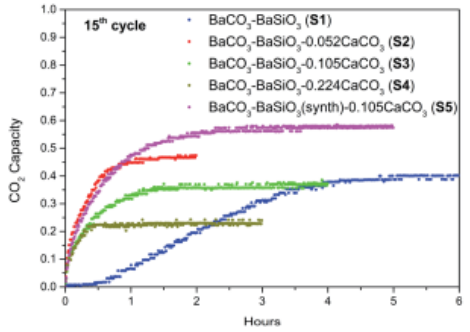

Fig. 3 Comparison of the reaction kinetics in the 15th desorption highlighting the positive effect of adding $CaCO_3$ to the system.

Cyclic energy capacity studies

The cyclic CO_2 storage stability is evaluated from the Sieverts experiments (see Fig. 2). Sample **S1** maintains a steady ~40–45% CO_2 capacity during 12 hour calcination/carbonation cycles. The low capacity is partly assigned to slow reaction kinetics during CO_2 release and absorption from the pristine $BaSiO_3$–$BaCO_3$ system, see Fig. 3 and S4.† Thus, an attempt to catalyse the CO_2 absorption and release was undertaken using $CaCO_3$, which shows excellent kinetics in its pure form.[13] Previously, a solid-solution regime has been reported for $Ca_{1-x}Ba_xCO_3$ above ~850 °C.[27] Thus, it was hypothesised that this solid solution could enhance the CO_2 and/or Ba^{2+} diffusion through the metal carbonate. Addition of 2.5 (**S2**) and 5 mol% (**S3**) $CaCO_3$ influences the cyclic capacity to a small extent (~45% and ~37% CO_2 capacity, respectively). However, the addition of a larger quantity, *i.e.* 10 mol%, of $CaCO_3$ reduces the CO_2 capacity to ~20–25%. Sample **S5** increases in capacity for the first 15 cycles before stabilising at ~60% and thus proves superior to the other samples (see Fig. 2). The absorption/desorption time was decreased to 5 hours as the sample reached a plateau within this time frame, see also Fig. S4.† Despite the reduction in time, the capacity increases along with reaction kinetics. Hence, an activation of the sample, possibly through the formation of $Ba_{2-x}Ca_xSiO_4$ (*c.f.* Powder X-ray diffraction section) and homogenisation of the sample seem necessary.

Although the CO_2 capacity suffers from adding a large amount of $CaCO_3$ to the system, the reaction kinetics improve significantly (see Fig. 3). The difference is apparent in the 15th desorption, where calcination is ~10 times faster in sample **S2** compared to the pristine RCC, sample **S1**, (~40 min compared to ~4.5 hours, respectively). Generally, the calcination reaction kinetics for samples **S2** through **S5** are more than doubled compared to sample **S1** (see Fig. S4†).

Powder X-ray diffraction

Powder X-ray diffraction (PXD) data indicate that the as-purchased $BaSiO_3$ (Alfa Aesar) contains multiple Ba–Si–O compositions (see Fig. S5†), since the as-milled samples (**S1–S4**) contain major fractions of, *e.g.* $Ba_4Si_6O_{16}$ (barium-poor). Hence, the decreased cyclic CO_2 capacity, which is close to half of that expected, is attributed to the fact that the commercial $BaSiO_3$ contains a large amount of impurities, which retards reaction (2). However, quantification of the amorphous fraction is not possible through Rietveld refinement as unidentified crystalline compounds are also present. Sample **S5**, containing the synthesised $BaSiO_3$, is a more homogenous mixture of $BaCO_3$ and $BaSiO_3$ and hence the cyclic capacity is superior (see Fig. 2 and S6†). However, impurities of $Ba_4Si_6O_{16}$ and an amorphous content (likely SiO_2) are still an issue (see Fig. S6†), and thus the $BaSiO_3$ content only amounts to 62.1 wt% of what is expected. Hence, the cyclic capacity of sample **S5** is theoretically decreased to 62.4%, due to the lower amount of $BaSiO_3$ available for reaction (2), and thus proves that the sample's cyclic stability is close to the theoretical maximum when considering the unreactive impurities. The addition of small quantities of $CaCO_3$ does not influence the PXD pattern of the ball-milled samples due to overlapping Bragg reflections and the smaller X-ray scattering power of Ca^{2+} compared to Ba^{2+} (see Fig. S5†).

After CO_2 pressure cycling of $BaCO_3$–$BaSiO_3$ (**S1**) it is evident that reaction (2) is occurring through absorption and desorption of CO_2 (see Fig. 4A). However, Bragg reflections from $BaSiO_3$ are still present after CO_2 absorption due to an incomplete reaction although an intensity decrease is observed due to consumption. The addition of $CaCO_3$ to the system proved to enhance reaction kinetics significantly during cyclic measurements. The increased kinetics are in-fact not assigned to the hypothesised $Ca_{1-x}Ba_xCO_3$,[27] but to the formation of $Ba_{2-x}Ca_xSiO_4$ that offers increased cation mobility of Ba^{2+} as the smaller Ca^{2+} cation introduces defects in the Ba_2SiO_4 crystal structure[28,29] (see Fig. 4B and reaction scheme (3)). The composition of $Ba_{2-x}Ca_xSiO_4$ varies depending on the absorbed or desorbed state of the sample and the loading level of $CaCO_3$. Higher loading of $CaCO_3$ leads to a higher fraction of $Ba_{2-x}Ca_xSiO_4$ after cycling, probably due to an extended reaction between $CaCO_3$ and $BaSiO_3$, which may cause the significantly lower cyclic capacity observed in sample **S4**. The findings imply that $CaCO_3$ has reacted with $BaSiO_3$ to form Ca_2SiO_4, which is favourable according to thermodynamic calculations, see reaction scheme (4):[18]

$$(1-x)Ba_2SiO_4\,(s) + xCa_2SiO_4\,(s) \rightarrow Ba_{2-2x}Ca_{2x}SiO_4\,(s) \quad (3)$$

$$2CaCO_3\,(s) + BaSiO_3\,(s) \rightarrow Ca_2SiO_4\,(s) + BaCO_3\,(s) + CO_2\,(g) \quad T_{1\ bar} = 450\ ^\circ C\ \Delta G_r \approx 0\ J\ mol^{-1} \quad (4)$$

Reaction scheme (4) suggests that a higher loading of $BaSiO_3$ is necessary to increase the CO_2 cyclic capacity, as a part of the $BaSiO_3$ is consumed in this reaction and thus is not available for reaction with $BaCO_3$ to cycle through reaction scheme (2). This is further supported by TGA data on sample **S5** after 25 cycles

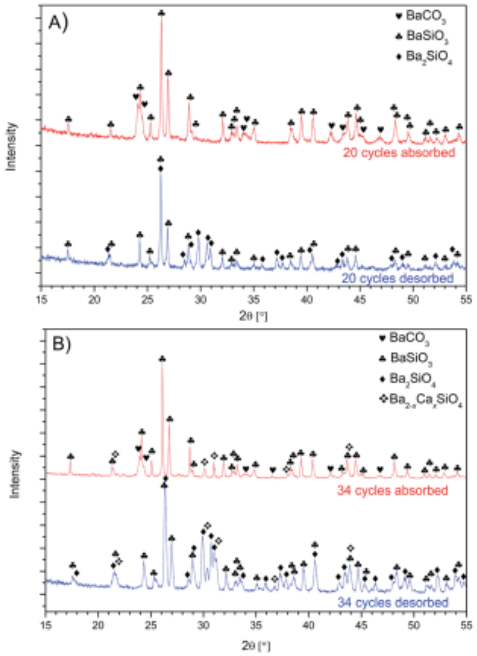

Fig. 4 PXD data ($\lambda = 1.54056$ Å) of (A) the cycled $BaCO_3$–$BaSiO_3$ (S1) in the CO_2 absorbed and desorbed state confirming the expected reaction (2) occurring and (B) the cycled $BaCO_3$–$BaSiO_3$–0.052$CaCO_3$ (S2) in the CO_2 absorbed and desorbed state showing the influence of $CaCO_3$ on the system.

and absorption, where two calcination steps are observed; the first from reaction (2) and the second from leftover $BaCO_3$ (see Fig. S3†).

Insight into the reaction mechanism using *in situ* powder X-ray diffraction

The *in situ* SR-PXD data of $BaCO_3$–$BaSiO_3$ (**S1**) supports the in-house PXD, as the initial sample primarily contains witherite but also a range of Ba–Si–O compounds, *i.e.* $BaSiO_3$, $BaSi_2O_5$, $Ba_4Si_6O_{16}$, and $Ba_5Si_8O_{21}$ (see Fig. 5). Upon heating, the witherite undergoes a first-order polymorphic transition into its high-temperature polymorph (space-group $R\bar{3}m$, $BaCO_3$-HT) between $T \sim 782$ and 835 °C. Simultaneously, Bragg reflections from the reaction product Ba_2SiO_4 appear at $T \sim 782$ °C. The Bragg reflections from $BaCO_3$-HT indicate that one, or more, unit cell axes expand while one or more contract as some reflections move towards lower angle and some towards higher angle, respectively. Bragg reflections from $BaCO_3$-HT disappear at $T \sim 940$ °C, however, the low temperature polymorph is not re-formed upon cooling, hence it is concluded that $BaCO_3$ is consumed in reaction (2). The slow and continuous formation of Ba_2SiO_4 at $T \sim 940$ °C

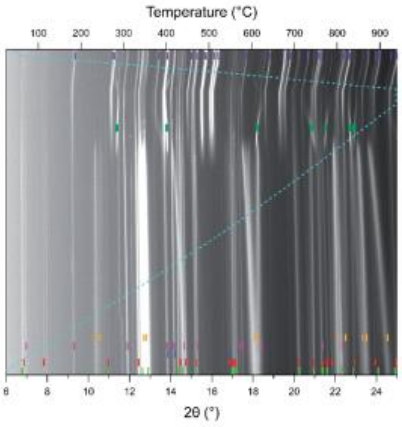

Fig. 5 *In situ* SR-PXD data of $BaCO_3$–$BaSiO_3$ (S1) heated from room temperature to 935 °C ($\Delta T/\Delta t$ = 6 °C min^{-1}; λ = 0.825018 Å, $p(CO_2)$ = 1 bar). Colour code: $BaCO_3$ (orange); $BaCO_3$-HT (dark green); $BaSi_2O_5$ (pink), $BaSiO_3$ (blue); $Ba_5Si_8O_{21}$ (red); $Ba_4Si_6O_{16}$ (green); Ba_2SiO_4 (purple). The dashed line represents the temperature profile.

supports the broad DSC signal previously observed over a wide temperature range as reaction kinetics are slow (see Fig. 1). During cooling, the Ba_2SiO_4 undergoes thermal contraction. Similarly, *in situ* SR-PXD data of $BaCO_3$–$BaSiO_3$–$0.224CaCO_3$ (**S4**) is presented in Fig. S7,† while the main difference at high temperature (850 °C) between samples **S1** and **S4** is highlighted in Fig. 6. The presence of $Ba_{2-x}Ca_xSiO_4$ and a lower fraction of Ba_2SiO_4 in sample **S4** is believed to be the reason for the major difference observed in reaction kinetics.

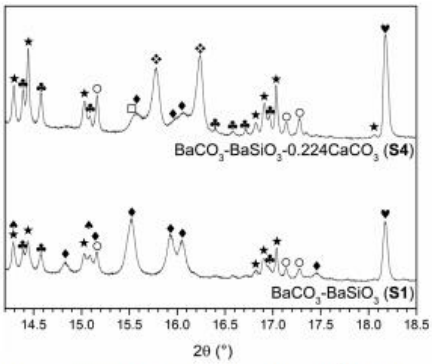

Fig. 6 Comparison of *in situ* SR-PXD (λ = 0.825018 Å) data of $BaCO_3$–$BaSiO_3$ (S1) and $BaCO_3$–$BaSiO_3$–0.224$CaCO_3$ (S4) at T = 850 °C and $p(CO_2)$ = 1 bar. Markers: $BaCO_3$-HT (heart); $CaCO_3$ (open square), $BaSi_2O_5$ (open circle), $BaSiO_3$ (spades); $Ba_5Si_8O_{21}$ (clove); $Ba_4Si_6O_{16}$ (star); Ba_2SiO_4 (diamonds); $Ba_{2-x}Ca_xSiO_4$ (four squares).

Influence on activation energy

The activation energy, E_a, was determined for the calcination (CO_2 release) of $BaCO_3$ in the as-milled and cycled samples of $BaCO_3$–$BaSiO_3$ (**S1**), $BaCO_3$–$BaSiO_3$–0.052$CaCO_3$ (**S2**), and $BaCO_3$–$BaSiO_3$–0.105$CaCO_3$ (**S5**) based on Kissinger's relation:

$$\ln[\beta/T_p^2] = -E_a/RT_p + A \quad (5)$$

here, β is the heating rate, T_p is the DSC peak temperature for calcination, E_a is the activation energy of calcination, R is the gas constant, and A is a reaction specific constant. The sample (**S1**) was thus calcinated at three different heating rates, *i.e.* $\Delta T/\Delta t$ = 10, 20, and 30 K min^{-1} (Fig. 7a) and the peak endotherm temperature was determined to be 994, 1040, and 1065 °C,

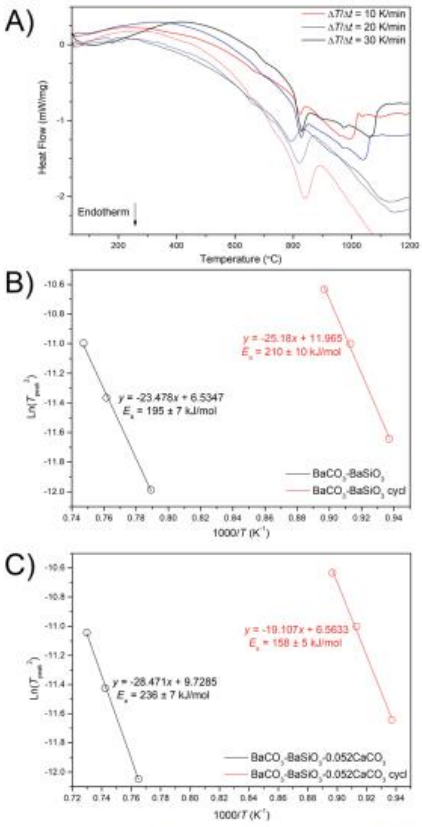

Fig. 7 Differential scanning calorimetry of (A) as-milled $BaCO_3$–$BaSiO_3$ (S1, bold line) and the cycled S1 sample (thin line) at three different heating rates to construct (B) the Kissinger plot of $BaCO_3$–$BaSiO_3$. (C) The Kissinger plot of $BaCO_3$–$BaSiO_3$–0.052$CaCO_3$ (S2). The slope of the Kissinger plot makes it possible to extract the activation energy, E_a, of calcination.

respectively. A Kissinger plot was constructed (Fig. 7b), and the activation energy for calcination of the $BaCO_3$–$BaSiO_3$ composite (**S1**) was determined to 195 ± 7 kJ mol^{-1}. In comparison, the calcination activation energy of pristine $BaCO_3$ has been reported between 283–305 kJ mol^{-1} (vacuum and argon flow, respectively).[24,30] Hence, a significant decrease in the decomposition activation energy is observed in the thermodynamically destabilised $BaCO_3$–$BaSiO_3$ composite. The activation energy was further determined for the $BaCO_3$–$BaSiO_3$ reactive carbonate composite after 35 cycles of calcination/carbonation and it is evident that the activation energy increases slightly to 210 ± 10 kJ mol^{-1}, which agrees well with the rather constant reaction kinetics observed throughout cycling (see Fig. S4†).

The opposite effect is observed for the $CaCO_3$ catalysed sample (**S2**), where an activation energy for the as-milled sample is determined to be 236 ± 7 kJ mol^{-1} (Fig. 7c), which is slightly higher than that for the primary $BaCO_3$–$BaSiO_3$ composite (**S1**). It is hypothesised to be due to either a slight difference in particle size arising from ball-milling or the additional reaction of Ca^{2+} incorporation into the Ba_2SiO_4 structure. However, after the conducted cyclic measurements, the activation energy is eventually lowered to 158 ± 5 kJ mol^{-1} after 34 cycles (see Fig. 7c), which is lower than the uncatalysed sample and in agreement with the observed increase in reaction kinetics, see Fig. S4.† The DSC data for sample **S2** is presented in Fig. S8† while the activation energies of sample **S5** is presented in Fig. S9.†

Sample morphology

The as-milled samples of $BaCO_3$–$BaSiO_3$(–$CaCO_3$, 2.5, 5, and 10 wt%; **S1–S4**, respectively) all reveal large particles are present (>10 μm), which are identified through EDS mapping to be Ba depleted and mainly contain Si and O, *i.e.* SiO_2 (see Fig. 8a). The presence of large SiO_2 particles are still evident after CO_2 cycling of the samples, illustrated by sample **S2** in Fig. 8b. Hence, this impurity, present in the commercial $BaSiO_3$, does not participate in the reaction and thus the low cyclic capacity of <50% is believed to be due to the discrepancy in molar ratio between $BaCO_3$ and $BaSiO_3$. The SiO_2 was not identified through PXD and is thus believed to be amorphous.

The $BaCO_3$–$BaSiO_3$(synthesised)–0.105$CaCO_3$ sample (**S5**) does not contain large SiO_2 particles, possibly due to the starting reagent being nanoparticle size, and thus the sample is more homogenous and leads to a higher energy capacity through increased reactivity. Generally, sintering seems not to be an issue, as seen in other carbonate systems,[9] as the reverse reaction (reaction scheme (**2**)) ensures segregation of the reactants whilst maintaining a good surface contact. The as-milled sample **S5** has calcium and silicon rich regions (see Fig. S10†). However, after cycling and absorption, the elements are well distributed in the sample as evident from Fig. 8c. This may also explain the stabilisation in reaction kinetics after cycling, once the sample morphology is uniform.

Cost analysis

A cost comparison between the developed $BaCO_3$-based thermochemical energy storage material, the state-of-the-art molten salt and a previously suggested Li_2CO_3-based material is given in Table 2. Although the Li_2CO_3–Li_2SiO_3 system shows a good cyclability at ~100% over 5 cycles at 700 °C, the expensive $LiCO_3$ makes the materials cost for producing a thermal energy storage system capable of storing 1 TJ_e ~10 times more

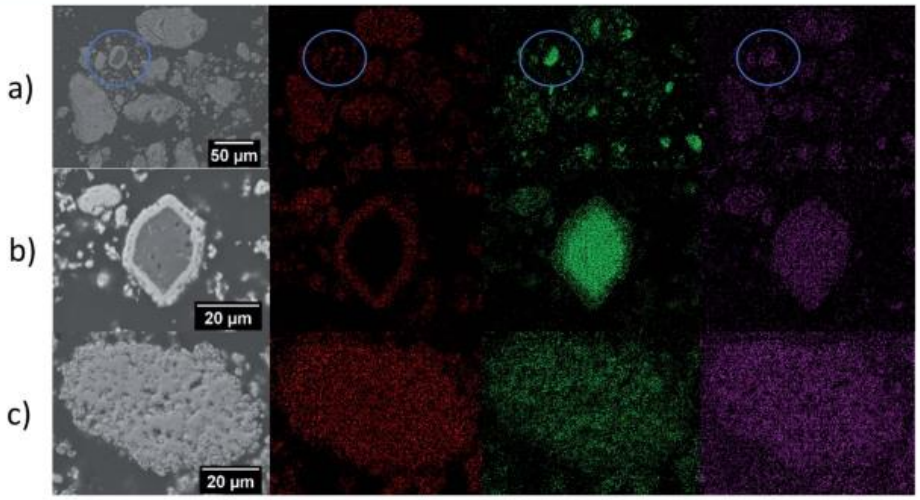

Fig. 8 SEM and EDS of (a) sample S2 as-milled. The blue highlight marks a region rich in SiO_2 (b) sample S2 after 34 cycles and absorbed and (c) sample S5 after 25 cycles and absorbed. Element colour code: Ba: red; Si: green; O: purple.

Table 2 Cost comparison (USD) of materials for producing 1 TJ of electrical energy

	Molten salt ($40NaNO_3$:$60KNO_3$)	Li_2CO_3 + Li_2SiO_3 ⇄ Li_4SiO_4 + CO_2	$BaCO_3$ + $BaSiO_3$ ⇄ Ba_2SiO_4 + CO_2
Enthalpy ΔH (kJ mol^{-1})	39.0	109.0	126.9
Molar mass (g mol^{-1})	94.60	163.86	410.75
Density (g cm^{-3})	2.17	2.3[d]	4.4[e]
CO_2 capacity (wt%)	—	26.86	10.71
Gravimetric energy density (kJ kg^{-1})	413	665	309
Volumetric energy density (MJ m^{-3})[a]	895	1530	1359
Operating temperature range (°C)	290–565	700	850
Operating pressure range (bar)	—	0.1–0.8	5–25
Carnot efficiency (%)[b]	46	69	73
Estimated practical efficiency (%)	27	44	48
Mass required (tonnes)[c]	9100	3401	6903
Volume required (m^3)[f]	4194	1479	1569
Materials cost ($ per tonne)[14,17,31]	630	17 000[f]	494[f]
Total materials cost required ($)[c]	**5 730 000**	**57 800 000**	**3 410 000**

[a] Based on crystalline data. [b] Lower temperature. [c] To generate 1 TJ of electrical energy. [d] Applies to Li_4SiO_4. [e] Applies to the mixture $BaCO_3$–$BaSiO_3$. [f] Based entirely on the cost of M_xCO_3, as this is also the starting reagent for synthesising M_xSiO_3 (M = Li or Ba).

expensive than molten salts. Thus, an energy storage system based on this material is unlikely to be commercial. Additionally, the high cyclic stability is attributed to melting of Li_2CO_3, which enhances CO_2 diffusivity, but also increases requirements for the materials container to avoid molten salt corrosivity, *i.e.* the engineering costs may also be increased. Contrary, the $BaCO_3$–$BaSiO_3$ system materials are ~40% cheaper than molten salt while the footprint of the system is also reduced (~1/3), which makes it worth considering as a successor for current technology. The higher operating temperature (850 *vs.* 550 °C) and thus higher Carnot efficiency is favourable and makes the system compatible with the Rankine–Brayton combined cycle and Stirling engines for thermal to electrical energy conversion.[32] Finally, abundance of the materials play a crucial role, *i.e.* $BaCO_3$ is widely available, whereas shortage of battery-quality lithium and other battery components, *e.g.* cobalt, may become an issue if large-scale thermal energy storage and electrical vehicles adopt lithium-ion batteries as their main storage system.[17,33,34]

Conclusions

Thermodynamic destabilisation of $BaCO_3$ is achieved by addition of $BaSiO_3$, which promotes a chemical reaction on CO_2 release resulting in a lowering of the decomposition temperature of $BaCO_3$ by more than 350 °C. Hence, $BaCO_3$ is tailored for utilisation in thermal energy storage applications. The commercial sample of $BaSiO_3$ contains a large quantity of impurities, *e.g.* large particles of SiO_2, which hampers the cyclic energy storage capacity of the $BaCO_3$–$BaSiO_3$ system compared to the more pure, synthesised $BaSiO_3$, which provides the highest energy capacity retention, *i.e.* ~60%, which is very close to the theoretical maximum determined to be 62.4%. The capacity may be improved by optimising the molar ratio of $BaCO_3$ to $BaSiO_3$ and $CaCO_3$ as the formation of Ca_2SiO_4 and eventually $Ba_{2-x}Ca_xSiO_4$ is evident, while unreacted SiO_2 is also found in sample **S5**. Hence, $BaSiO_3$ and $BaCO_3$ are consumed, which leaves a discrepancy in molar ratio causing an energy capacity loss as the pristine $BaCO_3$ is thermodynamically too stable to calcine at the physical conditions applied here. Addition of $CaCO_3$ in various amounts, *i.e.* 2.5–10 mol%, significantly improves the reaction kinetics by up to 10 times, through the formation of $Ba_{2-x}Ca_xSiO_4$ intermediates. However, addition of 10 mol% influences the energy capacity negatively. The possibility to significantly improve reaction kinetics by introducing a second metal carbonate is a new, interesting approach, which opens up new avenues for future research in this materials class for thermal energy storage. Finally, it is proven here that $BaCO_3$ is able to operate at 850 °C, which is suitable in combination with a Stirling engine. However, lowering the temperature to 670 °C where the equilibrium pressure is 1 bar makes it suitable to combine with commercially available steam turbines, and may thus be worth further investigation.

Conflicts of interest

There are no conflicts to declare.

Acknowledgements

KTM acknowledges the Independent Research Fund Denmark for an International Postdoctoral Grant (case-number: 8028-00009B). MP and CEB acknowledges the Australian Research Council for FT160100303 and LP150100730, respectively. CEB, MP, and KTM acknowledge the Global Innovation Linkage Project for grant GIL73589. KW acknowledge the Australian Government for an Australian Government Research Training Program Scholarship. Part of this research was undertaken using the EM/XRD instrumentation (ARC LE0775553 and LE0775551) at the John de Laeter Centre, Curtin University. Dr Nigel Chen-Tan and Anna Emenheiser are acknowledged for assistance with initial sample preparation and thermal stability

analysis. ANSTO is acknowledged for providing access to the PD beamline at the Australian Synchrotron, Melbourne, Australia.

References

1 K. T. Møller, D. Sheppard, D. B. Ravnsbæk, C. E. Buckley, E. Akiba, H.-W. Li and T. R. Jensen, *Energies*, 2017, **10**, 1645.
2 K. T. Møller, T. R. Jensen, E. Akiba and H. Li, *Prog. Nat. Sci.: Mater. Int.*, 2017, **27**, 34–40.
3 M. Paskevicius, L. H. Jepsen, P. Schouwink, R. Černý, D. B. Ravnsbæk, Y. Filinchuk, M. Dornheim, F. Besenbacher and T. R. Jensen, *Chem. Soc. Rev.*, 2017, **46**, 1565–1634.
4 D. N. Harries, M. Paskevicius, D. A. Sheppard, T. E. C. Price and C. E. Buckley, *Proc. IEEE*, 2012, **100**, 539–549.
5 H. Zeng, F. Sun, W. Ge, A. Su, K. Gao, Y. Ge, T. Li, Y. Zhu, B. Shao, T. Xu, G. Liu, J. Whng, Y. Duan, X. Quan, L. Yue, K. Xu, M. Sun, J. Tang, F. Jiang, D. Cui, Z. Feng and A. Liu, in *2018 China International Conference on Electricity Distribution (CICED)*, 2018, pp. 2895–2900.
6 T. D. Humphries, K. T. Møller, W. D. A. Rickard, M. V. Sofianos, S. Liu, C. E. Buckley and M. Paskevicius, *J. Mater. Chem. A*, 2019, **7**, 1206–1215.
7 A. A. Olajire, *J. Pet. Sci. Eng.*, 2013, **109**, 364–392.
8 H. Geerlings and R. Zevenhoven, *Annu. Rev. Chem. Biomol. Eng.*, 2013, **4**, 103–117.
9 A. J. Carrillo, J. González-Aguilar, M. Romero and J. M. Coronado, *Chem. Rev.*, 2019, **119**, 4777–4816.
10 A. Bayon, R. Bader, M. Jafarian, L. Fedunik-Hofman, Y. Sun, J. Hinkley, S. Miller and W. Lipiński, *Energy*, 2018, **149**, 473–484.
11 L. André, S. Abanades and G. Flamant, *Renewable Sustainable Energy Rev.*, 2016, **64**, 703–715.
12 C. Ortiz, J. M. Valverde, R. Chacartegui and L. A. Perez-Maqueda, *ACS Sustainable Chem. Eng.*, 2018, **6**, 6404–6417.
13 K. T. Møller, *et al.*, *J. Mater. Chem. A*, 2020, **8**, 9646–9653.
14 P. M. Dibello, J. L. Manganaro, E. R. Aguinaldo, T. Mahmood and C. B. Lindahl, in *Kirk-Othmer Encyclopedia of Chemical Technology*, American Cancer Society, 2003.
15 L. André and S. Abanades, *Journal of Energy Storage*, 2017, **13**, 193–205.
16 H. Takasu, J. Ryu and Y. Kato, *Appl. Energy*, 2017, **193**, 74–83.
17 U.S. Geological Survey, *U.S. Geological Survey Mineral Commodity Summaries 2019*, available at: https://pubs.er.usgs.gov/publication/70202434, accessed 11-05-2020.
18 Outukumpu, *HSC Chemistry*, Houston, 1 edn, 2006, vol. 6.
19 D. A. Sheppard, M. Paskevicius, P. Javadian, I. J. Davies and C. E. Buckley, *J. Alloys Compd.*, 2019, **787**, 1225–1237.
20 E. W. Lemmon, *NIST Standard Reference Database 23: Reference Fluid Thermodynamic and Transport Properties—REFPROP*, 2013.
21 K. S. Wallwork, B. J. Kennedy and D. Wang, *AIP Conf. Proc.*, 2007, **879**, 879–882.
22 S. M. Antao and I. Hassan, *Phys. Chem. Miner.*, 2007, **34**, 573–580.
23 T. Kanti Basu and A. W. Searcy, *J. Chem. Soc., Faraday Trans. 1*, 1976, **72**, 1889–1895.
24 I. Arvanitidis, Du. Siche and S. Seetharaman, *Metall. Mater. Trans. B*, 1996, **27**, 409–416.
25 J. J. Lander, *J. Am. Chem. Soc.*, 1951, **73**, 5893–5894.
26 S. Nie, Y. Liu, Q. Liu, M. Wang and H. Wang, *Eur. J. Mineral.*, 2017, 433–443.
27 L. L. Y. Chang, *J. Geol.*, 1965, **73**, 346–368.
28 K. Fukuda, M. Ito and T. Iwata, *J. Solid State Chem.*, 2007, **180**, 2305–2309.
29 B. Matković, S. Popović, B. Gržeta and R. Halle, *J. Am. Ceram. Soc.*, 1986, **69**, 132–134.
30 M. Judd and M. Pope, *J. Therm. Anal. Calorim.*, 1972, **4**, 31–38.
31 C. Y. Zhao, Y. Ji and Z. Xu, *Sol. Energy Mater. Sol. Cells*, 2015, **140**, 281–288.
32 V. Zare and M. Hasanzadeh, *Energy Convers. Manage.*, 2016, **128**, 227–237.
33 J. F. Peters and M. Weil, *Resources*, 2016, **5**, 46.
34 T. P. Narins, *Extr. Ind. Soc.*, 2017, **4**, 321–328.

Electronic Supplementary Material (ESI) for Journal of Materials Chemistry A.

Supplementary Information:

Thermochemical Energy Storage Properties of a Barium Based Reactive Carbonate Composite

Kasper T. Møller,[1*] Kyran Williamson,[1] Craig E. Buckley,[1] Mark Paskevicius[1*]

[1]*Department of Imaging and Applied Physics, Fuels and Energy Technology Institute, Curtin University, GPO Box U1987, Perth 6845, WA, Australia.*

*Corresponding Authors

Kasper T. Møller, kasper.moller@curtin.edu.au and Mark Paskevicius, mark.paskevicius@gmail.com

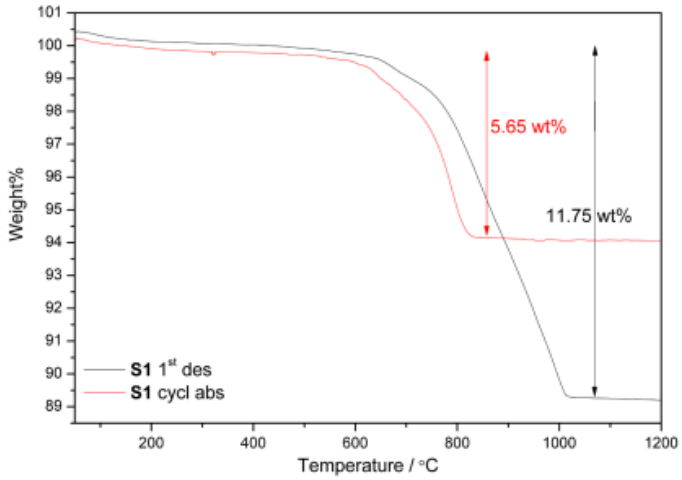

Figure S1. Thermogravimetric data for $BaCO_3$-$BaSiO_3$ (**S1**) as-milled (black line) and of the cycled sample (red line, 20 cycles). $\Delta T/\Delta t$ = 10 K min^{-1}, 20 mL argon flow.

The TG data of **S1** shows a slightly high weight loss of 11.75 wt% compared to the theoretical maximum of 10.71 wt%, which may be due to moisture present on the surface of the sample. The sample after 20 cycles and absorption displays a weight loss of 5.65 %, which equals a capacity retention of 52.7 %. The latter is slightly higher than the 40 - 45 % observed in the Sieverts measurements.

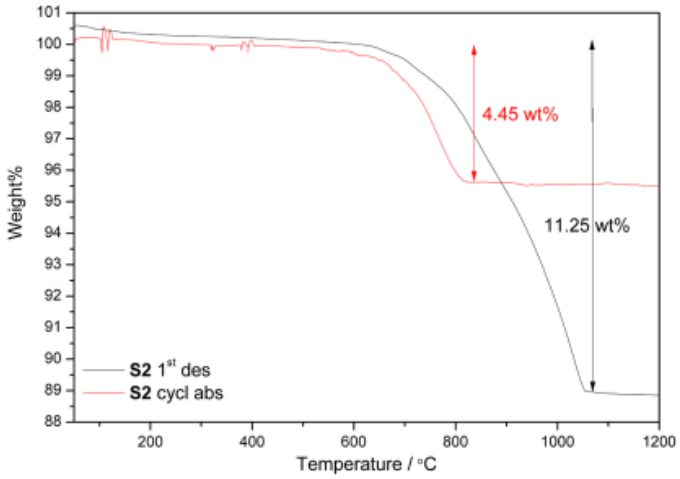

Figure S2. Thermogravimetric data for $BaCO_3$-$BaSiO_3$-0.052$CaCO_3$ (**S2**) as-milled (black line) and of the cycled sample (red line). $\Delta T/\Delta t$ = 10 K min^{-1}, 20 mL argon flow.

The TG data of **S2** shows a slightly high weight loss of 11.25 wt% compared to the theoretical maximum of 11.12 wt% (including decomposition of $CaCO_3$), which may be due to a minor amount of moisture present on the surface of the sample. The sample after cycling and absorption displays a weight loss of 4.45 %, which equals a capacity retention of 42.1 %. The latter is in agreement with the ~ 45 % observed in the Sieverts measurements.

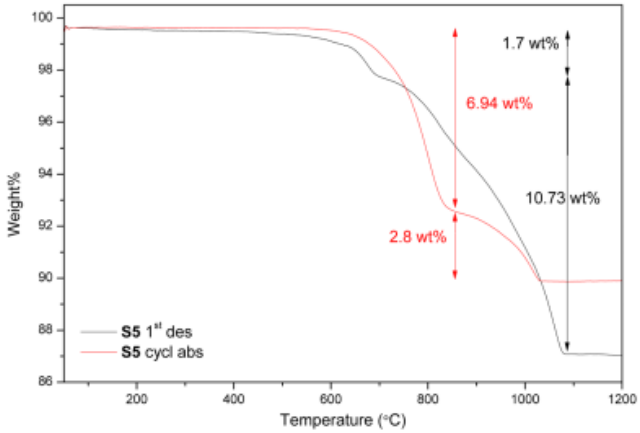

Figure S3. Thermogravimetric data for $BaCO_3$-$BaSiO_3$(synth)-0.105$CaCO_3$ (**S5**) as-milled (black line) and of the cycled sample (red line). $\Delta T/\Delta t$ = 10 K min^{-1}, 20 mL argon flow.

The TG data on sample **S5** indicates that reaction 4 takes place, *e.g.* $BaSiO_3$ reacts with $CaCO_3$ to form Ca_2SiO_4, evident from the 1.7 wt% mass loss and the DSC signals between 685 – 735 °C (heat rate dependent, see Figure S9). The total mass loss is 12.43 wt%, which indicates that a small amount of moisture is present, as the theoretical mass loss is 11.54 wt%. The sample **S5** (cycled and absorbed) shows a similar trend as sample **S2** with decomposition initiating at $T \sim 600$ °C. However, a second desorption step is observed, which originates from calcination of excess $BaCO_3$.

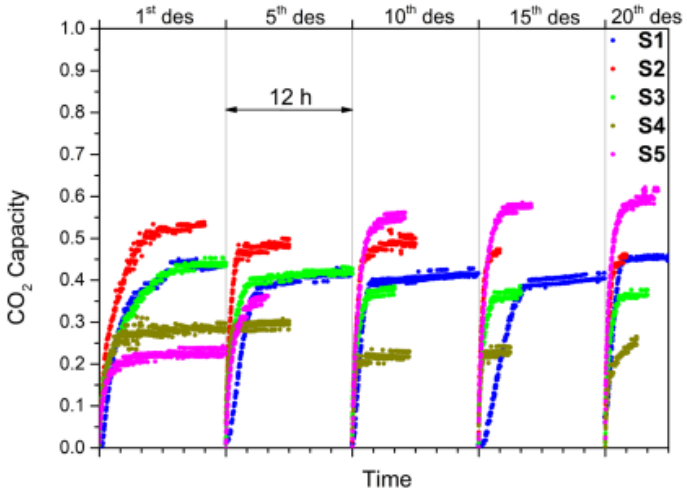

Figure S4. Comparison of the reaction kinetics every 5th desorption highlighting the effect of adding $CaCO_3$ to the system.

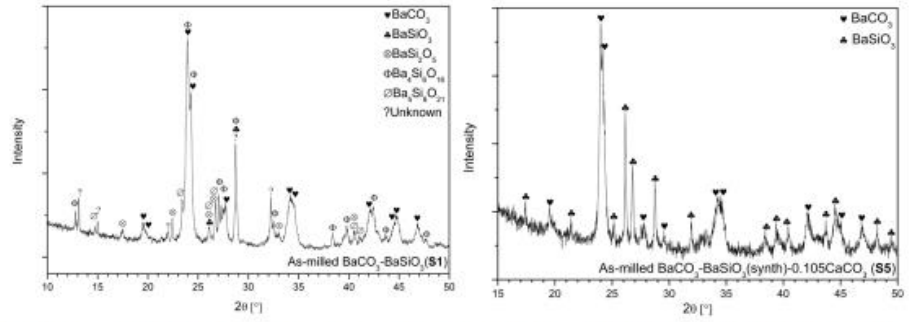

Figure S5. PXD data (λ = 1.54056 Å) of *left*: as-milled $BaCO_3$-$BaSiO_3$ (**S1**) highlighting the different Ba-Si-O compositions initially present in the sample originating from impure, commercial $BaSiO_3$, and *right*: as-milled $BaCO_3$-$BaSiO_3$(synthesised)-0.105$CaCO_3$ (**S5**) highlighting the insignificant influence $CaCO_3$ has on the PXD pattern.

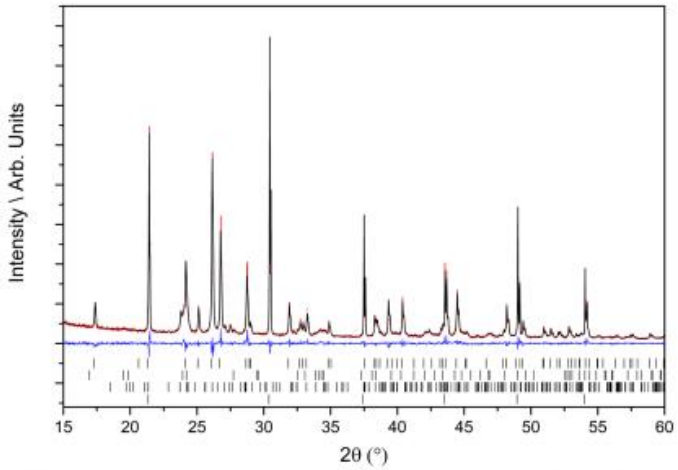

Figure S6. Rietveld refinement of the as-synthesised $BaSiO_3$ with 21.2 wt% added NIST LaB_6 standard revealing that the sample contains $BaSiO_3$ (62.1 wt%), $BaCO_3$ (10.0 wt%), $Ba_4Si_6O_{16}$ (8.1 wt%), and a large amorphous content (19.8 wt%). Y_{obs}: red; Y_{calc}: black; Y_{diff}: blue. *hkl* markers (bottom singular markers) from top to bottom: $BaSiO_3$, $BaCO_3$, $Ba_4Si_6O_{16}$, LaB_6. R_{wp} = 6.18 %; λ = 1.54056 Å.

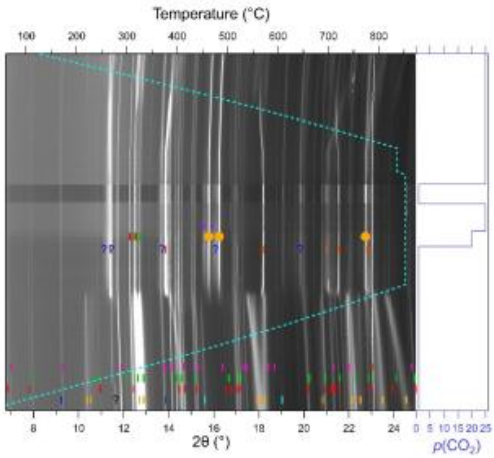

Figure S7. *In situ* SR-PXD data of $BaCO_3$-$BaSiO_3$-0.224$CaCO_3$ (**S4**) with added diamond heated from room temperature to 850 °C ($\Delta T/\Delta t$ = 6 °C min^{-1}; λ = 0.825018 Å, $p(CO_2)$ = 1 bar). Colour code: $BaCO_3$ (Orange); $BaCO_3$-HT (dark green); $BaSi_2O_5$ (pink), $BaSiO_3$ (blue); $Ba_5Si_8O_{21}$ (red); $Ba_4Si_6O_{16}$ (green); $Ba_{2-x}Ca_xSiO_4$ (orange circles); Diamond (gold); $CaCO_3$ (turqoise); Unknown 1 (black question mark); Unknown 2 (blue question mark).

The *in situ* SR-PXD data of $BaCO_3$-$BaSiO_3$-0.224$CaCO_3$ (**S4**) reveals a complex system where a partial substitution of Ca_2SiO_4 into Ba_2SiO_4 resulting in a $Ba_{2-x}Ca_xSiO_4$ compound seem to occur simultaneously with the appearance of Ba_2SiO_4 and an unknown intermediate (Unknown 2), which is believed to be a metastable Ba-Si-O compound, as it is not observed in the *ex situ* PXD. Although the CO_2 pressure is varied, no significant changes are observed due to slow reaction kinetics. However, the $Ba_{2-x}Ca_xSiO_4$ compound may be key to enhanced reaction kinetics, as the introduction of the smaller Ca cation induces distortions of the unit cell and thus creates structural defects, which enables a higher reactivity with the CO_2 gas. Thus the observed increase in reaction kinetics.

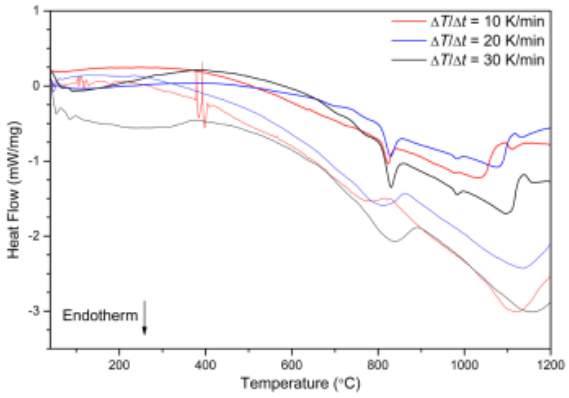

Figure S8. DSC data of as-milled $BaCO_3$-$BaSiO_3$-0.052$CaCO_3$ (**S2**, bold) and the absorbed cycled **S2** sample (thin line).

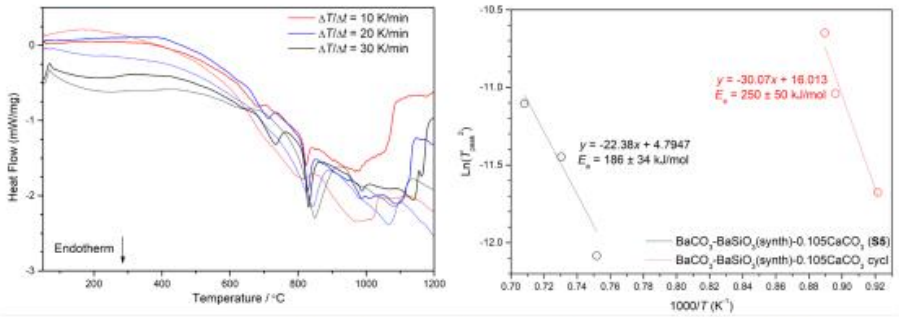

Figure S9. Differential Scanning Calorimetry of as-milled $BaCO_3$-$BaSiO_3$(synth)-0.105$CaCO_3$ (**S5,** bold line) and after 25 calcination/carbonation cycles (thin line) at three different heating rates to construct (B) the Kissinger plot. The slope of the Kissinger plot makes it possible to extract the activation energy, E_a, of calcination.

Figure S9 shows the DSC data and the corresponding Kissinger plot of the sample $BaCO_3$-$BaSiO_3$(synth)-0.105$CaCO_3$ (**S5**). The DSC signal at T ~ 700 °C belongs to the reaction between excess SiO_2 and $BaCO_3$, which is also evident in Figure S3. The signal at T ~ 800 °C originates from the phase transition of $BaCO_3$ in the as-milled sample, whilst it represents the decomposition of $BaCO_3$ in the cycled sample. The activation energy for the as-milled sample is determined to be 186 ± 34 kJ mol^{-1}, which is the lowest compared to samples **S1** and **S2** presented in Figure 7. However, a significant increase is observed in the activation energy after 25 calcination/carbonation cycles to 250 ± 50 kJ mol^{-1} although sample **S5** is the most homogenous sample, which enables the highest energy capacity. The increase may be explained by the excess of $BaCO_3$ that does not decompose at 850 °C, but acts as an inert species in the sample.

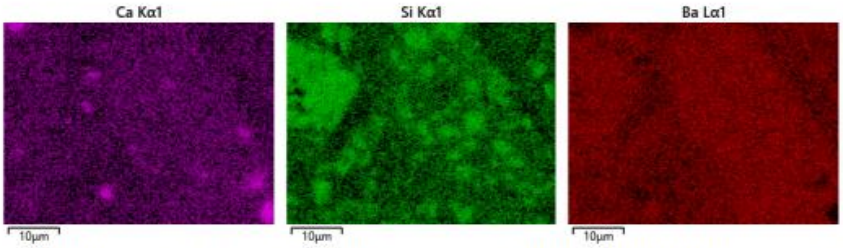

Figure S10. EDS mapping of as-milled $BaCO_3$-$BaSiO_3$(synthesised)-0.105$CaCO_3$ (**S5**) highlighting the Si and Ca rich regions that are present before cycling was initiated.

Appendix B: A New Strontium Based Reactive Carbonate Composite for Thermochemical Energy Storage

---

Vieira, A. P.; Williamson, K.; Humphries, T. D.; Paskevicius, M.; Buckley, C. E. A New Strontium Based Reactive Carbonate Composite for Thermochemical Energy Storage. *J. Mater. Chem. A* **2021**, *9* (36), 20585–20594. https://doi.org/10.1039/D1TA04363C.

Journal of Materials Chemistry A

ROYAL SOCIETY OF CHEMISTRY

PAPER

View Article Online
View Journal | View Issue

Cite this: J. Mater. Chem. A, 2021, 9, 20585

A new strontium based reactive carbonate composite for thermochemical energy storage†

Adriana P. Vieira, * Kyran Williamson, Terry D. Humphries, Mark Paskevicius and Craig E. Buckley *

Received 24th May 2021
Accepted 12th August 2021

DOI: 10.1039/d1ta04363c

rsc.li/materials-a

Stable power generation from renewable energy requires the development of new materials that can be used for energy storage. A new reactive carbonate composite (RCC) based on $SrCO_3$ is proposed as a material with high energy density for thermochemical energy storage. $SrCO_3$–$SrSiO_3$ can promote the thermodynamic destabilisation of $SrCO_3$, making its operating temperature (700 °C) more suitable for concentrated solar thermal power applications. Utilising a eutectic mixture of salts as a catalyst, the reversible carbonation reaction achieves cycle stability of ~80% of efficiency over multiple cycles. The high volumetric (1878 MJ m^{-3}) and gravimetric energy density (500 kJ kg^{-1}) of the RCC allows a compact thermal battery to be developed. Additionally, the low cost of $SrCO_3$ makes the RCC a highly competitive alternative energy storage material in terms of cost and efficiency when compared to existing molten salt based energy storage technology.

Introduction

Motivated by climate emergency concerns, countries around the world have signed the Paris Agreement, which joins forces around the globe to combat climate change.[1] Part of this effort includes the search for attractive alternative energy solutions to replace the use of the current fossil fuels.[1,2] Renewable energy, which can be harnessed from natural resources such as solar, wind, tidal, and geothermal, emerges as an appealing substitute due to its promising social, environmental and economic benefits.

Solar irradiation can directly generate electricity through two main approaches: solar photovoltaic (PV) and concentrated solar thermal power (CSP). Both present limitations in supplying constant power due to the daily, seasonal and climatic dependence of solar irradiation.[3] However, CSP has cost-effective advantages when integrated with a thermal energy storage system (TESS), in which energy can be used during the absence of solar irradiation.[4] A highly efficient TESS can be obtained through the development of low-cost materials with a high energy density that can be used for thermal energy storage.[5,6] Among the three types of TESS, sensible heat storage (SHS) is the only one currently commercially available for CSP applications.[7,8] Typically, this system consists of a two-tank sensible heat energy storage system employing a molten salt consisting of $NaNO_3$ and KNO_3 (60 : 40 wt%), which stores heat using the heat capacity and the change in temperature of the material during the process of charging or discharging the 'thermal battery'.[6,8] Another option is latent heat storage (LHS), where heat is generated/stored when a phase change of the material occurs about some critical temperature.[9] Nevertheless, both SHS and LHS present limitations such as a low energy density, requiring massive storage volumes and material quantities, whilst the corrosion of containment vessels is also a concern.[10] As a promising alternative, thermochemical energy storage (TCES) systems are emerging as a viable option in terms of cost and efficiency, where the TCES materials store energy *via* reversible chemical reactions.[5,6,11,12] In other words, an endothermic reaction absorbs energy (charging the thermal battery), which can then be stored for as long as desired, and then this energy can be released by an exothermic reaction (thermal battery discharge).[13] Furthermore, there is a large selection of materials that can undergo reversible gas–solid reactions, such as metal hydrides, oxides, sulphates, carbonates and hydroxides, all of which present high energy storage densities due to their favourable thermodynamic properties.[5,6,11,14,15] Among them, metal carbonates stand out due to their relatively high operating temperature, typically over 600 °C, possibility of low operating pressure, non-corrosive chemical nature, and also their high abundance and low cost.[16] As such, $CaCO_3$ has recently gained attention, but $BaCO_3$ and $SrCO_3$ are also viable materials despite their high operating temperatures.[5,17,18]

Strontium is the 15th most abundant element on earth,[19] its mineral form $SrCO_3$, also known as strontianite, has been patented as a TCES material in 2011.[20,21] However, only a few studies have been undertaken to improve its efficiency and overcome issues including slow reaction kinetics (eqn (1)) and

Physics and Astronomy, Fuels and Energy Technology Institute, Curtin University, GPO Box U1987, Perth, WA 6845, Australia. E-mail: apiresvieira@gmail.com; c.buckley@curtin.edu.au

† Electronic supplementary information (ESI) available. See DOI: 10.1039/d1ta04363c

particle agglomeration causing loss of cyclability.[17,22,23] MgO, $SrZrO_3$, $CaSO_4$ and $Sr_3(PO_4)_2$ have been introduced as sintering inhibitors and have been shown to improve the cyclability of $SrCO_3$.[17,22,23] Nonetheless, the operational temperature of $SrCO_3$ is greater than 1200 °C (under 1 bar pressure),[24] which is considered too high for next generation TCES for CSP applications, where reaction temperatures between 700 and 1100 °C are desired.[25]

Recently, a novel concept was introduced to utilise reactive carbonate composites (RCC) for TCES, where, for example, a $BaSiO_3$ could be stoichiometrically added to $BaCO_3$ to alter the decomposition reaction pathway, and thus thermodynamically destabilise $BaCO_3$, allowing it to operate at 850 °C, rather than 1200 °C.[12] Studies with Li_2CO_3 and Li_2SiO_3 have also been undertaken to alter reaction thermodynamics, although Li_2CO_3 is quite expensive.[26] The decomposition reaction of $SrCO_3$ is thermodynamically reversible as expressed in eqn (1).[24] The thermodynamics for a solid–gas reaction define the gas pressure required to drive the reaction forward (or reverse) at any particular temperature, denoted as the equilibrium pressure. The 1 bar equilibrium temperature is provided for traditional and destabilised $SrCO_3$ in eqn (1) and (2), defining a desired operating temperature for the reactions where CO_2 release will occur below 1 bar, and CO_2 absorption above 1 bar (Fig. SI-1†).[24] Encouraged by predicted reaction thermodynamics, this study experimentally investigates the energy storage properties of the proposed novel RCC based on $SrCO_3$ and $SrSiO_3$.

$$SrCO_{3(s)} \rightleftharpoons SrO_{(s)} + CO_{2(g)}$$

$$\Delta G_{1220\ ^\circ C} = 0\ \text{J mol}^{-1};\quad \Delta H_{1220\ ^\circ C,\ 1\ \text{bar}} = 201.39\ \text{kJ mol}^{-1}\ CO_2 \tag{1}$$

$$SrSiO_{3(s)} + SrCO_{3(s)} \rightleftharpoons Sr_2SiO_{4(s)} + CO_{2(g)}$$

$$\Delta G_{700\ ^\circ C} = 0\ \text{J mol}^{-1};\quad \Delta H_{700\ ^\circ C,\ 1\ \text{bar}} = 155.75\ \text{kJ mol}^{-1}\ CO_2 \tag{2}$$

Experimental

Chemicals

All chemicals were purchased from Sigma-Aldrich and used as received: strontium carbonate ($SrCO_3$, ≥99.9%); silicon dioxide (SiO_2, 99.5%); sodium chloride (NaCl, ≥99.0%) and magnesium chloride ($MgCl_2$, ≥98.0%).

Synthesis of $SrSiO_3$

$SrSiO_3$ was prepared by a solid-state reaction between $SrCO_3$ and SiO_2 (eqn (3)) according to a method adapted from literature.[27] Firstly, $SrCO_3$ and SiO_2 were separately pre-heated for 3 h at a temperature of 600 °C. A 1 : 1.1 molar mixture ($SrCO_3$: SiO_2) was then ball-milled for 16 hours (60 min milling and 1 min break, repeated 16 times), in stainless steel milling vials (80 mL) with stainless steel balls (10 mm diameter) before heating the powder to 1000 °C for 3 h. All milling was performed using an Across International Planetary Ball Mill (PQ-N04) with a ball-to-powder mass ratio of 10 : 1.

$$SiO_{2(s)} + SrCO_{3(s)} \rightleftharpoons SrSiO_{3(s)} + CO_{2(g)} \tag{3}$$

Sample preparation

Samples of $SrCO_3$ and $SrSiO_3$ (molar ratio 1 : 1) were all ball-milled for 1 hour (20 min milling, 1 min break, repeated three times). When required, a eutectic mixture of $MgCl_2$ and NaCl (molar ratio 0.44 : 0.56)[28] was ground in a mortar and then ball-milled for either 1 or 5 h (using the same protocol above) with the previously ball-milled $SrCO_3$–$SrSiO_3$ mixture in a 20 wt% loading. An overview of samples and preparation methods can be seen in Table 1.

Characterisation

Thermogravimetric analysis (TGA) was performed on a Netzsch STA 449 F3 Jupiter instrument by heating ~10 mg of sample at a rate of 10 °C min^{-1} in an Al_2O_3 crucible covered with a lid with a pin-hole to allow for gas release from room temperature to 1200 °C, under a flowing argon atmosphere (40 mL min^{-1}).

Powder X-ray diffraction (XRD) data were collected on a Bruker D8 Advance equipped with a Cu X-ray source (Cu $K\alpha_{1,2}$ radiation) in flat-plate Bragg–Brentano geometry. Data were collected in the 2θ range 5–80° using a Lynxeye PSD detector. XRD data for the samples after TGA, CO_2 desorption and absorption were collected after the samples were cooled to ambient temperature (25 °C). Diffraction patterns were quantitatively analysed with the Rietveld method[29] using TOPAS (Bruker-AXS).

The specific surface area and the porosity of the samples were determined through nitrogen (N_2) adsorption/desorption measurements at 77 K using a Micromeritics TriStar II plus (Micromeritics, Norcross, GA, USA). N_2 adsorption data, at relative pressures (p/p_0) between 0.05 and 0.30, were used to calculate the specific surface area by employing the Brunauer–Emmett–Teller (BET) multi-point method.[30] The Barrett–Joyner–Halenda (BJH) method from the adsorption branch of the isotherm[31] was used to calculate the average pore width and volume.

Morphological images were collected by Scanning Electron Microscopy (SEM) using a Tescan Mira3 field emission microscope coupled with a secondary electron (SE) and backscattered electron (BSE) detectors and integrated with an Energy Dispersive Spectroscopy (EDS) Oxford Instrument detector controlled by the Aztec software.

The powdered samples were prepared by sputter-coating with 3 nm of Pt and the images collected using an accelerating voltage of 5 kV (for SEM image) and 20 kV (for EDS), aperture size 10 mm, and a working distance of 5 mm.

Table 1 Details of the sample preparation

Samples		wt%	Total ball-milling time (h)	Theoretical CO_2 wt%
S1	$SrCO_3$–$SrSiO_3$ (1 : 1)	100	1	14.14
S2	$SrCO_3$–$SrSiO_3$ (1 : 1)	80	2	9.46
	NaCl : $MgCl_2$ (0.44 : 0.56)	20		
S3	$SrCO_3$–$SrSiO_3$ (1 : 1)	80	6	9.46
	NaCl : $MgCl_2$ (0.44 : 0.56)	20		

Sievert's measurements

CO_2 cycling measurements were performed on a HyEnergy PCTpro E&E with the sample placed in a custom-built SiC sample holder.[32] Samples (~0.5 g) were heated to either 750 or 670 °C at a rate of 10 °C min^{-1} for single-step desorption and absorption measurements. Cycling measurements were undertaken isothermally at 700 °C where desorption and absorption steps were performed under initial $p(CO_2)$ 0.1 and 6.0 bar, respectively, in a reservoir volume of 10.3 cm^3 for 3–6 hours each step of CO_2 desorption and absorption. Overall, the samples were CO_2 cycled >15 times, totalling 204 hours of thermal treatment.

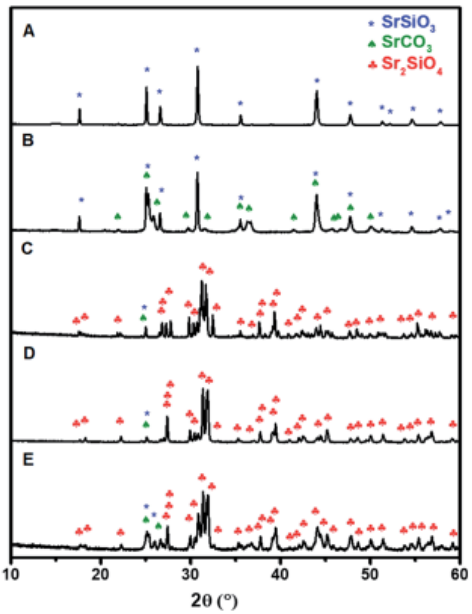

Fig. 1 XRD data of (A) synthesised $SrSiO_3$; (B) S1; (C) S1 after TGA up to 1200 °C; (D) S1 after CO_2 desorption for 14 h, from 0.1 bar at 750 °C; (E) S1 after CO_2 desorption for 14 h, from 0.1 bar at 750 °C and then CO_2 absorption attempt for 35 h under 12 bar at 670 °C. Samples C, D and E were cooled to ambient temperature (25 °C) before analysis.

Results and discussion

Strontium metasilicate, $SrSiO_3$, was successfully synthesised by solid–solid reaction (eqn (3)) as evidenced by the X-ray diffraction data (Fig. 1A), which show peaks corresponding to $SrSiO_3$ with no evidence of impurities. The reactive carbonate composite (RCC), $SrSiO_3$–$SrCO_3$, was also analysed by XRD and is illustrated in Fig. 1B where the characteristic peaks of both individual compounds can be seen. Initial studies by TGA (Fig. 2) show that the decomposition of $SrCO_3$ (eqn (1)) commences at 850 °C through the release of CO_2. TGA of the RCC indicates that the onset temperature of decomposition for $SrSiO_3$–$SrCO_3$ (eqn (2)) is 650 °C and is complete by 980 °C. A weight loss of 14.1% is observed in the TGA curve for $SrSiO_3$–$SrCO_3$, which corresponds to the theoretical CO_2 value desorbed (14.14%). XRD data (Fig. 1C) indicates that strontium orthosilicate, Sr_2SiO_4, is the solid decomposition product of eqn (2), however, traces of $SrSiO_3$ and $SrCO_3$ are also observed, which can be due to the CO_2 reabsorption upon cooling the sample to ambient temperature (25 °C). The combination of XRD and TGA data shows that the RCC thermodynamically destabilises the $SrCO_3$ decomposition pathway, resulting in a lower operating temperature, and as such more favourable for its application as a material for TCES. These experimental results corroborate with the values of Gibbs free energy (ΔG), which are 0 J mol^{-1} at 1220 °C for the decomposition of $SrCO_3$ and at 700 °C for $SrSiO_3$–$SrCO_3$ (see Fig. SI-1† and eqn (1) and (2), respectively).[24]

Temperatures of 750 (p_{eq} = 2.3 bar) and 670 °C (p_{eq} = 0.4 bar)[24] were selected to perform a single CO_2 desorption and

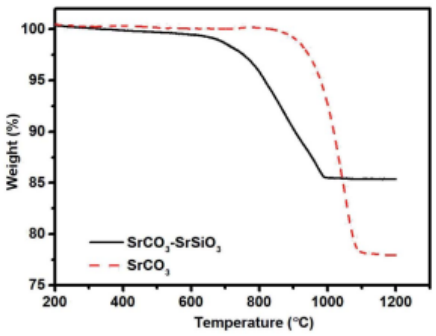

Fig. 2 TGA data for ball-milled (1 h) $SrCO_3$ and $SrCO_3$–$SrSiO_3$.

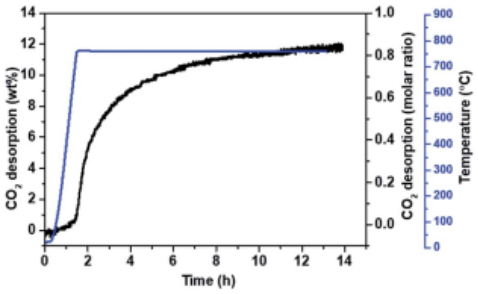

Fig. 3 CO_2 desorption at 750 °C from 0.1 bar to 1.4 bar for S1 sample.

absorption (eqn (2)), respectively, to evaluate the reversibility of the reaction. The desorption of CO_2 was observed at 750 °C (Fig. 3) with approximately 12.1 wt% (0.85 molar ratio) of CO_2 evolved from an expected theoretical value of 14.1 wt%. The kinetics of CO_2 release was slow, with approximately 12 h being required to reach the plateau curve. After a single CO_2 desorption, the sample was cooled to ambient temperature and the XRD data was collected.

Sr_2SiO_4 was observed as the final solid product (Fig. 1D), although traces of $SrSiO_3$–$SrCO_3$ were also detected. Quantitative analysis of the XRD data (Table 2 and Fig. SI-2A†) for S1 after desorption, indicated ~82 wt% Sr_2SiO_4 (in two different crystallographic phases), 7.1 ± 0.7 wt% for $SrSiO_3$ and 10.7 ± 0.8 wt% for $SrCO_3$. The traces of $SrSiO_3$–$SrCO_3$ observed by XRD data may be due to incomplete CO_2 desorption, poor kinetics and the sample desorbed being cooled to ambient temperature before XRD analyses, which can cause CO_2 reabsorption. The desorbed sample S1 was subjected to 12 bar of CO_2 pressure at 670 °C to drive absorption by the pressure differential above the equilibrium pressure of 0.4 bar. Despite the high pressure applied, a significant CO_2 absorption was not observed. The sample was then cooled to ambient temperature and XRD data were collected. Sample S1 after CO_2 desorption and then an absorption attempt (Fig. 1E, Table 2 and Fig. SI-2B†), showed the presence of Sr_2SiO_4 (~61 wt% in two different crystallographic phases), $SrCO_3$ (11.6 ± 0.4 wt%) and $SrSiO_3$ (27.8 ± 0.7 wt%) in the final product. The amount of $SrCO_3$ observed in the sample S1 after desorption and an absorption attempt is similar to the amount of $SrCO_3$ in the sample S1 after desorption (10.7 ± 0.8 wt%), confirming that a significant CO_2 absorption did not occur.

The reversibility of the reaction is theoretically thermodynamically possible at 670 °C under 12 bar of pressure (p_{eq} = 0.4 bar),[24] however, there appears to be a kinetic barrier, which is more pronounced for CO_2 absorption that makes its application for thermochemical batteries unsuitable. Slow reaction kinetics have been observed for other metal carbonate systems.[6,33,34] During the carbonation of Sr_2SiO_4, a $SrCO_3$ layer can be formed on the surface of Sr_2SiO_4, which leads to a CO_2 being inaccessible to the unreacted portion of Sr_2SiO_4 as illustrated in Fig. 1E.[35] To better understand the particle morphology, the specific surface area of ball-milled S1 was measured as 5.92 ± 0.06 $m^2 g^{-1}$, however, after desorption and absorption attempt at elevated temperature, this value decreased to 2.00 ± 0.03 $m^2 g^{-1}$ (Table 3). This represents a loss of approximately 66% of specific surface area with a consequent increase in the average pore width and decrease of the pore volume, as shown in Table 3. The loss of specific surface area and pore volume is evidence of sintering, which is a frequent issue suffered by carbonates over multiple cycles of CO_2 absorption/desorption at high temperature.[17,22,36–38] Therefore, the sintering and agglomeration of the particles reduce the number of sites available for the reaction, which ultimately contributes to the slow kinetics of the reaction.

Scanning electron microscopy SE images presented in Fig. 4A show morphological features for the samples S1 before and after CO_2 desorption and attempt of absorption (Fig. 4A-a and b, respectively). Comparing both samples, it is possible to observe the porous surface in S1 (Fig. 4A-a) and their pore volume decrease in S1 after des/abs (Fig. 4A-b), which corroborates the data in Table 3. In addition, the formation of needle shaped crystals of $SrCO_3$ can be seen along the surface of the sample after CO_2 desorption and absorption attempt (Fig. 4A-b1). $SrCO_3$ with this kind of morphology can be obtained through thermal reaction and has been previously reported.[39,40] It indicates the formation of $SrCO_3$ crystals on the sample surface during the carbonation reaction, which may inhibit the interaction between CO_2 and Sr_2SiO_4, limiting the CO_2 absorption process. EDS mapping shows the spatial

Table 3 Structural properties of samples S1, S2 and S3 before and after cycling determined by BET and BJH analysis

	Specific surface area ($m^2 g^{-1}$)	Pore volume ($cm^3 g^{-1}$)	Average pore width (nm)
S1	5.92 ± 0.06	0.011	7.9
S1 after des/abs	2.00 ± 0.03	0.006	13.6
S2	12.43 ± 0.12	0.006	3.2
S2 after cycles	2.58 ± 0.09	0.004	7.7
S3	21.21 ± 0.16	0.016	4.5
S3 after cycles	3.00 ± 0.06	0.002	5.0

Table 2 Quantitative composition of the crystalline components (wt%) provided from X-ray diffraction-based Rietveld analysis

	Sr_2SiO_4 (orthorhombic)	Sr_2SiO_4 (monoclinic)	$SrSiO_3$	$SrCO_3$	NaCl	$MgCl_2$
S1 after des	80.2 ± 0.7	1.8 ± 0.3	7.1 ± 0.7	10.7 ± 0.8	—	—
S1 after des/abs	51.7 ± 0.8	8.9 ± 0.8	27.8 ± 0.7	11.6 ± 0.4	—	—
S2 after cycles	7.9 ± 0.8	36.0 ± 0.5	22.8 ± 1.8	18.2 ± 1.4	1.1 ± 0.4	13.9 ± 1.2
S3 after cycles	59.2 ± 1.7	8.2 ± 1.3	13.9 ± 0.8	3.2 ± 0.6	3.6 ± 0.5	11.9 ± 1.9

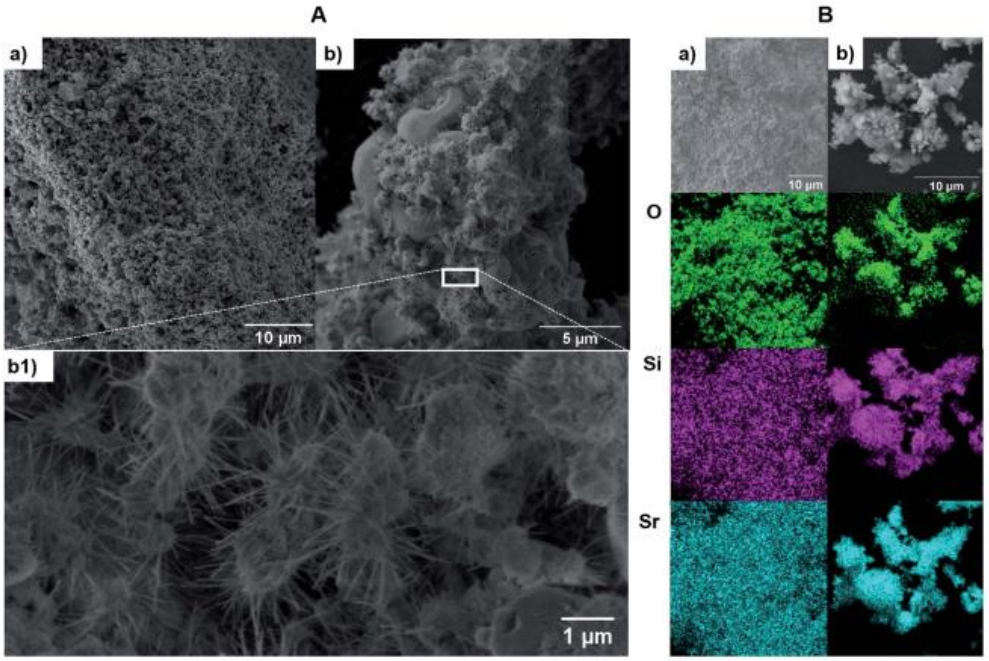

Fig. 4 (A) SEM of the sample (a) S1, (b) S1 after CO_2 desorption and absorption attempt, (b1) S1 after CO_2 desorption and absorption attempt amplified. SE mode, 5 kV. (B) EDS mapping of the sample (a) S1, (b) S1 after CO_2 desorption and attempt of absorption 20 kV.

distribution of the elements in the samples and links their concentration to certain morphologies. Sample S1 before and after des/abs (Fig. 4B-a and b, respectively) shows a homogeneous distribution of O (green), Si (purple) and Sr (cyan). Due to the small size of the needle-shaped crystals of $SrCO_3$, it was not possible to distinguish them from $SrSiO_3$ and Sr_2SiO_4 by the absence of Si by EDS.

In an attempt to improve the reaction kinetics, a eutectic mixture of NaCl and $MgCl_2$ was added to the RCC. Previously, a molten salt mixture of $MgCl_2$ and NaCl (0.438 : 0.562), which has a eutectic point of 442 °C, was reported as a catalyst for improving the CO_2 cycling capacity of $CaMg(CO_3)_2$ (dolomite).[6] In addition, the reasons why the molten salts were selected for this study were the possibility of melting at 700 °C, the high solubility of CO_2 in molten NaCl and $MgCl_2$ and the low cost of both salts.[6,41,42]

To determine the influence of specific surface area of the RCC, $MgCl_2$ and NaCl (0.44 : 0.56) were ball-milled for 1 h (S2) and 5 h (S3) with the previously ball-milled $SrCO_3$–$SrSiO_3$ (S1). The XRD patterns for S2 and S3 are illustrated in Fig. 5B and D, respectively. Comparing the XRD patterns of S2 and S3 with that of S1 (Fig. 5A), it is clear that the only additional peaks observed are characteristic of NaCl (α) and $MgCl_2$ (ϕ). Therefore, no reaction occurred between the salts and the RCC during the ball-mill process.

Sorption studies were undertaken on the catalysed material to assess the reaction rate and yield of CO_2 desorption and absorption for samples S2 and S3 (Fig. 6). By assessing the CO_2 sorption kinetic curves (Fig. 6), it is apparent that the addition of the eutectic salt mixture allows for a substantial improvement in the kinetic rate of reaction, and also promotes the yield of CO_2 release and uptake in comparison to the uncatalyzed sample S1.

In approximately 1 h, S2 and S3 reach the CO_2 desorption plateau with 60 and 70% of the theoretical capacity, respectively, while S1 requires ~12 h to reach the CO_2 desorption plateau (also see Fig. 3). The effect of the catalyst is most important in promoting CO_2 absorption, signified by the CO_2 absorption results (Fig. 6B). S2 showed a CO_2 absorption capacity of 50% of the theoretical capacity while S3 reaches 80% of the CO_2 theoretical capacity.

The $SrCO_3$ crystals on the surface of the sample (confirmed by SEM images in Fig. 4A-b1) that are formed during the carbonation process are covered by the eutectic mixture of salts. At 700 °C the catalyst is molten through the sample (also see Fig. 8). CO_2 is highly soluble in molten NaCl and $MgCl_2$ at atmospheric pressure, as is well known in the literature.[6,41] As a consequence, at 6 bar of pressure, it can dissolve through the molten salts and pass through the $SrCO_3$ layer and unreacted Sr_2SiO_4, promoting CO_2 absorption.[6,43,44] The addition of molten

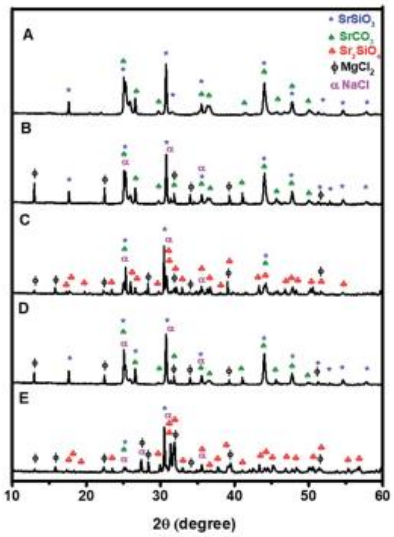

Fig. 5 XRD patterns for (A) S1, (B) S2, (C) S2 after CO_2 cycling (15 cycles, final stage: absorption), (D) S3, (E) S3 after CO_2 cycling (17 cycles, final stage: absorption). Samples C and E were cooled to ambient temperature (25 °C) before analysis.

salts can improve the kinetics of CO_2 des/absorption by metal carbonates. Some studies have been done to elucidate this mechanism and the role of the molten salt on the CO_2 sorption.[43–47] The molten salts may act as a phase transfer catalyst that can remove the high lattice energy restraint which limits direct reaction between the metal oxide and CO_2.[43,48] Essentially, the molten salt allows for some partial solubility of the reactants, which decreases the activation energy of the Sr_2SiO_4 decomposition reaction and improves ion diffusivity.[49] However, further investigations must to be conducted to clarify specific aspects as energy activation for reaction in eqn (2).

The CO_2 sorption kinetics of the catalysed RCC show great promise, which means these doped samples (S2 and S3, ball-milled for different times) were evaluated through multiple CO_2 des/absorption cycles to assess their capacity and reversibility at a single 700 °C operating temperature. The resulting equilibrium pressure of the thermochemical reaction (eqn (2)) is 1 bar, and desorption and absorption were initiated by changing the system gas pressure to 0.1 and 6.0 bar, respectively. For the first cycle, S2 (Fig. 7A) has a CO_2 release of 6.4 wt% CO_2 (68% of the theoretical capacity). The subsequent CO_2 absorption has an uptake of 5.3 wt% of CO_2, corresponding to 54% of the theoretical value. S2 continued to lose capacity from the second cycle, with CO_2 desorption and absorption of 42 and 37% of the theoretical capacity, respectively. The capacity stabilises from the third to fifteenth cycle with a stable ~35% theoretical capacity of CO_2 desorption and absorption for each cycle. S3 (Fig. 7B) showed significantly better sorption capacity with 80% (7.6 wt% CO_2) and 82% (7.7 wt% CO_2) of the CO_2

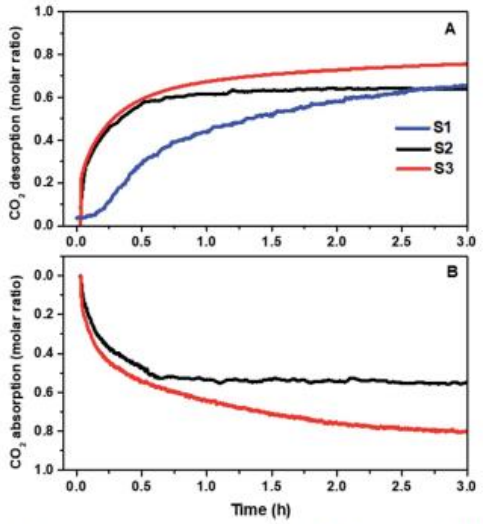

Fig. 6 CO_2 (A) desorption for the samples S1 (initial pressure of 0.1 bar at 750 °C), S2 and S3 (initial pressure of 0.1 bar at 700 °C) and (B) absorption for samples S2 and S3 (desorption from 0.1 bar and absorption under 6.0 bar CO_2 at 700 °C).

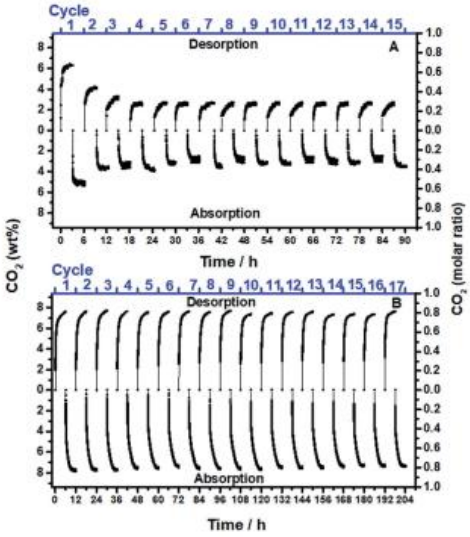

Fig. 7 CO_2 desorption and absorption cycles for the samples (A) S2 and (B) S3. Desorption from 0.1 bar and absorption under 6 bar CO_2 at 700 °C.

theoretical capacity, for desorption and absorption, respectively. Remarkably, this high cyclic capacity remains stable over 17 cycles. Although 17 cycles is generally a low number of cycles, the stability of the material over cycles can show its potential for TCES.

The final sorption capacity for S3 is 14% greater than the 1st sorption cycle for S2. This may be attributed to a diffusion-limited process related to the specific surface area of the materials (Table 3). The key difference between S2 and S3 is that S3 was ball-milled 4 hours longer than S2 (Table 1). As a consequence, S3 has a larger surface area of $21.2 \pm 0.1\ m^2\ g^{-1}$, in comparison with $12.4 \pm 0.1\ m^2\ g^{-1}$ for S2, enabling more active sites for reaction to occur. It is also noted that both samples showed favourable kinetics. However, CO_2 desorption for S2 becomes slow over cycles (Fig. SI-3†). These results highlight the importance of the material's morphology, as in gas–solid reactions a high specific surface area means high reactivity due to the high gas–solid interface that is established. The XRD data of the cycled S2 and S3 materials show that the eutectic mixture ($NaCl : MgCl_2$) does not participate in the reaction and remains inert (Fig. 5C and E). After several cycles, the composition of the samples S2 and S3 are Sr_2SiO_4 (monoclinic and orthorhombic), NaCl, $MgCl_2$, along with remnant $SrSiO_3$ and $SrCO_3$ (see wt% values in Table 2 and Fig. SI-2C, D†). This reinforces that the role of molten salt is to dissolve the CO_2 allowing absorption by Sr_2SiO_4, improving the cycling capacity of the material (eqn (2)).

Despite the existence of two polymorphs of Sr_2SiO_4 (monoclinic and orthorhombic) after several CO_2 cycling, this does not affect the CO_2 cycling stability as can be seen in Fig. 7B.

Scanning electron microscopy SE images presented in Fig. 8A show morphological features for S2 and S3. Comparison between S2 before and S2 after cycling (Fig. 8A-a and b, respectively) shows the formation of needle-shaped extrusions formed by the molten salt mixture upon freezing (identified using EDS mapping). Similar morphologies are observed for the samples of S3 before and after cycling (Fig. 8A-c and d, respectively). EDS mapping for the samples S2 and S3 before cycling (Fig. 8B-a and c, respectively) show a homogeneous distribution of O (green), Si (purple), Sr (cyan) and Mg (blue) and a concentrated area of Cl (yellow), and Na (orange). S2 and S3 after cycling (Fig. 8B-b and d, respectively) show the Sr, Si, O, Cl, Na and Mg through the samples, including in the needle-shaped extrusions that are formed by the molten salt mixture upon freezing.

The appropriate selection of a material for TCES can significantly reduce the capital cost of the CSP plant. Based on the premise that a high energy density allows for a smaller volume of storage materials, leading to a low energy storage cost, $SrCO_3$ has been identified as a competitive alternative for use of molten salts in the near term.[20,50]

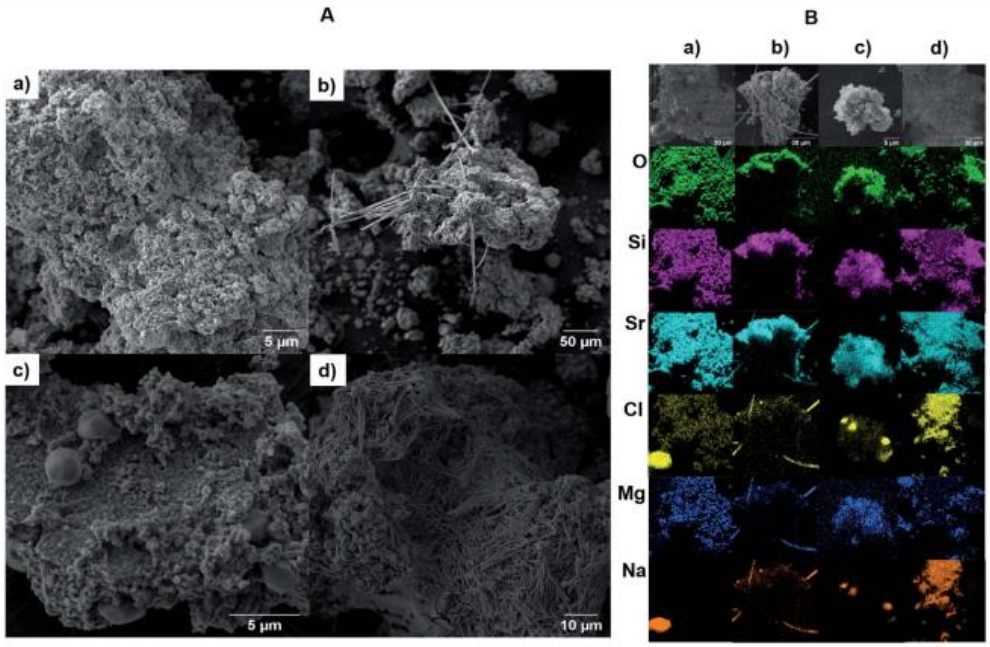

Fig. 8 (A) SEM of the sample (a) S2, (b) S2 after CO_2 cycling, (c) S3, (d) S3 after CO_2 cycling. SE mode, 5 kV. (B) EDS mapping of the sample (a) S2, (b) S2 after CO_2 cycling, (c) S3, (d) S3 after CO_2 cycling 20 kV.

Table 4 Comparison of thermochemical properties, system variables, and cost parameters for select energy storage materials[5,6,12,24]

	$SrCO_3$ + $SrSiO_3$ ⇌ Sr_2SiO_4 + CO_2	$BaCO_3$ + $BaSiO_3$ ⇌ Ba_2SiO_4 + CO_2	Li_2CO_3 + Li_2SiO_3 ⇌ Li_4SiO_4 + CO_2	$CaCO_3$ ⇌ CaO + CO_2	Molten salt (40 $NaNO_3$: 60 KNO_3)
Enthalpy ΔH (kJ mol^{-1})[24]	155.75	126.9	109	165.5	39
Molar mass (g mol^{-1})	311.33	410.75	163.86	100.9	94.6
Density (g cm^{-3})[a]	3.75[b]	4.4[b]	2.3[c]	2.71	2.17
CO_2 capacity (wt%)	14.13	10.71	26.86	44.0	—
Gravimetric energy density (kJ kg^{-1})[a]	500	309	665	1657	413
Volumetric energy density (MJ m^{-3})[a,d]	1878	1359	1530	4489	895
Operating temperature (°C)	700	850	700	900	290–565
Operating CO_2 pressure (bar)	0.1–6.0	5–25	0.1–0.8	—	—
Theoretical carnot efficiency (%)[e]	69	73	69	74	46
Estimated practical efficiency (%)[e]	45	48	44	49	27
Mass required (tonnes)[f]	4700[g]	6903	3401	1228	9100
Volume required (m^3)[f]	1711[g]	1569	1479	453	4194
Materials cost ($ per tonne)[12,42,51]	480[g]	495[h]	17 000[h]	10	630
Total materials cost required ($)[f]	2 258 099	3 410 000	57 800 000	12 298	5 730 000

[a] Intrinsic density. [b] Applies to the mixture MCO_3–$MSiO_3$. [c] Applies to Li_4SiO_4. [d] Based on crystalline data. [e] Lower temperature. [f] To generate 1 TJ of electrical energy. The conversion of thermochemical energy (T_{th}) to electrical energy (E_e) is $E_e = e_p \times E_{th}$, where e_p is the estimated practical efficiency. [g] 80 wt% $SrSiO_3$: $SrCO_3$ + 20 wt% NaCl : $MgCl_2$. [h] Based entirely on the cost of M_xCO_3, as this is also the starting reagent for synthesing M_xSiO_3 (M = Li or Ba).

Furthermore, the $SrCO_3$–$SrSiO_3$ RCC is a better alternative than $SrCO_3$ for next-generation TCES since its operating temperature of 700 °C is more appropriate for CSP while for $SrCO_3$ it is above 1200 °C. Table 4 summarises and compares similar RCC's to $SrCO_3$–$SrSiO_3$ and current-generation molten salts. Li_2CO_3–Li_2SiO_3, despite having a gravimetric and volumetric energy density of 665 kJ kg^{-1} and 1530 MJ m^{-3}, respectively, is extremely expensive making it a poor candidate compared to $SrCO_3$–$SrSiO_3$ and $BaCO_3$–$BaSiO_3$.[12] $SrCO_3$–$SrSiO_3$, in comparison with the $BaCO_3$–$BaSiO_3$ system, has a higher reaction enthalpy, 155.75 kJ mol^{-1} and lower molar mass, 311.33 g mol^{-1}, and consequently, it has a higher gravimetric and volumetric energy density, 500 kJ kg^{-1} and 1878 MJ m^{-3}, respectively. Therefore, this requires a reduced volume and mass of TCES material even with the addition of 20 wt% of catalyst (NaCl : $MgCl_2$) making $SrCO_3$–$SrSiO_3$ the RCC with the best cost-efficiency to generate 1 TJ of electrical energy from these candidates (Fig. 9). The material cost for $SrCO_3$–$SrSiO_3$ (including catalyst) to generate 1 TJ of electrical energy is 60% cheaper than molten salt and 34% cheaper than $BaCO_3$–$BaSiO_3$. In addition, $CaCO_3$ at 900 °C has been considered a potential option for TCES, due to its low cost: USD$ 12 298 to generate 1 TJ of electrical energy.[5] However, $SrCO_3$–$SrSiO_3$ has a lower operation temperature (around 6 bar CO_2 at 700 °C). Other alternative systems, such as $BaCO_3$–$BaSiO_3$ demand higher operational pressures of 5–25 bar CO_2 to function rapidly at 850 °C. It is possible that the lower operational temperature of $SrCO_3$–$SrSiO_3$ and its lower working pressure may reduce the engineering challenges and costs of a full scale TCES.

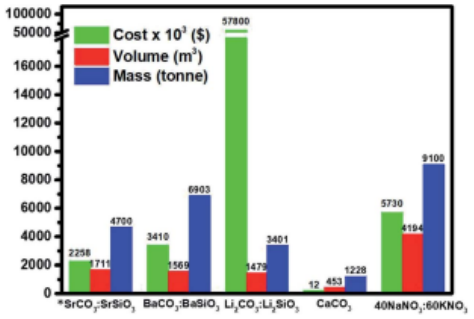

Fig. 9 Materials cost comparison of thermal energy storage options to generate 1 TJ of electrical energy (volume based on crystalline density).*Considering 80 wt% $SrCO_3$–$SrSiO_3$ + 20 wt% NaCl : $MgCl_2$.

The operating temperature is compatible with both the Rankine–Brayton combined cycle and with the Stirling engine for thermal to electrical energy conversion.[52] Apart from the material cost, the operational cost also needs to be taken into account, since the use of carbonates as a thermochemical energy material require CO_2 storage, which can be through a compressed gas or adsorption using a low energy adsorbent. A probabilistic analysis, comparing both CO_2 storage methods showed that the use of an adsorbent has a better cost-benefit.[20] A further decrease in this cost may be achieved using a sorbent under pressure such as activated carbon.[53] Future studies considering the selection of low cost CO_2 adsorbent materials must be performed. Overall, since $SrCO_3$–$SrSiO_3$ has a high volumetric energy density and requires a small footprint, a TCES system based on this material would be ideal for remote areas and can also be adapted for other renewable energy resources such as photovoltaics and wind farms.

Conclusions

The addition of $SrSiO_3$ can thermodynamically destabilise $SrCO_3$ and promotes the CO_2 release from $SrCO_3$, lowering the decomposition temperature from 1200 °C to 700 °C.

Consequently, the reactive carbonate composite (RCC) $SrCO_3$–$SrSiO_3$ can be tailored for application as a thermal energy storage material, as 700 °C is ideal for CSP plant operational conditions. The thermochemical reaction between uncatalyzed $SrCO_3$ and $SrSiO_3$ has slow (>12 h) reaction kinetics, especially during the exothermic absorption of CO_2. The addition of 20 wt% NaCl : $MgCl_2$ catalyst to the RCC promotes a dramatic increase in the kinetics of absorption and desorption of CO_2 to less than 2 h. In addition, increased milling times (5 h) of the RCC with NaCl : $MgCl_2$ enables a high level of capacity retention (80%) during cyclic CO_2 capacity over several cycles. Its high volumetric energy density, 1878 MJ m^{-3}, low operation pressure, <6.0 bar, and appropriate operating temperature of 700 °C, makes this material highly competitive for TCES. Its cost-benefit is 60% cheaper on a materials basis than the molten salts currently used in CSP applications. A TCES system based on $SrCO_3$–$SrSiO_3$ requires a small footprint, which is essential for remote areas. It is also compatible with the Rankine–Brayton combined cycle and with a Stirling engine for thermal to electrical energy conversion and can be adapted for other forms of renewable energy such as photovoltaics and wind farms.

Conflicts of interest

There are no conflicts to declare.

Acknowledgements

CEB, MP and TDH acknowledge the Global Innovation Linkage project for grant GIL73589. KW acknowledges the Australian Government for an Australian Government Research Training Program Scholarship. CEB, MP, TDH, and APV acknowledge the Australian Research Council for ARC Discovery project grant DP200102301. MP thanks the Australian Research Council for ARC Future Fellowship FT160100303. SEM and XRD research was undertaken using the Tescan Mira3 EM (ARC LE130100053) and the Bruker D8 Advance XRD instrumentation (ARC LE0775551) at the John de Laeter Centre, Curtin University.

References

1 International Energy Agency, *World Energy Outlook*, 2016.
2 D. Archer, *Global Warming: Understanding the Forecast*, John Wiley & Sons, Inc., 2nd edn, 2012.
3 J. Sunku Prasad, P. Muthukumar, F. Desai, D. N. Basu and M. M. Rahman, *Appl. Energy*, 2019, **254**, 113733.
4 U. Desideri and P. Elia, *Appl. Energy*, 2014, **113**, 422–433.
5 K. T. Møller, A. Ibrahim, C. E. Buckley and M. Paskevicius, *J. Mater. Chem. A*, 2020, **8**, 9646–9653.
6 T. D. Humphries, K. T. Møller, W. D. A. Rickard, M. V. Sofianos, S. Liu, C. E. Buckley and M. Paskevicius, *J. Mater. Chem. A*, 2019, **7**, 1206–1215.
7 H. B. Dizaji and H. Hosseini, *Renewable Sustainable Energy Rev.*, 2018, **98**, 9–26.
8 M. Liu, N. H. Steven Tay, S. Bell, M. Belusko, R. Jacob, G. Will, W. Saman and F. Bruno, *Renewable Sustainable Energy Rev.*, 2016, **53**, 1411–1432.
9 H. Peng, D. Zhang, X. Ling, Y. Li, Y. Wang, Q. Yu, X. She, Y. Li and Y. Ding, *Energy Fuels*, 2018, **32**, 7262–7293.
10 D. Lefebvre and F. H. Tezel, *Renewable Sustainable Energy Rev.*, 2017, **67**, 116–125.
11 L. André, S. Abanades and G. Flamant, *Renewable Sustainable Energy Rev.*, 2016, **64**, 703–715.
12 K. T. Møller, K. Williamson, C. E. Buckley and M. Paskevicius, *J. Mater. Chem. A*, 2020, **8**, 10935–10942.
13 A. Solé, I. Martorell and L. F. Cabeza, *Renewable Sustainable Energy Rev.*, 2015, **47**, 386–398.
14 V. A. Yartys, M. V. Lototskyy, E. Akiba, R. Albert, V. E. Antonov, J. R. Ares, M. Baricco, N. Bourgeois, C. E. Buckley, J. M. Bellosta von Colbe, J. C. Crivello, F. Cuevas, R. V. Denys, M. Dornheim, M. Felderhoff, D. M. Grant, B. C. Hauback, T. D. Humphries, I. Jacob, T. R. Jensen, P. E. de Jongh, J. M. Joubert, M. A. Kuzovnikov, M. Latroche, M. Paskevicius, L. Pasquini, L. Popilevsky, V. M. Skripnyuk, E. Rabkin, M. V. Sofianos, A. Stuart, G. Walker, H. Wang, C. J. Webb and M. Zhu, *Int. J. Hydrogen Energy*, 2019, **44**, 7809–7859.
15 D. A. Sheppard, M. Paskevicius, T. D. Humphries, M. Felderhoff, G. Capurso, J. Bellosta von Colbe, M. Dornheim, T. Klassen, P. A. Ward, J. A. Teprovich, C. Corgnale, R. Zidan, D. M. Grant and C. E. Buckley, *Appl. Phys. A: Mater. Sci. Process.*, 2016, **122**, 1–15.
16 L. André and S. Abanades, *Energies*, 2020, **13**, 5859.
17 L. André and S. Abanades, *J. Energy Storage*, 2017, **13**, 193–205.
18 C. Ortiz, J. M. Valverde, R. Chacartegui, L. A. Perez-Maqueda and P. Giménez, *Renewable Sustainable Energy Rev.*, 2019, **113**, 109252.
19 K. K. Turekian and K. H. Wedepohl, *Geol. Soc. Am. Bull.*, 1961, **72**, 175–192.
20 L. Meroueh, K. Yenduru, A. Dasgupta, D. Jiang and N. AuYeung, *Renewable Energy*, 2019, **133**, 770–786.
21 P. Wasserscheid, W. Arlt, *German patent*, DE102010009543A1, 2011.
22 N. R. Rhodes, A. Barde, K. Randhir, L. Li, D. W. Hahn, R. Mei, J. F. Klausner and N. Auyeung, *ChemSusChem*, 2015, **8**, 3793–3798.
23 E. Bagherisereshki, J. Tran, F. Lei and N. AuYeung, *Sol. Energy*, 2018, **160**, 85–93.
24 Metso Outotec, *HSC Chemistry*, 2019, 9.
25 T. Block and M. Schmu, *Sol. Energy*, 2016, **126**, 195–207.
26 H. Takasu, J. Ryu and Y. Kato, *Appl. Energy*, 2017, **193**, 74–83.
27 O. Yamaguchi, K. Yabuno, K. Takeoka and K. Shimizu, *Chem. Lett.*, 1979, **8**, 401–404.
28 G. J. Janz, C. B. Allen, J. R. Downey Jr and R. P. T. Tomkins, *National Bureau of Standards*, 1978, SRDS-NBS 61, part I.
29 R. A. Young and R. A. Young, *The Rietveld Method*, Oxford University Press, 1995.
30 S. Brunauer, P. H. Emmett and E. Teller, *J. Am. Chem. Soc.*, 1938, **60**, 309–319.
31 E. P. Barrett, L. G. Joyner and P. P. Halenda, *J. Am. Chem. Soc.*, 1951, **73**, 373–380.
32 D. A. Sheppard, M. Paskevicius, P. Javadian, I. J. Davies and C. E. Buckley, *J. Alloys Compd.*, 2019, **787**, 1225–1237.

33 V. Manovic and E. J. Anthony, *Energy Fuels*, 2010, **24**, 5790–5796.
34 S. Kumar and S. K. Saxena, *Mater. Renew. Sustain. Energy*, 2014, **30**, 1–15.
35 J. Ichi Ida, R. Xiong and Y. S. Lin, *Sep. Purif. Technol.*, 2004, **36**, 41–51.
36 C. Qin, W. Liu, H. An, J. Yin and B. Feng, *Environ. Sci. Technol.*, 2012, **46**, 1932–1939.
37 J. M. Valverde, *J. Mater. Chem. A*, 2013, **1**, 447–468.
38 J. M. Valverde, P. E. Sanchez-Jimenez and L. A. Perez-Maqueda, *J. Phys. Chem. C*, 2015, **119**, 1623–1641.
39 G. Wang and L. Wang, *Fullerenes, Nanotubes, Carbon Nanostruct.*, 2019, **27**, 46–51.
40 P. Wichannananon, T. Kobkeatthawin and S. M. Smith, *Catalysts*, 2020, **10**, 1–14.
41 R. P. T. Tomkins and N. P. Bansal, *Gases in Molten Salts*, Pergamon Press, Oxford, 1st edn, 1991, vol. 45.
42 D. L. Kelting and C. L. Laxson, *Review of Effects and Costs of Road De-icing with Recommendations for Winter Road Management in the Adirondack Park Prepared by, Saranac Lake*, 2010.
43 K. Zhang, X. S. Li, H. Chen, P. Singh and D. L. King, *J. Phys. Chem. C*, 2016, **120**, 1089–1096.
44 A. H. Bork, M. Rekhtina, E. Willinger, P. Castro-Fernández, J. Drnec, P. M. Abdala and C. R. Müller, *Proc. Natl. Acad. Sci. U. S. A.*, 2021, **118**, e2103971118.
45 S. I. Jo, Y. I. An, K. Y. Kim, S. Y. Choi, J. S. Kwak, K. R. Oh and Y. U. Kwon, *Phys. Chem. Chem. Phys.*, 2017, **19**, 6224–6232.
46 A. Dal Pozzo, A. Armutlulu, M. Rekhtina, P. M. Abdala and C. R. Müller, *ACS Appl. Energy Mater.*, 2019, **2**, 1295–1307.
47 T. Harada, F. Simeon, E. Z. Hamad and T. A. Hatton, *Chem. Mater.*, 2015, **27**, 1943–1949.
48 K. Zhang, X. S. Li, W. Z. Li, A. Rohatgi, Y. Duan, P. Singh, L. Li and D. L. King, *Adv. Mater. Interfaces*, 2014, **1**, 1–6.
49 H. Cui, Q. Zhang, Y. Hu, C. Peng, X. Fang, Z. Cheng, V. V. Galvita and Z. Zhou, *ACS Appl. Mater. Interfaces*, 2018, **10**, 20611–20620.
50 A. Bayon, R. Bader, M. Jafarian, L. Fedunik-Hofman, Y. Sun, J. Hinkley, S. Miller and W. Lipiński, *Energy*, 2018, **149**, 473–484.
51 S. Jin, G. Dong, J. Luo, F. Ma and C. Wang, *Appl. Catal., B*, 2018, **227**, 24–34.
52 V. Zare and M. Hasanzadeh, *Energy Convers. Manage.*, 2016, **128**, 227–237.
53 J. S. Bae and S. K. Bhatia, *Energy Fuels*, 2006, **20**, 2599–2607.

Electronic Supplementary Material (ESI) for Journal of Materials Chemistry A.

Supplementary Information:

A New Strontium Based Reactive Carbonate Composite for Thermochemical Energy Storage

Adriana P. Vieira,* Kyran Williamson, Terry D. Humphries, Mark Paskevicius, Craig E. Buckley*

Physics and Astronomy, Fuels and Energy Technology Institute, Curtin University, GPO Box U1987, Perth, WA 6845, Australia. E-mail: apiresvieira@gmail.com; c.buckley@curtin.edu.au

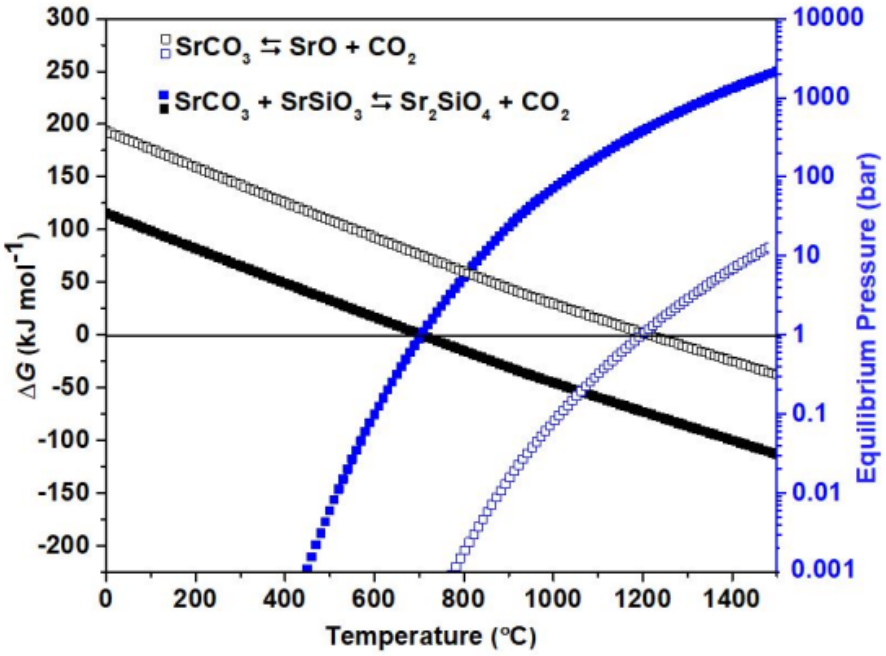

Figure **SI-1:** Gibbs free energy and equilibrium pressure dependence on temperature based on thermodynamics of the reactions.[24]

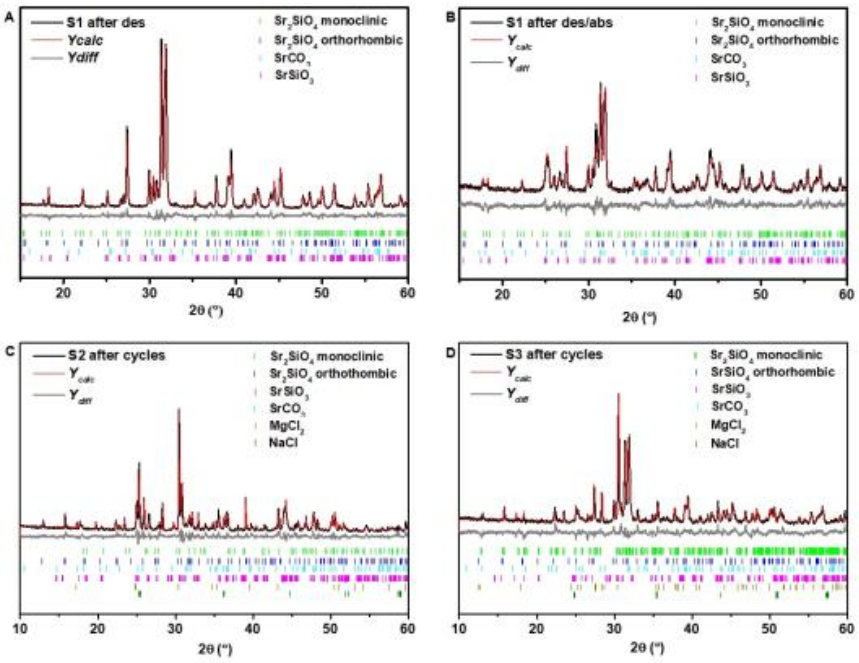

Figure **SI-2**: Rietveld refinement of (A) **S1** after desorption. R_{wp} = 7.89%; (B) **S1** after des/abs. R_{wp} = 8.34%; (C) **S2** after cycles. R_{wp} = 7.24% (C); (D) **S3** after cycles. R_{wp} = 7.61%.

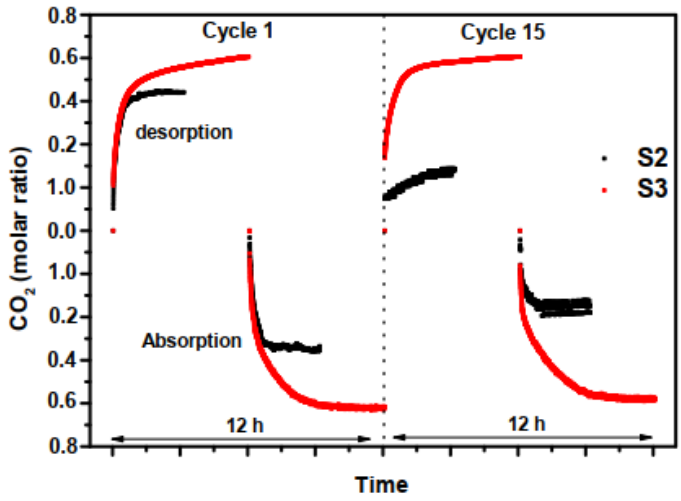

Figure SI-3. Comparison of the kinetics of CO_2 desorption/absorption between the 1st and 15th cycles for samples **S2** and **S3.**

APPENDIX – C Supplementary information

The following pre-liminary screening results were used in the material selection process and relate to Chapter 2

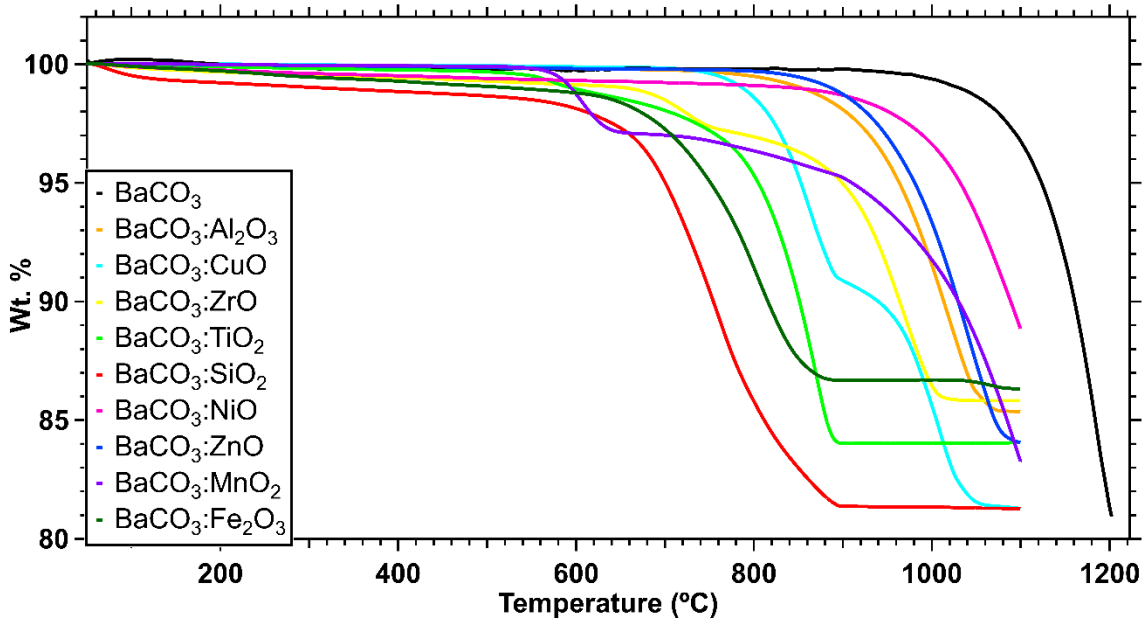

Figure S-6-1: TGA measurements comparing the decomposition of $BaCO_3$ combined with various metal oxides heated from room temperature to 1200 °C at $\Delta T/\Delta t$ = 10 °C min^{-1} under an argon flow of 20 mL min^{-1}.

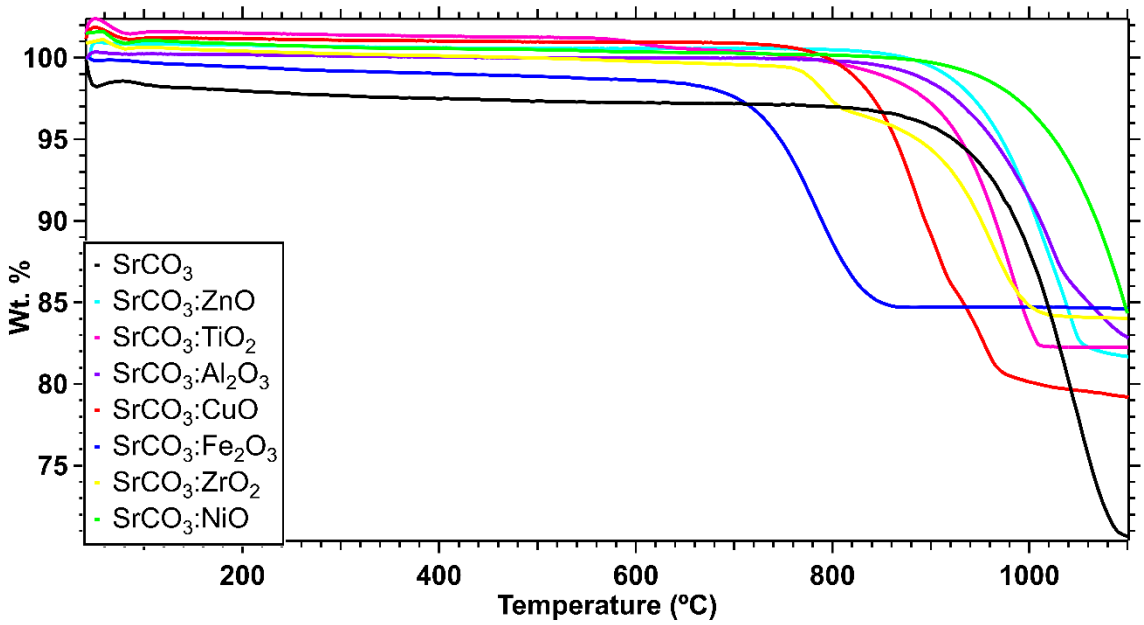

Figure S-6-2: TGA measurements comparing the decomposition of $SrCO_3$ combined with various metal oxides heated from room temperature to 1200 °C at $\Delta T/\Delta t$ = 10 °C min^{-1} under an argon flow of 20 mL min^{-1}.

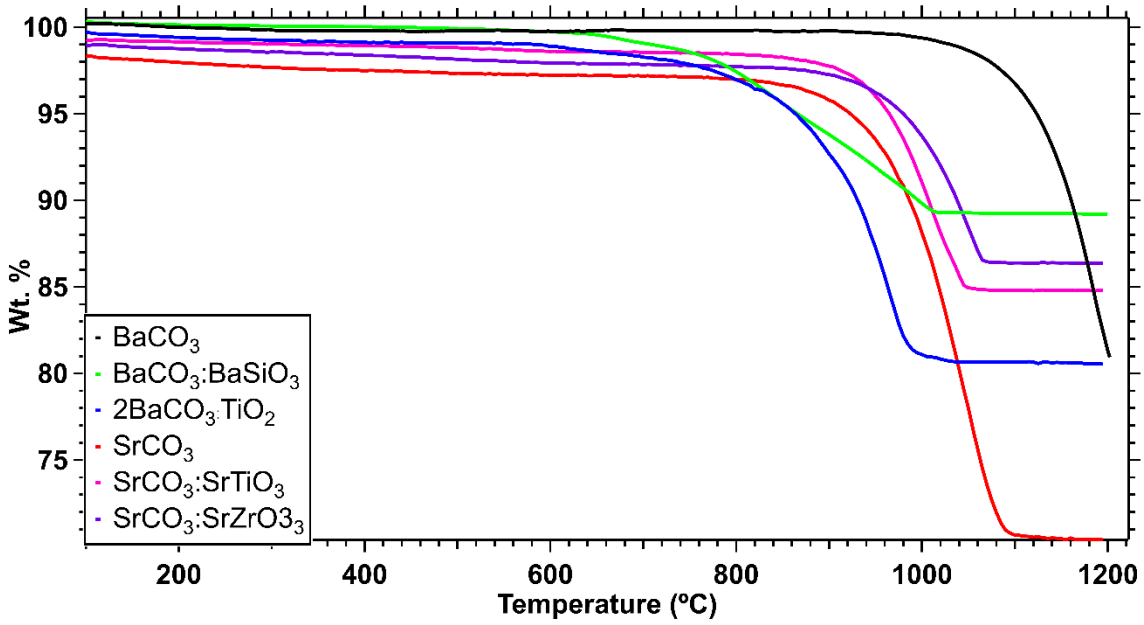

Figure S-6-3: TGA measurements comparing the decomposition of potential TCES materials made from $BaCO_3$ or $SrCO_3$ heated from room temperature to 1200 °C at $\Delta T/\Delta t$ = 10 °C min^{-1} under an argon flow of 20 mL min^{-1}.

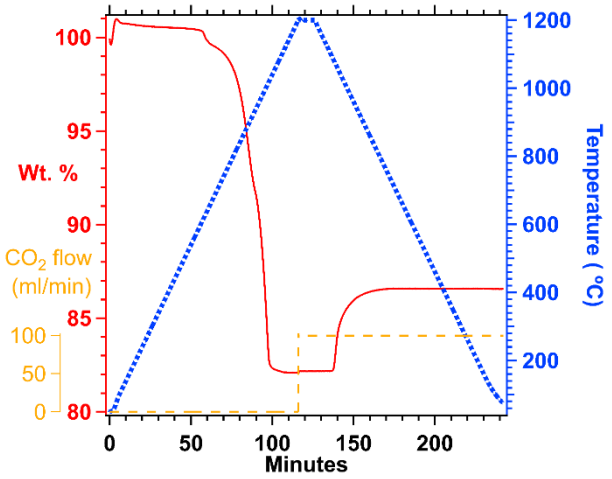

Figure S-6-4: TGA wt% (red) measurements of milled $BaCO_3$:Al_2O_3 heated ($\Delta T/\Delta t$= 10°C·min^{-1}) and cooled ($\Delta T/\Delta t$ = -10°C·min^{-1}) (blue) in an Al_2O_3 crucible with CO_2 gas flow rate (orange) and a constant flow of argon (20 mL·min^{-1}).

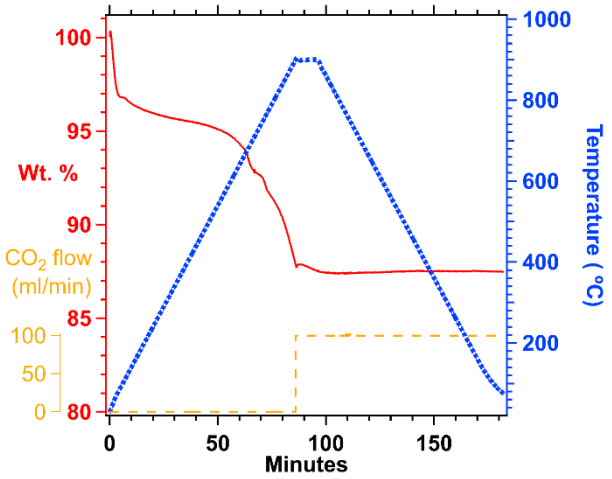

Figure S-6-5: TGA wt% (red) measurements of milled $BaCO_3$:$BaSiO_3$:0.05$CaCO_3$ heated ($\Delta T/\Delta t$= 10°C·min^{-1}) and cooled ($\Delta T/\Delta t$ = -10°C·min^{-1}) (blue) in an Al_2O_3 crucible with CO_2 gas flow rate (orange) and a constant flow of argon (20 mL·min^{-1}).

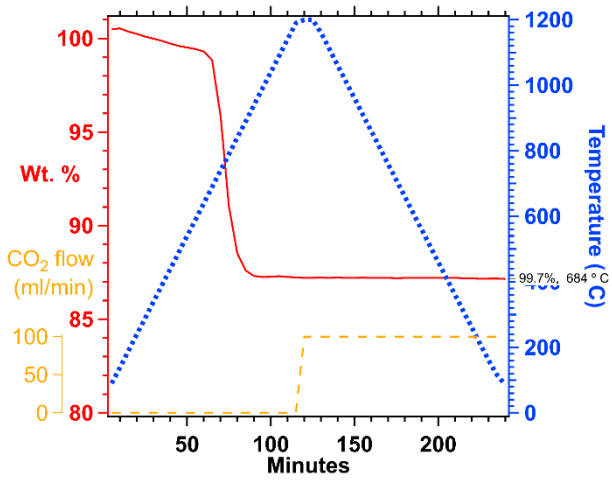

Figure S-6-6: TGA Wt% (red) measurements of milled $BaCO_3$:Fe_2O_3 heated ($\Delta T/\Delta t$ = 10°C·min^{-1}) and cooled ($\Delta T/\Delta t$ = -10°C·min^{-1}) (blue) in an Al_2O_3 crucible with CO_2 gas flow rate (orange) and a constant flow of argon (20 mL·min^{-1}).

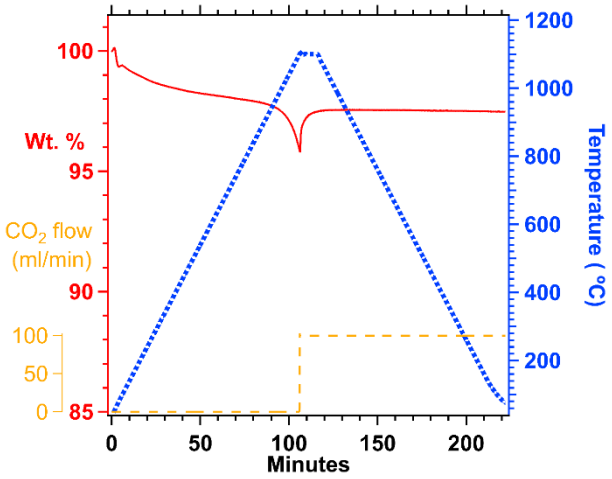

Figure S-6-7: TGA wt% (red) measurements of milled $BaCO_3$:NiO heated ($\Delta T/\Delta t$ = 10°C·min^{-1}) and cooled ($\Delta T/\Delta t$ = -10°C·min^{-1}) (blue) in an Al_2O_3 crucible with CO_2 gas flow rate (orange) and a constant flow of argon (20 mL·min^{-1}).

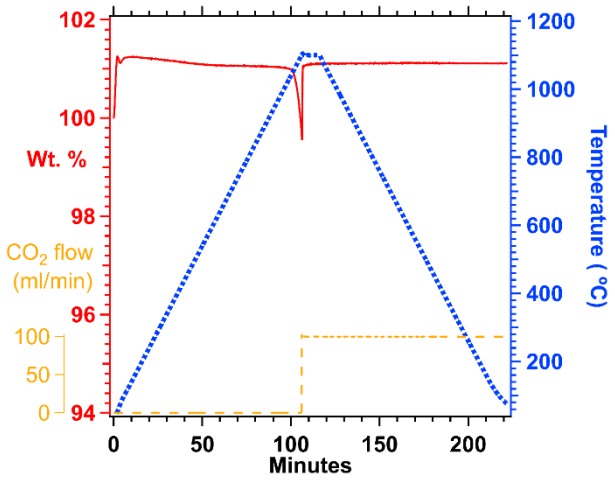

Figure S-6-8: TGA wt% (red) measurements of milled $BaCO_3$:ZnO heated ($\Delta T/\Delta t$ = 10°C·min^{-1}) and cooled ($\Delta T/\Delta t$ = -10°C·min^{-1}) (blue) in an Al_2O_3 crucible with CO_2 gas flow rate (orange) and a constant flow of argon (20 mL·min^{-1}).

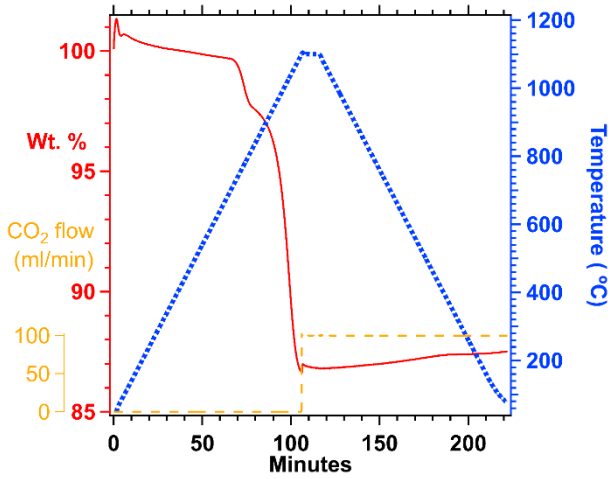

Figure S-6-9: TGA wt% (red) measurements of milled $BaCO_3$:ZrO_2 heated ($\Delta T/\Delta t$ = 10°C·min^{-1}) and cooled ($\Delta T/\Delta t$ = -10°C·min^{-1}) (blue) in an Al_2O_3 crucible with CO_2 gas flow rate (orange) and a constant flow of argon (20 mL·min^{-1}).

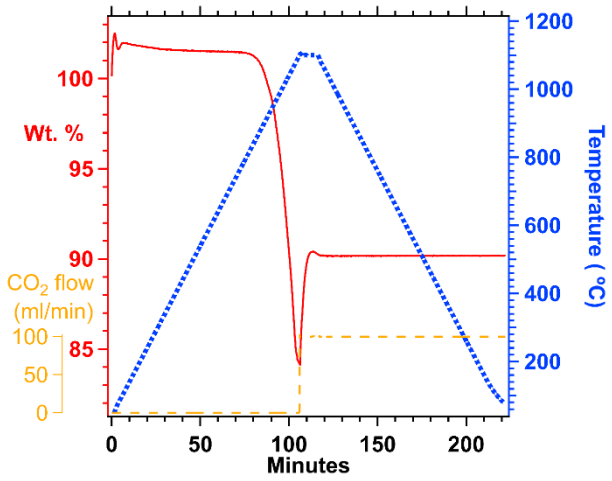

Figure S-6-10: TGA wt% (red) measurements of milled $SrCO_3$:Al_2O_3 heated ($\Delta T/\Delta t$ = 10°C·min^{-1}) and cooled ($\Delta T/\Delta t$ = -10°C·min^{-1}) (blue) in an Al_2O_3 crucible with CO_2 gas flow rate (orange) and a constant flow of argon (20 mL·min^{-1}).

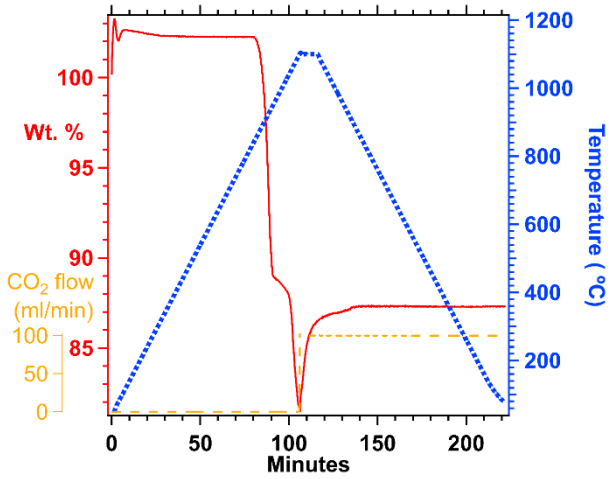

Figure S-6-11: TGA wt% (red) measurements of milled $SrCO_3$:CuO heated ($\Delta T/\Delta t$ = 10°C·min^{-1}) and cooled ($\Delta T/\Delta t$ = -10°C·min^{-1}) (blue) in an Al_2O_3 crucible with CO_2 gas flow rate (orange) and a constant flow of argon (20 mL·min^{-1}).

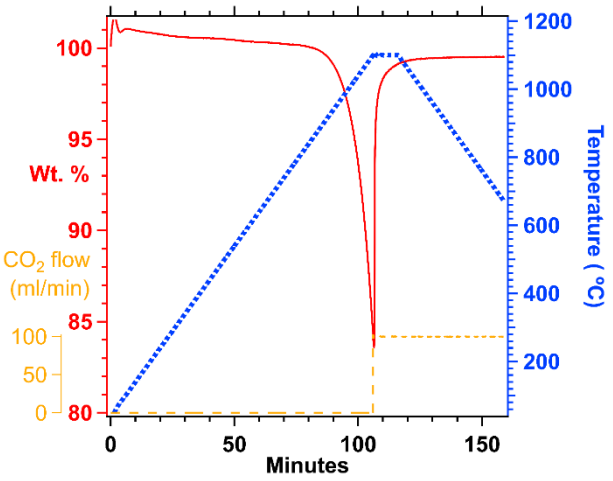

Figure S-6-12: TGA wt% (red) measurements of milled $SrCO_3$:NiO heated ($\Delta T/\Delta t$ = 10°C·min^{-1}) and cooled ($\Delta T/\Delta t$ = -10°C·min^{-1}) (blue) in an Al_2O_3 crucible with CO_2 gas flow rate (orange) and a constant flow of argon (20 mL·min^{-1}).

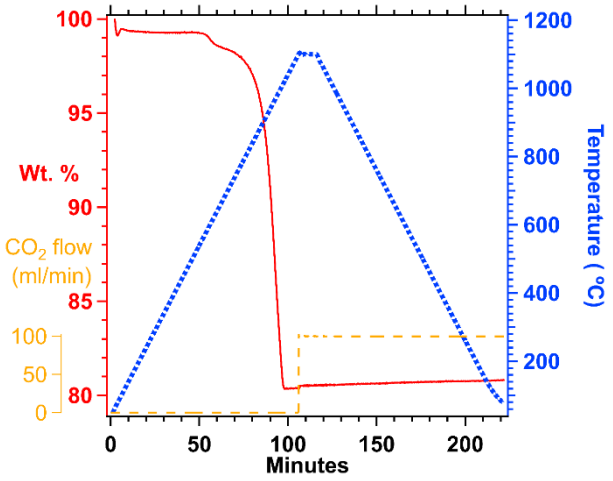

Figure S-6-13: TGA wt% (red) measurements of milled $SrCO_3$:TiO_2 heated ($\Delta T/\Delta t$ = 10°C·min^{-1}) and cooled ($\Delta T/\Delta t$ = -10°C·min^{-1}) (blue) in an Al_2O_3 crucible with CO_2 gas flow rate (orange) and a constant flow of argon (20 mL·min^{-1}).

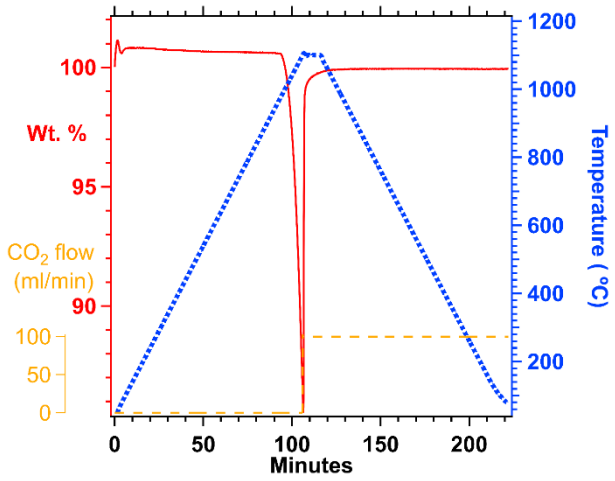

Figure S-6-14: TGA wt% (red) measurements of milled $SrCO_3$:ZnO heated ($\Delta T/\Delta t$ = 10°C·min^{-1}) and cooled ($\Delta T/\Delta t$ = -10°C·min^{-1}) (blue) in an Al_2O_3 crucible with CO_2 gas flow rate (orange) and a constant flow of argon (20 mL·min^{-1}).

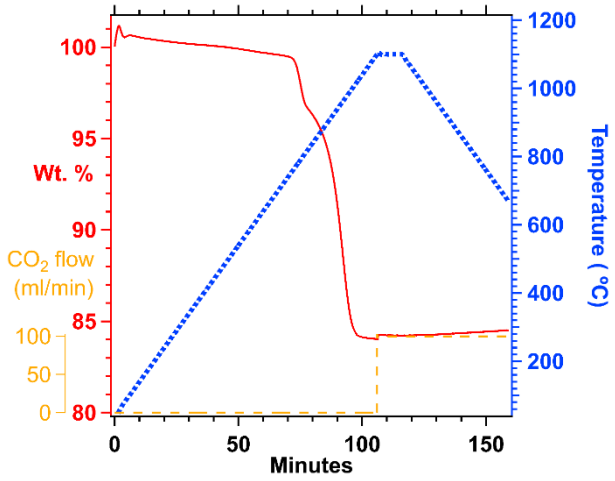

Figure S-6-15: TGA wt% (red) measurements of milled $SrCO_3$:ZrO_2 heated ($\Delta T/\Delta t$ = 10°C·min^{-1}) and cooled ($\Delta T/\Delta t$ = -10°C·min^{-1}) (blue) in an Al_2O_3 crucible with CO_2 gas flow rate (orange) and a constant flow of argon (20 mL·min^{-1}).

Supplementary information for Chapter 3

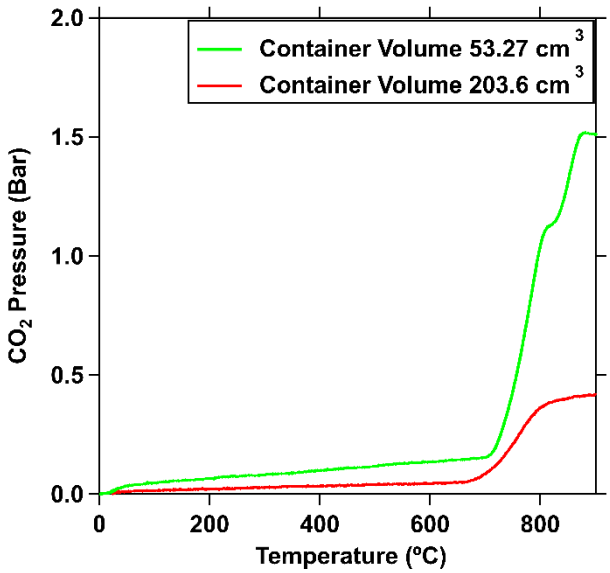

Figure S-6-16: ~ 1 g of BaCO3-Fe2O3 heated from room temperature to 900 °C. ΔT/Δt = 10 °C min-1) using a sealed volume in a Sieverts apparatus at pinitial(CO2) = 10-2 bar: using a volume of either 53.27 cm3 (green curve) or 203.6 cm3 (red curve), which influences the CO2 pressure achieved during decomposition of the BaCO3-Fe2O3 RCC.

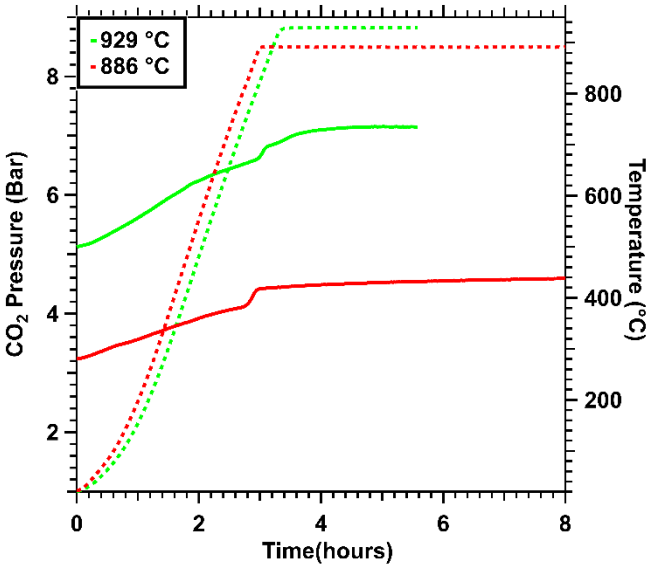

Figure S-6-17: ~ 1 g of BaCO3-Fe2O3 heated from room temperature to 900 °C. ΔT/Δt = 10 °C min-1) in a sealed volume (53.27 cm3) using Sieverts apparatus. Dashed curve represents the temperature and solid curve represents the pressure.

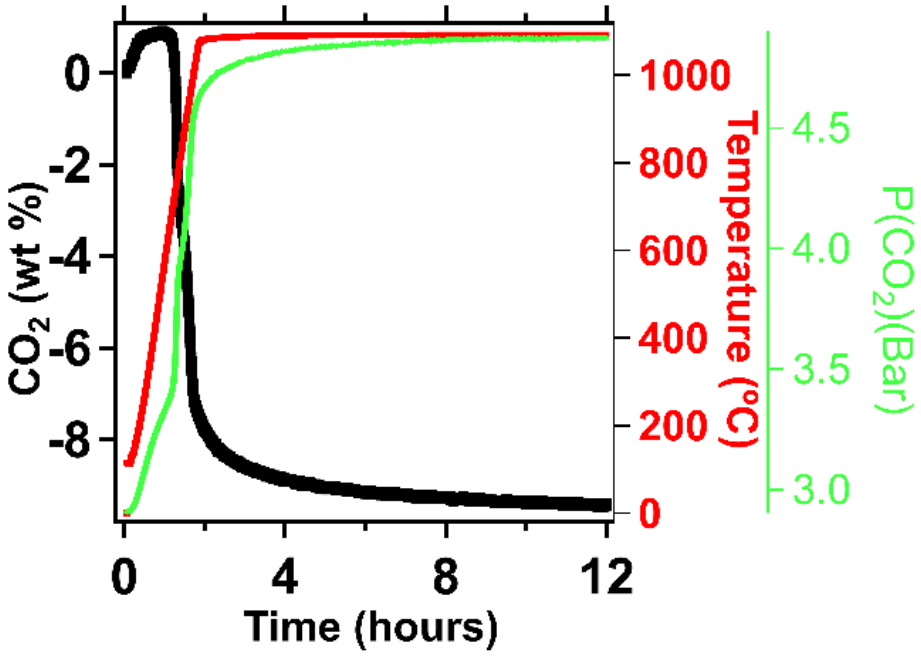

Figure S-18: 1.07 g of $2BaCO_3$:TiO_2 was heated ($\Delta T/\Delta t$ =10 °C) from room temperature and $p(CO_2)$ = 3 bar to 1091 °C in a sealed volume using sieverts apparatus V = 63.7 cc

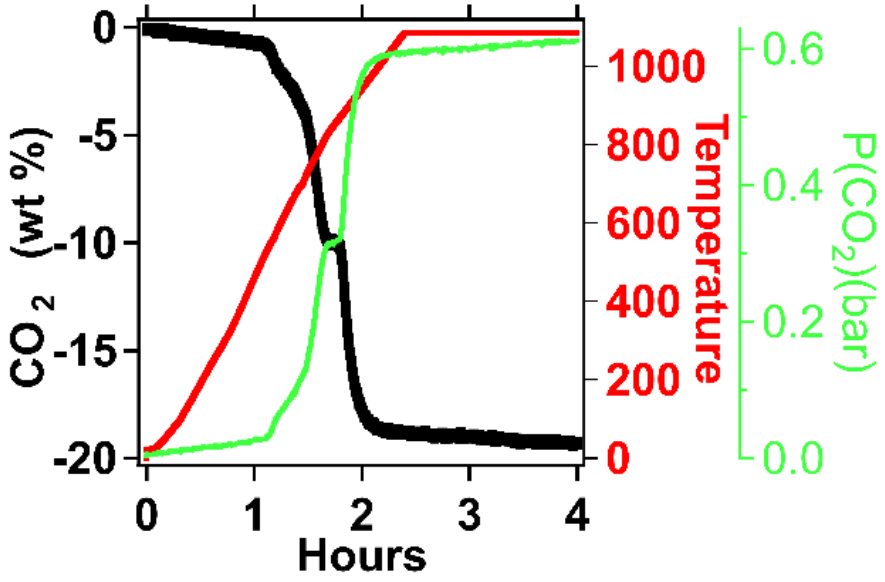

Figure S-19: 1.12 g of $2BaCO_3$:TiO_2 was heated from room temperature and static vacuum ($p_{initial}(CO_2)$ = 10^{-2} bar) to 1085 °C in a sealed volume using sieverts apparatus V = 195.30 cm^3.

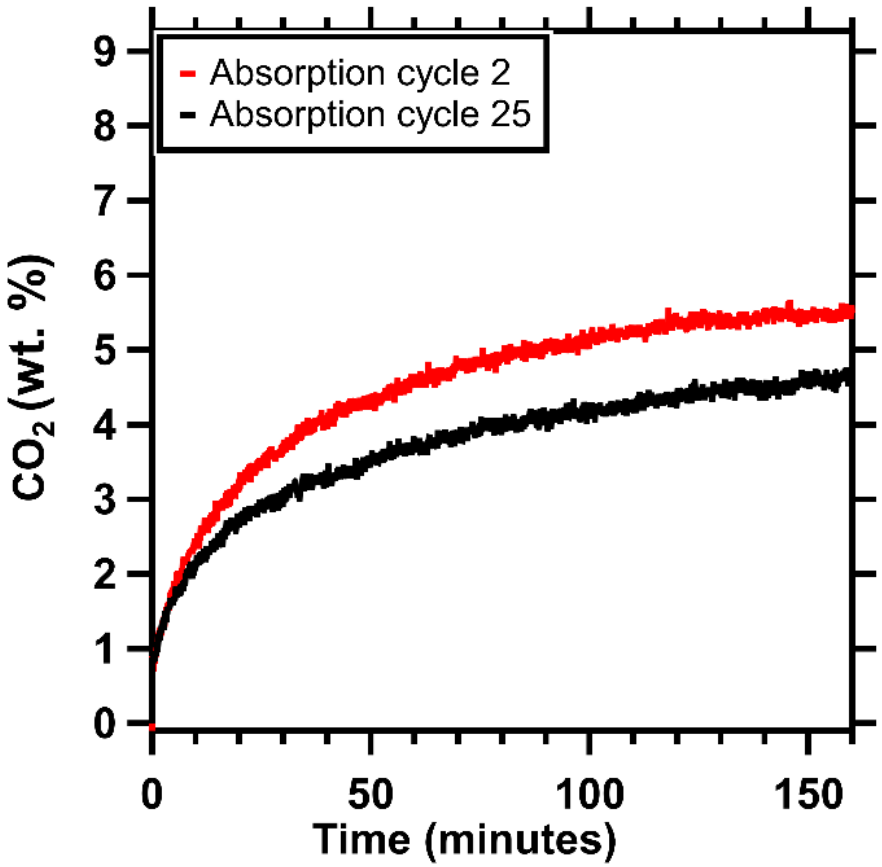

Figure S-20:1.12 grams of $2BaCO_3$:TiO_2 was exposed to 25 pressure cycles of absorption (2.15 bar), and desorption using Sieverts apparatus (p_{des} = 0.35 bar), T = 1085 °C, this is a comparison of the kinetics of absorption for the 2nd and 25th cycle.

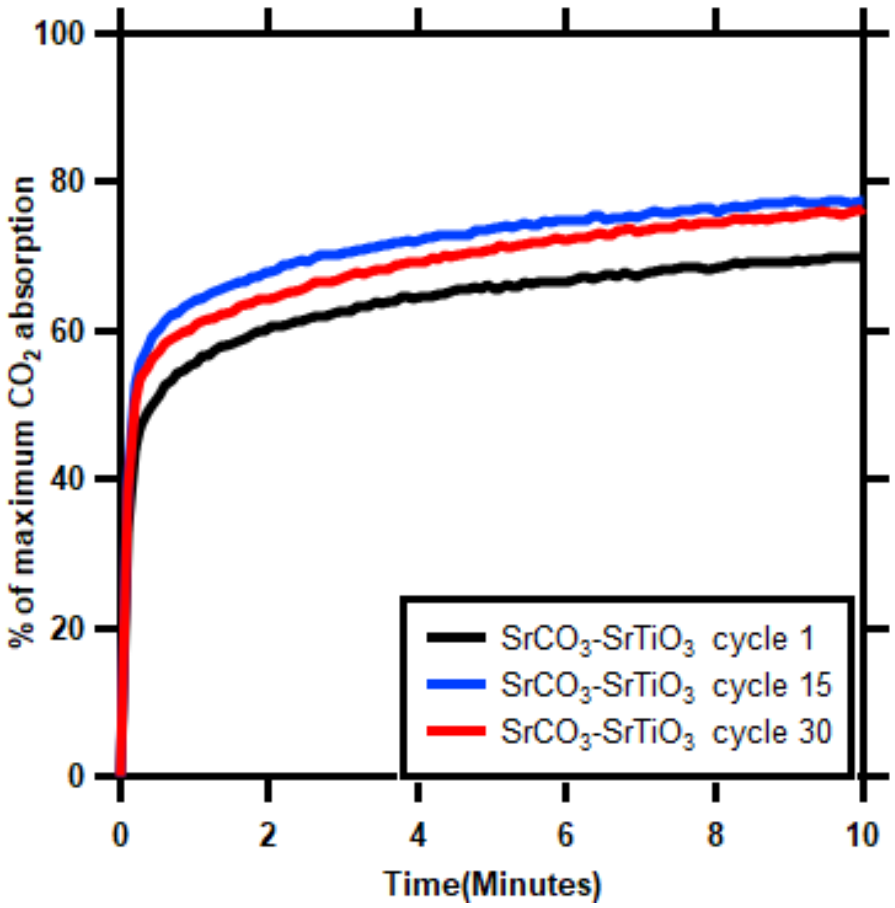

Figure S-21:. Absorption kinetic curves of $SrCO_3$ – 1M $SrTiO_3$. Measurements were carried out using Sieverts method at 1100 °C, mass = 0.81 g, abs p(CO2) = (5 bar), t = (1 hour)

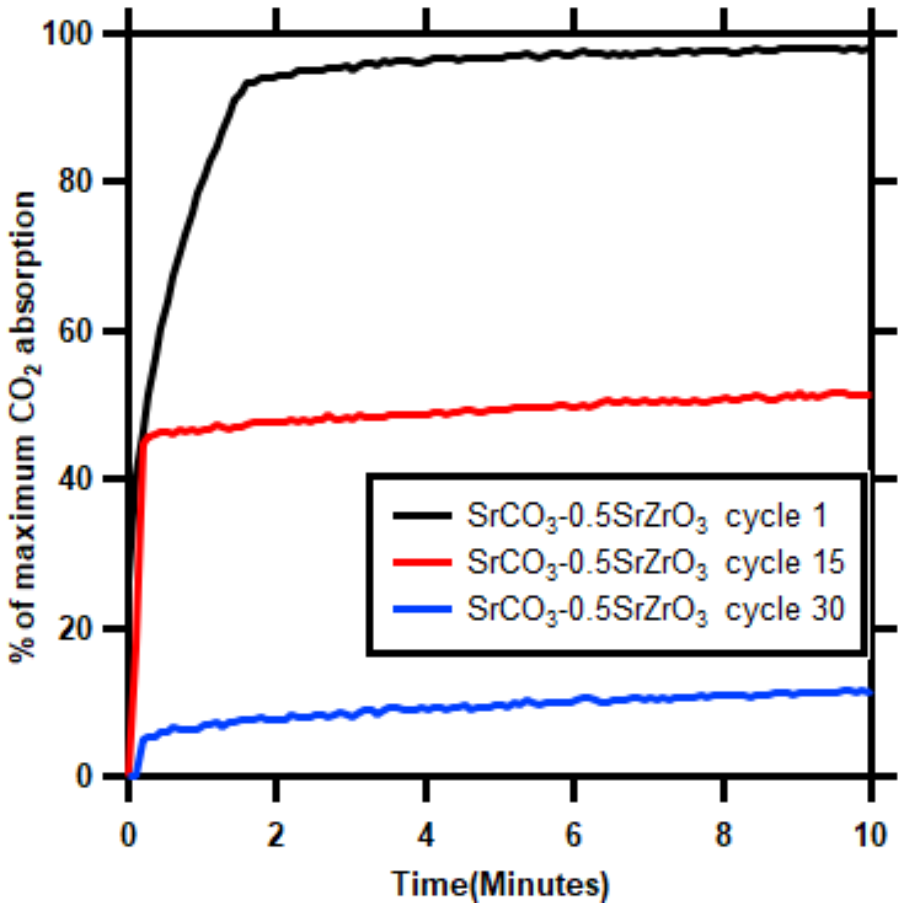

Figure S-22: Absorption kinetic curves of $SrCO_3$ – 1M $SrZrO_3$. Measurements were carried out using Sieverts method at 1100 °C, mass = 0.81 g, abs p(CO2) = (5 bar), t = (1 hour)

APPENDIX – D Permission from copyright owners

Licence Figure 1-1 and Figure 1-2

Licence for Figure 1-5

ELSEVIER LICENSE
TERMS AND CONDITIONS
Aug 25, 2023

This Agreement between Curtin University -- Kyran Williamson ("You") and Elsevier ("Elsevier") consists of your license details and the terms and conditions provided by Elsevier and Copyright Clearance Center.

License Number	5615820163784
License date	Aug 25, 2023
Licensed Content Publisher	Elsevier
Licensed Content Publication	Journal of Energy Storage
Licensed Content Title	Thermochemical batteries using metal carbonates: A review of heat storage and extraction
Licensed Content Author	Lucie Desage,Eleanor McCabe,Adriana P. Vieira,Terry D. Humphries,Mark Paskevicius,Craig E. Buckley

Licensed Content Date	Nov 1, 2023
Licensed Content Volume	71
Licensed Content Issue	n/a
Licensed Content Pages	1
Start Page	107901
End Page	0
Type of Use	reuse in a thesis/dissertation
Portion	figures/tables/illustrations
Number of figures/tables/illustrations	1
Format	both print and electronic
Are you the author of this Elsevier article?	No
Will you be translating?	No
Title	Investigation of Metal Carbonates for Cost competitive thermal batteries.
Institution name	Curtin University
Expected presentation date	Aug 2023
Portions	Fig. 2. Schematic of a TCES cycle, adapted from [36].

Licence for content of Chapter 3

Thermochemical energy storage in barium carbonate enhanced by iron(III) oxide

K. Williamson, K. T. Møller, A. M. D'Angelo, T. D. Humphries, M. Paskevicius and C. E. Buckley, *Phys. Chem. Chem. Phys.*, 2023, **25**, 7268 **DOI:** 10.1039/D2CP05745J

Licence for content of Appendix A

Thermochemical energy storage properties of a barium based reactive carbonate composite

K. T. Møller, K. Williamson, C. E. Buckley and M. Paskevicius, *J. Mater. Chem. A*, 2020, **8**, 10935 **DOI:** 10.1039/D0TA03671D

Licence for content of Appendix B

A new strontium based reactive carbonate composite for thermochemical energy storage

A. P. Vieira, K. Williamson, T. D. Humphries, M. Paskevicius and C. E. Buckley, *J. Mater. Chem. A*, 2021, **9**, 20585 **DOI:** 10.1039/D1TA04363C

All reasonable efforts have been made to acknowledge the owners of copyright material. I would love to hear from any copyright owners that have been omitted or incorrectly acknowledged.

APPENDIX – E Co-author attribution Statements

Chapter 3: Williamson, K.; Møller, K. T.; D'Angelo, A. M.; Humphries, T. D.; Paskevicius, M.; Buckley, C. E. Thermochemical Energy Storage in Barium Carbonate Enhanced by Iron(III) Oxide. *Phys. Chem. Chem. Phys.* **2023**, *25* (10), 7268–7277. https://doi.org/10.1039/D2CP05745J.

Name	Conception and design	Experiments conduction and data acquisition	Data processing and analysis	Interpretation and discussion	Manuscript writing and revision
Kyran Williamson	X	X	X	X	X
I acknowledge that these represent my contribution to the above research output and I have approved the final version. **Signature:**					
Anita M. D' Angelo		**x**		**x**	x
I acknowledge that these represent my contribution to the above research output and I have approved the final version. **Signature:**					
Kasper T. Møller	X	X	x		X
I acknowledge that these represent my contribution to the above research output and I have approved the final version. **Signature:**					
Terry D. Humphries		X			x
I acknowledge that these represent my contribution to the above research output and I have approved the final version. **Signature:**					
Mark Paskevicius			x	x	x
I acknowledge that these represent my contribution to the above research output and I have approved the final version. **Signature:**					
Craig E. Buckley					X
I acknowledge that these represent my contribution to the above research output and I have approved the final version. **Signature:**					

Chapter 4: Williamson, K.; D'Angelo, A. M.; Humphries, T. D.; Paskevicius, M.; Buckley, C. E. Barium carbonate and barium titanate for ultra-high-temperature thermal energy storage. [In press]

Name	Conception and design	Experiments conduction and data acquisition	Data processing and analysis	Interpretation and discussion	Manuscript writing and revision
Kyran Williamson	X	X	X	X	X
I acknowledge that these represent my contribution to the above research output and I have approved the final version. **Signature:**					
Anita M. D' Angelo		X			X
I acknowledge that these represent my contribution to the above research output and I have approved the final version. **Signature:**					
Terry D. Humphries		X			x
I acknowledge that these represent my contribution to the above research output and I have approved the final version. **Signature:**					
Mark Paskevicius			x	x	x
I acknowledge that these represent my contribution to the above research output and I have approved the final version. **Signature:**					
Craig E. Buckley				x	X
I acknowledge that these represent my contribution to the above research output and I have approved the final version. **Signature:**					

Chapter 5: Williamson, K.; Liu, Y; Humphries, T. D.; D'Angelo, A. M.; Paskevicius, M.; Buckley, C. E. Thermochemical energy storage in $SrCO_3$ composites with $SrTiO_3$ or $SrZrO_3$ [In press]

Name	Conception and design	Experiments conduction and data acquisition	Data processing and analysis	Interpretation and discussion	Manuscript writing and revision
Kyran Williamson	x	X	X	X	X
I acknowledge that these represent my contribution to the above research output and I have approved the final version. **Signature:**					
Yurong Liu	**x**	**x**	**x**	**x**	x
I acknowledge that these represent my contribution to the above research output and I have approved the final version. **Signature:**					
Terry D. Humphries		x			x
I acknowledge that these represent my contribution to the above research output and I have approved the final version. **Signature:**					
Anita M. D' Angelo		X			x
I acknowledge that these represent my contribution to the above research output and I have approved the final version. **Signature:**					
Mark Paskevicius	X	X			X
I acknowledge that these represent my contribution to the above research output and I have approved the final version. **Signature:**					
Craig E. Buckley					x
I acknowledge that these represent my contribution to the above research output and I have approved the final version. **Signature:**					

Appendix A: Møller, K. T.; Williamson, K.; Buckley, C. E.; Paskevicius, M. Thermochemical Energy Storage Properties of a Barium Based Reactive Carbonate Composite. *J. Mater. Chem. A* **2020**, *8* (21), 10935–10942. https://doi.org/10.1039/D0TA03671D.

Name	Conception and design	Experiments conduction and data acquisition	Data processing and analysis	Interpretation and discussion	Manuscript writing and revision
Kasper T. Møller	X	X	X	X	X
I acknowledge that these represent my contribution to the above research output and I have approved the final version. **Signature:**					
Kyran Williamson		X	X	x	X
I acknowledge that these represent my contribution to the above research output and I have approved the final version. **Signature:**					
Craig E. Buckley					x
I acknowledge that these represent my contribution to the above research output and I have approved the final version. **Signature:**					
Mark Paskevicius	X				X
I acknowledge that these represent my contribution to the above research output and I have approved the final version. **Signature:**					

Appendix B : Vieira, A. P.; Williamson, K.; Humphries, T. D.; Paskevicius, M.; Buckley, C. E. A New Strontium Based Reactive Carbonate Composite for Thermochemical Energy Storage. *J. Mater. Chem. A* **2021**, *9* (36), 20585–20594. https://doi.org/10.1039/D1TA04363C.

Name	Conception and design	Experiments conduction and data acquisition	Data processing and analysis	Interpretation and discussion	Manuscript writing and revision
Adriana Pires Vieira	X	X	X	X	X
I acknowledge that these represent my contribution to the above research output and I have approved the final version. **Signature:**					
Kyran Williamson	X	X	x		X
I acknowledge that these represent my contribution to the above research output and I have approved the final version. **Signature:**					
Terry Humphries		X			x
I acknowledge that these represent my contribution to the above research output and I have approved the final version. **Signature:**					
Mark Paskevicius			x	x	x
I acknowledge that these represent my contribution to the above research output and I have approved the final version. **Signature:**					
Craig E. Buckley					X
I acknowledge that these represent my contribution to the above research output and I have approved the final version. **Signature:**					